VOLUME 81 DECEMBER 1, 1977 NUMBER 24

JPCHAx

THE JOURNAL OF PHYSICAL CHEMISTRY

PUBLISHED BIWEEKLY BY THE AMERICAN CHEMICAL SOCIETY

THE JOURNAL OF

PHYSICAL CHEMISTRY

BRYCE CRAWFORD, Jr., *Editor*
STEPHEN PRAGER, *Associate Editor*
ROBERT W. CARR, Jr., C. ALDEN MEAD, *Assistant Editors*

EDITORIAL BOARD: C. A. ANGELL (1973–1977), F. C. ANSON (1974–1978), V. A. BLOOMFIELD (1974–1978), J. R. BOLTON (1976–1980), L. M. DORFMAN (1974–1978), W. E. FALCONER (1977–1978), H. L. FRIEDMAN (1975–1979), H. L. FRISCH (1976–1980), W. A. GODDARD (1976–1980), E. J. HART (1975–1979), W. J. KAUZMANN (1974–1978), R. L. KAY (1977–1981), D. W. McCLURE (1974–1978), K. MYSELS (1977–1981), R. M. NOYES (1973–1977), R. G. PARR (1977–1979), W. B. PERSON (1976–1980), J. C. POLANYI (1976–1980), S. A. RICE (1976–1980), F. S. ROWLAND (1973–1977), R. L. SCOTT (1973–1977), W. A. STEELE (1976–1980), J. B. STOTHERS (1974–1978), F. A. VAN-CATLEDGE (1977–1981), B. WEINSTOCK (1977)

Published by the
AMERICAN CHEMICAL SOCIETY
BOOKS AND JOURNALS DIVISION

D. H. Michael Bowen, Director

Marjorie Laflin, Assistant to the Director

Editorial Department: Charles R. Bertsch, Head; Marianne C. Brogan, Associate Head; Joseph E. Yurvati, Assistant Editor

Magazine and Production Department: Bacil Guiley, Head

Research and Development Department: Seldon W. Terrant, Head

Advertising Office: Centcom, Ltd., 25 Sylvan Road South, Westport, Conn. 06880.

© Copyright, 1977, by the American Chemical Society. No part of this publication may be reproduced in any form without permission in writing from the American Chemical Society.

Published biweekly by the American Chemical Society at 20th and Northampton Sts., Easton, Pennsylvania 18042. Second class postage paid at Washington, D.C. and at additional mailing offices.

Editorial Information

Instructions for authors are printed in the first issue of each volume. Please conform to these instructions when submitting manuscripts.

Manuscripts for publication should be submitted to *The Journal of Physical Chemistry*, Department of Chemistry, University of Minnesota, Minneapolis, Minn. 55455. Correspondence regarding **accepted papers and proofs** should be directed to the Editorial Department at the address below.

Page charges of $60.00 per page may be paid for papers published in this journal. Payment does not affect acceptance or scheduling of papers.

Bulk reprints or photocopies of individual articles are available. For information write to Business Operations, Books and Journals Division at the ACS Washington address.

Requests for **permission to reprint** should be directed to Permissions, Books and Journals Division at the ACS Washington address. The American Chemical Society and its Editors assume no responsibility for the statements and opinions advanced by contributors.

Subscription and Business Information

1977 Subscription rates—including surface postage

	U.S.	PUAS	Canada, Foreign
Member	$24.00	$33.00	$34.00
Nonmember	96.00	105.00	106.00
Supplementary material	15.00	19.00	20.00

Air mail and air freight rates are available from Membership & Subscription Services, at the address below.

New and renewal subscriptions should be sent with payment to the Office of the Controller at the ACS Washington address. **Changes of address** must include both old and new addresses with ZIP code and a recent mailing label. Send all address changes to Membership & Subscription Services. Please allow six weeks for change to become effective. **Claims for missing numbers** will not be allowed if loss was due to failure of notice of change of address to be received in the time specified: if claim is dated (a) North America—more than 90 days beyond issue date, (b) all other foreign—more than 1 year beyond issue date; or if the reason given is "missing from files". Hard copy claims are handled by Membership & Subscription Services.

Microfiche subscriptions are available at the same rates but are mailed first class to U.S. subscribers, air mail to the rest of the world. Direct all inquiries to Special Issues Sales, at the ACS Washington address or call (202) 872-4554. **Single issues** in hard copy and/or microfiche are available from Special Issues Sales at the ACS Washington address. Current year $4.75. Back issue rates available from Special Issues Sales. **Back volumes** are available in hard copy and/or microform. Write to Special Issues Sales at the ACS Washington address for further information. **Microfilm** editions of ACS periodical publications are available from volume 1 to the present. For further information, contact Special Issues Sales at the ACS Washington address. **Supplementary material** mentioned in the journal appears in the microfilm edition. Single copies may be ordered directly from Business Operations, Books and Journals Division, at the ACS Washington address.

	U.S.	PUAS, Canada	Other Foreign
Microfiche	$2.50	$3.00	$3.50
Photocopy			
1–7 pages	4.00	5.50	7.00
8–20 pages	5.00	6.50	8.00

Orders over 20 pages are available only on microfiche, 4 × 6 in., 24X, negative, silver halide. Orders must state photocopy or microfiche if both are available. Full bibliographic citation including names of all authors and prepayment are required. Prices are subject to change.

American Chemical Society
1155 16th Street, N.W.
Washington, D.C. 20036
(202) 872-4600

Editorial Department
American Chemical Society
P.O. Box 3330
Columbus, Ohio 43210
(614) 421-6940 ext 3171

Membership & Subscription Services
American Chemical Society
P.O. Box 3337
Columbus, Ohio 43210
(614) 421-7230

Notice to Authors last printed in the issue of January 13, 1977

THE JOURNAL OF

PHYSICAL CHEMISTRY

Volume 81, Number 24 December 1, 1977

JPCHAx 81(24) 2215–2308 (1977)

ISSN 0022-3654

หอสมุดกลาง จุฬาลงกรณ์มหาวิทยาลัย
1A 31 มี.ค. 2521

COMMUNICATIONS TO THE EDITOR

■ Supplementary and/or miniprint material for this paper is available separately (consult the masthead page for ordering information); it will also appear following the paper in the microfilm edition of this journal.

* In papers with more than one author, the asterisk indicates the name of the author to whom inquiries about the paper should be addressed.

AUTHOR INDEX

PUBLISHER'S NOTE

To conform to provisions of U.S. copyright law effective January 1, 1978, the American Chemical Society is instituting new procedures.

Contributors and readers will notice two changes:

(1) Authors will be required to transfer copyright to ACS by means of a simple form. The relationship between the Society and the author will remain unchanged, however, since under prior copyright law ACS has in fact been the copyright owner of individual articles.

(2) Issues published after January 1, 1978 will have a multiple-digit code at the foot of the first page of most articles. This code signifies ACS participation in the not-for-profit Copyright Clearance Center. Operation of the Center will permit libraries and other institutions to reproduce legally and without delay journal articles beyond "fair use" as described in the new law and accompanying guidelines.

Questions on the new copyright law or ACS procedures may be addressed to the Office of the Director, Books and Journals Division, American Chemical Society, 1155 16th Street, N.W., Washington, D.C. 20036. Or call (202) 872-4556 or 872-4367.

THE JOURNAL OF
PHYSICAL CHEMISTRY

Registered in U. S. Patent Office © Copyright, 1977, by the American Chemical Society

VOLUME 81, NUMBER 24 DECEMBER 1, 1977

Formation and Decay Kinetics of the 2p Levels of Neon, Argon, Krypton, and Xenon Produced by Electron-Beam Pulses[1]

R. Cooper, F. Grieser,

Department of Physical Chemistry, University of Melbourne, Parkville, Victoria, Australia 3052

Myran C. Sauer, Jr.,*

Chemistry Division, Argonne National Laboratory, Argonne, Illinois 60439

and David F. Sangster

Australian Atomic Energy Commission, Lucas Heights, New South Wales 2232, Australia *(Received April 1, 1977)*

Publication costs assisted by Argonne National Laboratory

Observations of the kinetics of light emission show that the 2p levels of the rare gases Ne, Ar, Kr, and Xe are produced by three different processes: (1) direct excitation by the electron beam; (2) degradation of higher energy levels; (3) ion recombination. The time dependences of the visible and near-IR emission spectra observed from these gases reveal that process 3 produces a significantly different distribution of 2p levels than does the combination of processes 1 and 2.

Introduction

Pulse radiolysis has proven to be a useful technique for studying the production and decay of excited states and intermediate species in the gas phase.[2-4]

This paper presents a study of the kinetics of rare gas atoms in their 2p electronic states which resolves apparent incongruities in the results of previous studies[5,6] of the production and decay of these states.

Experimental Section

The optical system used in this gas phase pulse radiolysis study is similar to one described in detail elsewhere.[7] The perturbation source was a Field Emission Corp. 706 Febetron system, which emits an intense pulse of electrons (7000 A) having a maximum energy of 0.5 MeV. The pulse shape is approximately triangular with a half-width of ~3 ns. The electron pulse entered a 1-L stainless steel cell containing the rare gas. The dose was sometimes reduced by passing the electron beam through perforated steel plates. The light emitted was focussed onto a 0.75-m Jarrell-Ash Model 75-000 spectrograph. The bandpass was ~2 nm. To avoid possible interference from second- or third-order transmission, an appropriate filter was placed in front of the entrance slits. The emission signals were monitored with an RCA 4832 photomultiplier tube, the output of which was amplified 100 times with a HP-462A amplifier and displayed on a Tektronix 7904 oscilloscope. This display was photographed using a Polaroid camera with 10 000 ASA film. The photomultiplier was shielded from x rays produced by the pulse, and the cell windows were out of the electron beam path; thus, no Cerenkov light was detected. The overall rise time of the equipment was 6–8 ns, which was due mainly to the photomultiplier. The spectrograph and all of the electronics were enclosed in a double-screened room[8] so that electromagnetic interference from the Febetron was essentially eliminated.

Computer simulation studies were performed with a Data General "Nova" Computer.

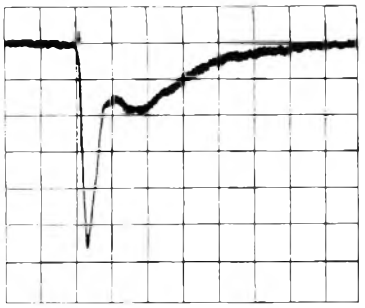

Figure 1. Emission vs. time at 725 nm ($2p_{10} \rightarrow 1s_4$) in 840 Torr of Ne. The time scale is 100 ns/division. The arrow indicates the end of the approximately 5-ns wide electron pulse.

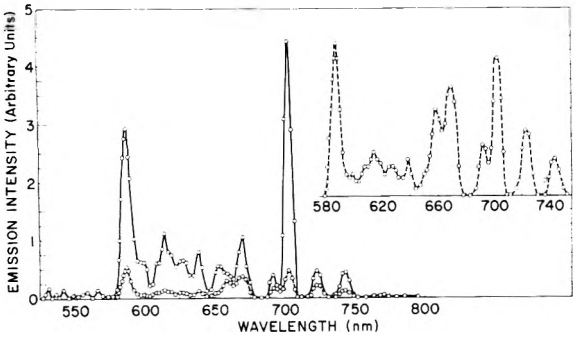

Figure 2. Emission spectrum of 840 Torr of Ne. The full curve represents the spectrum of the "fast" emission and dashed curve the delayed emission. The insert is an expansion of the delayed emission spectrum.

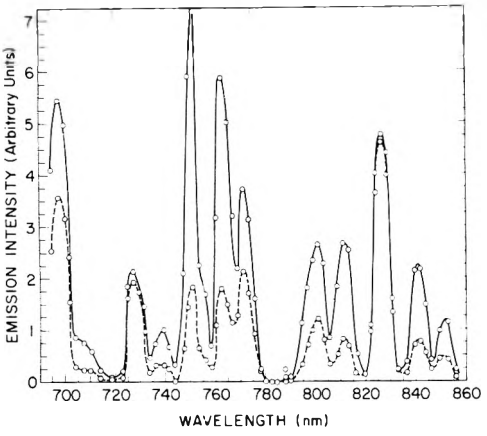

Figure 3. Emission spectrum of 600 Torr of Ar. The full curve represents the spectrum of the "fast" emission and dashed curve the delayed emission.

Materials. The rare gases used were Matheson Research Grade, except for argon, which was Airco Ultrapure (99.999%). All these gases were used as supplied. SF_6 (Matheson Research Grade) was purified by a few freeze–pump–thaw cycles. Triply distilled water was degassed in a similar manner.

Results and Discussion

The emission signal depicted in Figure 1 was obtained at 725 nm from a sample of 840 Torr of neon. The trace distinctly shows that the excited rare gas species is produced by two reaction sequences which are partially resolved in time. This behavior was common to all observed 2p emissions.

Emission spectra for the four rare gases are shown in Figures 2–5, and were plotted using the intensity maxima of the primary and secondary peaks from the emission vs. time traces. These figures are presented mainly to indicate the nature of the variation of primary to secondary

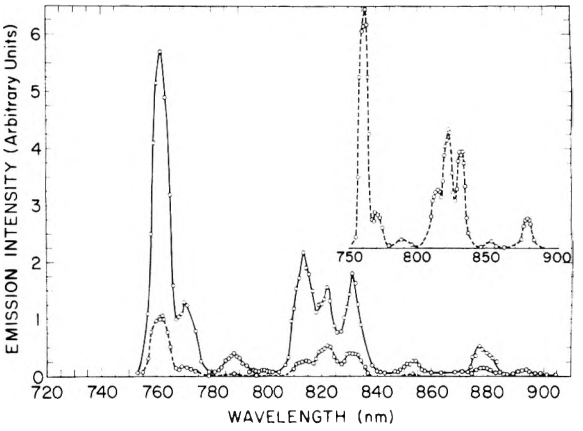

Figure 4. Emission spectrum of 420 Torr of Kr The spectrum was measured using a lower dose per pulse than in the case of neon or argon (see text). The full curve represents the spectrum of the "fast" emission and dashed curve the delayed emission. The insert is an expansion of delayed emission spectrum.

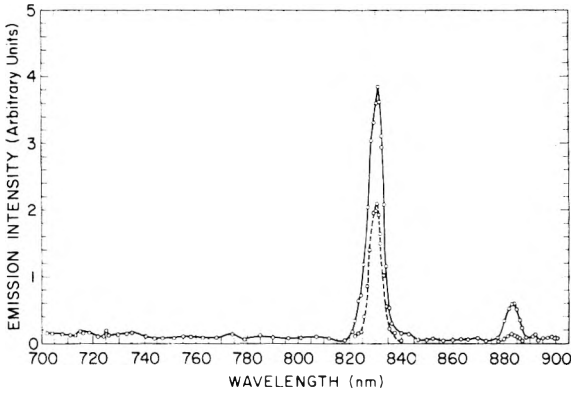

Figure 5. Emission spectrum of 560 Torr of Xe. The spectrum was measured using a lower dose per pulse than in the case of neon or argon (see text). The full curve represents the spectrum of the "fast" emission and the dashed curve the delayed em ssion.

emission with wavelength, and no correction has been made for the variation in photomultiplier sensitivity with wavelength. For krypton and xenon, the two intensity maxima were not very well resolved at the pressures used; however, by reducing the pulse intensity, good resolution was achieved (this will be described in greater detail in the following section). The spectra reported for Kr and Xe were therefore obtained at lower dose per pulse.

All the emission lines have been previously observed in a pulse radiolysis study by Arai and Firestone,[5] and correspond with tabulated 2p–1s atomic transitions.[9]

The time dependence of the two types of processes exemplified in Figure 1 was studied as a function of rare gas pressure, dose per pulse, and additives for all of the $2p \rightarrow 1s$ transitions which were of great enough intensity.

I. *"Delayed" Excited State Formation.* The qualitative effects of changes in the aforementioned experimental parameters on the delayed emission (e.g., the second peak in Figure 1) were the same for all four gases and independent of the emission band monitored. The decay rate (e.g., $\tau \sim 140$ ns for 840 Torr of Ne) decreased linearly with decreasing pressure and the emission maxima shifted to longer times.

Figures 6a and 6b show that decreasing the dose causes the emission maximum to move to longer times, but causes no appreciable change in decay rate. Figures 7a and 7b show that 1 Torr of SF_6, a good electron scavenger, completely eliminates the delayed emission. The effects of dose and SF_6 strongly suggest that ion recombination is responsible for the production of the excited rare gas

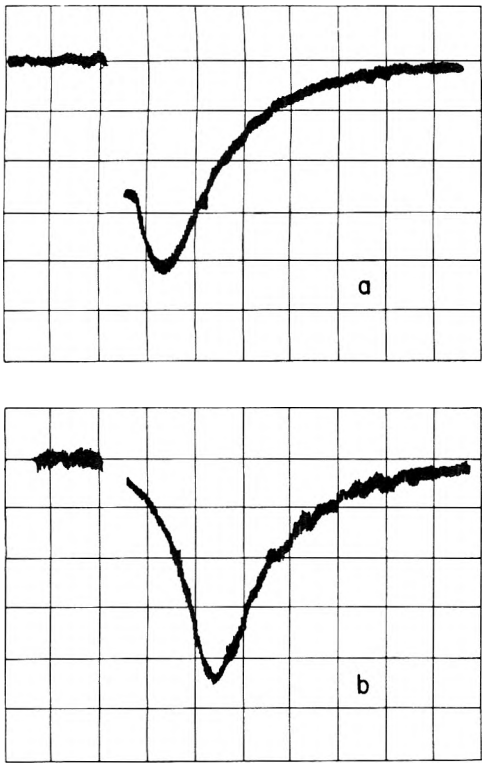

Figure 6. Emission vs. time at 585 nm ($2p_1 \rightarrow 1s_2$) in 840 Torr of neon using the maximum dose per pulse (a), and using 1/4 of the maximum dose per pulse (b). The time scale is 100 ns/division, and the signal has been amplified by a factor of 7 in (b). In both cases the "fast" emission is off-scale and is not shown.

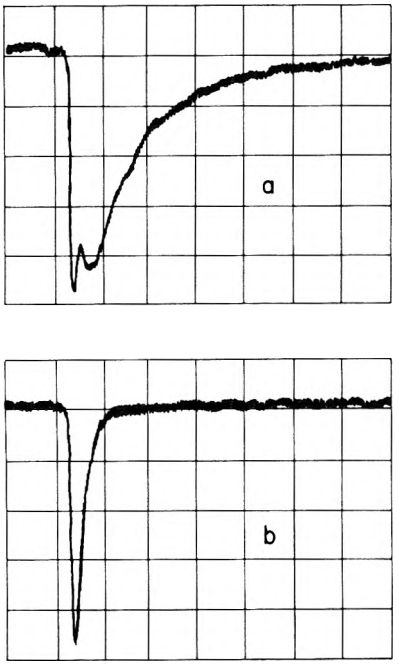

Figure 7. Emission vs. time at 826 nm ($2p_2 \rightarrow 1s_2$) in Ar: (a) 600 Torr of Ar, (b) 600 Torr of Ar + 1 Torr of SF_6. The time scale is 100 ns/division, and the gain is the same in both cases.

atoms giving the delayed emission.

The temporal characteristics of the delayed emission are in qualitative accord with the time scale expected for ion recombination on the basis of measured recombination coefficients for electrons with rare gas dimer ions[10,11] and our estimated ion concentrations (e.g., $\approx 2 \times 10^{13}$ ions/cm^3 for 600 Torr of Ar). Delayed production of excited argon has been observed in Ar/N_2 mixtures by LeCalvé and Bourène,[12] which they conclude is due to dissociative recombination of electrons with Ar_2^+.

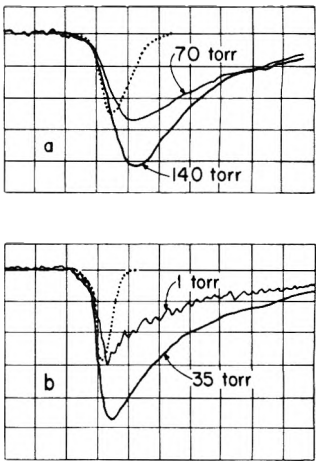

Figure 8. Emission vs. time at 830 nm ($2p_5 \rightarrow 1s_4$) in Xe at various pressures. The time scale is 10 ns/division (a) and 20 ns/division (b). The x-ray signals (dashed curves) are amplified two times.

We have not been able to devise a mechanism which quantitatively explains the delayed emission. The kinetics may be complicated by the fact that electron thermalization in argon is slow,[13,14] which would delay the recombination, and by the likelihood that impurities are present which could react with either the positive ion or the electron.

II. *"Fast" Excited State Formation.* By using low pressures ($\lesssim$100 Torr) or lowering the radiation dose to the rare gas samples, the delayed excited state production could be sufficiently reduced or separated from the prompt formation to allow the latter to be studied without significant interference from the ionic processes.

The following observations were common to the four rare gases studied: (1) The formation and decay kinetics of the fast emission are independent of dose. (2) Addition of small amounts of SF_6 ($\sim$1 Torr) or H_2O ($\sim$0.2 Torr) had essentially no effect on either the kinetics or the time-integrated intensity of the fast emission.

Certain other characteristics of the light emission depended on the particular rare gas; hence each gas will be discussed separately.

1. *Xenon.* The two transitions, $2p_5 \rightarrow 1s_4$ at 830 nm, and $2p_8 \rightarrow 1s_5$ at 884 nm, behave similarly with change in experimental conditions. In both cases the maximum intensity is reached near the end of the pulse and the decay rate decreases with decreasing pressure.

Figure 8 shows the time dependence of the 830-nm emission as a function of xenon pressure. The x-ray signal (which is due to x rays produced by the electron beam striking the photomultiplier) has been shown to compare the pulse shape, modified by the rise time, with the growth of the light emission.

It can be seen that the maximum emission intensity is reached about 7 ns after the maximum in the x-ray pulse. Part of this delay can be ascribed to the rise time of the system, so it is reasonable to conclude that the half-time for the formation of the emission is $\lesssim$5 ns. At pressures below $\sim$8 Torr, the decay of both the 830- and 884-nm emissions becomes complex, showing neither first- nor second-order behavior.

The first-order decay rate of the 830-nm emission, at a xenon pressure of 8 Torr, was about 1.5×10^7 s^{-1} ($\tau \simeq 67$ ns). The latter is much greater than the reported radiative lifetime (30–40 ns) of the $2p_5$ level.[15,16] Similarly, the decay rate of the 884-nm emission, at low pressures, is slower than predicted from the radiative lifetime of the $2p_8$ level.[17]

At a xenon pressure of 1 Torr, where the decay is no longer first order, the initial τ (measured beginning at the

maximum emission intensity) is ≃110 ns.

These long lifetimes suggest that the 2p levels are being repopulated from higher precursor levels with lifetimes longer than those of the 2p levels.

A further point to note is that even at the lower pressure limit of this study, the emission maxima (for the two transitions being discussed) are still observed to occur near the end of the electron pulse. If the 2p levels were exclusively populated by cascade from higher levels, this would not be the case. This can be shown by considering the following simplified mechanism:

$$A \xrightarrow{k_1} \text{2p level} \xrightarrow{k_2} \text{lower electronic state}$$

where A represents the precursor levels formed by the electron pulse. The expression for the time of maximum intensity of the 2p state is given by

$$t_{max} = \frac{\ln [k_1/k_2]}{k_1 - k_2} \qquad \text{for } k_1 > k_2 \text{ or } k_1 < k_2$$

From the results of the 1 Torr of xenon sample, using $k_1 \simeq 1 \times 10^7$ s^{-1}, and taking the radiative lifetime of the 830-nm emission to be 30 ns (collisional removal of the $2p_5$ level at this pressure is slow compared to the radiative lifetime, and the correction to k_2 can therefore be ignored), one obtains $t_{max} \simeq 52$ ns. Therefore, if the emission maximum occurs within 5–10 ns of the pulse, a major fraction of the 2p level must be formed by direct excitation during the electron pulse. The nonlinearity in the decay at lower pressures can be ascribed to the combination of two processes forming the 2p level, the first being the prompt formation during the electron pulse and the other being a cascade from either one or more upper levels which have appreciably longer lifetimes than the 2p level. Computer simulation results (section III) also support this interpretation.

2. *Neon.* In the case of neon, all of the 2p → 1s emission lines show variation in decay rate with pressure, although the $2p_1 \rightarrow 1s_2$ emission is only slightly affected (see Figure 9). The $2p_{10} \rightarrow 1s_5$ and the $2p_{10} \rightarrow 1s_4$ emissions show the same kinetics, as expected, and the time of the maximum in the emission signal was observed to increase with decreasing neon pressure, reaching 70 ns at 26 Torr (compare with Figure 1, 840 Torr of Ne, $t_{max} \approx 30$ ns). The large value of t_{max} indicates that the $2p_{10}$ level is produced predominantly from higher energy levels. The variation of t_{max} with pressure indicates that the decay of the higher levels is accelerated by increasing the pressure.

At low neon pressures (<30 Torr) there is little change in the decay rate of the various emission lines with pressure; the values of τ, except in the case of the $2p_1$ level, range between ~170 and ~250 ns. These values are much greater than measured radiative lifetimes of the 2p levels, which are of the order of ~20 ns.[18,19]

Hence, we conclude that the decay rates of most of the 2p levels of Ne are strongly influenced by the deactivation of higher energy states.

The lifetime of the $2p_1$ level at low pressures is in good agreement with previous lifetime measurements.[18,19] This indicates that most of the $2p_1$ level is produced directly by the pulse; the non-first-order decay does, however, suggest that there is also a contribution from upper electronic levels.

3. *Argon.* The decay rates of the argon 2p → 1s emissions decrease with decreasing argon pressure. Generally the emissions reach maximum intensity near the end of the electron pulse, although in the case of the $2p_2 \rightarrow 1s_2$ and $2p_2 \rightarrow 1s_5$ transitions the maximum intensity, at pressures ≤45 Torr, occurs ~20 ns after the x-ray peak.

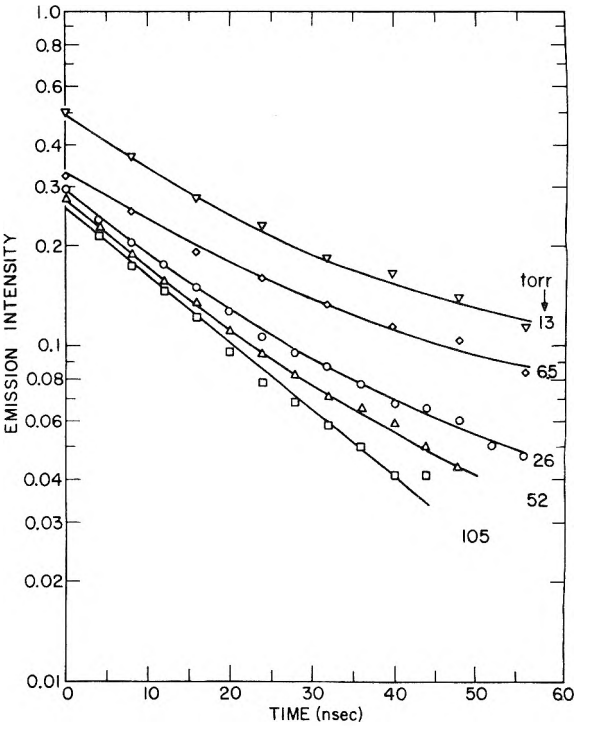

Figure 9. Emission vs. time for the $2p_1 \rightarrow 1s_2$ transition in Ne at 585 nm at various pressures. Zero time is 25 ns after the beginning of the pulse. The ordinate is in arbitrary units, and the curves have been shifted vertically for clarity in presenting the decay kinetics.

As in the case of neon, the decay rate of the $2p_1 \rightarrow 1s_2$ transition is much faster than the decay rates of the other emission lines observed, the decay lifetime, τ, being about 25 ns at the lowest pressure studied (10 Torr). This value is close to the measured radiative lifetime of this state.[20] The effect of pressure on the decay rate of this state is more marked than in the case of the $2p_1$ level of neon; the decay rate approximately doubles with a change in pressure from 10 to 350 Torr. This may indicate a greater quenching capacity of the larger argon atom, or perhaps a difference in the rate of dimerization reactions.[21]

The other argon emissions, at low pressures (<10 Torr), decay at rates (τ values from 170 to 290 ns) which are slower than expected from the radiative lifetimes of the states involved.[20] Again, this type of behavior indicates that the 2p levels are being populated both by direct excitation and from higher levels, and that the latter governs the decay kinetics at lower pressures. The decay rate also deviates from first-order behavior in the lower pressure range, which may indicate that more than one higher level is involved in the cascading process.

4. *Krypton.* All the krypton emission lines studied reach maximum emission intensity near the end of the electron pulse. The decay rates become slower at lower pressures. Generally, at pressures <25 Torr, the decays do not follow first- or second-order kinetics. No measured radiative lifetimes of the 2p states of krypton are available, but if they are similar to those of the other three rare gases (i.e., about 20–30 ns) then the decay rates in the case of Kr (τ values range from 120 to 170 ns at pressures of ~6 Torr) are also too slow to be ascribed to simple radiative decay of the 2p level.

The pattern among the four rare gases seems consistent; except in the case of the highest energy 2p state, i.e., the $2p_1$ level, the decays do not reflect the radiative lifetime of the emitting state. Instead, the kinetics of light emission from the 2p levels are apparently determined by the decay kinetics of higher energy presursors. Ballou and Lin[22] have pointed out that the 2p levels are subject to cascade from

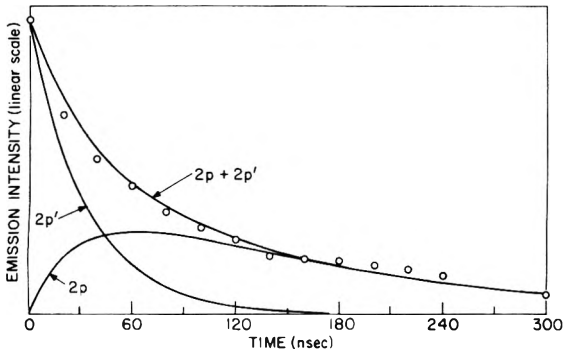

Figure 10. Observed and calculated emission from 1 Torr of Xe at 830 nm ($2p_5 \rightarrow 1s_4$); the circles represent the experimental points. The values used in the calculation are $k_1 = 0.7 \times 10^7\ s^{-1}$, $k_2 = 3.0 \times 10^7\ s^{-1}$ ($\tau = 33$ ns) and A/2p′ = 0.575 (see text for definition of terms).

the $3p^5$ *n*s and $3p^5$ *n*d groups. The effect of pressure which we observe must be ascribed then to the disappearance of the precursor levels by two- or three-body dimerization reactions, or by collision induced transitions involving the precursor levels which alter their decay rates. On the basis of work of Bondybey and Miller[23] on relaxation of highly excited states of rare gases, population of 2p levels both by collisionally induced radiationless transitions from states higher than the 2p levels, as well as from other 2p levels, is likely.

III. *Computer Simulation Studies.* Assuming that each 2p level is populated directly by the electron pulse and from a higher state also formed by direct excitation, the appropriate reaction scheme is

$$A \xrightarrow{k_1} 2p$$

$$2p \xrightarrow{k_2} h\nu + 1s$$

$$2p' \xrightarrow{k_2} h\nu + 1s$$

where A represents the higher state and 2p and 2p′ the 2p level formed by cascade and direct excitation, respectively.

The differential equations representing the above reaction scheme can easily be solved in a closed form, with k_1, k_2, and the initial concentrations of A and 2p′ as variable parameters. The rate constant k_1 can be estimated from the emission decay curves at low rare gas pressure, where collisional effects are negligible. The rate constant k_2 is available from published lifetime studies of rare gas atomic levels. Using these conditions and adjusting the initial concentrations of A and 2p′, reasonably good fits to the experimental data can be obtained. An example is given in Figure 10. For simplification, time zero in this figure is taken to be the observed time of maximum emission, which is about 10 ns after the pulse. The error resulting from the assumption that the concentration of the 2p level formed by cascade is zero at $t = 0$ (i.e., 10 ns) is small. The calculated curves are normalized to the experimental point at $t = 0$.

These results indicate that a simple two-stage process can account for the temporal characteristics of such emission curves. The computer results also illustrate another point, which is, that in order for the emission maximum to be at about 70 ns from the center of the electron pulse (e.g. $2p_{10} \rightarrow 1s$ in neon at 26 Torr) the 2p level must be formed almost entirely from higher levels. Even if comparable amounts were produced directly and from higher levels the maximum would occur much nearer near the end of the pulse than 70 ns.

Of course, it is quite possible that more than one higher level contributes to the formation of a 2p state, but this would not change the qualitative conclusion reached above.

TABLE I: Quantities[a] of Significance in the Energetics of the Reaction $e + X_2^+$

Rare gas, X	IP[b]	$D(X_2^+)$[c]	$E(2p_1)$[b]
Ne	21.559	1.1	18.96
Ar	15.755	1.4	12.9
Kr	13.996	1.2	12.2
Xe	12.127	1.1	11.14

[a] Energies are in eV. [b] Reference 26. [c] Reference 27.

IV. *The Spectra.* Examination of the spectra (Figures 2–4) of the immediate and delayed light emission observed in neon, argon, and krypton reveals that the relative intensity–wavelength profiles of the two processes are markedly different. This implies that the processes of ion recombination (probably $e + X_2^+$) and direct excitation result in different distributions of the 2p levels. Direct excitation of rare gas atoms will result in a population distribution which can be qualitatively predicted on the basis of the optical approximation.[24] On the other hand, the distribution of states formed by ion recombination will be influenced by the energetics of the dissociative recombination reaction, viz

$$E(X^{**}) = \mathrm{IP}(X) - D(X_2^+) - E_{kD} + T$$

where IP(X) is the ionization potential of X, $D(X_2^+)$ is the energy of dissociation into $X + X^+$ from ground state X_2^+, E_{kD} is the kinetic energy of the fragments from the reaction $e + X_2^+$, and T is the energy of the electron. If we consider a thermal electron, T can be neglected, since it is small compared to the other terms in the equation.

From the values in Table I, it can be seen that if E_{kD} is about 1 eV for Ne and Ar, and even less for Kr and Xe, the only excited levels produced by $e + X_2^+$ will be the 2p levels. Connor and Biondi,[25] and later Frommhold and Biondi,[28] have demonstrated for $e + Ne_2^+$ that E_{kD} values of about 1 eV are typical in the case of a number of 2p levels. Thus, transitions from higher levels would be expected to be less important in the production of the 2p levels by dissociative recombination, which allows the observed spectral differences to be rationalized.

Obviously this is an oversimplification in terms of the energies involved. The electron need not be thermal to react with X_2^+, nor is the kinetic energy of the fragment necessarily as high as 1 eV. Therefore levels higher than the 2p manifold would be produced from the dissociative recombination reaction;[28] however, the above reasoning shows that the population of the higher electronic levels should be different in comparison with the direct excitation process.

V. *Comparisons with Previous Work.* It is of interest to compare these results with those of Arai and Firestone[5] and Hanle et al.[6]

Arai and Firestone postulated that the 1s levels are populated essentially entirely via transitions from 2p levels, and that the latter are formed within about 40 ns (risetime limitation) after the pulse. It should be noted that the characteristics of the emission reported in their paper correspond closely to the emission which we ascribe to dissociative recombination. Our results are in qualitative agreement with those of Hanle et al., who observed both a fast process and a slower one. A major difference between the experimental conditions of Arai and Firestone and Hanle et al. is the initial high density of primary events in the former work. Our results show that under high dose conditions, the slow process can merge with the fast decay, especially if the rise time of the detection equipment is

≳10–20 ns. (The rise time of Arai and Firestone's system was 40 ns.) Thus we conclude that the emission decays observed by Arai and Firestone are due to the same reaction sequence as the slow process observed by us and by Hanle et al., and which our analysis suggests involves a dissociative ion-recombination reaction. The fast process observed by Hanle et al. is the same as the fast process observed in the present work, where the 2p levels are produced both by direct excitation and by cascade from higher electronic levels.

References and Notes

(1) Work performed in part under the auspices of the Division of Physical Research of the U.S. Energy Research and Development Administration and in part under the auspices of the Australian Research Grants Committee.
(2) R. F. Firestone and L. M. Dorfman, *Actions Chim. Biol. Radiat.*, **15**, 7–46 (1971).
(3) M. C. Sauer, Jr., *Adv. Radiat. Chem.*, **5**, 97–184 (1976).
(4) M. C. Sauer, Jr., *Int. J. Radiat. Phys. Chem.*, **8**, 33 (1976).
(5) S. Arai and R. F. Firestone, *J. Chem. Phys.*, **50**, 4575 (1969).
(6) W. Hanle, E. Kugle, and A. Schmillen, *Ann. Phys.*, **13**, 252 (1964).
(7) J. B. Cumming, Ph.D. Thesis, University of Melbourne, 1975.
(8) S. Gordon, W. Mulac, and P. Nangia, *J. Phys. Chem.*, **75**, 2087 (1971).
(9) Reference 5 above lists the sources which identify and designate the electronic levels involved in the atomic transitions.
(10) F. J. Mehr and M. A. Biondi, *Phys. Rev.*, **176**, 322 (1968).
(11) H. J. Oskam and V. R. Mittelstadt, *Phys. Rev.*, **132**, 1445 (1963).
(12) J. Le Calvé and M. Bourène, *J. Chem. Phys.*, **55**, 1446 (1973).
(13) J. M. Warman and M. C. Sauer, Jr., *J. Chem. Phys.*, **62**, 1971 (1975).
(14) J. M. Warman and M. P. de Haas, *J. Chem. Phys.*, **63**, 2094 (1975).
(15) Ya. F. Verolainen and A. L. Osherovich, *Opt. Spectrosc. (Engl. Trans.)*, **27**, 14 (1969).
(16) L. Allen, D. G. C. Jones, and D. G. Schofield, *J. Opt. Soc. Am.*, **59**, 842 (1969).
(17) R. S. Freiberg and L. A. Weaver, *J. Appl. Phys.*, **38**, 250 (1967).
(18) J. Z. Klose, *Phys. Rev.*, **141**, 181 (1966).
(19) W. R. Bennet, Jr., and P. J. Kindlmann, *Phys. Rev.*, **149**, 38 (1966).
(20) J. B. Shumaker and C. H. Popenoe, *J. Opt. Soc. Am.*, **32**, 8 (1967).
(21) R. Henck and R. Voltz, *J. Phys. (Paris)*, **29**, 149 (1968).
(22) J. K. Ballou and C. C. Lin, *Phys. Rev. A*, **8**, 1797 (1973).
(23) V. E. Bondybey and T. A. Miller, *J. Chem. Phys.*, **68**, 3337 (1977).
(24) R. L. Platzmann, *Radiat. Res., Proc. Int. Congr., 3rd*, 20–42 (1967).
(25) T. R. Connor and M. A. Biondi, *Phys. Rev. A*, **140**, 778 (1965).
(26) C. Moore, *Natl. Bur. Stand. Circ.*, **No. 467** (1949), Vols. I, II, and III.
(27) The values are estimates of rare gas ion dissociation energies which are listed with calculated and experimentally obtained values by R. S. Mulliken, *J. Chem. Phys.*, **52**, 5170 (1970).
(28) L. Frommhold and M. A. Biondi, *Phys. Rev.*, **185**, 244 (1969).

A Temperature Dependent Kinetics Study of the Reactions of HCl with OH and O(^{3}P)

A. R. Ravishankara, G. Smith, R. T. Watson,† and D. D. Davis*

Atmospheric Sciences Division, Applied Sciences Laboratory, Engineering Experiment Station, Georgia Institute of Technology, Atlanta, Georgia 30332

(Received January 25, 1977)

Publication costs assisted by the Georgia Institute of Technology

The flash photolysis–resonance fluorescence technique was employed to determine the temperature dependencies of the rate constants for the reaction of O(^{3}P) and OH radicals with HCl. These reactions were studied under pseudo-first-order conditions and in the absence of interfering secondary reactions. The Arrhenius expression for each bimolecular rate constant is given as follows in units of cm^3 molecule^{-1} s^{-1}: $k_1 = (3.3 \pm 0.3) \times 10^{-12}$ exp[$-(937 \pm 78)$ cal mol$^{-1}/RT$] 250–402 K, OH + HCl → H_2O + Cl (1) and $k_2 = (5.2 \pm 1.0) \times 10^{-11}$ exp[$-(7510 \pm 750)$ cal mol$^{-1}/RT$] 350–454 K, O(^{3}P) + HCl → OH + Cl (2). The stratospheric implications of this new rate data are discussed.

Introduction

According to present atmospheric models, hydrogen chloride is predicted to be one of the principal chlorine containing species in the stratosphere.[1] Recent measurements of the HCl concentration in the lower stratosphere now support this prediction.[2] In the stratosphere the formation of HCl proceeds through the reaction of chlorine atoms with RH species (i.e., CH_4, H_2, H_2O_2, and/or HO_2), thus removing reactive chlorine from the catalytic cycle:

$$\begin{aligned} &Cl + O_3 \rightarrow ClO + O_2 \\ &ClO + O \rightarrow Cl + O_2 \\ \hline &O + O_3 \rightarrow 2O_2 \end{aligned}$$

The chlorine atom in HCl, however, can be reintroduced into the catalytic ozone destruction cycle via reaction of OH or O(^{3}P) with HCl and/or by photolysis of HCl, e.g.

$$OH + HCl \xrightarrow{k_1} H_2O + Cl \quad (1)$$

$$O(^3P) + HCl \xrightarrow{k_2} OH + Cl \quad (2)$$

$$HCl \xrightarrow{h\nu} H + Cl \quad (3)$$

Since HCl is the dominant "temporary sink" for Cl atoms in the stratosphere, reliable rate constants for reactions 1 and 2 are essential for stratospheric modeling calculations.

Five measurements of the rate constant k_1 have been reported. Wilson et al.[4] measured k_1 at high temperatures, while Takacs and Glass[5] and Hack et al.[6] obtained room temperature values. In addition, there have been two measurements of k_1 over an extended temperature range, one by Smith and Zellner[7] and the other by Zahniser et al.[8] All measurements are in very good agreement at 300

† Present Address: Jet Propulsion Laboratories, Building 183-601, 4800 Oak Road Drive, Pasadena, Calif. 91103.

* This author acknowledges the partial support of this research by the National Aeronautics and Space Administration. Part of this work was carried out while this author was at the Department of Chemistry, University of Maryland, College Park, Md. 20742.

K; however, at stratospheric temperatures of 225 K, the k_1 value reported by Zahniser et al. is approximately 20% higher than that of Smith and Zellner.

Several investigations of reaction 2 have been reported over an extended temperature range where the activation energy could be evaluated. Balakhnin et al. were the first to study the kinetic behavior of reaction 2. These authors reported an activation energy of 4.52 kcal/mol. Brown and Smith[10] later obtained an E value of 5.95 kcal/mol, a number which agrees well with some recent work reported by Singleton and Cvetanovic.[11] Hack et al.[6] and Wong and Belles,[12] however, have reported values for reaction 2 of 6.44 and 7.2 kcal/mol^{-1}, respectively. Thus, at the present time the activation energy for process 2 must be considered to be in only fair shape.

Reported here are the results of a new study on both reactions 1 and 2, the purpose of which was to further test the reliability of the earlier rate data using a completely different experimental technique—flash photolysis–resonance fluorescence.

Experimental Section

Detailed descriptions of the flash photolysis–resonance fluorescence technique employed in this investigation have been described previously.[13-15] In this manuscript, therefore, we have pointed out only those experimental features necessary for an understanding of the present study. In this investigation, an all-Pyrex cell with an internal volume of ~150 cm^3 was used to study both reactions 1 and 2. The reaction mixture was maintained at a known constant temperature by circulating either methanol (250–300 K) or silicone oil (300–450 K) from a thermostated circulating bath through an outer jacket of the reaction cell. The temperature of the reaction cell was measured with an iron–constantan thermocouple. The transient species OH and O(^{3}P) were formed by the photolysis of a suitable photolyte using a nitrogen spark discharge.

The technique for detection of OH radicals by resonance fluorescence has been documented elsewhere.[13] The OH radicals in this study were produced either by directly photolyzing H_2O or by photolyzing a mixture of 50 mTorr of O_3 and 100 mTorr of H_2. In the latter case, OH was formed through the sequence of reactions:

$$O_3 \xrightarrow[\lambda < 310\ nm]{h\nu} O(^1D) + O_2$$

$$O(^1D) + H_2 \rightarrow OH + H$$

$$H + O_3 \rightarrow OH + O_2$$

Photolysis of H_2O was used as the source of OH at temperatures above 270 K. Below 270 K, the photolysis of O_3 and H_2 was employed as a means of avoiding the problem of HCl absorbing on the water-coated reaction vessel walls. To demonstrate that the rate constant for reaction 1 was independent of the OH source, k_1 was measured at 298 K using both photolytes. The results listed in Table I clearly show this independence.

O(^{3}P) was produced by the vacuum-UV photolysis of 150 mTorr of O_2. Since 100 Torr of Ar was used as the diluent gas in these experiments, all O(^{1}D) formed during the photolysis was quenched to O(^{3}P) within a few microseconds after its formation. The concentration of O(^{3}P) was monitored using an atomic oxygen resonance lamp as described in previous work from this laboratory.[14,15] One minor change in our present investigation was the inclusion of an EMR solar blind vacuum-UV photomultiplier tube (Model 542G) to detect atomic oxygen resonance radiation at ~1300 Å. In all cases, a calcium fluoride window was placed over the photomultiplier tube to filter out any background Lyman-α radiation. Reaction 2 was not studied at temperatures below 350 K due to the very small value of k_2 which dictated the use of very high concentrations of HCl. These high concentrations of HCl resulted in a significant decrease in the signal and the signal-to-noise ratio, making high-precision measurements difficult. This loss in signal can be correlated with the decrease in the intensity of the resonance radiation reaching the reaction zone and the attenuation of the fluorescence light arriving at the photomultiplier tube, both due to the absorption of the 1303-Å atomic oxygen resonance line by HCl.[16,17] Hence, we attribute our lower signal levels primarily to an absorption by HCl rather than quenching of the upper excited states of oxygen atoms by HCl.

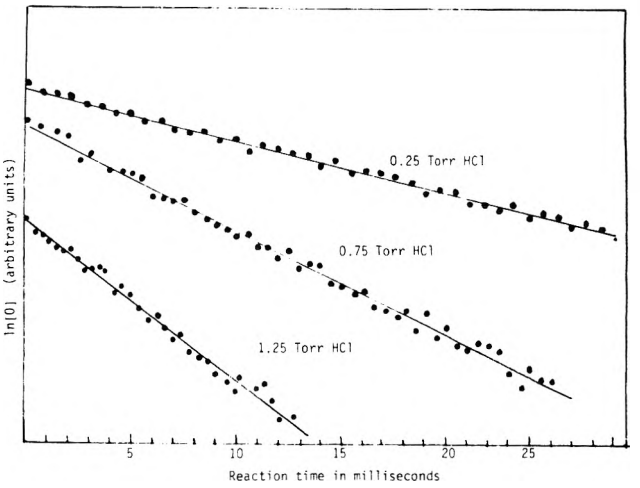

Figure 1. Plots of [O] vs. reaction time for different concentrations of HCl.

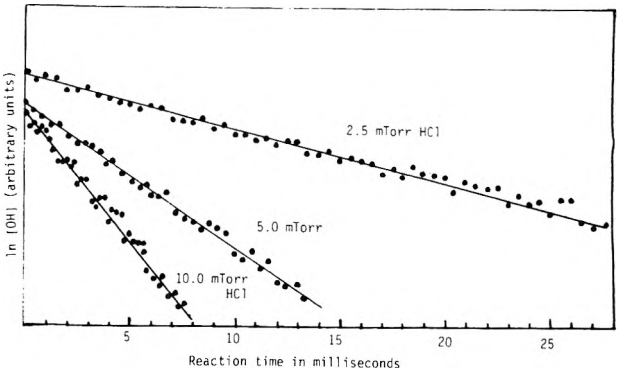

Figure 2. Plots of [OH] vs. reaction time for different concentrations of HCl.

Reactions 1 and 2 were studied under pseudo-first-order conditions, with the concentration of HCl in excess. In this investigation, the decay rates of O(^{3}P) and OH were followed for at least two mean lifetimes. The plots of ln [O] and ln [OH] vs. reaction time, shown in Figures 1 and 2, were linear. This linearity confirms the existence of pseudo-first-order conditions in the system. Under these conditions, the typical concentrations of OH and O(^{3}P) were in the range of 1×10^{11} to 5×10^{11}/cm^3. The ratios of reactants were as follows: [HCl]/[O(^{3}P)] > 10^4 and [HCl]/[OH] > 600.

A MKS Baratron and a two turn bourdon gauge (Wallace and a Tiernan Type FA145) were used to measured low pressures (1–300 mTorr) and high pressures (800 Torr), respectively. The precision with which reaction gas mixtures could be made up was ~4%.

The argon and oxygen used in this study were Air Products UHP grade gases with a stated purity of

TABLE I: Reaction Data for OH + HCl → H_2O + Cl

Temp, K	Diluent	Photolyte	P_{HCl}, mTorr	Flash energy, J	k_1', s^{-1}	$10^{13}k_{bimol}$[e] cm^3 $molecule^{-1}$ s^{-1}
250	40 Torr of He	50 mTorr of O_3 + 100 mTorr of H_2	0.0	88	90	
			2.5		125	
			5.0		166	
			10.0		263	
			15.0		361	
			20.0		438	4.8 ± 0.2
270	50 Torr of He	150 mTorr of H_2O	0.0	88	47	
			2.5		53	
			5.0		89	
			7.5		169	
			10.0		207	
			12.5		256	
			15.0		293	
			17.5		414	
			20.0		444	5.9 ± 0.6
298	20 Torr of He	150 mTorr of H_2O	0.0	88	55[a]	
			5.0		150[a]	
			10.0		270[a]	
			15.0		393	
			20.0		472	6.7 ± 0.4
	40 Torr of He	50 mTorr of O_3 + 100 mTorr of H_2	0.0	88	120	
			5.0		215	
			10.0		320	6.4 ± 0.6
	20 Torr of He	150 mTorr of H_2O	5.0	250	160	
			10.0	88	260[c]	
			10.0	88	250[b,d]	
356	50 mTorr of He	150 mTorr of H_2O	0.0	88	40	
			2.5		62	
			5.0		142	
			7.5		173	
			10.0		260	
			15.0		397	
			20.0		487	8.8 ± 0.6
402	50 mTorr of He	150 mTorr of H_2O	0.0	88	130	
			2.5		179	
			5.0		238	
			10.0		335	
			12.5		413	
			15.0		500	9.9 ± 1.0

[a] Average of two runs. [b] Not used in the calculation of bimolecular rate constant. [c] Experiments carried out 10 min after the reactants were introduced into the cell. [d] Similar to *c*, however, with a 15-min delay. [e] The quoted errors for the values of k_{bimol} are two standard deviations.

TABLE II: Reaction Rate Data for $O(^3P)$ + HCl → OH + Cl

Temp, K	P_{HCl}, Torr	Flash energy, J	k_2', s^{-1}	$10^{15}k_{bimol}$[a] cm^3 $molecule^{-1}$ s^{-1}
350	0.0	88	16	
	0.5		31	
	1.0		48	
	1.5		58	
	2.0		71	(0.99 ± 0.09)
392	1.0	210	85	
	1.0	37	83	
401	0.0	88	22	
	0.25		52	
	0.25		63	
	0.50		87	
	0.75		118	
	1.00		136	
	1.00		145	
	1.25		165	(4.8 ± 0.4)
454	0.0	88	28	
	0.25		73	
	0.50		131	
	0.75		213	(11.6 ± 0.4)

[a] The quoted errors for the values of k_{bimol} are two standard deviations.

99.999%. Matheson "Electronic grade" HCl was purified to remove Cl_2 by bulb-to-bulb distillation at 195 K and was degassed before use. O_3 was prepared by passing O_2 through an Ozonator and stored at 195 K. Before use, ozone was purified by continuously pumping while at 195 K; its purity was checked by UV spectroscopy. Matheson UHP hydrogen was used without further purification. The H_2O used in this investigation was glass distilled and degassed at liquid N_2 temperatures prior to use.

Results and Discussion

The results from the OH–HCl study are shown in Table I. Reaction 1 was studied at five temperatures and over a wide range of experimental parameters. As pointed out earlier, pseudo-first-order conditions (i.e., [HCl] ≫ [OH]) were maintained throughout the investigation. In those experiments where water was used as the source of OH radicals, the first-order rate constant k_1 was also measured as a function of the residence time for the HCl gas mixture in the reaction cell (e.g., 0, 10, and 15 min). As can be seen from Table I, k_1 at 298 K was found to be only slightly dependent on the residence time of the gas mixture up to times of 15 min. These measurements indicate that HCl was not being depleted by its dissolution into water ab-

TABLE III: Summary of Rate Data for OH + HCl → H_2O + Cl

Ref	Arrhenius expression, cm^3 molecule^{-1} s^{-1}	$10^{13}k_{1(298)}$ cm^3 molecule^{-1} s^{-1}	Temp range, K	Technique[a]
8		6.4 ± 1.5 (295 K)		DF/ESR
b		6.5 ± 0.4		FF/RF
6		6.7 ± 1.7 (293 K)		DF/ESR
7	$(4.1^{+2.0}_{-1.4}) \times 10^{-12} \exp[-(1050 \pm 50)/RT]$	6.9 ± 1.0	220–480	FF/RA
8	$(2.0 \pm 0.1) \times 10^{-12} \exp[-(620 \pm 20)/RT]$	6.7 ± 0.4	224–440	DF/RF
This work	$(3.3 \pm 0.3) \times 10^{-12} \exp[-(937 \pm 78)/RT]$	6.6 ± 0.4	250–402	FF/RF

[a] FF/RF, flash photolysis with resonance fluorescence detection system; FF/RA, flash photolysis with resonance absorption detection system; DF/RF, discharge flow with resonance fluorescence detection system; DF/ESR, discharge flow with electron spin resonance detection system. [b] Davis et al., unpublished results.

sorbed on the reaction cell wall within the normal operating time of 5 min. In another series of tests at 270 K, k_1 was shown to decrease by ~10% in 10 min. Hence, at this temperature, all experiments were carried out within 3 min after the introduction of the reactant gas mixture to ensure only a very minor loss of reactant on the cell walls.

At each temperature, the bimolecular rate constant, k_1, was computed from the measured pseudo-first-order rate constant using a linear least-squares analysis. The quoted errors or each k_{bi} are 2σ. A plot of ln k_1 against $1/T$ is shown in Figure 3. A least-squares fit of this data produced the following Arrhenius expression:

$$k_1 = (3.3 \pm 0.3) \times 10^{12} \exp[-(937 \pm 78) \text{ cal mol}^{-1}/RT] \text{ cm}^3 \text{ molecule}^{-1} \text{ s}^{-1}$$

Again the quoted errors are 2σ for the temperature range covered. This expression has been defined from a total of 39 experiments.

In previous kinetic investigations of our laboratory of the OH radical, under conditions similar to the present measurements, it was demonstrated that radical–radical reactions of the type H + OH and OH + OH were of negligible importance. Moreover, both calculations, as well as experimental variations of the OH concentration in this study, tend to confirm the negligible contribution of the above processes, as well as others (e.g., OH + Cl) to the measured rate constants (see Table I).

The results obtained from the O(^{3}P) + HCl study are shown in Table II. We could not measure k_2 below 350 K since below this temperature (i.e., 298 K) there was no measureable increase in the observed decay rate of O(^{3}P), even when 1 Torr of HCl was present in the reaction cell. Since the flash photolysis–resonance fluorescence technique in this case was capable of measuring a change of 10 s^{-1} in k_2', it can be concluded that the value of k_2 is less than 3×10^{-16} cm^3 molecule^{-1} s^{-1} at 298 K. This result suggests that the HCl pressure would have to be greater than 10 Torr to obtain an accurate value for k_2 at 298 K. At these high HCl concentrations, however, numerous complications develop, as were described earlier in the Experimental Section.

At 392 K, experiments were carried out to determine the possible importance of secondary reactions resulting from the high concentrations of HCl employed. In this case, the flash energy was varied by a factor of ~6. As seen from Table II, this variation in the radical concentration did not affect our measured value of k_2'. These results would tend to indicate that our measured values of k_2' were free of major errors originating from radical–radical processes.[18]

The bimolecular rate constant, k_2, at each temperature was computed by subjecting the pseudo-first-order data to a linear least-squares analysis. From these temperature dependent bimolecular rate constants, the following Arrhenius expression was derived:

$$k_2 = (5.2 \pm 1.03) \times 10^{-11} \exp[-(7510 \pm 750) \text{ cal mol}^{-1}/RT] \text{ cm}^3 \text{ molecule}^{-1} \text{ s}^{-1}$$

The quoted errors are 2σ for both k_{bi} and k_2. It is to be noted that the larger error in the A factor for reaction 2 vs. reaction 1 is the result of the more limited temperature range covered, the higher degree of uncertainty in each of the individual measurements, and the more limited number of experiments performed.

TABLE IV: Summary of Rate Data for O(^{3}P) + HCl → OH + Cl($^2P_{3/2}$)

Ref	Arrhenius expression, cm^3 molecule^{-1} s^{-1}	Temp range, K	Technique[a]
9	$(1.75 \pm 0.6) \times 10^{-12} \exp(-2260/T)$	295–371	DF/ESR
10	$(2.5^{+1.1}_{-0.8}) \times 10^{-12} \times \exp[-(2970 \pm 150)/T]$	293–440	F/AG
12	$(1.9 \pm 0.3) \times 10^{-11} \times \exp[-(3584 \pm 70)/T]$	356–628	SF/MS
This work	$(5.2 \pm 0.9) \times 10^{-11} \times \exp[-(3755 \pm 200)/T]$	350–454	FF/RF
6	$(8.5 \pm 1.7) \times 10^{-12} \times \exp[-(3220 \pm 150)/T]$	293–718	DF/ESR

[a] DF/ESR, discharge flow with ESR as the detection system; F/AG, flow tube with after glow as the detection system; SF/MS, stirred flow reactor with mass spectrometer as the detection system. FF/RF, flash photolysis with resonance fluorescence as the detection system.

Comparison with Previous Studies

Table III lists the three Arrhenius expressions which have now been reported for reaction 1. The calculated 298 K rate constants are seen to be in remarkably good agreement with each other. These values suggest that at room temperature, k_1 can be given as $(6.6 \pm 0.6) \times 10^{-13}$ cm^3 molecule^{-1} s^{-1}. The temperature dependence of k_1 obtained in the present study is seen to be in reasonably good agreement with previous measurements. The most significant disagreement is with the work of Zahniser et al.[8] As can be seen from Figure 3, the error bars on k_1, measured in this work, overlap the Arrhenius lines of both Zahniser et al.[8] and Smith and Zellner[7] at temperatures higher than 270 K. Below 270 K, our k_1 values are in good agreement with those of Smith and Zellner, but are ~20% lower than those measured by Zahniser et al.[8] at temperatures of 225 K. At the present time, we can give no explanation for this observed difference in k_1 at low temperatures.

Concerning reaction 2, the results from four previous studies, as well as the present investigation, are listed in Table IV. The most recent results obtained by Singleton

TABLE V: Rate of HCl Degradation in the Stratosphere

Altitude (A), km	Temp (T), K, at A	k_1[c] at $T \times 10^{13}$	OH concn, radicals per cm^3 at A $\times 10^{-7}$	k_1[OH] $\times 10^9$	k_2[d] at $T \times 10^{17}$	O(^{3}P)[a] atom concn, atoms per cm^3	k_2[O(^{3}P)] $\times 10^9$	k_1[OH]/k_2[O]	J_{HCl}[b]
20	220	4.2	0.11	463	0.20	0.02	0.004	1.2×10^5	$<10^{-10}$
25	220	4.2	0.18	737	0.20	0.14	0.03	2.6×10^4	$\sim 6 \times 10^{-10}$
30	230	4.6	0.30	1370	0.42	0.62	0.26	5.3×10^3	$\sim 8 \times 10^{-9}$
35	240	5.0	0.63	3120	0.83	2.4	2.0	1.6×10^3	$\sim 2.5 \times 10^{-8}$
40	250	5.3	1.4	7450	1.6	8	12	6.0×10^2	$\sim 4 \times 10^{-8}$
45	265	5.9	1.6	9380	3.7	22	80	1.2×10^2	$\sim 5.5 \times 10^{-8}$
50	270	6.0	1.1	6640	4.7	36	171	3.9×10^1	$\sim 6.5 \times 10^{-8}$

[a] Reference 20. [b] Reference 19. [c] k_1 from this work. [d] k_2 from this work.

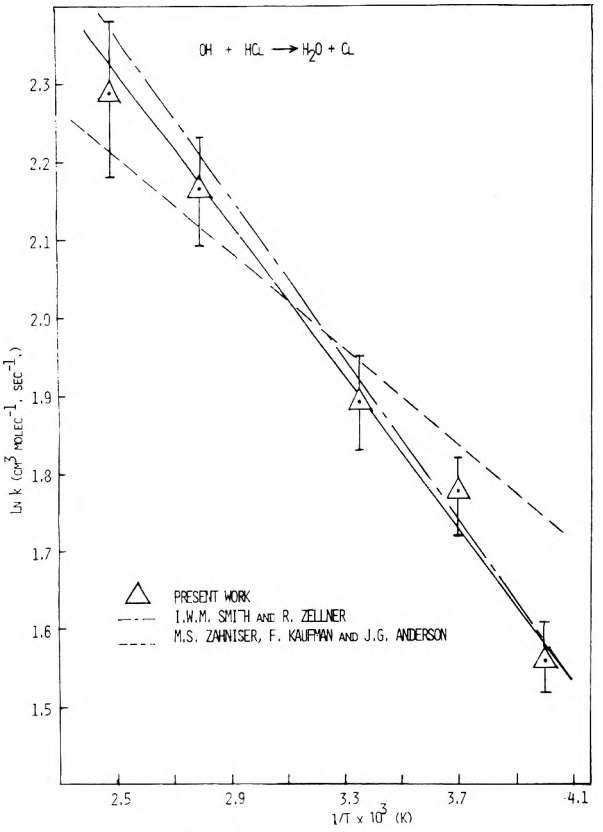

Figure 3. Arrhenius plots for the reaction OH + HCl → H_2O + Cl.

and Cvetanovic[11] have not been included in Table IV since these authors have yet to provide printed rate data at different temperatures. However, a value for E_{act} was verbally reported by these investigators[11] as ~6 kcal mol^{-1}. From Table IV, it would appear that the activation energy of 4.5 kcal mol^{-1}, obtained by Balakhnin et al.,[9] is quite low and probably incorrect. There is a discrepancy of ~1.5 kcal mol^{-1} between Brown and Smith's[10] value of E_2 and that reported in this work. The results from the other three investigations lie between these two values. At this juncture, there appears to be no basis for rejecting or accepting any one of these five values for E_2 (i.e., 6,[10] ~6,[11] 6.44,[6] 7.15,[12] and 7.5 kcal mol^{-1}). It should be noted, in fact, that the seemingly large discrepancy of ~25% in E_2 is not that unreasonable in view of the small value for the bimolecular rate constant. However, there is a large discrepancy in the values of the individual bimolecular rate constants measured at a given temperature by different authors. For example, at 401 K, the value of k_2 measured by Smith and Brown is a factor of 3 lower than that measured by us. In virtually all studies reported, involving four different techniques, it appears that the sensitivity of each apparatus was at its ultimate limit.

Atmospheric Implications

The three processes which reintroduce Cl atoms into the stratospheric O_3 destruction cycle are chemical reactions 1 and 2 and the photochemical process 3. At photochemical equilibrium with respect to Cl atoms, it can be shown that

$$[Cl]/[HCl] = (k_1[OH] + k_2[O(^3P)] + J_{HCl})/k_4[RH] \quad (I)$$

where J_{HCl} is the photodissociation rate constant for HCl and process 4 is given as

$$Cl + RH \rightarrow HCl - R \quad (4)$$

Presented in Table V are the values of k_1[OH], k_2[O(^{3}P)], and J_{HCl} as a function of altitude. From this table, it can be seen that reaction 1 totally dominates the conversion of HCl back to active chlorine atoms below 50 km. In point of fact, at the most favorable altitude of 50 km, reaction 2 makes only an approximate 3% contribution to the total conversion process. Thus, below 50 km, eq I can be simplified to

$$\frac{[Cl]}{[HCl]} = \frac{k_1[OH]}{k_4[RH]} \quad (II)$$

The maximum impact on stratospheric models from the k_1 value reported in this work would be in the stratospheric region of 13 to 30 km. In this region, our value of k_1 would predict an approximate 20% lower value for the steady-state Cl atom concentration than that suggested from the measurements of Zahniser et al.[8] It should again be noted, however, that no basis presently exists for excluding the Zahniser et al.[8] value; hence, it would seem reasonable to take a simple average of the k_1 values for modeling purposes.

References and Notes

(1) (a) P. Crutzen, *Ambio*, **3**, 210 (1974); (b) M. J. Molina and F. S. Rowland, *Nature (London)*, **249**, 810 (1974); (c) S. Wofsy, M. McElroy, and S. Sze, *Science*, **187**, 535 (1975); (d) R. J. Cicerone, R. S. Stolarski, and S. Walters, *Science*, **186**, 1165 (1974).
(2) (a) C. B. Farmer, O. F. Raper, and R. H. Norton, Proceedings of the Fourth Conference of the Climatic Impact Assessment Program, Feb 4–7, 1975; Cambridge, Mass. (b) A. Lazrus, B. Grandrud, R. Woodward, and W. Sedlucek, *Geophys. Res. Lett.*, **2**, 439–441 (1975).
(3) R. Stolarski, R. J. Cicerone, and R. D. Hudson, IAGA Program and Abstract for General Scientific Assembly, 1973, Kyoto, Japan.
(4) W. E. Wilson, Jr., J. T. O'Donovan, and R. M. Fristrom, *Symp. (Int.) Combust. [Proc.], 12th*, 929 (1969).
(5) R. G. Takacs and G. P. Glass, *J. Phys. Chem.*, **77**, 1949 (1973).
(6) W. Hack, G. Mex, and H. Gg. Wagner, Max-Planck-Institut für Festkörperforschung, Berich 3/1976.
(7) I. W. M. Smith and R. Zellner, *J. Chem. Soc., Faraday Trans. 2*, **70**, 1045 (1974).

(8) M. S. Zahniser, F. Kaufman, and J. G. Anderson, *Chem. Phys. Lett.*, **27**, 507 (1974).
(9) V. P. Balakhnin, V. I. Egorov, and E. I. Intezarova, *Kinet. Katal.*, **12**, 299 (1971); *Kinet. Catal.*, **12**, 258 (1971).
(10) R. D. H. Brown and I. W. M. Smith, *Int. J. Chem. Kinet.*, **7**, 301 (1975).
(11) D. L. Singleton and R. J. Cvetanovic, 12th Informal Conference of Photcchemistry, NBS, U.S. Department of Commerce, June 28–July 1, 1976.
(12) E. L. Wong and F. E. Beiles, *NASA Tech. Note* **D-6495** (1971); *Chem. Abstr.*, **76**, 1832*q* (1972).
(13) D. D. Davis, S. Fischer, and R. Schiff, *J. Chem. Phys.*, **61**, 2213 (1974).
(14) D. D. Davis, R. E. Huie, and J. T. Herron, *J. Chem. Phys.*, **59**, 628 (1973).
(15) (a) D. D. Davis, R. E. Huie, J. T. Herron, M. J. Kurylo, and W. Braun, *J. Chem. Phys.*, **56**, 4868 (1972); (b) D. D. Davis and R. B. Kemm, *Int. J. Chem. Kinet.*, **4**, 367 (1972).
(16) J. A. Myer and J. A. R. Samson, *J. Chem. Phys.*, **52**, 266 (1970).
(17) J. Romand, *Ann. Phys. (Paris)*, **4**, 527 (1949).
(18) It is easy to show that reactions of ClOO and ClO are of no consequence in our system. These radicals can be formed through the following sequence of reactions:

$$O + HCl \rightarrow OH + Cl$$
$$OH + HCl \rightarrow H_2O + Cl$$
$$Cl + O_2 + Ar \rightarrow ClOO + Ar$$
$$ClOO + O \rightarrow ClO + O_2$$
$$ClO + O \rightarrow Cl + O_2$$

Even if we assume that each $O(^3P)$ atom in the system led to the formation of one ClOO radical through the proposed reaction mechanism, the concentration of ClOO would be $\sim 10^{10}$ cm^{-3} *during* the decay of $O(^3P)$, since the pseudo-first-order rate constant for the formation of ClOO through the reaction, $Cl + O_2 + Ar \rightarrow ClOO + Ar$, is at most 86 s^{-1} under our experimental conditions (it is very likely to be an order of magnitude lower). Hence, the contribution of $ClOO + O \rightarrow ClO + O_2$ toward the measured pseudo-first-order rate constant k_2' would be at most 15%. When the flash energy was increased by a factor of 6, the concentrations of O atoms and ClOO would both be 6 times higher. Thus, this flash energy variation would have indicated the importance of that reaction.
(19) R. T. Watson, "The Natural Stratosphere of 1974", CIAP Monograph 1, 5-125 (1975).
(20) R. J. Cicerone, private communications.

Direct Measurement of the Radiative Lifetime and Collisional Quenching of the $C^3\Pi_u$ State of Nitrogen as Studied by Pulse Radiolysis

T. W. Carr[†] and S. Dondes*

Rensselaer Polytechnic Institute, Troy, New York 12181 *(Received June 24, 1977)*

The optical emission of $N_2(C^3\Pi_u \rightarrow B^3\Pi_g)$, the second positive system, has been measured by pulse radiolysis of pure nitrogen, helium–nitrogen, and argon–nitrogen gas systems as a function of total gas pressure in the range 50–20 000 Torr. The radiative lifetime, τ_0, was found to be 40.8×10^{-9} s and the quenching rate constants for nitrogen and helium were found to be 7.1×10^{-12} and 7.8×10^{-14} cm^3 particles^{-1} s^{-1}, respectively.

Introduction

The identity, lifetime, and reactivity of the short-lived transient species produced in a chemical reaction constitutes a central problem in the elucidation of reaction mechanisms. This information is often obtained from fast reaction techniques which generally involve a short-lived perturbation of the system from an external source, followed by the direct observation of some physical parameter as a function of time. Pulse radiolysis is a useful technique for determining this type of information.[1-14]

The recent development of the plasma chromatograph and atmospheric pressure ionization sources for mass spectrometry has created an interest in the fate of electronically excited ions and neutral molecules at total gas pressures of 1 atm and above.[5-9] In this work, the technique of gas phase pulse radiolysis was employed to directly measure the lifetime of the second positive emission bands of nitrogen, $C^3\Pi_u \rightarrow B^3\Pi_g$ transition, at total pressures ranging from 50 to 20 000 Torr.

Experimental Section

A schematic of the gas phase pulse radiolysis arrangement is shown in Figure 1. A 1-MeV Van de Graaff electron accelerator produces electron pulses of 1-, 3-, 10-, 30-, and 100-ns duration with a average pulse current of 0.5 A per pulse. The accelerator is capable of operating in a single or repetitive pulsing mode with a maximum of 150 pulses per second. The reaction cell is aligned on axis with the exit window of the accelerator and the light emissions are analyzed with a SPEX Model 1500, 3/4 meter, Czerny-Turner mount, optical grating spectrometer with a Bausch and Lomb 600 line/mm grating blazed at 3000 Å. A head-on, 12-stage, RCA 8575 photomultiplier is used to detect the light emission. The signal from the photomultiplier is transmitted through coaxial cable to a Tektronix 564B sampling-storage oscilloscope and is subsequently recorded on a Hewlett-Packard 7035B X-Y recorder. The photomultiplier tube, quartz light pipes, quartz prism, and the reaction cell are lead shielded to reduce the effects of x-rays and interfering Cerenkov radiation.

For the purpose of recording gross spectra, the quartz prism and exit slit of the monochromator could be removed and replaced by a film holder. The film holder is designed to contain a 2-in. piece of 35-mm film upon which a maximum of ten spectra, each covering 1000 Å, can be recorded. The excited species are then identified from their emission spectra.

Three gas mixtures were examined in this study at various total pressures ranging from 50 to 20 000 Torr. The gases were He + 0.1% N_2, pure N_2 (99.999 mol %), and Ar + 0.5% N_2. These gases were obtained from Matheson Gas Products, Inc., East Rutherford, N.J. The composition of the gases prior to irradiation were analyzed with a CEC Model 21-130 cycloidal focusing mass spectrometer.

Results and Discussion

The emission spectra resulting from the irradiation of pure nitrogen were studied in the region 2000–6000 Å. The

[†] Present address: IBM Corp., P.O. Box 390, Poughkeepsie, N.Y. 12602

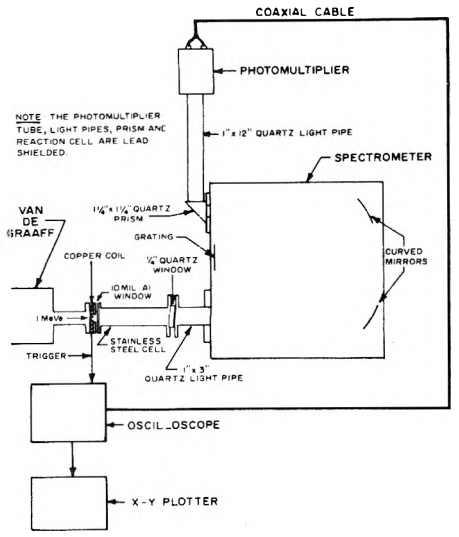

Figure 1. Schematic of the pulse radiolysis experimental arrangement.

TABLE I: Radiative Lifetime and Collisional Deactivation Rate Constants for the Second Positive System of Nitrogen in Pure Nitrogen

Band	τ_0, ns	$k_2^{N_2}$, cm³ particles⁻¹ s⁻¹
0, 0	41.5	7.86×10^{-12}
0, 1	36.8	6.69×10^{-12}
0, 2	38.5	6.75×10^{-12}

emission bands observed in this region were associated with the $C^3\Pi_u \rightarrow B^3\Pi_g$ (second positive) transition of nitrogen and they occurred primarily in the $v^1 = 0$ progression although some bands of the $v^1 = 1$ progression were visible with lesser intensity.

Pure nitrogen samples were irradiated at various pressures ranging from 55 to 20 000 Torr. At pressures greater than 760 Torr, these second positive bands ($C^3\Pi_u \rightarrow B^3\Pi_g$) of nitrogen were observed to rise and fall very sharply as a function of time. Lifetime observations in this pressure region were shorter than the response time of the photomultiplier tube. As the pressure was reduced below 760 Torr, the emission bands of the $v^1 = 0$ progression were found to rise sharply approximating the rise of the electron pulse and to decay exponentially. The exponential decay followed a first-order kinetic rate constant. The lifetime of these emission bands were observed to be pressure dependent and followed a Stern–Volmer relationship of the form:

$$k_T = \frac{1}{\tau_p} = \frac{1}{\tau_0} + k_2 PL \qquad (1)$$

where k_T is the rate constant for the transition in (seconds)$^{-1}$ and equal to $1/\tau_p$; τ_0 is the radiative lifetime in seconds; k_2 is the rate constant for collisional deactivation in (centimeters)^3 particles^{-1} second^{-1}; P is the total pressure in the system in atmospheres; and L is Loschmidt's number in particles centimeters^{-3} atmosphere^{-1}. The radiative lifetime, τ_0, and the rate constant for collisional deactivation, k_2, are shown in Table I for the (0, 0), (0, 1), and (0, 2) bands of the nitrogen second positive system as determined from a Stern–Volmer plot of k_T vs. pressure; the $1/\tau_0$ obtained from the intercept and k_2 from the slope.

The emission bands of the nitrogen second positive system were also observed in the spectra resulting from the irradiation of the He + 0.1% N_2 mixture at total pressures ranging from 55 to 20 000 Torr. These emission bands were observed to follow a first-order exponential decay at all pressures. A typical plot of the emission

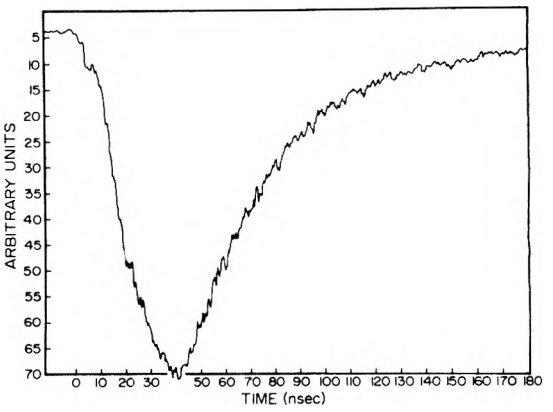

Figure 2. The emission of the (0, 0) band of the second positive system at 3371 Å as a function of time in a helium–0.1% nitrogen gas mixture at 1 atm pressure using a 30-ns pulse for excitation.

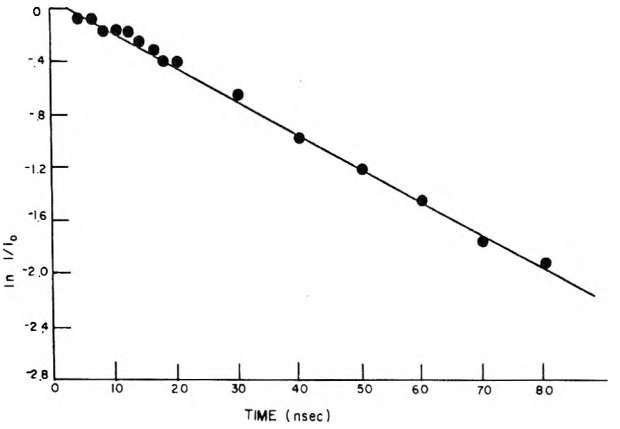

Figure 3. Plot of the logarithm of the decay of the fluorescence vs. time of the (0, 0) band of the second positive system at 3371 Å in a helium–0.1% nitrogen gas mixture at 1 atm pressure using a 30-ns electron pulse for excitation.

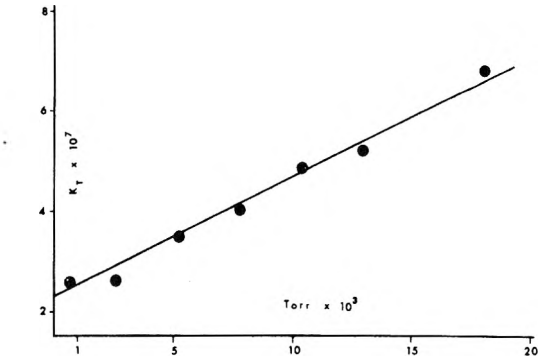

Figure 4. A Stern–Volmer plot of the decay constant vs. pressure for the (0, 0) band of the second positive system at 3371 Å in a helium–0.1% nitrogen gas mixture.

TABLE II: Radiative Lifetime and Collisional Deactivation Rate Constants for the Second Positive System of Nitrogen in He + 0.1% N_2 Gas Mixture

Band	τ_0, ns	$k_2^{He+N_2}$, cm³ particles⁻¹ s⁻¹
0, 0	43.5	7.67×10^{-14}
0, 1	41.2	8.63×10^{-14}
0, 2	41.8	8.91×10^{-14}
0, 3	42.2	8.91×10^{-14}

intensity as a function of time is shown in Figure 2 for the (0, 0) band at 3371 Å obtained at a total pressure of 760 Torr. A semilogarithmic plot of the decay portion of this curve is shown in Figure 3 and the Stern–Volmer plot is shown in Figure 4. The radiative lifetimes and collisional

deactivation rate constants for the nitrogen second positive system emission band in this helium–nitrogen mixture are listed in Table II.

The collisional deactivation rate constant determined in this helium–nitrogen system is the sum of the collisional quenching due to the nitrogen molecules and the collisionally induced transition from the helium atoms. Since the lowest excited state of helium lies at 19.82 eV above the ground state, an energy transfer from the nitrogen molecule at 10.98 eV to helium is not possible. The collisional quenching of the second positive system by nitrogen was determined from the study in pure nitrogen; the average rate constant being 7.1×10^{-12} cm^3 particles^{-1} s^{-1} (the average value of k_2 in Table I). The rate constant for the collisionally induced transition by helium is calculated to be 7.8×10^{-14} cm^3 particles^{-1} s^{-1} obtained from

$$[\mathrm{He} + \mathrm{N_2}]k_2^{\mathrm{He+N_2}} = [\mathrm{He}]k_2^{\mathrm{He}} + [\mathrm{N_2}]k_2^{\mathrm{N_2}} \quad (2)$$

$$k_2^{\mathrm{He}} = \frac{[\mathrm{He} + \mathrm{N_2}]}{[\mathrm{He}]}k_2^{\mathrm{He+N_2}} - \frac{[\mathrm{N_2}]}{[\mathrm{He}]}k_2^{\mathrm{N_2}} \quad (3)$$

since $[\mathrm{He} + \mathrm{N_2}] \simeq [\mathrm{He}]$, the above reduces to

$$k_2^{\mathrm{He}} = k_2^{\mathrm{He+N_2}} - \frac{[\mathrm{N_2}]}{[\mathrm{He}]}k_2^{\mathrm{N_2}} \quad (4)$$

Thus, the nitrogen molecules which can be involved in energy transfer are in the order of one hundred times more efficient in quenching the second positive system of nitrogen.

In both the pure nitrogen and the helium–nitrogen mixture, the second positive system is formed as a result of direct excitation by the electron pulse. Other mechanisms of formation such as the recombination of thermal or subexcitation electrons with ionized nitrogen molecules and cascading from a higher electronic state would probably have an associated induction period which was not observed (or was very short). The emission curves of the second positive system were observed to rise sharply approximating the shape of the electron pulse. Thus, in the helium–nitrogen mixture, the $C^3\Pi_u$ state of nitrogen is not populated by an energy transfer reaction involving excited helium and ground state nitrogen. The lowest excited state of helium, ^3S, lies at 19.82 eV above the ground state and the $C^3\Pi_u$ state of nitrogen is 10.98 eV above the ground state. Therefore, 8.84 eV would have to be accommodated in the form of translational, vibrational, and rotational energy of the nitrogen and by translational energy of the helium. The most probable energy transfer should be a Penning ionization reaction leading to the formation of the $B^2\Sigma^+$ (first negative) state of ionized nitrogen which lies at 18.75 eV above the ground state of the nitrogen molecule[11,12] which was observed. At total gas pressures above 1000 Torr these $B^2\Sigma^+ \rightarrow X^2\Sigma^+$ (first negative system) bands were found to rise and decay very sharply (shorter than the rise time of the photomultiplier tube). Below 1000 Torr the shape of the emission curves as a function of time were observed to be drastically different than those of the second positive system. Both the rise and decay were found to occur over a longer period of time. The energy transfer formation mechanism is a major reason for the difference in the shapes of these emission curves. The decay curve is not a simple first- or second-order exponential and is the subject of another paper.

The emission bands of the second positive system of nitrogen were also observed in the spectra resulting from the irradiation of Ar + 0.5% N_2. As in the case with the first negative system of nitrogen in helium, the shape of the emission curves indicate that an energy transfer reaction is the mechanism of their formation. Le Calve and Bourene[13] have measured the rate constant for the energy transfer from metastable argon atoms in the $^3P_{2,0}$ states at 11.54 and 11.72 eV to nitrogen exciting the latter to the $C^3\Pi_u$ state. Le Calve and Bourene[13] found an exponential decay with a time constant much greater than the radiative lifetime of the second positive system of nitrogen. In our study we did not observe an exponential decay at pressures ranging from 500 to 1500 Torr. A delayed production of metastable Ar* or Ar_2* by the recombination of Ar_2^+ ions with thermal electrons may be the cause of the observed nonexponential decay.

TABLE III: Values of τ_0, the Radiative Lifetime, for the $C^3\Pi_u$ State of Nitrogen

τ_0, ns	Investigator
27	Fink and Welge[15]
47	Jeunehomme[16]
44.5	Bennett and Dalby[17]
37	Anton[18]
35.5	Wagner[19]
46.3	Nichols and Wilson[20]
48	Hesser[21]
40.5	Calo and Axtman[22]
40.8	This work

Table III lists the literature values for the radiative lifetimes, τ_0, of the $C^3\Pi_u$ state of nitrogen. With the possible exception of Fink and Welge's[15] value, the data reported in this work agrees well considering the different techniques used. For example, Jeunehomme[16] employed a pulsed or modulated radiofrequency discharge in his fluorescence lifetime measuring technique; Hesser[21] measured the phase differences between the light emitted and a reference; Calo and Axtman[22] used Cf-252 fission fragments for excitation and employed interference filters which were optically coupled to photomultiplier tubes in their coincidence counting technique.

All the previous recorded values[15-22] were obtained at much lower pressures, usually 5–10 μm. The technique of pulse radiolysis can be applied over a wide range of pressures as demonstrated in this study. This technique can open many new areas of research such as the direct determination of the rate constants of energy transfer reactions. As such the pulse radiolysis technique can prove to be of great value in the elucidation of rates and mechanisms involved in the formation of product ions in the plasma chromatograph and atmospheric pressure ionization mass spectrometer.

Acknowledgment. Our thanks to Mr. R. Haskell for the modifications and maintenance of the apparatus which made this work possible. Research supported in part by the USAEC, Contract (AT11-1-3461), and the Office of Naval Research, Contract (N00014-68-A-0495).

References and Notes

(1) M. Ebert, J. P. Keene, A. J. Swallow, and J. H. Baxendale, Ed., "Pulse Radiolysis", Academic Press, New York, N.Y., 1965. M. S. Matheson and L. M. Dorfman, "Pulse Radiolysis", M.I.T. Press, Cambridge, Mass., 1969. R. F. Firestone and L. M. Dorfman, "Pulse Radiolysis of Gases", in Actions Chimiques et Biologiques des Radiations, M. Haissinsky, Ed., Masson & Co., Paris, France, 1971. M. S. Matheson, "Pulse Radiolysis" in "Advances in Radiation Research, Physics and Chemistry", Vol. I, J. F. Duplan and A. Chapiro, Ed., Gordon and Breach, New York, N.Y., 1973.
(2) M. C. Sauer and L. M. Dorfman, *J. Am. Chem. Soc.*, **87**, 3801 (1975).
(3) M. C. Sauer, *J. Phys. Chem.*, **71**, 3311 (1967).
(4) J. H. Brophy, J. S. Silver, and J. L. Kinsey, *Chem. Phys. Lett.*, **28(3)**, 418 (1974).
(5) F. W. Karasek, *Anal. Chem.*, **46**, 710A (1974).
(6) R. A. Keller and M. M. Metro, *Sep. Purif. Methods*, **3**, 207 (1974).
(7) D. J. Carroll, J. Dzidic, R. N. Stillwell, M. C. Horning, and E. C. Horning, *Anal. Chem.*, **46**, 706 (1974).
(8) M. McKeown and M. Siegel, *Am. Lab.* (Nov. 1975).

(9) D. J. Carroll, J. Dzidic, R. N. Stillwell, and E. C. Horning, *Anal. Chem.*, **47**, 1956 (1975).
(10) J. Dzidic, D. J. Carroll, R. N. Stillwell, and E. C. Horning, *Anal. Chem.*, **48**, 1763 (1976).
(11) W. C. Richardson and D. W. Setser, *J. Chem. Phys.*, **58**, 1809 (1973).
(12) S. Dondes, P. Harteck, and C. Kunz, *Radiat. Res.*, **27**, 174 (1973).
(13) J. Le Clave and M. Bourene, *J. Chem. Phys.*, **58**, 1446 (1973).
(14) M. Bourene and J. Le Calve, *J. Chem. Phys.*, **58**, 1452 (1973).
(15) E. Fink and K. Welge, *Z. Naturforsch. A*, **19**, 1193 (1964).
(16) M. Jeunehomme, *J. Chem. Phys.*, **44**, 2672 (1966).
(17) R. G. Bennett and F. W. Dalby, *J. Chem. Phys.*, **31**, 434 (1959).
(18) H. Centon, *Z. Naturforsch. A*, **19**, 178 (1964).
(19) K. H. Wagner, *Z. Naturforsch. A*, **19**, 716 (1964).
(20) L. L. Nichols and W. E. Wilson, *Appl. Opt.*, **7**, 167 (1968).
(21) J. E. Hesser, *J. Chem. Phys.*, **48**, 2518 (1968).
(22) J. Calo and R. Axtman, *J. Chem. Phys.*, **54**, 1332 (1971).

Molecular Complexes Formed by Interaction of Iron(II) Bromide, Aluminum(III) Bromide, and Bromine

N. W. Gregory* and W. C. Laughlin

Department of Chemistry, University of Washington, Seattle, Washington 98195 *(Received July 18, 1977)*

Publication costs assisted by the National Science Foundation

The molecular complexes $FeAl_2Br_8$ and $FeAlBr_6$ have been studied in the vapor phase in the temperature interval 500–775 K by transpiration and spectrophotometric methods. Standard enthalpies of formation and standard entropies of the vapor molecules of −298.3 and −180.8 kcal mol^{-1} and 222.1 and 169 cal deg^{-1} mol^{-1}, respectively, have been derived for the mean temperature of the experiments. $FeAlBr_6$ shows two strong absorbance bands, believed associated with charge transfer transitions, in the wavelength interval 250–800 nm with maxima observed ca. 280 and 460 nm. The molar absorptivity at 280 nm is found to be 6300 mol^{-1} L cm^{-1}. $FeAl_2Br_8$ shows no appreciable absorbance in this region of the spectrum.

Little is known about the properties of complexes formed between transition metal dibromides and aluminum bromide. A substantial number of chloride complexes have now been studied[1] and two papers have recently discussed properties of $CoAl_2Br_8$[2,21] and $CuAl_2Br_8$.[2] While the bromides are expected to behave similarly to the chlorides, important differences may be anticipated. Kendall, Crittenden, and Miller[3] have reported a qualitative examination of the melting points of mixtures of $FeBr_2$ and $AlBr_3$; while they express doubt as to the purity of their samples and a complete phase diagram was not established, they conclude that a solid state compound with composition $FeBr_2 \cdot 2AlBr_3$ is formed; the solubility of $FeBr_2$ in liquid $AlBr_3$ appears to be about 20 mol % at 300 °C. Gorenbein[4] has reported a study of the electrical conductivity of mixtures of aluminum bromide with zinc bromide and mercuric bromide and finds evidence for formation of similar addition complexes in these systems.

We have been interested in the nature of molecules formed in the vapor phases of such mixtures. In the present work transpiration experiments have been used to show that the presence of aluminum bromide vapor in an argon carrier gas results in a considerable increase in the amount of iron in the vapor phase in equilibrium with solid ferrous bromide at temperatures between 280 and 450 °C. The data correlate well if it is assumed that the principal vaporization reaction is

$$FeBr_2(s) + Al_2Br_6(g) = FeAl_2Br_8(g) \quad (1)$$

In separate experiments the equilibrium vapor mixture has also been examined spectrophotometrically; no appreciable absorbance attributable to the complex was detected in the wavelength interval 250–800 nm at temperatures below 500 °C. When bromine is added to the mixture, however, the equilibrium vapors show a strong absorbance in this region (above that expected from the bromine) with two maxima observed, at 280 and 460 nm, respectively. This absorbance is clearly dependent on the concentration of bromine and of aluminum bromide and in the presence of excess $FeBr_2(s)$ is considerably greater than observed for $FeBr_2$–Br_2 mixtures alone.[5] The observations can be correlated satisfactorily by assuming the principal absorbing species in the presence of bromine to be the mixed metal dimer $FeAlBr_6$, with reaction 2 the dominate

$$FeAlBr_6(g) + {}^1/_2 Al_2Br_6(g) = FeAl_2Br_8(g) + {}^1/_2 Br_2(g) \quad (2)$$

equilibrium controlling the relative concentrations in completely vaporized mixtures (200–500 °C). When $FeBr_2(s)$ is present the concentration of $FeAlBr_6$ may be considered independently of $FeAl_2Br_8$ and to be fixed by the equilibrium

$$FeBr_2(s) + {}^1/_2 Al_2Br_6(g) + {}^1/_2 Br_2(g) = FeAlBr_6(g) \quad (3)$$

Thermodynamic constants for the molecular complexes have been calculated from absorbance data using a derived value for the molar absorptivity of $FeAlBr_6$ at the peak maximum at 280 nm to follow the concentration of this molecular species in the various equilibrium mixtures. Results from the spectrophotometric study of reactions 2 and 3 have been combined to predict equilibrium constants for (1) and tested by comparison with the direct study of this reaction by the transpiration experiments.

Equilibrium constants for the disproportionation reaction 4, obtained by combining the results for (3) with

$$Al_2Br_6(g) + Fe_2Br_6(g) = 2FeAlBr_6(g) \quad (4)$$

those of an earlier study of reaction 5,[6] are found to be

$$2FeBr_2(s) + Br_2(g) = Fe_2Br_6(g) \quad (5)$$
$$\Delta G^\circ = 16\,300 - 18.0\,T \text{ cal } mol^{-1}$$

around 3, similar in magnitude to that reported recently for the corresponding reaction in the chloride system,[7] and

TABLE I: Absorbance Data

Sample (cell path length, cm)	C_0(Fe), mol L^{-1}	C_0(Al), mol L^{-1}	$C_0(Br_2)$, mol L^{-1}
A (2.5)	Excess $FeBr_2$(s)	3.634×10^{-4}	0.0
B (2.0)	Excess $FeBr_2$(s)	5.545×10^{-4}	$(2.778 \times 10^{-4})^a$
C (2.5)	8.095×10^{-5}	1.448×10^{-3}	4.024×10^{-3}
D (10.0)	5.345×10^{-5}	3.175×10^{-3}	3.879×10^{-4}
E (2.5)	8.481×10^{-5}	3.933×10^{-3}	3.010×10^{-3}
F (1.0)		1.643×10^{-3}	2.630×10^{-3}
G (10.0)	4.213×10^{-5}	4.359×10^{-3}	6.900×10^{-4}

$FeBr_2$(s) present				Samples completely vaporized		
Sample	T, K (solid)	T, K (vapor)	A_{280}	Sample	T, K	A_{280}
B	512	535	0.115	C	574	0.472
B	545	568	0.135	C	628	0.452
B	510	573	0.100	C	683	0.444
B	586	607	0.185	D	751	0.178
B	621	645	0.238	D	754	0.183
B	672	697	0.338	D	698	0.195
B	723	750	0.410	D	624	0.211
B	773	803	0.495	D	571	0.234
C	471	474	0.474	D	535	0.247
C	454	461	0.248	D	509	0.259
C	418	428	0.114	E	731	0.364
E	459	516	0.134	E	654	0.400
E	473	516	0.220	E	601	0.428
F	461	464	0.150	E	545	0.448
F	525	534	0.480	E	502	0.456
F	566	577	0.710	G	678	0.164
F	614	628	1.06	G	636	0.172
F	653	673	1.72	G	588	0.187
				G	547	0.198
				G	529	0.200

[a] See text.

generally expected for the formation of this type of complex.[1]

Experimental Section

Samples of $FeBr_2$ and $AlBr_3$ were prepared in all Pyrex–quartz vacuum systems by direct reaction of metallic wires (Merck Reagent Grade iron, 99.8%; Baker's Analyzed Reagent Grade aluminum (ACS Specification)) with dry bromine (Baker's Analyzed Reagent Grade, 99.3%). Desired amounts were sublimed directly into quartz absorption cells and isolated by vacuum flame seal-off of a connecting side arm or into appropriate sections of the transpiration apparatus.

A Cary 14H recording spectrophotometer was used to measure absorbances. Temperatures of the cell side arm, cell body, and cell windows were measured with calibrated chromel–alumel thermocouples. Procedures were similar to those described in earlier papers.[5,7] The transpiration apparatus and method was basically that developed in this laboratory by Richards[8] and used recently by us in a study of the CuCl–$AlCl_3$ system.[9] Argon at ca. 1000 Torr and at flow rates between 15 and 23 cm^3 min^{-1} was used as the principal carrier gas. The argon was made to flow first over a sample of $AlBr_3$ (solid or liquid) heated in a compartment adjacent to the main reactor furnace to a temperature appropriate to introduce the desired partial pressure of aluminum bromide; this mixture was then passed over a sample of $FeBr_2$(s), held in the main reactor vessel at various higher temperatures. Partial pressures in the final equilibrium vapor mixture were deduced from the relative number of moles of Al, Fe, and Ar in the effluent gas. Results showed no systematic variation with flow rates. Amounts of aluminum and iron transported were determined by atomic absorption analysis. The argon was condensed in a following liquid nitrogen cooled trap and the number of moles determined by evaporating the sample into a calibrated volume at a measured pressure and temperature; ideal gas behavior was assumed. The argon pressure in the reactor was monitored manometrically during the run.

Table I lists values of C_0(Fe), C_0(Al), and $C_0(Br_2)$, the concentration (mol L^{-1}) equivalents of the total moles of iron atoms, aluminum atoms, and bromine molecules (the latter in excess over the bromine present as part of the amount of $FeBr_2$ originally introduced into the cell), for the various samples studied spectrophotometrically. Sample A was a mixture of $FeBr_2$ and $AlBr_3$; sample B was isolated as a mixture of $FeBr_2$(s) and $FeAlBr_6$(s) with no measurable amount of free bromine present at low temperatures. For the other samples amounts of bromine were determined spectrophotometrically[10] at temperatures sufficiently high to prevent formation of $FeBr_3$(s)[6] but too low to form detectable concentrations of iron containing molecules in the vapor phase. The amount of bromine indicated in parentheses for sample B was assumed to be one-half C_0(Al) as expected if the complex decomposes according to equilibrium 3. The amounts of iron and aluminum in the cells were determined by atomic absorption analysis after measurements were completed.[11]

Results and Discussion

Transpiration Studies. Transpiration data are summarized in Table II. The contribution to the total number of moles of iron in the vapor phase expected from the vapor pressure of $FeBr_2$(s)[5] was significant only for the runs at the two highest temperatures. The additional iron in the vapor was assumed present as $FeAl_2Br_8$. Hence twice the indicated number of moles of this species was subtracted from the total number of gram atoms of aluminum transported to give the number of gram atoms of alu-

TABLE II: Transpiration Data

T, K	Flow rate, cm^3/min (STP)	Ar press, Torr	No. of gram atomic wt transported 10^2[Ar]	10^9[Fe][a]	10^7[Fe][b]	10^5[Al]	Calcd partial press (atm) $10^5 \cdot$ [Al_2Br_6]	$10^6 \cdot$ [$FeAl_2Br_8$]	10^2K_1
609	23.3	953	17.5	2.65	56.0	55.6	81.7	40.2	4.93
609	20.2	1012	15.2	2.24	0.460	2.33	0.571	0.403	7.06
647	18.8	982	12.8	32.4	4.32	10.1	3.77	4.36	11.6
649	18.2	1002	12.4	34.2	11.2	14.4	7.36	12.0	15.8
646	17.2	980	11.7	28.2	163	98.5	195	179	9.15
557	17.5	1003	14.3	0.0375	0.268	1.76	1.85	0.247	1.33
567	15.9	1005	10.8	0.0580	13.5	26.7	104	16.5	1.59
566	15.6	990	10.6	0.0920	18.8	28.9	116	23.0	1.99
681	17.5	995	13.1	185	34.1	35.6	16.2	34.0	21.0
723	17.1	978	8.17	818	32.3	37.5	15.7	51.0	32.5

[a] As $FeBr_2$ and Fe_2Br_4. [b] As $FeAl_2Br_8$.

minum in the form of $AlBr_3$ and Al_2Br_6. Relative amounts of these two species were calculated from thermodynamic data for reaction 6 taken from the JANAF Tables.[12]

$$2AlBr_3(g) = Al_2Br_6(g) \quad (6)$$
$$\Delta G^\circ = -26\,000 + 32.7\,T \text{ cal mol}^{-1}$$

Partial pressures of the various components were calculated from Dalton's law for ideal gases. The total pressure and total number of moles of gas were taken as values measured for argon (in the maximum case the minor components amounted to less than 0.4% of the gas mixture).

In several experiments $FeBr_2(s)$ at comparable temperatures (within a few degrees) was allowed to equilibrate with substantially different partial pressures of Al_2Br_6. At 647 K, for example, the Al_2Br_6 pressures in two of the runs differ by a factor of 52. The amount of iron transported as the complex showed a first power dependence on the Al_2Br_6 pressure in these cases, indicating that molecules containing two aluminum atoms in the complex are the dominant species. A similar test of the number of iron atoms in the complex was not feasible. However with the substantial evidence showing formation of complexes of the form $MX_2 \cdot 2AlX_3$ in similar systems,[1,13] it was assumed that reaction 1 represents the principal vaporization process. The formula $FeAl_2Br_8$ corresponds to the expected stoichiometry for the combination of ferrous ion with $AlBr_4^-$; however vapor molecules are expected to have iron and aluminum atoms bridged together by bromine atoms, similar to Al_2Br_6, although possibly with the Fe(II) atoms octahedrally coordinated between two $AlBr_4$ tetrahedra.[21]

There was no indication, either from the appearance of the sample or from the dependence of the amount of material transported on the aluminum bromide pressure, that the complex was condensed as a liquid or a solid phase or that if dissolved to any appreciable degree in the ferrous bromide phase under the conditions of the experiments. This would not be expected from the observations of Korshunov et al.[13] who report that the Al_2Cl_6 decomposition pressure reaches 1 atm over liquid $FeCl_2 \cdot 2AlCl_3$ at 258 °C. The data in Table II were measured in the order listed. In the midst of the series, between entries 5 and 6, the sample was cooled to ca. 170 °C and the partial pressure of aluminum bromide increased until a condensed liquid (presumed to be the complex saturated with $FeBr_2$) was observed in the reactor along with $FeBr_2(s)$. Flow experiments with the liquid phase present indicated relatively high partial pressures of Al_2Br_6 at 170 °C; since no iron could be detected in the transported material it was not analyzed quantitatively. Not until the temperature was raised to the range shown in Table II, after which the liquid was no longer present, did amounts of iron transported reach a level such that the study of reaction 1 could be resumed. Results obtained subsequently were consistent with those prior to formation of the liquid phase. After completion of the experiments analysis of the solid remaining in the reactor gave a percentage of iron very close to that expected for $FeBr_2$.

A least-squares treatment of the data in Table II, based on an equation of the form $\ln K_1 = AT^{-1} + B$, gave constants and standard deviations (in parentheses) corresponding to $\Delta H^\circ_1 = 15.9$ (6.3%) kcal mol^{-1} and $\Delta S^\circ_1 = 20.3$ (8.0%) cal mol^{-1} deg^{-1} for the mean temperature of 640 K. The data and the thermodynamic properties of the complex will be considered further after discussion of the results of the absorbance studies.

Absorbance Studies. As indicated in the introductory paragraph, no appreciable absorbance of vapors generated by sample A (no bromine present, mixture of $FeBr_2$ and $AlBr_3$) was observed over the wavelength interval 250–800 nm at temperatures below 500 °C. Since the transpiration experiments indicate the presence of substantial amounts of $FeAl_2Br_8$ (K_1 values approach unity at the higher temperatures in this range), this species does not show strong charge transfer bands in this wavelength range. A strong absorbance is observed, however, when bromine is added to such mixtures; two maxima, at ca. 280 and 460 nm, respectively, are observed. The latter overlaps strongly with the major peak in the bromine spectrum.[10] A representative spectrum from sample B, for which the bromine concentration is so low as to contribute little to the total absorbance, is shown in Figure 1.

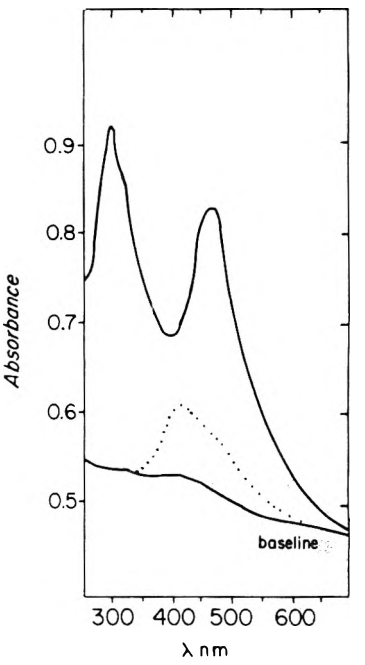

Figure 1. Tracing of vapor phase absorption spectrum of sample B with T(solid) = 587 K and T(vapor) = 607 K. Calculated concentrations: $C_1 = 2.78 \times 10^{-5}$, $C_2 = 6.06 \times 10^{-6}$, $C_3 = 1.91 \times 10^{-6}$, $C_4 = 4.11 \times 10^{-7}$, $C_5 = 2.02 \times 10^{-4}$, $C_6 = 1.10 \times 10^{-4}$, $C_7 = 2.62 \times 10^{-4}$ mol L^{-1}. Solid line is a trace of total absorbance as recorded; dotted line indicates predicted contribution from Br_2.[10]

To interpret the absorbance data for the mixtures containing bromine, reaction 7, in addition to reactions 1–6,

$$2FeBr_3(g) = Fe_2Br_6(g) \quad (7)$$
$$\Delta G^\circ = -33250 + 32.1\,T \text{ cal mol}^{-1}$$

must also be considered.[6] To simplify the following discussion equilibrium constants (in concentration units) will be identified by a corresponding reaction number subscript and the concentrations C (mol L^{-1}) abbreviated as follows: C_1 ($FeAlBr_6$), C_2 ($FeAl_2Br_8$), C_3 (Fe_2Br_6), C_4 ($FeBr_3$), C_5 (Al_2Br_6), C_6 ($AlBr_3$), and C_7 (Br_2), all in the gas phase. For example, $K_7 = C_3/C_4^2$. Neglecting other possible complexes the following relationships may be written for completely vaporized samples:

$$C_0(Fe) = C_1 + C_2 + 2C_3 + C_4 \quad (8)$$
$$C_0(Al) = C_1 + 2C_2 + 2C_5 + C_6 \quad (9)$$
$$C_0(Br_2) = C_7 - C_3 + (C_1 + C_4)/2 \quad (10)$$
$$A = \epsilon_1 C_1 + \epsilon_3 C_3 + \epsilon_4 C_4 \quad (11)$$

where, in (11), A represents the absorbance divided by the path length and ϵ_i the molar absorptivity of the indicated species, both at the wavelength of the absorption peak maximum ca. 280 nm, at which, on testing the data, the contribution of $FeAlBr_6$ appears dominant.

A preliminary calculation, assuming K_4 to be around unity as found in the chloride system,[7] and K_1 to have values given by the transpiration data, indicated that with samples C, D, E, and G completely vaporized, C_3 and C_4 were very small fractions of the total iron in the vapor phase and the expected contribution of these species to the total absorbance was of the order of a few percent or less. Hence it was assumed for these mixtures that the dominant absorbing species was $FeAlBr_6$. In a trial calculation, relationships 8, 9, 10, and 11 were simplified by neglecting C_3 and C_4 and used together with K_6 and values of ϵ_1, varied by increments of 100 over the range 5300–7300 mol^{-1} L cm^{-1}, to solve for the various concentrations and apparent values of the equilibrium constant K_2. Least-squares analysis of ln K_2 vs. $1/T$ for these solutions were found to give a minimum standard deviation for $\Delta H°_2$ = 4520 (7.8%) cal mol^{-1} and $\Delta S°_2$ = 5.2 (11.3%) cal deg^{-1} mol^{-1} when ϵ_1 had the value 6300 M^{-1} cm^{-1}. Values of $\Delta H°_2$ were relatively insensitive to the choice of ϵ_1 in the range tested.

This result was refined as follows. Using the preliminary values of K_2, together with K_7, K_6, and relationships 8–11, values of the concentrations of each of the seven species were calculated. The molar absorptivities of $FeBr_3$ and Fe_2Br_6 are not known at 280 nm, although values at the absorption maximum (300–305 nm) for these species have been assigned as ϵ_3 9600 and ϵ_4 2570.[5] The peak in this region is observed to be quite sharp, and as an estimate of the contribution of these species to the absorbance at 280 nm, molar absorptivities equal to 50% of the peak maximum values were used.[22] On this basis the predicted corrections to A ranged from 0.4 to 6.3% in the various samples. A least-squares treatment of the vapor phase data (Table I) was then repeated in the form $Y = mX + b$ where

$$Y = \frac{C_0(\mathrm{Fe}) - 2C_3 - C_4}{A - \epsilon_3 C_3 - \epsilon_4 C_4} = \frac{C_1 + C_2}{\epsilon_1 C_1} = \frac{1}{\epsilon_1} + \frac{K_2}{\epsilon_1}\left(\frac{C_5}{C_7}\right)^{1/2} = \frac{1}{\epsilon_1} + \frac{(e^{\Delta S°_2/R})}{\epsilon_1} X$$

and

$$X = e^{(-4520/RT)}(C_5/C_7)^{1/2}$$

i.e., the value of $\Delta H°_2$ was set as 4520 cal mol^{-1} and $\Delta S°_2$ and ϵ_1 treated as constants to be fitted. C_5 and C_7 were taken first as values given by the preliminary calculation, and iterations performed until results were consistent within 1% of the required relationships 8, 9, and 10. Resulting values (with standard deviations) were 4.94 cal deg^{-1} mol^{-1} (3.1%) and 6311 M^{-1} cm^{-1} (1.4%). Hence the recommended free energy expression for reaction 3 in the temperature range 500–750 K is $\Delta G°_2 = 4520 - 4.9\,T$ cal mol^{-1}. The correlation is shown graphically in Figure 2.

At lower temperatures it was apparent from the exponential rise of absorbance with temperature that a condensed phase, assumed to be $FeBr_2$(s), was present in the absorption cells. Data in this range (Table I) were correlated in terms of reaction 3. At still lower temperatures condensation of a brownish solid, believed to be $FeAlBr_6$, was observed during preparations. Absorbances were not measured with the mixed metal dimer present in the solid phase, however. To study reaction 3 concentrations of the various species in the vapor phase were calculated using K_7, K_6, K_2, and K_5 values together with (9), (10), and (11) and the molar absorptivities derived above. Values of K_3 were then calculated from each of the 18 measured absorbances. A least-squares treatment of

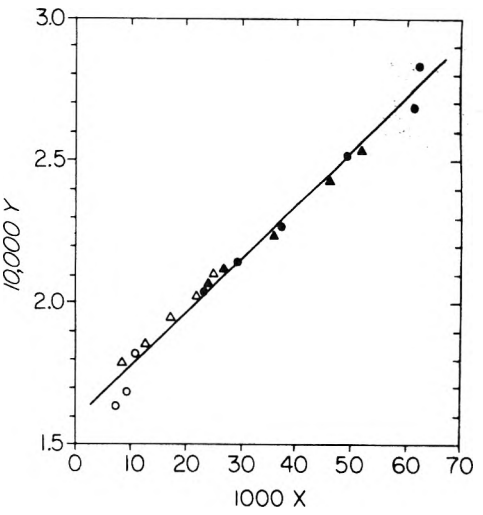

Figure 2. Absorbance data for completely vaporized samples: C, ○; D, ●; E, △; G, ▲. See discussion for definition of X and Y. Least-squares line shown.

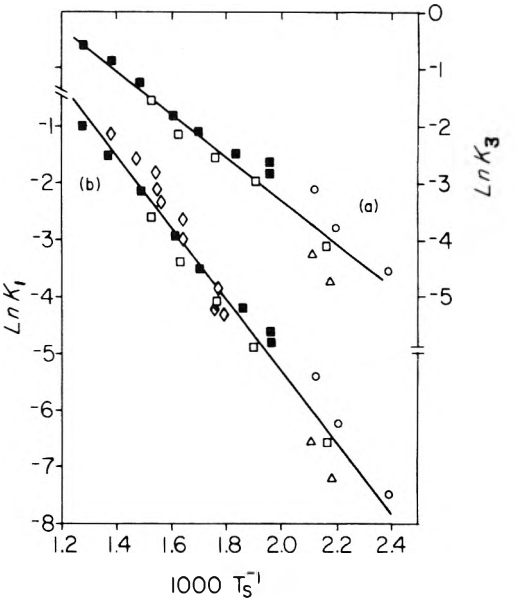

Figure 3. Calculated values of (a) ln K_3 (upper right) and (b) ln K_1 (lower left) for various vapor mixtures in equilibrium with $FeBr_2$(s) plotted against the reciprocal of the temperature of the solid phase. Least-squares lines shown. Absorbance data for sample B, ■; C, ○; E, △; F, □. Transpiration data: ◇.

ln K_3 vs. $1/T$ gave values (and standard deviations) of $\Delta H°_3$ = 7500 (7.5%) cal mol^{-1} and $\Delta S°_3$ = 8.6 (11.6%) cal deg^{-1} mol^{-1}. Results are shown graphically in Figure 3.

The calculated concentrations also lead to values for K_1 and a similar least-squares treatment gave $\Delta H°_1$ = 12000 (4.4%) cal mol^{-1} and $\Delta S°_1$ = 13.5 (7.4%) cal deg^{-1} mol^{-1}, confirming that expected by summing the results for (2) and (3). These values are appreciably lower than those derived for (1) from the transpiration data alone; however, as shown in Figure 3 the equilibrium constants derived from the two independent studies appear quite consistent when plotted together. A recommended result for reaction 1 was obtained by least squaring the combined sets of data, giving $\Delta H°_1$ = 12700 (3.7%) cal mol^{-1} and $\Delta S°_1$ = 14.8 (5.5%) cal deg^{-1} mol^{-1}.

Emmenegger[2] has recently discussed results for a number of reactions of the form MCl_2(s) + $2AlCl_3$(g) = MAl_2Cl_8(g) with M = Mg,[14] Ca, Cr,[15] Mn,[14] Co, Ni,[14] Cu, Pd,[16] and Pt.[17] Values of $\Delta H°$ range from −15 to −26 kcal mol^{-1}, averaging −19.6; and for the corresponding reaction with MBr_2 and $AlBr_3$, with M = Co and Ni, values of −16.8

TABLE III

	λ_{max}, nm	ϵ, mol^{-1} L cm^{-1}	λ_{max}, nm	ϵ, mol^{-1} L cm^{-1}
Fe_2Cl_6	250	10200	365	9600
$FeCl_3$	260	4000	350	6000
Fe_2Br_6	300	9600	450(?)	
$FeBr_3$	300	2570	450(?)	
$FeAlCl_6$	245	6900	365	5200
$FeAlBr_6$	280	6300	460	

and −10.0 are reported. For the corresponding reaction, our value is −13.5. Schäfer[1] provides a similar summary of an extended series of reactions of the form of (1) with various metal chlorides and Al_2Cl_6; $\Delta H°$ values are in the range 7–13, average 10 kcal mol^{-1}, and $\Delta S°$ in the range 8–12, average 10.3 cal deg^{-1} mol^{-1}. Our results seem generally compatible with these findings. However in view of the complexity of the system it is most likely that at least minor amounts of other complexes may be present in the vapor and it is possible that other sets of reactions could be proposed which would also be consistent with the observed behavior. However the set proposed here seem logically simple and adequate within the uncertainties of the measurements.

Using JANAF values[12] for aluminum bromide, bromine, and iron(II) bromide, the following thermodynamic constants for the mixed metal complexes were derived:

	$\Delta H°$(600 K), kcal mol^{-1}	$S°$(600 K), cal deg^{-1} mol^{-1}
$FeAl_2Br_8(g)$	−298.3	222.1
$FeAlBr_6(g)$	−180.8	169.0

The concentration of Fe_2Br_6 is too small in the all vapor samples to derive reasonably accurate values of C_3 from the measured absorbances. The relative contribution is somewhat larger when $FeBr_2(s)$ is present but derived K_4 values still show large variations, from 0.8 to 8.6. A least-squares treatment of K_4 gave $\Delta H°_4$ = −1700 (64%) cal mol^{-1} and $\Delta S°_4$ = −1.6 (123%) cal deg^{-1} mol^{-1}. Combination of results for (3) and (5) predicts −1300 and −0.8, respectively. Hence we can only conclude that $\Delta H°_4$ is near zero; neglecting temperature dependence, the average value of K_4, 2.6, corresponds to a value only slightly less than expected from the entropy effect associated with the change in symmetry numbers.

The spectral characteristics of Fe_2Cl_6,[7,18] Fe_2Br_6,[5] $FeAlCl_6$ and $FeAlBr_6$ in the wavelength interval 250–800 nm are similar. Bird and Day[19] have discussed transitions in $FeCl_4^-$ which seem similar in character and which they associate with charge transfer from states in which the major contribution comes from ligand π-bonding and nonbonding orbitals to states with largely the character of metal 3d orbitals. For the various species at ca. 600 K, λ_{max} and ϵ values are given in Table III. Values for the bromides are not readily resolved at the maximum near 450 nm because of the strong overlap with the bromine spectrum. The shift of λ_{max} to shorter wavelengths in the mixed metal dimer molecules for the short wavelength absorption may be related to the more electropositive character of aluminum as a receptor. A similar transition may occur in aluminum bromide in the vacuum ultraviolet region as a sharply rising shoulder is observed for aluminum bromide vapor as the cut-off limit (190 nm) of the Cary 14H instrument is approached. An absorbance peak in $AlI_3(g)$ has recently been reported at 210 nm.[20]

Acknowledgment. We acknowledge with thanks the financial assistance received from the National Science Foundation under Grant CHE 73-08473.

References and Notes

(1) For a recent review, see H. Schäfer, *Angew. Chem. Int. Ed. Engl.*, **15**, 713 (1976).
(2) F. P. Emmenegger, *Inorg. Chem.*, **16**, 343 (1977).
(3) J. Kendall, E. D. Crittenden, and H. K. Miller, *J. Am. Chem. Soc.*, **45**, 963 (1923).
(4) E. Y. Gorenbein, *Zh. Obshch. Khim.*, **18**, 1427 (1948); *J. Gen. Chem. (USSR)*, **15**, 729 (1945); **17**, 873 (1947).
(5) N. W. Gregory, *J. Phys. Chem.*, **81**, 1857 (1977).
(6) N. W. Gregory and R. O. MacLaren, *J. Phys. Chem.*, **59**, 110 (1955).
(7) C. F. Shieh and N. W. Gregory, *J. Phys. Chem.*, **79**, 828 (1975).
(8) R. R. Richards and N. W. Gregory, *J. Phys. Chem.*, **68**, 3089 (1964).
(9) W. C. Laughlin and N. W. Gregory, *J. Phys. Chem.*, **80**, 127 (1976).
(10) A. A. Passchier, J. D. Christian, and N. W. Gregory, *J. Phys. Chem.*, **71**, 937 (1967).
(11) Appreciation is expressed to Dr. Eric Knudsen for performing the analyses.
(12) "JANAF Thermochemical Tables", Revised Editions, Thermal Laboratory, Dow Chemical Co., Midland, Mich., 1961, 1966, 1972.
(13) B. G. Korshunov, G. A. Lovetskaya, and A. A. Palant, *Russ. J. Inorg. Chem.*, **12**, 102 (1967).
(14) E. W. Dewing, *Metall. Trans.*, **1**, 2169 (1970).
(15) M. Aits and H. Schäfer, *Z. Anorg. Allg. Chem.*, **408**, 37 (1974).
(16) G. N. Papatheodorou, *J. Phys. Chem.*, **77**, 1899 (1973).
(17) G. N. Papatheodorou, *Inorg. Chem.*, **12**, 1899 (1973).
(18) D. S. Rustad and N. W. Gregory, *Inorg. Chem.*, in press.
(19) B. D. Bird and P. Day, *J. Chem. Phys.*, **49**, 392 (1968).
(20) N. W. Gregory, *J. Phys. Chem.*, **81**, 1854 (1977).
(21) G. N. Papatheodorou and G. H. Kucera, *Inorg. Chem.*, **16**, 1006 (1977).
(22) A calculation with ϵ_3 and ϵ_4 estimated at 73% of peak values did not change results for (2) significantly but gave standard deviations for $\Delta H°_3$ and $\Delta H°_1$ 2 and 1% larger and for $\Delta S°_3$ and $\Delta S°_1$ 6 and 2.5% larger, respectively, than the 50% estimate.

A Thermodynamic Study of the Reactions of $Mg^+(g)$ and $MgH^+(g)$ with Magnesium

P. L. Po and Richard F. Porter*

Department of Chemistry, Cornell University, Ithaca, New York 14853 *(Received June 3, 1977)*

In the presence of solid magnesium, $Mg^+(g)$ and $MgH^+(g)$ undergo chemical reactions at elevated temperatures to form $Mg_2^+(g)$ and $Mg_2H^+(g)$, respectively. From experimental evidence obtained we propose that the mechanism of these reactions involves direct interaction of the reactant ions with the magnesium surface. Thermochemical data have been obtained for the reactions $Mg^+(g) + Mg(s) \rightleftharpoons Mg_2^+(g)$ and $MgH^+(g) + Mg(s) \rightleftharpoons Mg_2H^+(g)$. We find for the dissociation energy of $Mg_2^+ \rightarrow Mg^+ + Mg(g)$, $D°_0 = 1.01 \pm 0.09$ eV. The ionization potential and proton affinity of $Mg_2(g)$ are found to be 6.7 ± 0.1 and 9.5 ± 0.3 eV, respectively.

Introduction

In a recent paper[1] we described a high-temperature ion–molecule reactor for study of the kinetics of charge or proton transfer reactions of Mg(g) atoms with D_3^+ and CH_4D^+. The emphasis on that work was to examine reaction conditions that lead to formation of Mg^+ or MgH^+ as the stable products. We have observed subsequently that in the presence of Mg(s), Mg^+ and MgH^+ undergo further chemical reactions at elevated temperatures. This paper describes observations of what appears to be a unique type of ion chemistry.

Experimental Section

The quadrupole mass spectrometer and high temperature ion source[1] used in this study will be described briefly. The ion source–reaction chamber was constructed of stainless steel. A small aperture (0.025 in.) for the electron beam was located 1 cm below the ion exit aperture (0.025 in.). The source was maintained at a potential of +22.5 V and the drawout potential was held at −90 V with respect to ground. The electron accelerating energy was set at −140 V with respect to the source. A repeller was not employed in these experiments. The source was heated radiatively from a spiral-shaped heating filament formed by stranding three 0.030-in. annealed tantalum wires. The temperature of the reactor was measured with a chromel–alumel thermocouple spot welded to the base of the source. In all experiments magnesium vapor was generated within the source by heating thin strips of polished magnesium metal. The vapor pressure of magnesium was obtained from the JANAF tables.[2]

Magnesium ribbon was obtained from Mallinkrodt Chemicals. All gases were Matheson research grade.

Results

Pure Magnesium System. In the absence of a reagent gas, Mg^+ was the major ion species observed in the spectrum for a temperature range of 350 to 460 °C. A small ion signal of Mg_2^+, which was between 1 and 3% of the Mg^+ intensity, was also observed. In Figure 1 we illustrate how the ion intensity of Mg^+, and the ratio of ion intensities of Mg_2^+ to Mg^+, vary with temperature (vapor pressure of magnesium). It should be noted that the ratio of Mg_2^+ to Mg^+ intensities changed only by a factor of 2 over a temperature range of 400 to 468 °C, which corresponds to a magnesium vapor pressure range of 2.6 to 26.5 μm.

Xe/Mg System. When xenon gas was introduced into the cell, the intensity of Mg^+ increased markedly. This can be accounted for by the charge transfer reaction

$$Xe^+ + Mg \rightarrow Mg^+ + Xe \qquad (1)$$

The intensity of Mg_2^+ also increased with source pressure. Figure 2 shows how the ratio of Mg_2^+ to Mg^+ ion intensities vary as a function of source (xenon) pressure at a temperature of 360 °C (vapor pressure of magnesium = 0.40 μm). It is noted that the intensity of Mg_2^+ relative to that of Mg^+ rose sharply initially as the source pressure was increased to 50 μm. When the source pressure was above 50 μm, the intensity of Mg_2^+ remained relatively constant with respect to that of Mg^+ ($I_{Mg_2^+}/I_{Mg^+}$ reaching a value of about 0.024). When the xenon gas flow was terminated, the ratio of $I_{Mg_2^+}/I_{Mg^+}$ dropped to about 0.001. With the xenon gas maintained at about 100 μm, the ion signals corresponding to Mg^+ and Mg_2^+ disappeared when the source temperature was dropped below 330 °C.

CH_4/Mg System. When pure CH_4 was used as a reagent gas, Mg^+ and MgH^+ were observed to be the major ion species in the spectrum for a source temperature of 400 °C. We have discussed previously the origin of the formation of Mg^+ and MgH^+ in this system.[1] A series of ion intensity–pressure profile measurements for this system is shown in Figure 3. The feature to be noted here is the appearance of Mg_2H^+ which showed a dramatic increase in intensity with source pressure. The ratio of Mg_2^+ to Mg^+ intensities remained relatively constant at source pressures above 50 μm. Since MgH^+ is the major proton-bearing ion species in the spectrum at high source pressures, we conclude from mechanistic considerations that Mg_2H^+ must be formed predominately from a reaction involving this species. With the methane pressure held at about 120 μm, the ion signals corresponding to Mg^+, MgH^+, Mg_2^+, and Mg_2H^+ disappeared as the source temperature was lowered to 330 °C.

Xe/Neopentane/Mg System. A series of ion intensity–pressure profile measurements using a 200:1 mixture of Xe:neopentane as a reagent gas with the source temperature at 350 °C is shown in Figure 4. For comparison purposes a similar set of measurements at 400 °C is shown in Figure 5. The xenon ion intensity has been omitted to simplify the figures. It should be noted that, similar to the results observed for the CH_4/Mg system, Mg^+ and MgH^+ were the major ion species in the spectrum formed from charge and proton transfer reactions. A sharp rise in the Mg_2H^+ intensity and the relative constancy of Mg_2^+ to Mg^+ ion intensity ratio with source pressure are again noted. Furthermore the ratios of $I_{Mg_2^+}/I_{Mg^+}$ and $I_{Mg_2H^+}/I_{Mg_2H^+}$ ion intensities changed only slightly (by about a factor of 2) as the source conditions changed from 350 to 400 °C corresponding to a change in vapor pressure of magnesium from 0.33 to 2.6 μm. The intensities of hydrocarbon ions in these measurements remained small compared to the MgH^+ intensity.

Discussion

In this section we will discuss the physical evidence that lead us to the eventual conclusion that under our ex-

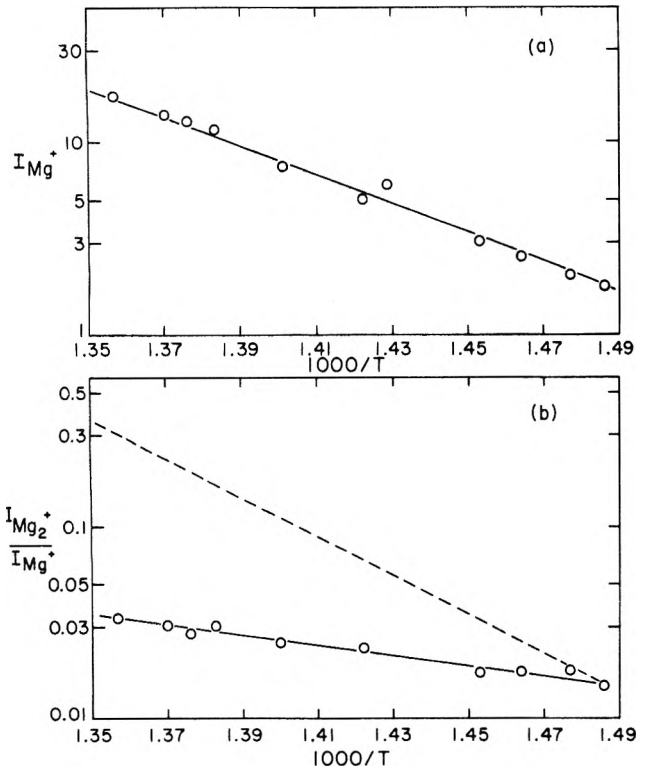

Figure 1. (a) Intensity of Mg^+ in arbitrary units as a function of temperature. Note that the temperature ranged from 400 (vapor pressure of Mg = 2.6 μm) to 468 °C. (Vapor pressure of Mg = 26.5 μm). (b) Ratio of Mg_2^+ to Mg^+ ion intensities as a function of temperature, same experimental condition as in Figure 1a. The dashed line is explained in the text.

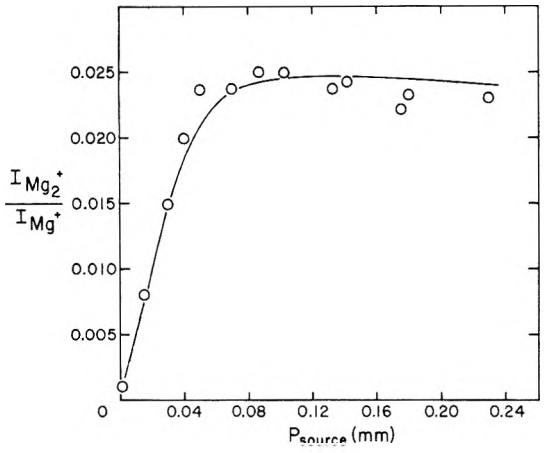

Figure 2. Ratio of Mg_2^+ to Mg^+ ion intensities as a function of source (xenon) pressure at T = 360 °C (vapor pressure of Mg = 0.40 μm).

perimental conditions Mg_2^+ reaches, through reaction of Mg^+ with solid Mg, a state of chemical equilibrium. We will discuss briefly alternate chemical mechanisms for the formation of Mg_2^+ and Mg_2H^+ as reaction products, but conclude that these are not consistent with experimental observations.

Mechanism A. Gas Phase Ion–Molecule Association Reactions

$$Mg^+ + Mg(g) \rightarrow Mg_2^+ \quad (2)$$

and

$$MgH^+ + Mg(g) \rightarrow Mg_2H^+ \quad (3)$$

Bimolecular processes of this type in the absence of a third body are expected to be very slow. Physical evidence for such reactions should be noted by second-order depen-

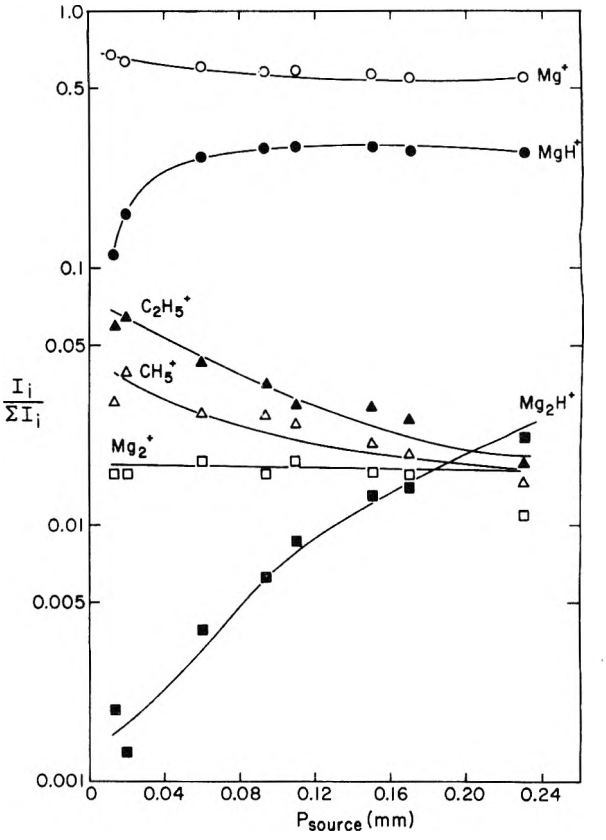

Figure 3. Ion intensity–pressure profile data obtained in CH_4/Mg system at T = 400 °C (vapor pressure of Mg = 2.6 μm). Intensities of CH_3^+, CH_4^+ and $C_2H_3^+$ were less than 1% of the total ionization and were omitted.

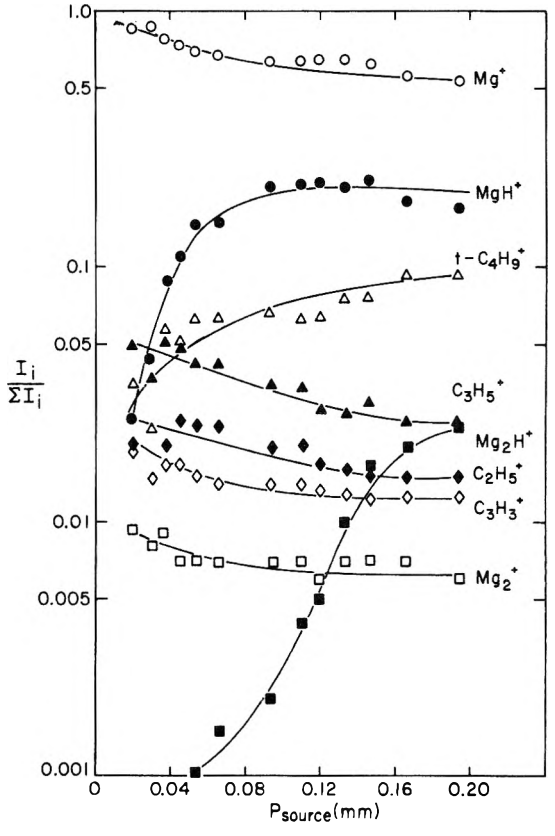

Figure 4. Ion intensity–pressure profile data obtained in Xe–neopentane–Mg mixture at T = 350 °C (Xe:neopentane ≈ 200:1, vapor pressure of Mg = 0.33 μm).

dence of the product ions on the primary ions. These effects are not observed in our experiments. The dashed

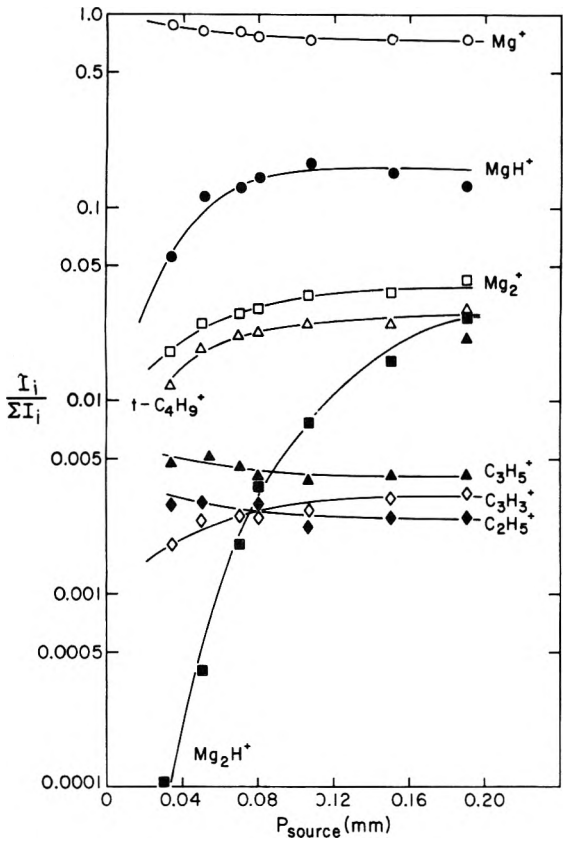

Figure 5. Ion intensity–pressure profile data obtained in Xe–neopentane–Mg mixture at $T = 400$ °C (Xe:neopentane ≈ 200:1, vapor pressure of Mg = 2.6 μm).

line in Figure 1b represents the behavior anticipated if a second-order mechanism applies. The possibility that reaction 2 is accelerated by a three-body interaction requiring two Mg atoms is ruled out for the following reasons. We estimate, assuming the Mg^+–Mg collision rate is Langevin limited, that the average time between collisions when the Mg(g) pressure is 0.33 μm ($T = 623$ K) is about 10^{-5} s. This would also be roughly the time required for a collision of the complex with a second Mg atom and would imply an unreasonably long lifetime for such a complex. Secondly, third-order behavior for reaction 2 is not observed. A small increase of 20 °C in source temperature causes a factor of 2 increase in Mg(g) pressure. We would expect to observe nearly an order of magnitude change in the Mg_2^+/Mg^+ ratio over the temperature range investigated. It could perhaps be argued that a presence of an inert third body could drive reaction 2 to equilibrium. However analyses of the intensity–pressure profiles obtained in experiments using Xe, CH_4, and Xe–C_4H_{10} mixtures as buffer gases (Figures 2–5) indicate that this is probably not the case since changes in the Mg_2^+/Mg^+ ratio, which are observed only at very low source pressures, would require an unusually efficient third body interaction.

Mechanism B. Electron Impact and/or Charge and Proton Transfer Mechanisms

$$Mg_2 + e^- \rightarrow Mg_2^+ + 2e^- \quad (4)$$

or

$$Mg^+ + Mg_2 \rightarrow Mg_2^+ + Mg \quad (5)$$

and

$$MgH^+ + Mg_2 \rightarrow Mg_2H^+ + Mg \quad (6)$$

It is conceivable that the relatively low intensity of Mg_2^+ could result from ionization of Mg_2 in the gas phase when the reagent gas is absent. However that would imply, assuming that the ionization cross sections of Mg_2 and Mg were of the same order of magnitude, that about 1% of the vapor consists of magnesium dimer (Mg_2). Accurate spectroscopic data indicate that the dissociation energy of Mg_2 is only about 1.2 kcal mol^{-1}.[3] This implies that the concentration of Mg_2 in equilibrium with solid magnesium at 400 °C would be approximately six orders of magnitude less than that of Mg monomer.[4,5] Hence it will be difficult to explain the relatively high proportion of Mg_2^+ in the system. Furthermore the ratio of Mg_2^+ to Mg^+ should show a much steeper temperature dependence than that observed in Figure 1b as the temperature is increased. The anticipated temperature dependence for such a system would be closer to that shown by the dashed line in Figure 1b.

Pressure calibrations (1) have shown that the vapor pressure of Mg(g) in our source is close to the correct equilibrium value. Thus an anomalously high ratio of Mg_2/Mg that may have resulted from nonequilibrium evaporation behavior is discounted. We conclude therefore that we are not ionizing Mg_2 molecules directly in our experiments. By the same type of argument, we can exclude the possibility that reactions 5 and 6 are occurring under our experimental conditions.

Mechanism C. State of Chemical Equilibrium.

$$Mg^+ + Mg(s) \rightleftharpoons Mg_2^+ \quad (7)$$

and

$$MgH^+ + Mg(s) \rightleftharpoons Mg_2H^+ \quad (8)$$

Having considered a number of possible mechanisms of production of Mg_2^+ and Mg_2H^+, we are left with the conclusion that the system is reaching a degree of equilibrium inside our ion source. Since it would be difficult to attain equilibrium through ion–molecule processes directly, we propose that equilibrium is attained through interactions of ions with the metal (magnesium) surface. The extent to which equilibrium is achieved depends on the length of time the reactant ions remain in the source. The data in Figure 2 show that in the presence of xenon, the ratio of Mg_2^+ to Mg^+ intensities reach a constant value as the residence time of the Mg^+ ions is increased. When a reagent gas is not present in the source, this ratio falls below the equilibrium value. Thus the temperature dependence data in Figure 1 are presumably offset somewhat from true equilibrium values. It should be noted that the ratio of Mg_2H^+ to MgH^+ intensities reaches a value somewhat above 0.1 at the highest source pressure regardless of the reagent gas used (methane or xenon/neopentane mixture).

Thermodynamic Analyses

A van't Hoff type plot for the temperature dependence of Mg^+ in Figure 1a, based on the assumption that Mg^+ is produced directly by electron impact of Mg vapor, yields $\Delta H_{1a}(Mg) = 34.0 \pm 1.0$ kcal mol^{-1} at 700 K. This is in reasonably good agreement with the value of $\Delta H°_{subl}$ of 34.6 kcal mol^{-1} at 700 K obtained from the JANAF tables.[2] Similar analysis of the data in Figure 1b gives an apparent value of $\Delta H_{1b} = 12.5 \pm 1.0$ kcal mol^{-1} for reaction 7. However since reaction 7 is apparently not at total equilibrium in the absence of a buffer gas, it is more appropriate to evaluate $\Delta H°$ (7) by third law procedures in which $\Delta S°$ for reaction 7 is calculated through statistical thermodynamics and K_{eq} is obtained from our Xe–Mg data (Figure 2). Estimates of $S°$ for Mg_2^+ were obtained by assuming the species has approximately the same fun-

TABLE I: Thermochemical Data for Mg_2^+ and Mg_2H^+

	D°_0, kcal mol^{-1}	ΔH_f°,[a] kcal mol^{-1}	IP, eV	PA, eV
Na_2^+	22.4[c]	142.5[c]		
Mg_2^+	23.4 ± 2.0	224.1 ± 2.0		
Mg_2H^+[b]	24 ± 5	215 ± 5		
Na_2	16.9[d]		4.90[e]	
Mg_2	1.2[f]		6.7 ± 0.1	9.5 ± 0.3

[a] ΔH_f° values at 700 K. [b] D°_0 calculated for the reaction $Mg_2H^+ \rightarrow MgH^+ + Mg(g)$. [c] Value calculated from data given in ref 2, 6, and 7. [d] Value obtained from ref 6. [e] Value obtained from ref 7. [f] Value obtained from ref 3.

damental vibration frequency and internuclear distance as Na_2. Using $\omega_{Mg_2^+} \simeq 159$ cm^{-1} and $r_e(Mg_2^+) \simeq 3.08$ Å,[6] we obtain $S°(Mg_2^+) = 63.07$ cal deg^{-1} mol^{-1}. Based on a value of $S°(Mg^+) = 41.12$ cal deg^{-1} mol^{-1} and $S°(Mg(s)) = 13.33$ cal deg^{-1} mol^{-1},[2] we calculate $\Delta S°(700\ K) = 8.6$ eu, with an estimated uncertainty of ±1.0 eu. With a value of $K_{eq} = 0.024$ for reaction 7 at 700 K, we find $\Delta G° = 5.19$ kcal mol^{-1}. From the equation

$$\Delta H^\circ = \Delta G^\circ - T\Delta S^\circ \quad (9)$$

we then obtain a value of $\Delta H°(7) = 11.2 \pm 0.9$ kcal mol^{-1}. Assuming this value for $\Delta H°$, and using published data for the ionization potential of Mg[7] (176.3 kcal mol^{-1}), the dissociation energy of Mg_2[3] (1.2 kcal mol^{-1}), and the $\Delta H°$ of sublimation of Mg[2] (34.6 kcal mol^{-1}), we obtain the thermochemical values listed in Table I.

Estimations of thermodynamic properties of Mg_2H^+ were made from the ion intensity data available for reaction 8. The results shown in Figures 4 and 5 with CH_4 and Xe/neopentane as reagent gas indicate that the ratio of $I_{Mg_2H^+}/I_{MgH^+}$ reaches a value of about 0.1 at the highest source pressure studied, although the true equilibrium value may be slightly higher than this. From these data we estimate $\Delta G° = 3.2$ kcal mol^{-1} for reaction 8 at 700 K. The $\Delta S°$ for reaction 8 was estimated by assuming that Mg_2H^+ has a linear configuration ($[Mg–Mg–H]^+$). The $S°$ of rotation of Mg_2H^+ was obtained by correcting the entropy of rotation of Mg_2 for the additional Mg–H bond. The high frequency Mg–H vibrations do not contribute significantly to $S°$ at 700 K. The major problem is estimation of the Mg–Mg Σ^+ stretching vibration and the degenerate bending modes in Mg_2H^+. However we can probably assume that these are low frequency vibrations and their contribution to $S°$ is offset to a large extent by the entropy of rotation of MgH^+. Thus we have assumed $\Delta S°$ for reaction 8 is that for reaction 7, but with a somewhat larger uncertainty. Using $\Delta G° = 3.2$ kcal mol^{-1} for reaction 8, we then obtain $\Delta H° = 9.9$ kcal mol^{-1} with an estimated uncertainty of ±3.5 kcal mol^{-1}. Using the proton affinity for the Mg atom,[1] 196 ± 3 kcal mol^{-1}, we obtain the thermochemical values shown in Table I.

Results of thermochemical calculations of the stability of Mg_2^+ and Mg_2H^+ indicate that, while the neutral Mg_2 molecule is highly unstable, the corresponding singly charged species Mg_2^+ is relatively stable with respect to dissociation to Mg^+ and Mg(g). This stability presumably arises from the removal of an antibonding σ_u electron from Mg_2 leaving an ion with a bond order of one-half. In Table I, the stability of Mg_2^+ is compared to that of Na_2^+ which also has a bond order of one-half. It is noted that the proton affinity of Mg_2 is nearly 1 eV higher than that of Mg. The stability of Mg_2H^+ presumably arises from the interaction from a σ_u antibonding orbital of Mg_2 with a proton. It is noted that the Mg–Mg bond dissociation energies for Mg_2^+ and Mg_2H^+ are nearly equal.

Acknowledgment. We are grateful for support of this work by the National Science Foundation (Grant GH-33637) through the Material Science Center, Cornell University.

References and Notes

(1) P. L. Po and R. F. Porter, *J. Am. Chem. Soc.*, **99**, 4922 (1977).
(2) D. R. Stull and H. Prophet, et al., *Natl. Stand. Ref. Data Ser., Natl. Bur. Stand.*, **No. 37** (1971).
(3) W. J. Balfour and A. E. Douglas, *Can. J. Phys.*, **48**, 901 (1970).
(4) A. C. Brett and W. J. Balfour, *J. Chem. Phys.*, **54**, 3240 (1971).
(5) A. M. Mellor, *J. Chem. Phys.*, **54**, 3241 (1971).
(6) G. Herzberg, "Molecular Spectra and Molecular Structure, I. Spectra of Diatomic Molecules", 2nd ed, Van Nostrand, Princeton, N.J., 1955.
(7) J. L. Franklin, J. G. Dillard, H. M. Rosenstock, J. T. Herron, K. Draxl, and F. H. Field, *Natl. Stand. Ref. Data Ser., Natl. Bur. Stand.*, **No. 26** (1969).

Solvation Effects on the Thermodynamics of Hydrogen Bonded Systems. 3

J. N. Spencer,* Judy R. Sweigart, Michael E. Brown, Ronald L. Bensing, Thomas L. Hassinger, William Kelly, Donna L. Housel, G. William Reisinger, Daniel S. Reifsnyder, Jeffrey E. Gleim, and J. Christopher Pelper

Department of Chemistry, Lebanon Valley College, Annville, Pennsylvania 17003 *(Received September 22, 1976; Revised Manuscript Received July 18, 1977)*

Publication costs assisted by the Petroleum Research Fund

Thermodynamic functions for the hydrogen bonded complexes of guaiacol with triethylamine and dimethylformamide in cyclohexane, benzene, and CCl_4 solvents were determined by infrared spectroscopy. Heats of solution at infinite dilution for phenol, guaiacol, Me_2SO, pyridine, and dimethylformamide were determined calorimetrically. Previously reported enthalpies of complex formation for phenol and guaiacol with Me_2SO and pyridine in cyclohexane, CCl_4, benzene, CS_2, 1,2-dichloroethane, and chloroform solvents were combined with the heat of solution data to calculate transfer enthalpies for acid, base, and complex between various solvent pairs.

Introduction

Drago et al.[1-4] have described an elimination of solvation procedure (ESP) for relating enthalpies of hydrogen bond formation in polar solvents to solvation minimized data for nonpolar solvents such as CCl_4 or hexane. These investigators report general success but caution that extrapolation to new systems cannot be done with confidence. In certain cases it has been necessary to infer specific interactions between base and solvent in order to account for deviations between ESP and experiment.[3,5]

Christian et al.[6-8] have proposed that the transfer enthalpy of a given complex between any two solvents is proportional to the sum of the transfer enthalpies of the acid and the base.

The present investigation was undertaken to determine if thermodynamic evidence for certain specific interactions proposed by ESP adherents could be detected. From heat of solution data transfer enthalpies may be calculated for all species and used for an examination of Christian's proposal.

Experimental Section

Purifications of the phenols and solvents have been previously reported.[9-11] Mallinckrodt SpectrAR grade dimethylformamide was first "benzene dried"[12] then further dried over Drierite before distilling under a nitrogen atmosphere. Eastman practical grade triethylamine was distilled under nitrogen from barium oxide. The index of refraction was used as a purity criterion.

TEA is known to interact with CCl_4.[13,14] Therefore TEA and CCl_4 were distilled immediately prior to use. Care was taken to exclude oxygen and light. Solutions were stable for periods of 2–3 h. After about 3 h a precipitate of thin needles was observed, apparently similar to that reported by Drago et al.[5] in solutions of pyridine or quinuclidine in methylene chloride.

Frequency shifts were obtained from spectra recorded in 2-mm path length cells and are given in Table I. The complex absorption bands are broad for all systems. The assignment of the complex frequency for DMF systems in cyclohexane are less reliable due to solubility problems.

For the determination of the equilibrium constants, guaiacol concentrations were about 0.0015 M, TEA concentrations were about 0.25 M. Higher concentrations were used to determine the frequency shifts.

The enthalpies of formation for certain complexes were taken from previously reported spectrophotometric studies.[9,10] The data for the guaiacol–pyridine complexes given in an earlier report[9] were found to be in error due to a transposition of two digits in the molecular mass of guaiacol. The corrected enthalpy data and equilibrium constants are given in Table II. Woolley et al.[15] have pointed out that when a standard state based on molarity is used, a direct application of the van't Hoff equation cannot be made. The enthalpy change must be calculated from

$$\Delta H = -R \frac{\mathrm{d} \ln K_c}{\mathrm{d}(1/T)} - RT^2 \alpha \qquad (1)$$

where α is the coefficient of thermal expansion of the solvent. At 298 K this correction is about 0.2 kcal/mol^{-1} for the solvents of this work. All the enthalpies in Table II have been calculated according to eq 1.

TABLE I: Frequency Data for the Complexes of Guaiacol with TEA and DMF (cm^{-1})

Solvent	Nonbonded frequency	Bonded frequency	
		TEA	DMF
Cyclohexane	3561	3220	3274
Benzene	3544	3220	3287
CCl_4	3557	3240	3286

The calorimeter design was similar to that reported by Arnett et al.[16] The calorimeter vessel is a standard 250-mL silvered Dewar flask immersed in a thermostatted water jacket. The temperature sensing elements are two YSI 44011 100-kΩ thermistors encased in No. 26 Teflon tubing. The stirrer was driven by a Barber-Colman synchronous motor. Actual time–temperature data were recorded by interfacing the temperature sensing circuit to a Hewlett-Packard Model 2100A microprogrammable computer. The computer program used a least-squares criterion to establish preinjection, post-injection, and heating base lines.

Solid samples were injected into the Dewar by a delivery system similar to that used by Arnett et al.[16] Liquid samples were injected from syringes immersed in the solvent in the Dewar. Sample quantities of 1–10 mmol were injected. Extrapolated heats obtained from repeated sets of successive injections were averaged and the precision reported in Table III is the standard deviation of a single measurement.

Results and Discussion

The enthalpies of hydrogen bond formation and the equilibrium constants for the complexes of guaiacol with

TABLE II: Enthalpies of Hydrogen Bond Formation[a]

Solvent	ΔH°_{298}, kcal mol^{-1}				K_{293}[b] guaiacol-pyridine
	Me_2SO		Pyridine		
	Phenol	Guaiacol	Phenol	Guaiacol[c]	
Cyclohexane	−9.18 ± 0.25	−3.99 ± 0.25	−7.49 ± 0.34	−3.35 ± 0.07	2.71
Carbon disulfide	−7.29 ± 0.24	−4.71 ± 0.05	−6.18 ± 0.41	−3.95 ± 0.13	2.67
CCl_4	−6.55 ± 0.07	−3.26 ± 0.14	−5.92 ± 0.29	−3.29 ± 0.38	1.44
Benzene	−5.36 ± 0.12	−4.10 ± 0.06	−5.25 ± 0.32	−4.33 ± 0.15	1.72
1,2-Dichloroethane	−6.28 ± 0.14	−3.64 ± 0.09	−5.76 ± 0.15	−3.33 ± 0.41	2.10
Chloroform	−3.34 ± 0.03	−2.31 ± 0.18	−5.32 ± 0.12	−2.75 ± 0.30	1.90

[a] Data from ref 9 and 10. [b] Corrected equilibrium constants erroneously reported in ref 9, vide infra. [c] Corrected enthalpies erroneously reported in ref 9, vide infra.

TABLE III: Partial Molar Heats of Solution ($\overline{\Delta H_s}$, kcal mol^{-1}) at 25 °C

Solvent	Phenol	Guaiacol	Me_2SO	Pyridine	DMF	TEA
Cyclohexane	+7.625 ± 0.02[a]	+3.56 ± 0.05	+4.18 ± 0.21	+2.01[e]	+3.65 ± 0.07	+0.26 ± 0.04[b]
Carbon disulfide	+6.90 ± 0.06	+2.60 ± 0.06	+3.02 ± 0.02	+1.25 ± 0.01		
CCl_4	+6.27 ± 0.07[b]	+2.05 ± 0.03	+1.83[c]	+0.36 ± 0.01[f]	+0.76 ± 0.02[g]	−0.64 ± 0.08[g]
Benzene	+4.72 ± 0.01[b]	+1.35 ± 0.07	+1.15 ± 0.03[d]	0.00 ± 0.01[f]	+0.09 ± 0.02	−0.54 ± 0.04[d]
1,2-Dichloroethane	+4.59 ± 0.18	+1.01 ± 0.12	−0.31[e]	+0.01[e]		
Chloroform	+4.47 ± 0.04	+0.15 ± 0.06	−3.30 ± 0.01	−1.95 ± 0.01		

[a] Reference 20. [b] Reference 21. [c] Average of data from ref 23 and 2. [d] Reference 2. [e] Calculated from ref 3, precision not given. [f] Reference 1. [g] Reference 23.

TABLE IV: Thermodynamic Data for the Complexes of TEA and DMF with Guaiacol

Solvent	$-\Delta H^\circ$,[a] kcal mol^{-1}		$-\Delta S^\circ$,[b] cal deg^{-1} mol^{-1}		$K_{20°C}$	
	DMF	TEA	DMF	TEA	DMF	TEA
Cyclohexane	4.64 ± 0.08	4.92 ± 0.11	−13.4	−14.9	3.40	2.58
Benzene	3.50 ± 0.25	6.00 ± 0.16	−11.8	−19.0	1.06	2.06
CCl_4	3.74 ± 0.18	5.39 ± 0.16	−12.1	−17.5	1.38	1.56

[a] The error given was obtained from the slope of a least-squares plot of ln K vs. T^{-1}. [b] Calculated from $\Delta G^\circ = \Delta H^\circ - T\Delta S^\circ$ at 20 °C.

TABLE V: Enthalpies of Complex Formation for Various Bases with Guaiacol

Solvent	$-\Delta H^\circ$, kcal mol^{-1}			
	DMF	TEA	Pyridine	Me_2SO
Cyclohexane	4.64 ± 0.08	4.92 ± 0.11	3.35 ± 0.07	3.99 ± 0.37
Benzene	3.50 ± 0.25	6.00 ± 0.16	4.33 ± 0.15	4.10 ± 0.06
CCl_4	3.74 ± 0.18	5.39 ± 0.16	3.29 ± 0.38	3.26 ± 0.14

DMF and TEA in the solvents of this study are given in Table IV. Enthalpies previously reported[9,10,17] for the pyridine and Me_2SO complexes with phenol and guaiacol are given in Table II.

According to ESP, pyridine interacts with CCl_4, benzene, and o-dichlorobenzene and TEA interacts with CCl_4 but not with aromatic solvents.[3] ESP workers have also suggested that oxygen containing proton acceptors form aggregates in cyclohexane which solvate the adduct causing the enthalpy of hydrogen bond formation to be higher in cyclohexane than in CCl_4.[3,13,18] According to Drago and Nozari[3] neither TEA nor pyridine aggregate significantly in cyclohexane but because of their interaction with CCl_4, the enthalpy of complex formation with these bases is lower in CCl_4 than in cyclohexane. Several investigators[19-23] have proposed an interaction of the phenolic hydroxyl proton with CCl_4 to account for differences found in enthalpies determined in CCl_4 and other solvents. Because specific interaction of the hydroxyl hydrogen with the solvent is minimized by the intramolecular bond of guaiacol, the bulk of the solvent effects in guaiacol systems should be due to interactions of the solvent with base, adduct, or both.

The data in Table V, show that the enthalpy is larger for the Me_2SO and DMF complexes in cyclohexane than in CCl_4. According to Drago et al.,[2,13,18] aggregation of these oxygen containing donors about the complex could cause the enthalpy in cyclohexane to be larger than that in CCl_4.

If aggregation of DMF occurs only in cyclohexane and if other solvent effects are not thermodynamically significant, the enthalpy of complex formation with DMF should be nearly the same in benzene and CCl_4. Within error limits, the enthalpies are the same in these latter two solvents. If aggregation of Me_2SO in cyclohexane is to be accepted, the solvation of Me_2SO, its adduct, or both by benzene must be different from that of DMF.

Only for DMF in cyclohexane and in the comparison of TEA complexes in benzene and CCl_4 do the predicted base interactions of ESP seem to be supported. Thus other solvation effects must be supposed in order to provide a generally satisfactory treatment for these complexes. In order to attempt to identify these effects, partial molar heats of solution were determined and combined with existing literature values so that enthalpies of transfer for the various complexes could be calculated.

The following thermodynamic cycle was used to calculate the transfer enthalpies from solvent I to solvent II.

$$\begin{array}{ccccc} A(I) & + & B(I) & \rightleftharpoons & A{\cdot}B(I) \\ \Big| \Delta H_A & & \Big| \Delta H_B & & \Big| \Delta H_C \\ A(II) & + & B(II) & \rightleftharpoons & A{\cdot}B(II) \end{array} \qquad (2)$$

TABLE VI: Heats of Transfer from Cyclohexane to Other Solvents (kcal mol^{-1})

Solvent	CS_2	CCl_4	C_6H_6	$C_2H_4Cl_2$	$CHCl_3$
Phenol	−0.73 ± 0.21	−1.36 ± 0.09	−2.91 ± 0.03	−3.04 ± 0.20	−3.16 ± 0.06
Guaiacol	−0.96 ± 0.11	−1.51 ± 0.08	−2.21 ± 0.12	−2.55 ± 0.17	−3.41 ± 0.11
Pyridine	−0.76 ± 0.02[a]	−1.65 ± 0.02[a]	−2.01 ± 0.02[a]	−2.00 ± 0.02[a]	−3.96 ± 0.02[a]
Me_2SO	−1.16 ± 0.23	−2.35 ± 0.22[a]	−3.03 ± 0.24	−4.49 ± 0.22[a]	−7.48 ± 0.22
Phenol–pyridine	−0.18 ± 0.97	−1.44 ± 0.73	−2.68 ± 0.93	−3.31 ± 0.69	−4.95 ± 0.53
Phenol–Me_2SO	+0.01 ± 0.93	−1.08 ± 0.62	−2.12 ± 0.65	−4.63 ± 0.80	−4.80 ± 0.56
Guaiacol–pyridine	−2.32 ± 0.32	−3.10 ± 0.54	−5.20 ± 0.35	−4.53 ± 0.65	−6.77 ± 0.49
Guaiacol–Me_2SO	−2.84 ± 0.85	−3.13 ± 0.51	−5.35 ± 1.02	−6.69 ± 0.84	−9.21 ± 0.88
TEA		−0.90 ± 0.12	+0.28 ± 0.08		
DMF		−2.89 ± 0.09	−3.46 ± 0.09		
Guaiacol–TEA		−2.88 ± 0.47	−3.01 ± 0.47		
Guaiacol–DMF		−3.50 ± 0.43	−4.63 ± 0.54		

[a] Estimated error.

Table VI lists the enthalpies of transfer of acid, base, and adduct from cyclohexane to all other solvents. These transfer enthalpies relate the solvation of each species in the different solvents to that in the relatively inert cyclohexane. Thus Table VI is arranged in order of increasing solvation of each species. The relative solvation of the adducts increases in the same order as that of the acid and base. The Me_2SO complex of guaiacol in 1,2-dichloroethane and chloroform is more solvated relative to cyclohexane than the guaiacol–pyridine complex. This effect appears to be due to the solvation of Me_2SO being greater than that of pyridine in 1,2-dichloroethane and chloroform. In the other three solvents, CS_2, CCl_4, and benzene, the differences in solvation of Me_2SO and pyridine relative to cyclohexane are not as great as with 1,2-dichloroethane and chloroform. Consequently the difference between the solvation of the guaiacol–pyridine and the guaiacol–Me_2SO complexes is not as pronounced in these three solvents. Similar conclusions may be applied to the phenol complexes for CS_2, CCl_4, benzene, and possibly 1,2-dichloroethane. The phenol–$CHCl_3$ data do not conform to this analysis.

Relative to cyclohexane any difference between the transfer enthalpies of the phenol–pyridine and guaiacol–pyridine or the phenol–Me_2SO and guaiacol–Me_2SO adducts must be due to differences in solvation of the acid part of the adduct. With the exception of benzene, the enthalpies of transfer of phenol and guaiacol from cyclohexane to the other solvents are nearly equal, however, the transfer enthalpies of the phenol–Me_2SO and guaiacol–Me_2SO adducts differ by more than would be expected if only the phenol and guaiacol transfer enthalpies are considered. The discrepancy can be attributed to the solvation of the guaiacol methoxy group which is freed upon complex formation providing an additional solvation site. Similar considerations apply to the phenol and guaiacol complexes with pyridine.

In cyclohexane, CS_2, CCl_4, and chloroform, the value of

$$\overline{\Delta H_s}(\text{phenol}) - \overline{\Delta H_s}(\text{guaiacol})$$

is relatively constant at 4.23 ± 0.11 kcal mol^{-1}. If the intramolecular bond of guaiacol effectively squeezes out solvent interaction sites so that the number of sites for solvent interactions are about equal for phenol and guaiacol, the solvation differences between phenol and guaiacol would not be expected to differ greatly in the absence of strong specific effects. For benzene and 1,2-dichloroethane, $\overline{\Delta H_s}$(phenol) − $\overline{\Delta H_s}$(guaiacol) is 3.37 and 3.58 kcal mol^{-1}, respectively. In benzene solvent, this results from the well-known interaction of the phenol hydroxy[1] proton with the π cloud. Although a similar explanation for 1,2-dichloroethane would seem to be implied, Drago et al.[3,5] have argued that 1,2-dichloroethane cannot behave as a basic solvent and have given a molecular interpretation to the unusual solvent effects observed in 1,2-dichloroethane. The heats of solution indicate that pyridine behaves similarly in 1,2-dichloroethane and in benzene. Phenol also appears to behave similarly toward these two solvents. Since both the acid and base show similar trends, 1,2-dichloroethane appears to behave in an unusual manner, supporting Drago's contention that solvent interactions in 1,2-dichloroethane are nonspecific.

Christian et al.[6] have proposed that the transfer enthalpy of the adduct should be proportional to the enthalpies of transfer for acid and base

$$\Delta H_C = \alpha(\Delta H_A + \Delta H_B) \quad (3)$$

where α is a constant not strongly dependent upon temperature or solvent pairs. Evaluation of α should allow inferences about the physical nature of the adduct and the adduct interaction with the solvent. Weak complexes should have α less than unity because at least one solvent molecule has been lost from each solvation shell about the acid and upon complex formation. An α value in excess of unity indicates a strong complex and a large interaction between the dipole of the complex and the medium. Drago et al.[5] have argued that one possible reason for the success of ESP is that a slight increase in the nonspecific solvation of the complex could compensate for the loss of solvent molecules when complexation occurs.

According to eq 3, α is the slope of the plot of ΔH_C vs. $\Delta H_A + \Delta H_B$. The data in Tables II, III, and IV were used to calculate α for each acid–base pair by least-squares analysis. The least-squares plots were not forced through the origin. This value of α, along with ΔH_A and ΔH_B from Table II, was then used in eq 2 for each acid–base pair to calculate ΔH_C for each possible solvent transfer. Although the trends in solvation of the adduct followed those predicted by eq 3, agreement between ΔH_C found from the cycle and that calculated by eq 3 was no better than about 0.5 kcal mol^{-1}.

Acknowledgment. Acknowledgment is made to the Donors of the Petroleum Research Fund, administered by the American Chemical Society, for partial support of this research and to the Cottrell College Science Grants Program of the Research Corporation.

References and Notes

(1) R. M. Guidry and R. S. Drago, *J. Phys. Chem.*, **78**, 454 (1974).
(2) R. S. Drago, M. S. Nozari, and G. C. Vogel, *J. Am. Chem. Soc.*, **94**, 90 (1972).
(3) M. S. Nozari and R. S. Drago, *J. Am. Chem. Soc.*, **94**, 6877 (1972).
(4) M. S. Nozari, C. D. Jensen, and R. S. Drago, *J. Am. Chem. Soc.*, **95**, 3162 (1973).
(5) R. S. Drago, A. Nusz, and R. C. Courtright, *J. Am. Chem. Soc.*, **96**, 2082 (1974).

(6) S. D. Christian, J. R. Johnson, H. E. Affsprung, and P. J. Kilpatrick, *J. Phys. Chem.*, **70**, 3376 (1966).
(7) J. Grundnes and S. D. Christian, *Acta Chem. Scand.*, **23**, 3583 (1969).
(8) S. D. Christian and E. E. Tucker, *J. Phys. Chem.*, **74**, 214 (1970).
(9) J. N. Spencer, J. R. Sweigart, M. E. Brown, R. L. Bensing, T. L. Hassinger, W. Kelly, D. L. Housel, and G. W. Reisinger, *J. Phys. Chem.*, **80**, 811 (1976).
(10) J. N. Spencer, R. S. Harner, and C. D. Penturelli, *J. Phys. Chem.*, **79**, 2488 (1975).
(11) J. N. Spencer, R. A. Heckman, R. S. Harner, S. L. Shoop, and K. S. Robertson, *J. Phys. Chem.*, **77**, 3103 (1973).
(12) A. B. Thomas and E. C. Rochow, *J. Am. Chem. Soc.*, **79**, 1843 (1957).
(13) R. S. Drago and T. D. Epley, *J. Am. Chem. Soc.*, **91**, 2883 (1969).
(14) W. J. Lautenberger, E. N. Jones, and J. G. Miller, *J. Am. Chem. Soc.*, **90**, 1110 (1968).
(15) E. M. Woolley, J. G. Travers, B. P. Erno, and L. G. Hepler, *J. Phys. Chem.*, **75**, 3591 (1971).
(16) E. M. Arnett, W. G. Bentrude, J. J. Burke, and P. McC. Duggleby, *J. Am. Chem. Soc.*, **87**, 1541 (1965).
(17) J. N. Spencer, K. S. Robertson, and E. E. Quick, *J. Phys. Chem.*, **78**, 2236 (1974).
(18) W. Partenheimer, T. D. Epley, and R. S. Drago, *J. Am. Chem. Soc.*, **90**, 3886 (1968).
(19) T. Gramstad and W. J. Fuglevik, *Acta Chem. Scand.*, **16**, 6 (1962).
(20) W. C. Duer and G. L. Bertrand, *J. Am. Chem. Soc.*, **92**, 2587 (1970).
(21) E. M. Arnett, L. Joris, E. Mitchell, T. S. S. R. Murty, T. M. Gorrie, and P. v. R. Schleyer, *J. Am. Chem. Soc.*, **92**, 2365 (1970).
(22) A. N. Fletcher and C. A. Heller, *J. Phys. Chem.*, **71**, 3742 (1967).
(23) E. M. Arnett, E. J. Mitchell, and T. S. S. R. Murty, *J. Am. Chem. Soc.*, **96**, 3875 (1974).

The Infrared Spectrum of a Molecular Aggregate. The HCN Dimer Isolated in an Argon Matrix

J. Pacansky

IBM Research Laboratory, San Jose, California 95193 *(Received June 9, 1977)*

Publication costs assisted by IBM Research Laboratory

Spectral properties of well-defined molecular aggregates are difficult to obtain. A study is presented which demonstrates that a well-defined molecular aggregate may be produced by photochemical methods. This is specifically shown by producing the HCN dimer from the photochemical decomposition of *s*-tetrazine. The infrared spectrum of the dimer clearly shows that the vibrational bands associated with the hydrogen bond are intensified and broadened in comparison to those not involved in the hydrogen bond.

Introduction

The matrix isolation technique has amply demonstrated that spectroscopic properties of isolated molecules may be readily obtained.[1] Here, and in subsequent studies, we show that spectroscopic properties of *well-defined* aggregates of molecules may also be observed utilizing the matrix isolation technique. This is demonstrated by showing the infrared spectrum of the matrix isolated HCN dimer. The unique feature of this spectrum and the manner in which the dimer was formed is that all of the sites in the matrix are occupied by *only dimers*. The spectra thus clearly reveal the spectroscopic changes which are manifestations of the rather strong hydrogen bond[2] (ΔH = 3.8 kcal/mol) in the dimer.

The method used to produce molecular aggregates consist of selecting a system that upon exposure to light photochemically decomposes to the particular aggregate desired. For example, tetrazine[3,4] has been studied in both the gas and solid phase and appears to quantitatively decompose when exposed to light with wavelength λ <5000 Å as shown in reaction 1. Consequently, this system offers

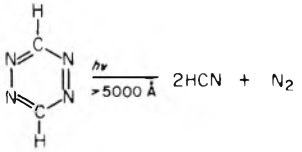

$$\xrightarrow{h\nu,\ >5000\ \text{Å}} 2\text{HCN} + \text{N}_2 \qquad (1)$$

the unique opportunity of photochemically producing a matrix isolated hydrogen bonded system.

Several gas phase studies exist on HCN aggregates[5] and complexes[6] of other species with HCN in the gas phase. King and Nixon[7] performed matrix isolation studies on HCN aggregates in argon, nitrogen, and carbon monoxide matrices by mixing the respective gases with HCN vapor. (HCN vapor consists of approximately 10% dimer and 3% trimer.) From their elegant infrared studies they were able to assign bands to the dimer but could not detect any increase in band intensity or width for the vibrational modes involved in the hydrogen bond. The band assignments reported here are in essential agreement with theirs; however, there is a sharp disagreement over band intensity and band width observations.

Experimental Section

The tetrazine was synthesized according to the method given by Spencer, Cross, and Wilberg.[3] Further purification of the tetrazine crystals was accomplished by resublimation at low temperatures as outlined by Hochstrasser and King.[4] The vapor pressure of the tetrazine was measured in a glass vacuum system ($p < 10^{-6}$ mmHg) fitted with a Wallace and Tiernan differential pressure manometer and found to be approximately 1 mm at room temperature.

Samples for matrix isolation were prepared by mixing the tetrazine vapor at room temperature in a 3-L gas handling system with 500 mm of argon (Linde, Research purity). Essentially, the gas handling system is the same system used to measure the tetrazine vapor pressure except that a 3-L bulb was appended to facilitate mixing of the argon and tetrazine gas. Nominally, 100 mm of this mixture was deposited on a CsI substrate at a rate of 0.25 mm/min.

The cryogenic system used to maintain the low temperature was an Air Products Displex CS-202 closed cycle refrigerator fitted with CsI windows. The infrared spectra were recorded with a Perkin-Elmer 521 spectrometer.

The photochemical apparatus consisted of a 1500-W General Electric HBD high-pressure mercury lamp in

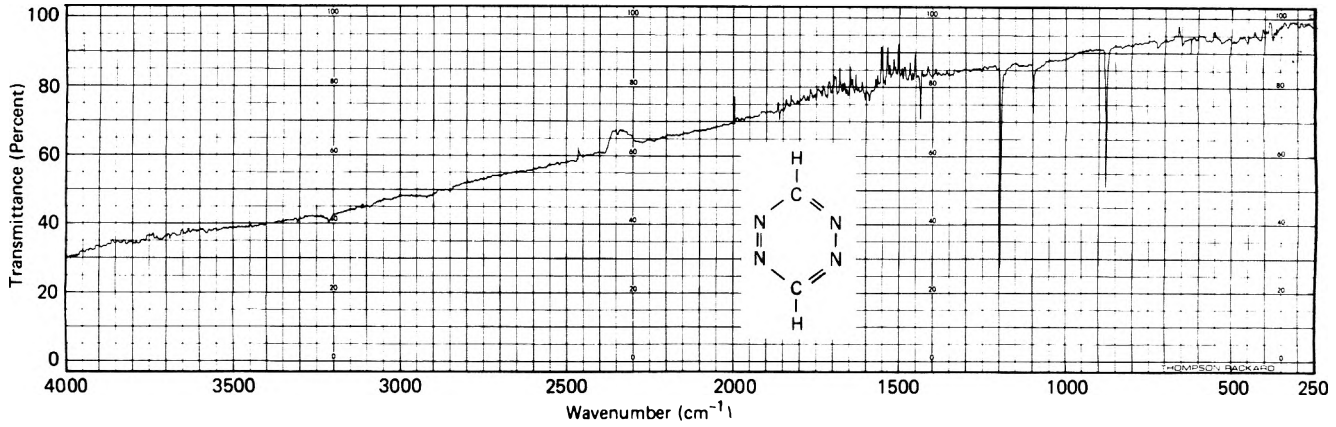

Figure 1. The infrared spectrum of *s*-tetrazine in argon (concentration 1/500) recorded with the sample at 8 K.

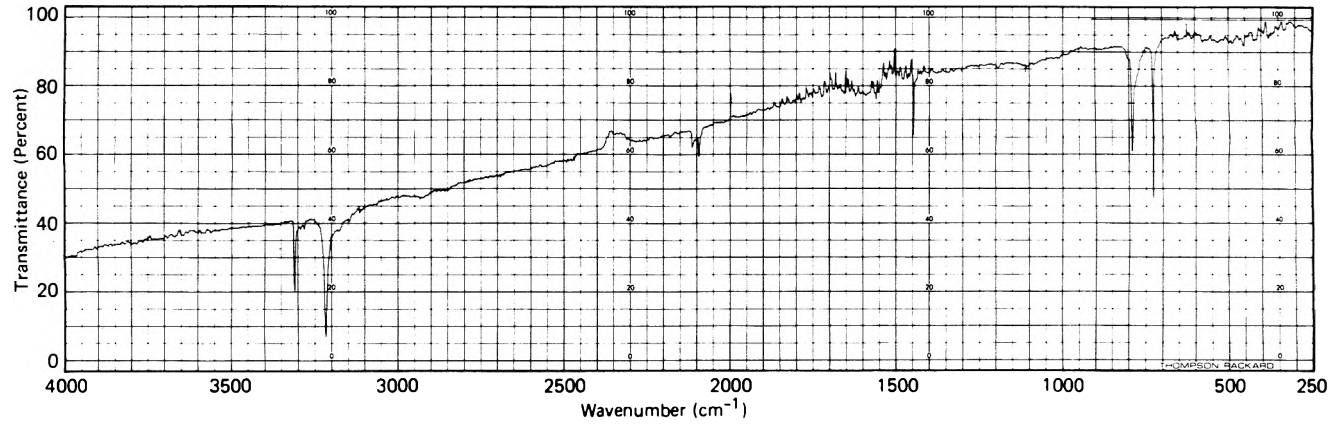

Figure 2. The infrared spectrum of *s*-tetrazine after irradiation with light $\lambda > 5100$ Å for $t = 30$ min.

conjunction with a 20-cm water filter. The spectral region of interest was isolated using standard Corning glass filters.

Results and Discussion

The infrared spectrum of tetrazine isolated in an argon matrix (concentration, 1/500 tetrazine to argon) is shown in Figure 1. The infrared spectrum shown in Figure 2 results after $t = 30$ min of irradiation with light emitted from a high-pressure mercury lamp in conjunction with a Corning glass filter no. 3-69 (0% T at 5100 Å). Further irradiation with no filter in the photolysis apparatus created no changes in this spectrum. The new species produced during the irradiation appears to be the primary and only product of the irradiation.

This spectrum (Figure 2) is assigned to the HCN linear dimer on the following basis:

(1) All photochemical studies thus far on tetrazine[4] indicate a quantitative decomposition to HCN and N_2.

(2) After the argon was pumped away at 40 K the dimer spectrum synchronously transformed to the well-known spectrum of solid HCN.

(3) The intense features in the spectrum agree with those assigned to the HCN dimer by King and Nixon[7] obtained by a completely different procedure.

(4) Warming the matrix to 35 K for 30 min and subsequently recording an infrared spectrum at 8 K produces no new spectral changes. Consequently, it is believed that the two HCN molecules locked in each site in solid argon are in their most stable linear conformation as predicted by theoretical methods.[8]

The infrared spectrum of monomeric HCN[9] isolated in argon matrices consists of two intense bands at 3305 and 720 cm^{-1}. The band at 3305 cm^{-1}, ν_3, is the CH stretching motion while the 720-cm^{-1} band is ν_2, the bond angle deformation. The CN stretch, ν_1, is very weak and difficult to observe since intense bands due to aggregates obscure this region.

TABLE I: Infrared Band Centers for the HCN Monomer and Dimer (cm^{-1})

	Dimer[a]	Monomer
ν_3, CH stretch	A 3306 A′ 3213	3305
ν_1, CN stretch	B 2112 B′ 2093	
ν_2, bond angle deformation	θ 731 θ' 793	721
$2\nu_2$	2θ 1449 $2\theta'$ 1560	1425

[a] The definitions of A, A′, B, B′, θ, and θ' are given in Figure 3.

The infrared spectrum of the HCN dimer is quite different from the monomer in that it exhibits two bands in each of the regions ν_1, ν_2, and ν_3 where the fundamental vibrations of monomeric HCN appear. The band centers for the monomer and dimer are listed in Table I. Each of these regions is now discussed.

ν_3. *CH Stretch.* The dimer bands in the ν_3 region clearly show the effects of hydrogen bonding. The band marked A (Figure 3) at 3306 cm^{-1} is virtually identical with that for monomeric HCN and is assigned to the stretching motion of the CH bond not involved in the hydrogen bond. The band at 3213 cm^{-1} marked A′ is assigned to the hydrogen bonded CH stretching frequency. This shift of $\approx$100 cm^{-1} is a reflection of the rather strong hydrogen bond in the dimer. In addition to the lower stretching

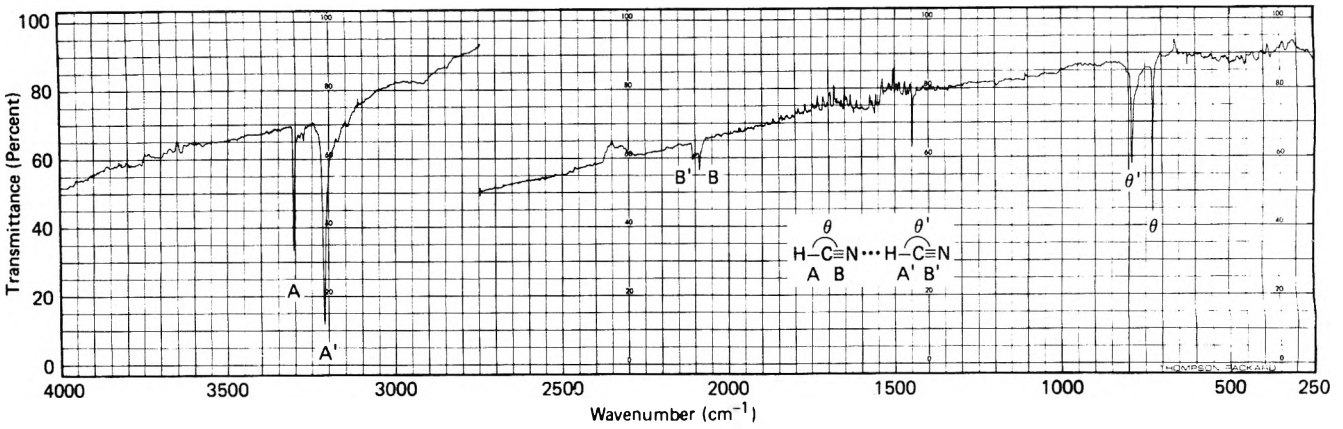

Figure 3. The infrared spectrum of the HCN dimer. (This spectrum is essentially that shown in Figure 2 with the exception that the baseline is changed.)

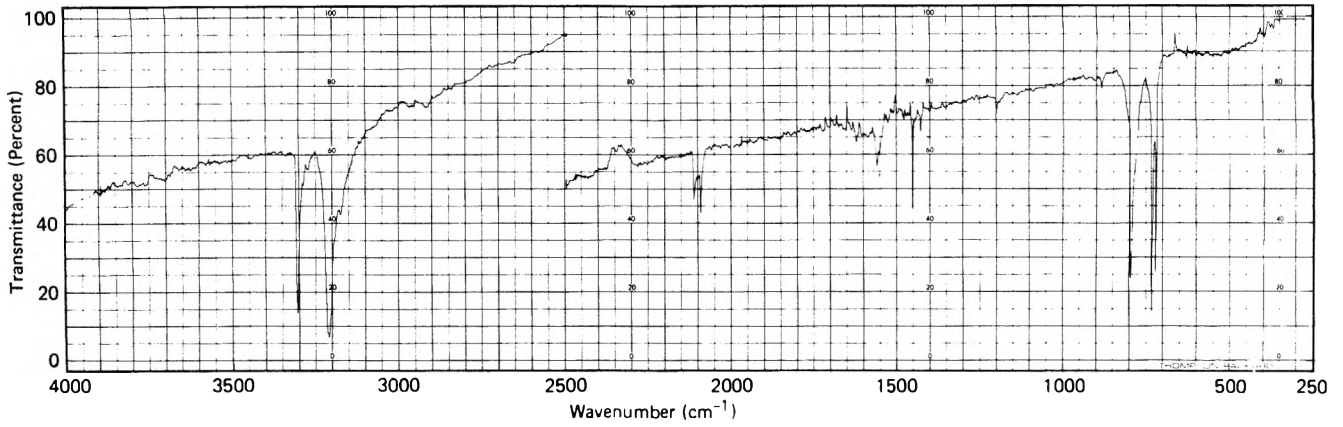

Figure 4. The infrared spectrum of the HCN monomer and dimer isolated in an argon matrix.

frequency the hydrogen bond also creates a large increase in band intensity and band width as shown by the 3213-cm^{-1} feature. These effects on vibrational spectra by hydrogen bonding (i.e., intensity enhancement and band broadening) have been predicted theoretically[10] but attempts to experimentally verify this in solution are always shrouded by the possibility of "cooperative effects" of aggregates. The important feature in the study presented here is that the dimer is isolated in an argon matrix and within the dimer there is a non-hydrogen-bonded CH bond to compare to one that is hydrogen bonded.

ν_2. *Bond Angle Deformation.* The bands in the ν_2 region marked θ' and θ are assigned to the bond angle deformation of each HCN monomeric unit in the dimer. Since for the monomer the bond angle deformation consists primarily of movement of the hydrogen atom perpendicular to the internuclear axis of the HCN molecule then it is reasonable to expect an increase in the frequency for bond angle deformation whose motion is impeded by the hydrogen bonding. On this basis the bands marked θ' (793 cm^{-1}) and θ (731 cm^{-1}) are assigned to the hydrogen- and non-hydrogen-bonded bond angle deformations of the dimer. Again it should be noted that the band width of the hydrogen-bonded feature θ' is much broader than that for θ.

ν_1. *The CN Stretching Region.* The ν_1 for monomeric HCN is very weak and very difficult to detect in argon matrices. However, the corresponding bands for the dimer (marked B and B') are clearly seen. The CN stretch not involved in the hydrogen bonding is assigned to B' (2112 cm^{-1}) while B (2093 cm^{-1}) is assigned to the hydrogen-bonded CN stretch. The reason why these bands are seen in the dimer is probably due to a change in the normal coordinate upon hydrogen bonding. The band intensity for CN stretch which is hydrogen bonded appears to be more than that for the non-hydrogen-bonded motion. However, this is complicated by the band at 2102 cm^{-1} which presently is believed to be due to a higher order aggregate.

$2\nu_2$. *The Overtone Region for Bond Angle Deformation.* In Figure 4 the composite infrared spectrum is shown for the HCN monomer and dimer. This spectrum was produced by first allowing ≈50% thermal decomposition of tetrazine vapor mixed in argon gas to occur at room temperature and then subsequently depositing this mixture (i.e., tetrazine and HCN). This mixture was then exposed to light λ >5100 Å in order to photolytically convert the tetrazine to HCN dimer, thus, giving the spectrum shown in Figure 4. It should be noted that in order to obtain this spectrum the tetrazine to argon ratio was initially 1/300. Although the band centers for the intense features of this spectrum are identical with those obtained using more favorable guest to host ratios they are unquestionably broader due to some higher order aggregates. The new features in this spectrum are the ν_2 for monomer at 721 cm^{-1}, and ν_3 for the monomer which is practically coincident with ν_3 for the dimer. The band at 1425 cm^{-1} is $2\nu_2$ for the monomer while the band at 1449 cm^{-1} is $2\nu_2$ for the deformation in the dimer marked θ (Figure 3) at 731 cm^{-1}. The band marked θ' as discussed above is intimately involved in the hydrogen bond and is broadened. This is also true for its overtone at 1560 cm^{-1} as shown in Figure 4.

Thus far it has been shown that the HCN dimer is formed upon photochemical decomposition of *s*-tetrazine in argon. This photochemical reaction also produces a molecule of nitrogen that should also reside in the same cavity as the HCN dimer; consequently, the influence of

the nitrogen molecule must be assessed. In order to do so, it is first noted that the band centers for the HCN dimer in the experiments reported here are identical with those reported for the dimer obtained by thermal diffusion of HCN in argon matrices.[7] Furthermore, similar thermal studies in nitrogen matrices[7] only revealed sharper spectra features for the dimer. In the experiments reported here, no evidence could be found which indicated that the nitrogen molecule perceptibly perturbed the HCN dimer. These results are understandable in terms of the large differences between the energy of interaction of two HCN molecules as compared to that for HCN with nitrogen. For the former, the intermolecular energy is large and due to a hydrogen bond while for the latter, the intermolecular energy is van der Waals in nature and very small.

Summary

A study on the infrared spectrum HCN dimer is presented which describes a method by which well-defined aggregates of molecules may be photochemically produced from a suitable parent species. The infrared spectrum of the HCN dimer clearly shows that band intensities and band widths for vibrations involved in the hydrogen bond are intensified and broadened.

References and Notes

(1) H. F. Hallman, Ed., "Vibrational Spectroscopy of Trapped Species", Wiley, New York, N.Y., 1973.
(2) W. F. Giauque and R. A. Ruehrwein, *J. Am. Chem. Soc.*, **61**, 2626 (1939).
(3) G. H. Spencer, Jr., P. C. Cross, and K. B. Wiberg, *J. Chem. Phys.*, **35**, 1925, 1939 (1961).
(4) R. M. Hochstrasser and D. S. King, *J. Am. Chem. Soc.*, **98**, 5443 (1976).
(5) G. E. Hyde and D. F. Hornig, *J. Chem. Phys.*, **10**, 491 (1942).
(6) R. K. Thomas, *Proc. R. Soc. London, Ser. A*, **325**, 113 (1971).
(7) C. M. King and E. R. Nixon, *J. Chem. Phys.*, **48**, 1685 (1968).
(8) A. Johansson, P. Kollman, and S. Rothenberg, *Theor. Chim. Acta*, **26**, 97 (1972).
(9) J. Pacansky and G. V. Calder, *J. Mol. Structure*, **14**, 363 (1972).
(10) J. Yarwood, Ed., "Spectroscopy and Structure of Molecular Complexes", Plenum Press, New York, N.Y., 1973.

Isotope and Substituent Effects on the Intramolecular Proton Transfer in the Excited State of 6-(2-Hydroxy-5-methylphenyl)-s-triazines

Haruo Shizuka,* Kohji Matsui,

Department of Chemistry, Gunma University, Kiryu, Gunma 376, Japan

Yoshinori Hirata, and Ikuzo Tanaka

Department of Chemistry, Tokyo Institute of Technology, Meguro-ku, Tokyo, Japan *(Received June 23, 1977)*

Publication costs assisted by Gunma University

Isotope and substituent effects on the intramolecular proton transfer in the excited singlet state of the title compounds have been studied by means of picosecond and nanosecond time-resolved spectroscopy. The absolute rate constants k_{PT} for proton transfer were determined from the build up curve of the $S_n' \leftarrow S_1'$ absorption to be 1.2×10^{10} s^{-1} [for $(ON)_h$ and $(ON)_d$] and 1.8×10^{10} s^{-1} for $(NN)_h$ at 298 K. No isotope effect on proton transfer was observed, indicating that the intramolecular proton transfer in the excited state does not proceeds via quantum mechanical tunneling but via a radiationless transition $S_1 \rightarrow S_1'$ having no potential barrier. Substitution of electron-donating groups into the *s*-triazinyl moiety favors proton transfer in the excited state.

Introduction

In previous papers,[1,2] it has been shown that (1) intramolecular proton transfer in the excited singlet of 2,4-bis(dimethylamino)-6-(2-hydroxy-5-methylphenyl)-*s*-triazine competes with a rapid radiationless decay k_d, (2) the proton transfer rate constant k_{PT} is measured directly by the build up curve of the induced emission from the excited proton-transferred species (keto form) with picosecond pulses, and (3) intramolecular proton transfer originates from the vibrationally relaxed S_1 state.

The question that arises is whether the intramolecular proton transfer proceeds via quantum mechanical tunneling or a pathway involving a potential barrier E_{PT}. Using $\nu_{OH} = 10^{14}$ s^{-1} (frequency of the OH stretching vibration), the value of E_{PT} in the excited salicylic acid was estimated to be ≤ 0.12 kcal/mol, and proton transfer involving proton tunneling was suggested.[3] However, little is known about the proton transfer mechanism. The substituent effect of electron-donating groups into the *s*-triazinyl moiety on the intramolecular proton transfer in the excited state was of interest from the viewpoint of the excited electronic structure responsible for proton transfer.

TABLE I: Samples of 6-(2-Hydroxy-5-methylphenyl)-*s*-triazines[a]

Samples	X	Y	Z
$(OO)_h$	H	OCH_3	OCH_3
$(ON)_h$	H	OCH_3	$N(CH_3)_2$
$(ON)_d$	D	OCH_3	$N(CH_3)_2$
$(NN)_h$	H	$N(CH_3)_2$	$N(CH_3)_2$
$(NN)_d$	D	$N(CH_3)_2$	$N(CH_3)_2$

[a] 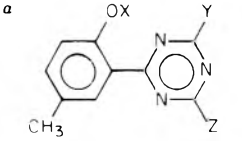

In the present work, isotope and substituent effects on intramolecular proton transfer have been studied by means of picosecond and nanosecond time-resolved spectroscopy in addition to fluorometry, and the proton transfer mechanism is discussed.

Experimental Section

The preparation and purification of materials were described previously.[4] The samples used are listed in

TABLE II: Fluorescence Quantum Yields Φ_f', Lifetimes τ' and τ_{S_1}, and Fluorescence Maxima $\bar{\nu}_{max}$ in MP at 298 and 77 K

	298 K					77 K		
Samples	Φ_f'	τ'/ns	$\bar{\nu}_{max}/\mu m^{-1}$	$\Delta\bar{\nu}^a/\mu m^{-1}$	$\tau_{S_1}{}^b$/ps	$\Phi_f'{}^c$	τ'/ns	$\nu_{max}/\mu m^{-1}$
$(OO)_h$	$(6.6 \pm 1) \times 10^{-3}$	<1	1.87	1.0_1		$0.2_1(\pm 0.06)$	3 ± 0.5	1.92
$(ON)_h$	$(7.5 \pm 1) \times 10^{-2}$	1.2 ± 0.5	1.94	1.0_2	~48	$0.5_4(\pm 0.07)$	5 ± 0.5	2.03
$(ON)_d$	$(7.5 \pm 1) \times 10^{-2}$	1.2 ± 0.5	1.94	1.0_2	~48	$0.5_4(\pm 0.07)$	5 ± 0.5	2.03
$(NN)_h$	$(3.8 \pm 0.3) \times 10^{-1}$	5 ± 0.5	1.99	1.0_1	~38	$0.6_4(\pm 0.1)$	6 ± 0.5	2.10
$(NN)_d$	$(3.8 \pm 0.3) \times 10^{-1}$	5 ± 0.5	1.99	1.0_1	~38	$0.6_4(\pm 0.1)$	6 ± 0.5	2.10

[a] $\Delta\bar{\nu}$ denotes Stokes shift. [b] τ_{S_1} is the lifetime of the S_1 state (enol form), which is equal to $(k_{S_1})^{-1}$. The values of k_{S_1} are given in eq 5 and 6. [c] Absolute values of Φ_f' at 77 K were determined by comparison with the phosphorescence emission ($\Phi_p = 0.74$) of benzophenone: S. L. Murov, "Handbook of Photochemistry", Marcel Dekker, New York, N.Y., 1973, p 41.

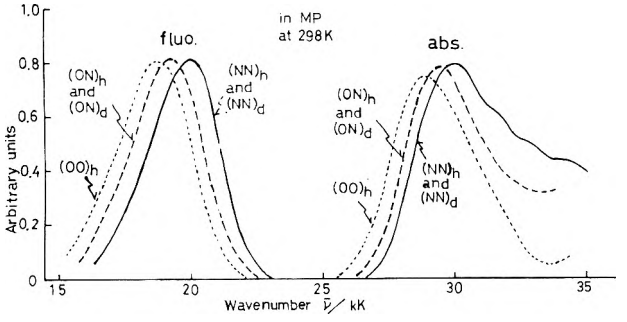

Figure 1. Absorption and corrected fluorescence spectra of 6-(2-hydroxy-5-methylphenyl)-s-triazines.

Table I. The deuterium isomer $(ON)_d$ or $(NN)_d$ was prepared by treating $(ON)_h$ or $(NN)_h$ with a mixed solution of D_2O and acetone in the presence of a trace of NaOH, whose isotope purity was greater than 90%.

The experimental methods for measurement of the fluorescence spectra and quantum yields were the same as previously.[1] The fluorescence decay was measured by a Hitachi nanosecond time-resolved spectrophotometer (11-ns-pulse width) and the lifetime was determined by the convolution method.

The essentials of the picosecond optical measurements were the same as reported previously.[2] In the present work, a cell containing H_2O was also used as a self-phase modulator, which generates a picosecond continuum having shorter wavelengths than that of CCl_4. It permitted direct measurement of the build up curve of the $S_n' \leftarrow S_1'$ absorption.

Results and Discussion

Absorption and fluorescence spectra of 6-(2-hydroxy-5-methylphenyl)-s-triazines in MP (3:1 in volume) at 298 K are shown in Figure 1. The normal fluorescence could not be observed, but only a green emission with a large Stokes shift. The lack of normal fluorescence indicates that (1) the lifetime τ_{S_1} of the fluorescent state of the enol form S_1 is very short ($\sim 10^{-11}$ s) and (2) the enthalpy change $|\Delta H^*|$ between S_1 and S_1' (keto form) is large enough to prevent reverse proton transfer.[1]

The fluorescence quantum yields Φ_f' and the lifetimes τ' of S_1' at 298 and 77 K in MP are listed in Table II. Temperature effects[5] on Φ_f' and τ' are shown in Figures 2 and 3, respectively.

From the steady state approximation, Φ_f' is given by[1]

$$\Phi_f' = \frac{k_{PT} k_f' \tau'}{k_{PT} + k_d} = \gamma k_f' \tau' \qquad (1)$$

where k_d is the rate constant in a rapid deactivation process[1] competing with k_{PT}, γ the proton transfer efficiency, and k_f' the rate constant in the radiative transition $S_1' \rightarrow S_0'$ (the ground state of keto form).

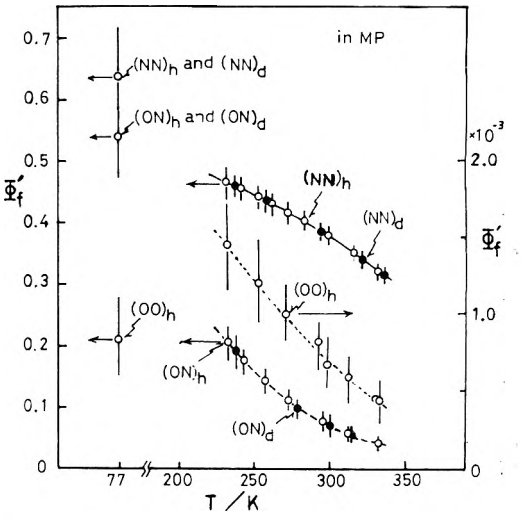

Figure 2. The temperature dependence of the fluorescence quantum yields Φ_f'.

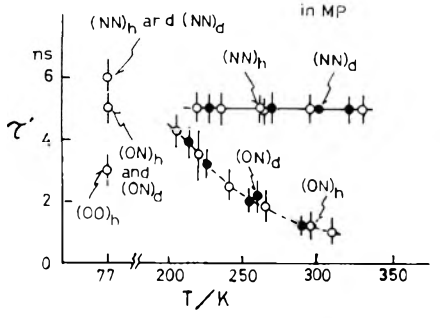

Figure 3. The temperature effect on the fluorescence lifetimes τ'.

Substituting the electron-donating groups into the s-triazinyl moiety, the values of Φ_f' and τ' became large. The τ' value of $(OO)_h$ could not be measured except at 77 K by means of nanosecond time-resolved spectroscopy, since it was very small. The Φ_f' value of $(ON)_h$ or $(ON)_d$ increased with decreasing temperature; this is due to the increase both in γ_{ON} (i.e., decrease in k_d) and τ' (see eq 1). A similar tendency was observed in the cases of $(OO)_h$, $(NN)_h$, and $(NN)_d$. Figure 4 shows a plot of Φ_f'/τ' vs. temperature T. At 77 K, the Φ_f'/τ' of (ON) was equal to that of (NN), where both γ_{ON} and γ_{NN} values might be close to unity as will be discussed later. This fact shows that the k_f' value of (ON) is almost the same as that of (NN). Thus, it can be said that the values of γ_{ON} are less than those of γ_{NN} at temperatures higher than 230 K. The ratio of γ_{ON} to γ_{NN} ($\simeq 0.69$)[1] at 298 K can be estimated to be ~0.82 from Figure 4. The value of γ_{ON} is therefore

$$\gamma_{ON} \simeq 0.57 \quad \text{at 298 K} \qquad (2)$$

It is noteworthy that there is no isotope effect on γ_{ON} or

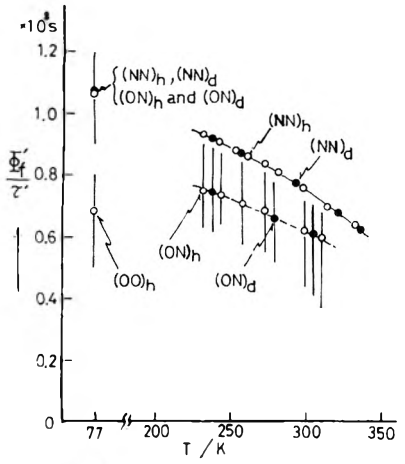

Figure 4. Plots of Φ_f'/τ' vs. T.

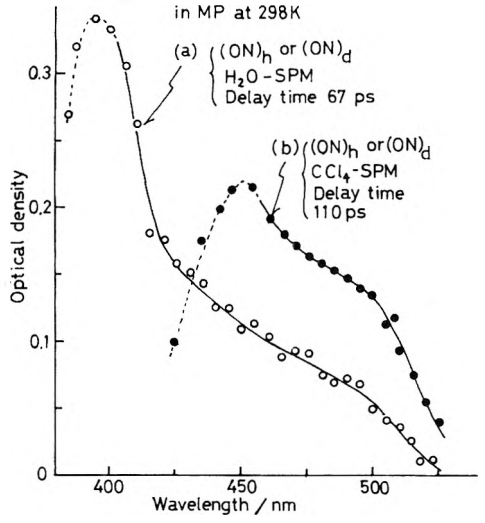

Figure 5. The transient absorption spectra of a 4×10^{-4} M MP solution of $(ON)_h$ or $(ON)_d$ at 298 K measured by the H_2O SPM (a) or the CCl_4 SPM (b) taken 67 and 110 ps after excitation, respectively.

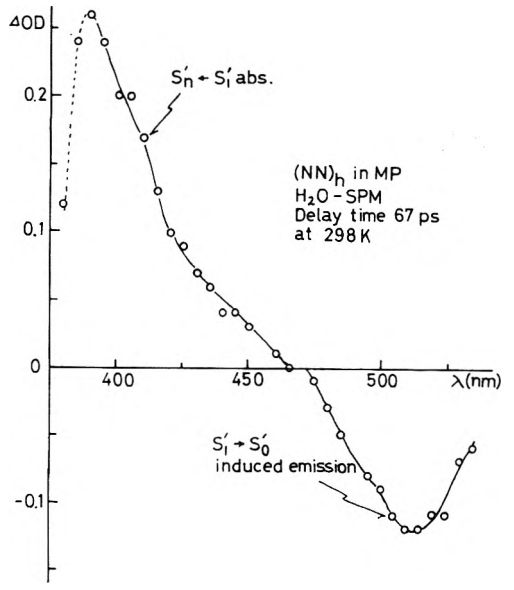

Figure 6. The transient absorption and the induced emission spectra of a 4×10^{-4} M MP solution of $(NN)_h$ measured by the H_2O SPM at 298 K taken 67 ps after excitation.

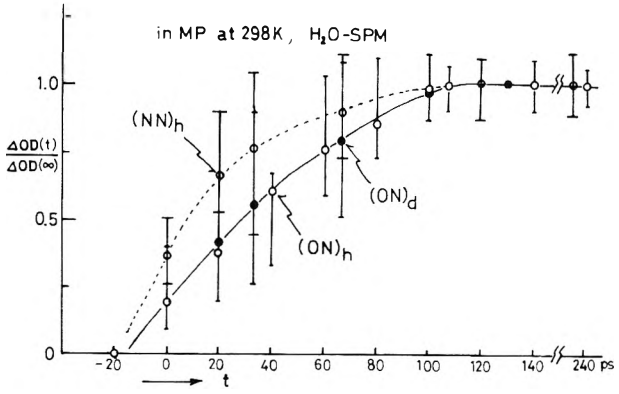

Figure 7. The S_1' state formation, $\Delta OD(t)/\Delta OD(\infty)$, vs. delay time t in MP at 298 K.

γ_{NN}. Figure 4 also shows that a rapid radiationless decay process k_d in the S_1 state of $(ON)_h$ or $(ON)_d$ has an activation energy of 2–3 kcal/mol as well as that[1] of $(NN)_h$ or $(NN)_d$.

In a previous paper,[2] we measured the build up curve of the induced emission from the S_1' state of $(NN)_h$ instead of that of the $S_n' \leftarrow S_1'$ absorption, because the absorption was too weak to measure the build up curve. This is due to the fact that the self-phase modulator containing CCl_4 used produces a weak picosecond continuum at wavelengths shorter than ~450 nm. In the present work, we also used a self-phase modulator (SPM) containing H_2O. It generates a highly intense continuum at short wavelengths upto 390 nm. The kinetic analysis of the build up curve of the $S_n' \leftarrow S_1'$ absorption is much more accurate than that of the induced emission reported previously.[2]

Figure 5 shows the transient $S_n' \leftarrow S_1'$ absorption spectra of a 4×10^{-4} M MP solution of $(ON)_h$ or $(ON)_d$ at 298 K measured by the H_2O SPM (a) or the CCl_4 SPM (b) taken 67 and 110 ps after excitation, respectively. Similarly, the transient absorption and induced emission spectra of S_1' of $(NN)_h$ measured by the H_2O SPM are shown in Figure 6. As for $(OO)_h$, no transient absorption could be observed, since the intensity was very weak. The transient absorption is assigned to the $S_n' \leftarrow S_1'$ transition.[1] Its absorption maximum λ_{max} seems to appear at wavelengths shorter than 390 nm. Unfortunately, it is impossible to measure λ_{max} since the light intensity of the H_2O SPM decreases at the corresponding wavelengths.

Figure 7 shows plots of $\Delta OD(t)/\Delta OD(\infty)$ as a function of delay time t, where $\Delta OD(\infty)$ at 420 nm was determined by averaging data over the range 100 ps $\leq t \leq$ 230 ps for each shot and $\Delta OD(t)$ is the intensity of the $S_n' \leftarrow S_1'$ absorption at 420 nm measured by the H_2O SPM. The production of S_1' is related to the decay of the S_1 state (the excited enol form), and the following equations can be derived:[2]

$$[S_1]_t \propto 1 - \frac{\Delta OD(t)}{\Delta OD(\infty)} \tag{3}$$

and

$$\ln\left[1 - \frac{\Delta OD(t)}{\Delta OD(\infty)}\right] = -k_{S_1} t + \text{constant} \tag{4}$$

where $k_{S_1} = k_{PT} + k_d$. Figure 8 shows plots of ln $[1 - \Delta OD(t)/\Delta OD(\infty)]$ vs. the delay time t, whose data were measured by the H_2O SPM. The values of k_{S_1} at 298 K can be obtained from the slopes of the linear plots in Figure 8 as follows: $(ON)_h$ and $(ON)_d$:

$$k_{S_1} = 2.1(\pm 0.4) \times 10^{10}\ s^{-1} \tag{5}$$

$(NN)_h$:

$$k_{S_1} = 2.6(\pm 0.5) \times 10^{10}\ s^{-1} \tag{6}$$

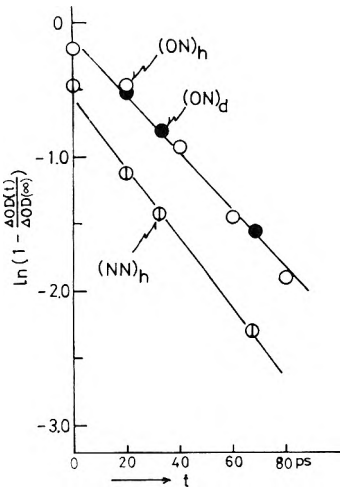

Figure 8. Plots of ln $\{1 - \Delta OD(t)/\Delta OD(\infty)\}$ vs. t.

Using the values of γ_{ON} ($\simeq$0.57 in eq 1) and γ_{NN} ($\simeq$0.69),[1] we can determine the values of k_{PT} and k_d at 298 K: $(ON)_h$ and $(ON)_d$:

$$k_{PT} = 1.2(\pm 0.2) \times 10^{10}\ s^{-1} \quad (7)$$

$$k_d = 0.9(\pm 0.2) \times 10^{10}\ s^{-1} \quad (8)$$

$(NN)_h$:

$$k_{PT} = 1.8(\pm 0.4) \times 10^{10}\ s^{-1} \quad (9)$$

$$k_d = 0.8(\pm 0.2) \times 10^{10}\ s^{-1} \quad (10)$$

Thus, it can be said that (1) there is no isotope effect for the intramolecular proton transfer in the excited singlet of 6-(2-hydroxy-5-methylphenyl)-*s*-triazines and (2) the substitution of electron-donating groups into the *s*-triazinyl moiety favors proton transfer in the excited state.

At first, let us consider the proton transfer mechanism. The experimental results for the isotope effect make the hypothesis of proton tunneling very unlikely. Equation 1 can be simplified at 77 K, where k_d becomes negligibly small.

$$\Phi_f' = k_f'\tau' \quad (11)$$

The value of k_{PT} should be about 10^2 times greater than those of another relaxation processes in the S_1 state of (ON) or (NN) at 77 K, since no normal fluorescence from the S_1 state could be observed in contrast to the large value of Φ_f' at 77 K. That is, the value of k_{PT} at 77 K scarcely decreases in comparison with that at room temperature, indicating that the potential barrier E_{PT} in the intramolecular proton transfer process should be very low (<0.2 kcal/mol). If there were a low value of E_{PT} in the excited $(ON)_h$ or $(ON)_d$, isotope effects on the values of k_{PT}, Φ_f', and τ' would be observed according to the difference in zero-point energies between O–H and O–D bonds. A number of isotope effects in the intermolecular proton transfer both in the ground[6] and excited[7] states are known. However, in the present case there was no such effect. This may suggest that the value of E_{PT} is close to zero. From the Arrhenius equation, the following may hold:

$$k_{PT} \simeq A_{PT} \quad (12)$$

where A_{PT} denotes the frequency factor in the intramolecular proton transfer process. It is of interest that the value of A_{PT} is the order of $10^{10}\ s^{-1}$ which is different from that of the OH vibrational frequency ($\nu_{OH} \simeq 10^{14}\ s^{-1}$). It takes much time $\sim 10^{-11}$ s for the nucleus of H^+ or D^+ to move into the proper place in the excited state. In other words, the radiationless transition $S_1 \rightarrow S_1'$ needs a time of $\sim 10^{-11}$ s.

Chart I

Sample	Proper atom	π formal charges S_0	S_1	S_0'	S_1'
(ON)[a]	N	−0.3704	−0.3884	+0.4024	+0.3702
	O	+0.1432	+0.2729	−0.5837	−0.3909
(ON)[b]	N	−0.3724	−0.3812	+0.3967	+0.3590
	O	+0.1423	+0.2679	−0.5846	−0.3940
(ON)[c]	N	−0.3714	−0.3848	+0.3996	+0.3646
	O	+0.1425	+0.2704	−0.5842	−0.3925

[a] Y = OCH_3, Z = $N(CH_3)_2$ (see Table I). [b] Y = $N(CH_3)_2$, Z = OCH_3. [c] Averaging data. As for (NN), they are listed in ref 1. The above data show that proton transfer originates from S_1 or S_0'.

As mentioned previously,[1] the n, π* states in both the enol and keto forms lie energetically above the π, π* states of S_1 and S_1'. The electronic structure in the excited state of the sample molecules affects the k_{PT} value of the intramolecular proton transfer process. The π-formal charge Q_N of −0.4084 at the proper nitrogen atom in the S_1 state of (NN)[1] is greater than that (−0.3848) of (ON).[8] While, there is little change in the π-formal charge at the proper oxygen atom in the S_1 state. Therefore, it is expected that (NN) is favored over (ON) for proton transfer. The experimental values of k_{PT} correspond to the above relation (see eq 7 and 9). The π-formal charge (Chart I) at the proper nitrogen atom in the S_1' state (the excited keto form)[8] affects the τ' value; a small positive charge may be responsible for the stability of S_1'. Substituting electron-donating groups into the triazinyl moiety permits intramolecular proton transfer in the S_1 state to take place easily.

In conclusion, intramolecular proton transfer in the S_1 state of the sample molecules needs a time of $\sim 10^{-11}$ s at room temperature. The absence of an isotope effect on proton transfer indicates that the process does not proceeds via quantum mechanical tunneling but via a radiationless transition $S_1 \rightarrow S_1'$ having no activation barrier. Substitution of electron-donating groups into the triazinyl moiety favors proton transfer in the excited state.

References and Notes

(1) H. Shizuka, K. Matsui, T. Okamura, and I. Tanaka, *J. Phys. Chem.*, **79**, 2731 (1975).
(2) H. Shizuka, K. Matsui, Y. Hirata, and I. Tanaka, *J. Phys. Chem.*, **80**, 2070 (1976).
(3) H. Beens, K. H. Grellmann, M. Gurr, and A. Weller, *Discuss. Faraday Soc.*, **39**, 183 (1965).
(4) H. Shizuka, T. Kanai, T. Morita, Y. Ohto, and K. Matsui, *Tetrahedron*, **27**, 4021 (1971); Y. Ohto, H. Shizuka, S. Sekiguchi, and K. Matsui, *Bull. Chem. Soc. Jpn.*, **47**, 1209 (1974).
(5) Unfortunately, precipitation of the starting materials took place in MP at low temperatures (≤220 K). Polar solvents are unsuitable for the experiment because they interact with both S_1 and S_1' states resulting in a shortening of their lifetimes (see ref 1) and the kinetic analyses are really complicated.
(6) E.g., R. A. More O'Ferrall in "Proton-Transfer Reactions", E. Caldin and V. Gold, Ed., Chapman and Hall, London, 1975, p 201, and many references cited therein.
(7) M. A. El-Bayoumi, P. Avouris, and W. R. Ware, *J. Chem. Phys.*, **62**, 2499 (1975).
(8) The π formal charges (Chart I) were calculated by a semiempirical SCF–MO–CI method. The calculations were carried out with an electronic computer, a HITAC 8800, located at the Computer Center, the University of Tokyo.

Hydrogen Bonding in Guanidinium Fluoride

O. D. Bonner

Department of Chemistry, University of South Carolina, Columbia, South Carolina 29208 *(Received May 26, 1977)*

Guanidinium fluoride was prepared and the osmotic and activity coefficients of aqueous solutions at 298.15 K are reported. A comparison of these data with those for solutions of other fluoride salts indicates a considerable degree of association and Raman spectra of the solutions show that the guanidinium ion protons are strongly hydrogen bonded. Infrared and Raman spectra of the solid guanidinium fluoride suggest the possibility that the guanidinium protons form bridges between the nitrogen and fluoride atoms with partial bonds to each atom.

Introduction

Guanidinium salts and urea are known to be effective protein denaturants but the mechanism of the denaturation process is incompletely understood. Spectral studies[1] and measurement of the colligative properties[2] of aqueous solutions have indicated that the guanidinium ion forms rather strong hydrogen bonds both with the chloride ion, when guanidinium chloride is the salt in question, and with the solvent. Since we have also determined[3] that the peptide carbonyl group is a very effective hydrogen bond acceptor, it is reasonable to expect that hydrogen bonding of the denaturant to the protein may be involved in the denaturation process. Recent evidence[3a] indicates, moreover, that denaturants possessing the $-NH_2$ group may successfully compete with water protons for hydrogen bonding sites in aqueous solutions.

These considerations induced us to investigate a system which may furnish an indication of the maximum strength possible for hydrogen bonds; a combination of the guanidinium ion which not only possess $-NH_2$ groups but also a positive charge and the fluoride ion having a very large negative charge density. The isopiestic equilibration technique was employed to measure the osmotic and activity coefficients of guanidinium fluoride solutions while Raman and infrared spectra of the solid salt were recorded.

Experimental Section

Sample Preparation. Guanidine carbonate, as supplied by Eastman Organic Chemicals Co., was twice recrystallized from methanol and was then allowed to react with a slight excess of diluted reagent grade hydrofluoric acid. The solution of guanidinium fluoride was concentrated by evaporation under vacuum and finally dried in vacuo. The dried salt was then recrystallized three times from anhydrous methanol and again dried in vacuo. The molecular weight of the pure sample was checked by ion-exchange methods. A sample of the salt was partially deuterated (~70% D) by three successive equilibrations with anhydrous CH_3OD.

Isopiestic Equilibration. The isopiestic equilibrations of guanidinium fluoride solutions vs. sodium chloride solutions as a reference were performed in the same manner as those of the other guanidinium salts which have been reported[2] recently.

Spectral Measurements. Raman spectra were recorded on a Cary Model 82 spectrophotometer equipped with a Coherent Radiation 53K krypton laser. The 6471-Å line furnished 600 mW power at the sample. The infrared spectra were recorded on a Perkin-Elmer Model 621 grating spectrophotometer. Mulls of the solids were prepared using carefully dried nujol and fluorolube LG-160 as supplied by Fisher Scientific Co.

TABLE I: Molalities of Isopiestic Solutions at 298.15 K

m_{NaCl}	m_{GuF}	m_{NaCl}	m_{GuF}	m_{NaCl}	m_{GuF}
0.1456	0.1492	1.797	2.210	3.976	5.577
0.3243	0.3427	1.951	2.424	4.242	6.022
0.4204	0.4502	2.064	2.583	4.489	6.447
0.5803	0.6340	2.328	2.965	4.932	7.210
0.948	1.087	2.649	3.450	5.225	7.699
1.127	1.315	2.922	3.870	5.668	8.480
1.241	1.463	3.138	4.208	5.888	8.870
1.434	1.712	3.490	4.793	6.089	9.226
1.631	1.980	3.726	5.175		

TABLE II: Osmotic and Activity Coefficients of Guanidinium Fluoride at 298.15 K

m	ϕ	γ
0.1	0.918	0.754
0.2	0.895	0.691
0.3	0.880	0.650
0.4	0.866	0.618
0.5	0.855	0.593
0.6	0.846	0.572
0.7	0.838	0.554
0.8	0.831	0.538
0.9	0.825	0.524
1.0	0.818	0.511
1.2	0.810	0.489
1.4	0.803	0.472
1.6	0.798	0.457
1.8	0.795	0.446
2.0	0.792	0.434
2.2	0.790	0.426
2.4	0.789	0.417
2.6	0.788	0.410
2.8	0.788	0.403
3.0	0.787	0.396
3.5	0.786	0.380
4.0	0.786	0.371
4.5	0.786	0.364
5.0	0.789	0.358
5.5	0.794	0.352
6.0	0.799	0.347
6.5	0.803	0.343
7.0	0.809	0.340
7.5	0.815	0.338
8.0	0.824	0.337
8.5	0.832	0.336
9.0	0.841	0.335
9.3	0.846	0.335

Results and Discussion

Isopiestic Experiments. The primary data are presented in Table I and the osmotic and activity coefficients

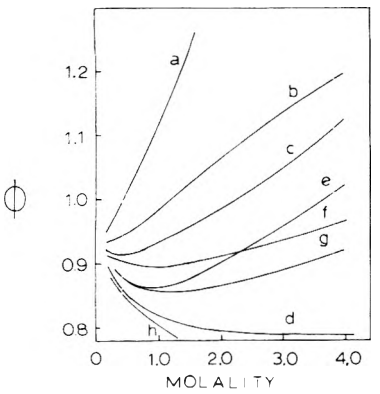

Figure 1. Osmotic coefficients of some fluoride and chloride salts: (a) $(CH_3)_4NF$, ref 6; (b) CsF, ref 7; (c) KF, ref 5; (d) GuF; (e) $(CH_3)_4NCl$, ref 8; (f) CsCl, ref 5; (g) KCl, ref 5; (h) GuCl, ref 2.

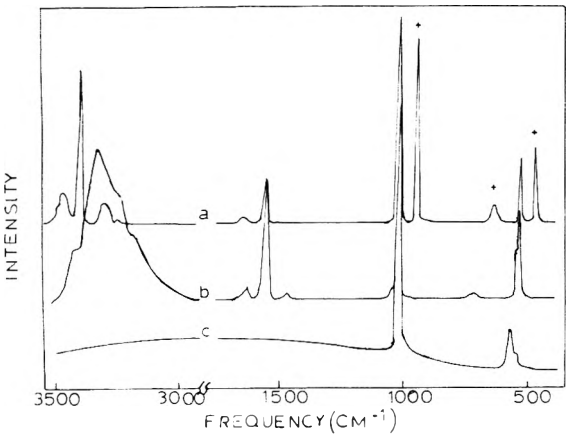

Figure 2. Raman spectra of solid guanidinium perchlorate, chloride, and fluoride: (a) $GuClO_4$; (b) GuCl; (c) GuF. (+) These bands arise from the perchlorate ion.

at rounded concentrations are given in Table II. Osmotic coefficients were calculated from the relationship

$$\phi = (m_{ref}/m)\phi_{ref}$$

activity coefficients were calculated from the equation[4]

$$\ln \gamma = \ln \gamma_{ref} + \ln (m_{ref}/m) + 2\int_0^{m\,ref}(m_{ref}/m - 1)\, d \ln (m\gamma)_{ref}^{1/2}$$

using an appropriate computer program. The values of the osmotic and activity coefficients of sodium chloride, the reference salt, are those of Robinson and Stokes.[5]

The osmotic coefficients of guanidinium fluoride in concentrated solutions are the largest of any of the guanidinium halides[2] but this observation should not be taken as evidence for a lesser degree of ion pairing. When one observes the spectacularly large coefficients (Figure 1) of cesium and tetramethylammonium fluorides (cations of size comparable to the guanidinium ion) it becomes obvious that the values less than unity which are observed for guanidinium fluoride are indeed due to ion association. The extent of this association cannot be accurately estimated, however, because of the compensating effect of ionic hydration. It was decided at this point that the crystalline state offered the best means of observing, at least qualitatively, the degree of ionic association.

Spectral Measurements. Infrared and Raman spectral data have been reported recently[1] for chloride and perchlorate salts of guanidinium ion. Hydrogen bonding of guanidinium and chloride ion was quite evident and a greater degree of association was expected for the fluoride salt. The Raman spectrum shown in Figure 2 was, however, entirely unexpected. There exists no trace of an

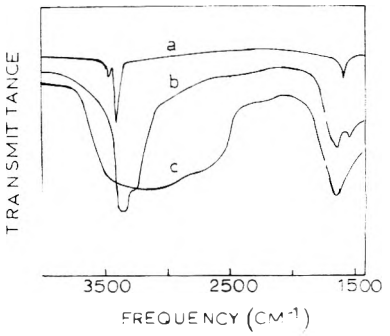

Figure 3. Infrared spectra of fluorolube mulls of guanidinium perchlorate, chloride, and fluoride: (a) $GuClO_4$; (b) GuCl; (c) GuF.

N–H stretching vibrational band in the 3000–3500-cm^{-1} region. Furthermore, the strong H–N–H scissors mode at about 1550 cm^{-1} is absent. The C–N stretching mode at about 1005 cm^{-1} is present and the low-frequency band which occurs at about 530 cm^{-1} for the chloride and perchlorate salt is shifted to about 570 cm^{-1} for the fluoride and considerably broadened. To further check the above observations the spectrum of a partially deuterated sample (~70% D) was recorded. No bands were observed above 920 cm^{-1}. This value agrees quite well with the observed band at 916 cm^{-1} for the deuterated chloride salt. The Raman spectrum of a 3 M aqueous solution of guanidinium fluoride showed a band in the N–H stretching region similar to that of the aqueous chloride salt but considerably broader with dual maxima at 3250 and 3375 cm^{-1}.

It was now obvious that the corresponding infrared spectra were essential. The spectra reported previously[1] for the chloride salt were those obtained from a KCl pellet. Unsuccessful attempts were made to prepare guanidinium fluoride pellets using NaF, CaF_2, and BaF_2. None of these pellets produced spectra of high quality. The hardness of the salts apparently prevented the obtaining of a transparent pellet. It was thus necessary to use mulls since pellets involving ions other than fluoride would be of no value. Fluorolube is transparent above 1500 cm^{-1} and was used for most of the reported mulls. Nujol has "windows" below 1500 cm^{-1} which enabled one to see the band at 1005 cm^{-1} which is very weak in the infrared although it is very intense in the Raman spectrum. Spectra of mulls of the perchlorate, chloride, and fluoride salts are shown in Figure 3. The perchlorate spectrum exhibits a very distinct band at 3394 cm^{-1} with a weaker band at 3454 cm^{-1} and a shoulder at 3380 cm^{-1}. The chloride N–H band is much broader with considerable absorbance between 3100 and 3500 cm^{-1} but a definite maximum absorbance occurs at 3396 cm^{-1} with a shoulder at 3300 cm^{-1}. The fluoride absorbance band on the other hand extends from about 2500 to 3650 cm^{-1} and is completely without distinguishing features. It is very difficult to exclude all traces of water from these mulls and it might be assumed that some of the absorbance in the high-frequency region may have this origin. This is, however, unlikely with the precautions which were taken and a more probable explanation would be the formation of partial H–F bonds. The H–F stretching frequency in the gas phase is[9] 3961.43 cm^{-1} and in the hydrogen bonded liquid[10] the broad band has its maximum at 3375 cm^{-1}. Water could certainly not be the cause of the absorbance in the 2400–3000-cm^{-1} range. A comparison of the infrared bands in the 1650-cm^{-1} region is also of interest. The perchlorate band is rather sharp with a maximum absorbance at 1584 cm^{-1}. The chloride band is split into two bands at 1536 and 1643 cm^{-1}. The fluoride band is quite broad with maximum absorbance at about 1660 cm^{-1}.

Conclusions

The absence of Raman bands in the N-H stretching and bending regions for solid guanidinium fluoride and the very broad and featureless band in the infrared extending from about 2500 to 3650 cm^{-1} indicates that the "hydrogen bonding" in this salt is quite different from that of the chloride salt. The chloride salt has been postulated from crystallographic data[11] to have C_{3v} symmetry. Each $-NH_2$ group has a one-third share of a chloride ion in the lattice structure. These spectroscopic data may be explained by assuming a similar structure for the fluoride salt except that in this instance it appears that the protons may form bridges between the nitrogen and fluoride atoms with partial bonds to each. The structure could be represented as

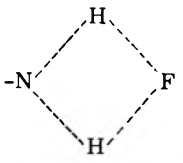

This structure would offer an explanation for the breadth of the $-NH_2$ band in the infrared with frequencies as low as 2500 cm^{-1}. The partial H-F bonds would also offer an explanation for the frequencies as high at 3650 cm^{-1}.

These experiments further emphasized the hydrogen bonding ability of the guanidinium ion and make more plausible the belief[3a] that the denaturation process for some proteins may involve hydrogen bonds between the denaturant and the peptide carbonyl group which is a better acceptor than the oxygen atom[3b] of the water molecule.

Acknowledgment. The author acknowledges the assistance of Mr. Barry J. Streusand who recorded the Raman spectra of guanidinium fluoride and its solutions.

References and Notes

(1) O. D. Bonner and C. F. Jordan, *Spectrochim. Acta, Part A*, **32**, 1243 (1976).
(2) O. D. Bonner, *J. Chem. Thermodyn.*, **8**, 1167 (1976).
(3) (a) O. D. Bonner, J. M. Bednarek, and R. K. Arisman, *J. Am. Chem. Soc.*, **99**, 2898 (1977); (b) O. D. Bonner and Y. S. Choi, *Spectrochim. Acta, Part A*, **31**, 1975 (1975).
(4) R. A. Robinson and D. A. Sinclair, *J. Am. Chem. Soc.*, **56**, 1830 (1934).
(5) R. A. Robinson and R. H. Stokes, "Electrolytic Solutions", 2nd ed, Academic Press, New York, N.Y., 1959.
(6) W. Y. Wen, S. Saito, and C. Lee, *J. Phys. Chem.*, **70**, 1244 (1966).
(7) H. Ti Tien, *J. Phys. Chem.*, **67**, 532 (1963).
(8) S. Lindenbaum and G. E. Boyd, *J. Phys. Chem.*, **68**, 911 (1964).
(9) W. F. Herget, W. E. Deeds, N. M. Gailar, R. J. Lovell, and A. H. Nielsen, *J. Opt. Soc. Am.*, **52**, 1113 (1962).
(10) R. M. Adams and J. J. Katz, *J. Opt. Soc. Am.*, **46**, 895 (1956).
(11) D. J. Haas, D. R. Harris, and H. H. Mills, *Acta Crystallogr.*, **19**, 676 (1965).

A Near Zero Coordinate Sodium Ion in Dehydrated Zeolite 4A, Na_{12}–A

V. Subramanian and Karl Seff*

Chemistry Department, University of Hawaii, Honolulu, Hawaii 96822 *(Received May 19, 1977)*

The crystal structure of dehydrated zeolite 4A, Na_{12}–A, stoichiometry $Na_{12}Al_{12}Si_{12}O_{48}$ per unit cell, has been redetermined from three-dimensional x-ray diffraction data collected by counter methods. At 25.5 °C the lattice constant, a, is 12.292(2) Å. All atoms in the structure were refined anisotropically in the cubic space group $Pm3m$ to a final weighted R index of 0.049. The twelve Na^+ cations are distributed over three crystallographically different sites: eight are on threefold axes near the centers of six-rings, three are on eight-ring planes, and the twelfth is loosely held in the large cavity on a twofold axis opposite a four-ring. Its nearest neighbors, each of which is about 2.33 Å away, are the four oxide ions of the nearest four-ring. This distance is 0.54 Å greater than the sum of the ionic radii of the oxide and sodium ions, and indicates the incipience of zero coordination. Fully zero coordinate K^+ and Rb^+ cations had previously been located in three zeolite A crystal structures; these ions are between 1.55 and 1.75 Å farther from their nearest neighbors than the sum of the appropriate ionic radii would indicate.

Introduction

To date, no more than seven cesium ions have been successfully ion-exchanged into Na_{12}–A[1,2] or K_{12}–A.[3] An attempt to prepare fully Cs^+-exchanged zeolite A by performing the following reaction intrazeolitically using a dehydrated crystal of Na_{12}–A was unsuccessful—cesium neither reacted nor was sorbed:

$$Cs + Na^+ \rightarrow Cs^+ + Na$$

However, the diffraction data set collected was nearly twice as large as that upon which the previously reported[4] structure of dehydrated 4A, Na_{12}–A, was based. As a result, new and interesting features of the structure are seen.

Monopositive cations of zero ligancy (K^+ [3,5] and Rb^+ [6]) or near zero ligancy (Tl^+,[7] Rb^+,[6] and Cs^+ [1,3]) have been found in ion-exchanged and dehydrated single crystals of zeolite A. This work confirms the existence of a near zero coordinate Na^+ ion in dehydrated zeolite 4A, stoichiometry $Na_{12}Al_{12}Si_{12}O_{48}$ per unit cell, the parent material and an item of commerce.

Experimental Section

A single crystal of Na_{12}–A approximately 85–90 μm on an edge was dehydrated for 2 days at 350 °C and 2×10^{-5} Torr, and was exposed at 150 °C to 7×10^{-3} Torr of cesium vapor, its equilibrium vapor pressure[8] at 125 °C. No obvious change in crystal color or form was observed. The capillary containing the crystal was sealed and removed from the vacuum system by torch.

Diffraction data were collected on a four-circle Syntex $P\bar{1}$ diffractometer, equipped with a pulse-height analyzer and a graphite monochromator, using Mo Kα radiation

TABLE I: Positional, Thermal, and Occupancy Parameters for Dehydrated Na_{12}-A[a]

	Wyckoff position	x	y	z	β_{11}	β_{22}	β_{33}	β_{12}	β_{13}	β_{23}	Occupancy factor
(Si, Al)	24(*k*)	0	1836(2)	3718(2)	32(2)	27(2)	17(2)	0	0	12(3)	1[b]
O(1)	12(*h*)	0	2277(6)	1/2	52(7)	48(7)	31(6)	0	0	0	1
O(2)	12(*i*)	0	2917(4)	2917(4)	77(8)	36(4)	36(4)	0	0	42(11)	1
O(3)	24(*m*)	1123(3)	1123(3)	3418(4)	48(3)	48(3)	42(4)	19(8)	0(5)	0(5)	1
Na(1)	8(*g*)	2014(3)	2014(3)	2014(3)	59(3)	59(3)	59(3)	31(6)	31(6)	31(6)	1
Na(2)	12(*i*)	0	4302(12)	4302(12)	141(27)	72(12)	72(12)	0	0	−38(33)	1/4
Na(3)	12(*j*)	2307(54)	2307(54)	1/2	157(63)	157(63)	51(58)	148(164)	0	0	1/12

[a] Positional and anisotropic thermal parameters are given × 10^4. Numbers in parentheses are the estimated standard deviations in the units of the least significant digit given for the corresponding parameter. See Figure 1 for the identities of the atoms. The anisotropic temperature factor = $\exp[-(\beta_{11}h^2 + \beta_{22}k^2 + \beta_{33}l^2 + \beta_{12}hk + \beta_{13}hl + \beta_{23}kl)]$. [b] Occupancy for (Si) = 1/2; occupancy for (Al) = 1/2.

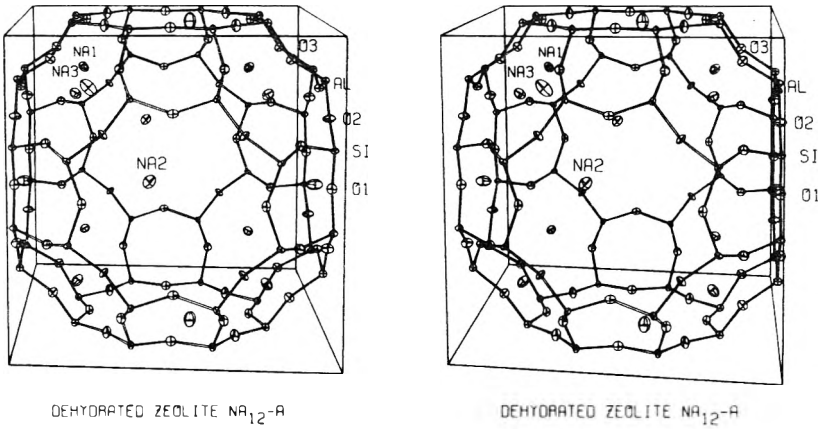

Figure 1. Stereoview[9] of dehydrated Na_{12}-A. Ellipsoids of 20% probability are shown.

($K\alpha_1$, λ 0.70930 Å; $K\alpha_2$, λ 0.71359 Å). The unit cell constant, *a*, determined by least-squares refinement of 15 intense reflections for which 19° < 2θ < 24°, is 12.292(2) Å at 25.5 °C. Data collection and reduction were done by methods described previously.[6a] Only those 288 reflections for which the net counts exceeded three times the corresponding esd's were used in structure solution and refinement.

Initial full-matrix least-squares refinement using the framework ((Si, Al), O(1), O(2), O(3)) coordinates, and those of the Na^+ ions in dehydrated zeolite 4A,[4b] led to the conventional error indices, $R_1 = \Sigma||F_o| - |F_c||/\Sigma F_o = 0.080$ and $R_2 = (\Sigma w(F_o - |F_c|)^2/\Sigma w F_o^2)^{1/2} = 0.067$. An ensuing Fourier function was nearly featureless, indicating the absence of cesium. Refining the ions on the threefold axes and in the eight-rings anisotropically further reduced R_1 to 0.061 and R_2 to 0.050, and the subsequent anisotropic refinement of Na(3), led to the final error indices, R_1 = 0.061 and R_2 = 0.049. The goodness-of-fit = $(\Sigma w(F_o - |F_c|)^2/(m - s))^{1/2}$ = 1.89, where *m* is the number of observations (288) and *s* is the number of variables in least-squares refinement (32). The final shifts in atomic parameters were all less than 0.4% of their corresponding standard deviations. The largest peak on the final difference Fourier synthesis (esd = 0.065 $e^-/Å^3$) was 0.8 $e^-/Å^3$ in height and was located at (0.0, 0.375, 1/2). When this peak was included in refinement as a sodium ion, it moved to within 1.74 Å of O(1) and its occupancy parameter approached zero, so it was rejected. Simultaneously, the occupancy of Na(2) approached four per unit cell, indicating that the trial position did not contain electron density deficient from Na(2). However, the number of Na^+ ions in the eight-rings cannot exceed three—apparently correlation with thermal parameters has led to this somewhat too-high result. The final positional, thermal, and occupancy parameters are presented in Table I.

TABLE II: Selected Interatomic Distances (Å) and Angles (deg)[a]

(Si,Al)-O(1)	1.666(3)
(Si,Al)-O(2)	1.653(3)
(Si,Al)-O(3)	1.676(2)
Na(1)-O(2)	2.931(4)
Na(1)-O(3)	2.319(5)
Na(2)-O(1)	2.632(11)
Na(2)-O(2)	2.408(22)
Na(3)-O(1)	2.84(7)
Na(3)-O(3)	2.83(7)
Na(3)-Na(1)	3.70(7)
Na(3)-Na(2)	5.11(7)
O(1)-(Si,Al)-O(2)	107.6(4)
O(1)-(Si,Al)-O(3)	112.2(3)
O(2)-(Si,Al)-O(3)	106.8(3)
O(3)-(Si,Al)-O(3)	110.9(5)
(Si,Al)-O(1)-(Si,Al)	142.0(3)
(Si,Al)-O(2)-(Si,Al)	165.1(3)
(Si,Al)-O(3)-(Si,Al)	144.3(2)
O(3)-Na(1)-O(3)	118.7(4)
O(1)-Na(2)-O(2)	64.0(4)
O(1)-Na(3)-O(3)	59(1)
O(1)-Na(3)-O(1)	86.5(8)
Na(1)-Na(3)-Na(1)	122(1)

[a] Numbers in parentheses are the estimated standard deviations in the units of the least significant digit given for the corresponding parameter.

Selected bond lengths and angles are given in Table II.

Discussion

Eight Na^+ ions at Na(1) lie on threefold axes of the unit cell near the six-ring planes, and approach the zeolite framework at a usual Na–O contact distance of 2.319(5) Å. Consistent with this location is the Na(1) thermal ellipsoid, which is smallest in the plane of its nearest six-ring neighbors and markedly longer normal to that plane (see Figure 1).

Three Na^+ ions at Na(2) lie in the planes of the eight-rings, but off their centers. Each of these is 2.41(2) Å from the nearest framework oxide ion at O(2) and 2.63(1) Å from two oxide ions at O(1). This coordination environment is unsatisfactory for the ion at Na(2), partly because its three ligand atoms are all to one side, not arranged around it. Also, these distances are somewhat greater than the sum of the ionic radii,[10] 2.30 Å. This is consistent with the near zero coordination found for the alkaline earth ions Ca^{2+} and Sr^{2+},[11] and the rare earth ion Eu^{2+},[12] located at similar sites in zeolite A which had been fully exchanged with the corresponding cation and dehydrated. The thermal ellipsoid for the ion at Na(2) is noticeably elongated perpendicular to the plane of the eight-ring in which its nearest neighbors lie, as was the case with the ion at Na(1), and seems reasonable.

All of the six-ring and eight-ring sites are occupied by the eleven Na^+ ions at Na(1) and Na(2). The twelfth cation per unit cell, needed to complete the balancing of the negative charge of the aluminosilicate framework, is located at Na(3) in the large cavity of the zeolite, on a twofold axis and opposite a four-ring, approximately as previously reported.[4b] Its nearest neighbors, all on one side, are two O(1) oxide ions at 2.83(7) Å and two O(2) oxide ions at 2.84(7) Å. These distances exceed the sum of the ionic radii of Na^+ and O^{2-} by about 0.54 Å. This Na^+ ion at Na(3) is therefore termed near zero coordinate, as was the case for one exchangeable ion per unit cell in dehydrated Tl_{12}–A.[7]

The magnitude and orientation of the thermal ellipsoid of the near zero coordinate sodium ion is completely consistent with its environment. Its shortest axis is limited by the confining repulsions it experiences from the two nearest Na(1) ions only 3.70(7) Å away and on opposite sides of the Na(3) position. Its intermediate axis is similarly limited by two ions farther away at Na(2). Its longest axis is normal to the four-ring plane, along the mean direction toward its four nearest oxide-ion neighbors. This motion is larger than that of any ion in the structure and indicates the presence of a shallow potential energy minimum for this ion along the twofold axis. This is consistent with the long near-zero-coordinate approach distances.

The ion at Na(3) is disordered within a 12-fold equipoint, but its environment is unambiguous. At any position it is near the middle of one edge of the cube of eight ions at Na(1), on a twofold axis, and opposite a four-ring. It has been assumed that the ions at Na(2) in the eight-rings nearest to Na(3) are as far as possible from the Na(3) cation, within the four equipoints available in each eight-ring.

The 3.70(7) Å Na(3)–Na(1) approach is short, and may be largely responsible for the shallowness of the Na(3) equilibrium position. As the ionic radius of the exchangeable cation increases, to that of a K^+ ion in K_{12}–A for example, the x coordinate of the ion at Na(1) must increase and the Na(1)–Na(3) distance must decrease. The position at Na(3) then becomes untenable, and the ion must locate elsewhere. In this situation, zero coordination can occur for one cation per unit cell, if it is an alkali metal ion larger than Na^+.[3,5,6]

The result that no cesium atoms exist within the crystal studied, and that the Na^+ ion positions differ only in their precision from those reported earlier,[4b] argues strongly that the zeolite is fully dehydrated in both cases. If water had remained in the zeolite, it would have reacted with the hot cesium vapor to form CsOH or Cs_2O whose Cs^+ ions would have been easy to locate within the zeolite, or the water could have been withdrawn from the zeolite to form one of those compounds outside the crystal, so that the sodium ion positions would have been altered. Because neither of these effects is observed, the dehydration conditions employed previously[4b] must have been adequate.

It is now clear that four of the twelve Na^+ ions per unit cell of this material, those at Na(2) and Na(3), were incorrectly located in a previous report.[4a] The coordinate found[4a] for the remaining eight of the twelve Na^+ ions, those at Na(1) on the threefold axis at 0.213(2), is more like that in hydrated Na_{12}–A,[13] 0.2128(4) (two times 0.1064(2) to convert from $Fm\bar{3}c$ to $Pm3m$), than to the value found here, 0.2014(3), or that reported previously,[4b] 0.200(1). The discrepancy between the values 0.213 and 0.2014 amounts to 0.25 Å. It appears, therefore, that the crystal studied by Smith and Dowell[4a] was at least partially hydrated.

Acknowledgment. This work was supported by the National Science Foundation (Grant No. CHE76-81586). We are also indebted to the University of Hawaii Computing Center.

Supplementary Material Available: A listing of the observed and calculated structure factors (Supplementary Table, 2 pages). Ordering information is given on any current masthead page.

References and Notes

(1) T. Blake Vance, Jr., and K. Seff, *J. Phys. Chem.*, **79**, 2163 (1975).
(2) The nomenclature refers to the contents of the unit cell. For example, Cs_7Na_5–A represents $Cs_7Na_5Al_{12}Si_{12}O_{48}$, exclusive of water molecules if a hydrated crystal is considered.
(3) R. L. Firor and K. Seff, *J. Am. Chem. Soc.*, **99**, 6249 (1977).
(4) (a) J. V. Smith and L. G. Dowell, *Z. Kristallogr.*, **126**, 135 (1968); (b) R. Y. Yanagida, A. A. Amaro, and K. Seff, *J. Phys. Chem.*, **77**, 805 (1973).
(5) P. C. W. Leung, K. B. Kunz, I. E. Maxwell, and K. Seff, *J. Phys. Chem.*, **79**, 2157 (1975).
(6) (a) R. L. Firor and K. Seff, *J. Am. Chem. Soc.*, **99**, 1112 (1977); (b) *ibid.*, **98**, 5031 (1976).
(7) R. L. Firor and K. Seff, *J. Am. Chem. Soc.*, **99**, 4039 (1977).
(8) "Comprehensive Inorganic Chemistry", Vol. 6, M. C. Sneed and R. C. Brasted, Ed., Van Nostrand, Princeton, N.J., 1957.
(9) C. K. Johnson, ORTEP, Report ORNL-3794, Oak Ridge National Laboratory, Oak Ridge, Tenn., 1965.
(10) "Handbook of Chemistry and Physics", 55th ed, Chemical Rubber Company, Cleveland, Ohio, 1975, p F-198.
(11) R. L. Firor and K. Seff, submitted for publication.
(12) R. L. Firor and K. Seff, *J. Am. Chem. Soc.*, **99**, 7059 (1977).
(13) V. Gramlich and W. M. Meier, *Z. Kristallogr.*, **133**, 134 (1971).

MINDO/2 Study of Equilibrium Carbon Vapor[1]

Z. Slanina and R. Zahradník*

J. Heyrovský Institute of Physical Chemistry and Electrochemistry, Czechoslovak Academy of Sciences, 12138 Prague 2, Czechoslovakia
(Received February 8, 1977)

Carbon atom aggregates, present at high temperatures in the gaseous phase above graphite, have been studied by means of the MINDO/2 method. This method has been used for generating all molecular constants needed for statistical-thermodynamic calculations of $\Delta H°_T$, $\Delta S°_T$, and log K for the nC(s) $\rightleftharpoons$ C_n(g) (n = 4–7) equilibria. Each of C_4–C_7 aggregates consists of at least two isomers; the most stable isomer is never a linear one. The plausibility of this finding is supported by the satisfactory agreement between the calculated and observed thermodynamic characteristics. MINDO/2 fails to agree with the experiment in case of the C_3 molecule, leading to a wrong symmetry group. The usefulness of the formerly suggested thermodynamic functions, based on estimated molecular constants, has been discussed.

Introduction

The subject of carbon vapor is of interest in several areas of chemistry and physics as well as in a variety of technologies.[2] It is well known that carbon vapor, usually produced by a discharge between graphite electrodes,[3] or by vaporizing carbon with electrical heating[4,5] or with a laser,[6] consists of the carbon species C_n.

Investigation of various chemically interesting problems[2,7,8] requires a knowledge of both the equilibrium composition of the gaseous phase above graphite and the structure of the constituents. The physical interest is largely connected with stellar[9] or flame spectra[10] in which lines have been observed that can be assigned to various carbon species. Composition of the vapor resulting from the ablation of carbonaceous bodies in extremely high temperature environments, especially the surfaces of atmospheric space reentry vehicles (carbonaceous heat shields)[9,11] is of technological interest. It has been shown recently that a correct description of homogeneous[12] and heterogeneous[13] systems involving carbon requires, at higher temperatures, explicit consideration of the C_n species. Their concentration at about 2000 K may be comparable with concentrations of other components. Physical-chemical analysis of all mentioned problems requires knowledge of the thermodynamic characteristics concerning the gas phase above graphite. It would be particularly useful to know the temperature dependences of $\Delta H°_T$ and $\Delta S°_T$. Attempts have been made to obtain these data along the following three lines: direct experiments, estimates based on analogies, and theoretical calculations (for a comprehensive review, see ref 2). Drowart et al.[14] using Knudsen effusion and mass spectrometry, produced relative ion intensity measurements for C_n, with n = 1 to 5, over a wide temperature range (1800–2700 K). In that work partial pressures were calculated for C_2, C_3, C_4, and C_5 relative to C_1 and upper limits for C_6 and C_7. Recently Zavitsanos and Carlson[15] experimentally obtained vapor pressures for C_1, C_2, C_3, and C_4 by the use of radiofrequency induction heating. These results[14,15] were treated further by means of the second and third law methods in order to obtain the respective $\Delta H°_T$ and $\Delta H°_0$ values. The free energy function, required by the latter method, had to be set up just on the basis of estimated molecular geometries and frequencies of vibrational modes.[16] A few different sets of $\Delta H°_T$ for graphite dissociation into C_n were obtained[2,17,18] from the same set of experimental data. The situation is satisfactory only with the three lowest members of the C_n series. Molecular constants of C_1, C_2, and C_3 needed for setting up partition functions are well known[17] and, due to Strauss and Thiele,[19] the vibrational–rotational effect has been exactly included into the entropy term of C_3. These calculated values fit very well recent experimental entropy data.[20] The situation with higher members of the series is less satisfactory, real knowledge of their structure being negligible. Estimates for C_n (n up to 10) made by Cowperthwaite and Bauer[21] are useful for thermochemical orientation. Pitzer and Clementi[22] treated, in a pioneering work, the set of C_n aggregates on the simple MO level. Heats of formation and thermodynamic functions for members of the series up to n = 17 were obtained. Strickler and Pitzer[23] later revised that treatment in order to satisfy newer experimental data.[14] Originally an assumption was made that the C_n systems were linear; in a newer paper[23] also cyclic structures were admitted. Hoffmann later performed an EHT study[24] of linear and cyclic C_n systems. Moreover, C_1–C_4 systems were treated on the ab initio level.[25,26]

It was only recently that methods were developed[27,28] for automatic molecular geometry optimization permitting, moreover, the analysis of the nature of stationary points on energy hypersurfaces. By means of such a procedure[28] the C_n aggregates (n = 1–7) have been investigated by the semiempirical MINDO/2 method.[29] Thermodynamic aspects of equilibrium in the ideal gas phase above graphite have been described using MINDO/2 molecular characteristics. The rigid rotator and harmonic oscillator (RRHO) approximation have been used for construction of partition functions.

Method

Calculations of thermodynamic characteristics of chemical equilibria, completely independent of any experimental information, assume connection of quantum chemical and statistical thermodynamic formalisms. Quantum chemical methods offer all the data necessary for setting up partition functions which permit the evaluation, in the next step, of all standard thermodynamic characteristics. MINDO/2 calculations[29] were combined, in case of molecules possessing a triplet ground state, with the restricted open shell "half-electron" method.[30,31] Molecular geometries of stationary points on MINDO/2 hypersurfaces of C_n (n = 2–7) were searched for by means of the automatic optimization procedure. For stationary points (i.e., minima and saddle points) all expressions $\partial E/\partial q_i$ (E represents the total energy of the system, and

TABLE I: A Survey of Fundamental Characteristics of Stationary Points Found on the C_n (n = 2 to 7) Energy Hypersurfaces

n	Point group	Type of stationary point[a]	$\Delta H_f^\circ{}_{298}$, kJ mol^{-1} MINDO/2	Exptl
2	$D_{\infty h}$	M	707.8	837.6[b]
3	D_{3h}	M[c]	867.7	820.1[b]
	C_{2v}	M	892.7	
	$D_{\infty h}$	S	965.8	
4	D_{2h}	M	929.7	970.7[b]
	D_2	M	977.1	
	D_{2h}	S	978.2	
	D_{4h}	S[c]	980.6	
	$D_{\infty h}$	S	1126.7	
	$D_{\infty h}$	S[c]	1138.9	
	D_{2d}	S	1209.3	
	T_d	M	1323.9	
5	D_{3h}	M	995.9	979.1[b]
	C_{4v}	S	1047.0	
	$D_{\infty h}$	M	1177.6	
	D_{5h}	S[c]	1271.7	
	T_d	S	1970.3	
6	C_{2v}	M	1116.2	≥1170[e]
	D_{6h}	S[c]	1203.6	
	$D_{\infty h}$	M[c]	1367.9	
	D_{3h}	S[c,d]	~2090	
7	D_{5h}	M	1187.1	≥1130[e]
	D_{7h}	S[c]	1271.0	
	$D_{\infty h}$	M	1424.1	
	D_{4h}	S[c,d]	~2500	

[a] M is a minimum on the potential energy surface, S a saddle point. [b] Taken from ref 17. [c] Triplet state. [d] Unsatisfactory SCF convergency. [e] $\Delta H_f^\circ{}_0$ were taken from ref 14.

q_i the coordinate of the ith nuclei) vanish. For both the restricted closed shell[29] and the restricted open shell[30,31] "half-electron" methods analytical expressions for the components of the energy gradient were used which were derived from the corresponding relations for the total energy under the assumption of a constant density matrix.[27,28] An analysis of eigenvalues and eigenvectors of the force constants matrix (belonging the stationary points) permits us to distinguish real minima and saddle points of the energy hypersurface.[32,33] The force constant matrices have been set up numerically by means of the finite difference method[32,33] and used, moreover, for performing the $\mathbf{G} \times \mathbf{F}$ matrix analysis.[34] This analysis, which supplies frequencies of normal vibrational modes in the harmonic approximation, has been performed with Cartesian coordinates. The evaluation of electronic partition functions (important for molecules having a triplet ground state) is based on energies of the respective electronically excited states. Their energies have been obtained within the framework of the one-electron approximation.[30,31]

Molecular constants calculated for all minima found have been exploited for setting up the partition functions in the RRHO approximations.[35] MINDO/2 heats of formation, valid for 298 K, were reduced to absolute zero by means of partition functions and used for determination of zero point energies for the following processes:

$$nC(s) \rightleftharpoons C_n(g) \quad (1)$$

The standard values of ΔH°_T, ΔS°_T, and ΔG°_T, for a given value of n, have been calculated for all minima on the C_n hypersurfaces. For the sake of correct comparisons between calculated and observed values, weighted contributions[36] of the individual isomers were used for calculating effective values which represent real partners to the effective values accessible from experiments. Thermodynamic functions of graphite, needed for description of equilibria 1, were taken from the literature.[17]

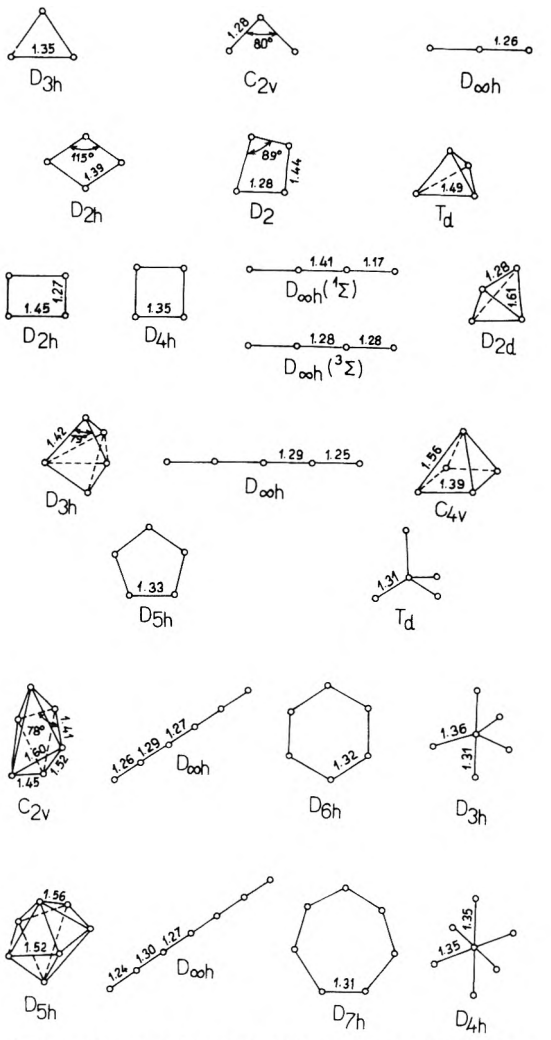

Figure 1. Formulas of stationary points found on the MINDO/2 energy hypersurfaces. The indicated bond lengths are given in 10^{-10} m.

Results and Discussion

First of all we had to find, within the framework of the MINDO/2 method, the stationary points on the individual C_n hypersurfaces. There does not exist any procedure which would permit us to say a priori how many stationary points occur on the given hypersurface. Therefore, it is necessary to vary systematically initial geometries within the optimization procedure. All possible symmetry groups for the C_n species have to be taken into consideration because the variable metric minimization procedure is symmetry conservative.[27] There is no experimental information available on geometry of aggregates with $n >$ 3 and, therefore, all described types of compounds possessing n atoms[37] were taken into consideration. Clearly enough, also previously intuitively chosen[23,24] linear and cyclic forms were included.

Stationary points of the C_n ($2 \leq n \leq 7$) hypersurfaces found are summarized in Table I. The nature of the individual points, presented in order of increasing energy, is specified. For the sake of completeness also experimental ΔH°_f values are given; a more careful comparison follows later. The representation of the symmetry group does not allow us, particularly with higher n, to assign the structure unequivocally. Hence the stationary points found are visualized in Figure 1; the indicated geometric parameters characterize the systems unambiguously. We are interested, in connection with the presently studied equilibrium processes, in real minima only. It is possible,

however, to distinguish between minima and saddle points only after having performed the diagonalization of the force constant matrix. In case of minima all eigenvalues of this matrix are positive; one negative eigenvalue is typical for saddle points. Their geometries and properties in general play a fundamental role in the absolute reaction rates theory.[38]

The C and C_2 systems lie out of the scope of applicability of the MINDO/2 method. Therefore only thermodynamic functions based either on experimental or SCF–CI characteristics are meaningful. The largest experimentally well-known system in the C_n series is the C_3 molecule. This system is linear in both the ground state ($^1\Sigma_g^+$) and first excited state ($^1\Pi_u$). The extremely low frequency[39] of the deformation mode, 63.1 cm^{-1}, represents quite an interesting spectroscopic and thermodynamic feature of it. Liskow et al.[40] have confirmed both the linearity and the unexpected frequency value by means of ab initio SCF calculations using extensive basis sets. These two independent pieces of information clearly prove the failure of MINDO/2 with this system. MINDO/2 gives two nonlinear minima and the linear form represents just a saddle point (cf. Table I). We have found,[41] qualitatively speaking, the same failure also with the CNDO/2 optimization. The only difference concerns the opposite order of stability of nonlinear systems. Failures of semiempirical methods with small rings, in particular with three-membered rings, are well known.[42-44] More specifically, e.g., CNDO/2 and MINDO/1 predict[45] for ozone point symmetry group D_{3h}. In fact, however, ozone deviates only slightly from linearity. The poor quality of MINDO/1 and MINDO/2 descriptions[29,42] of the strain in the cyclopropane ring is also well established. Keeping these findings in mind, the failure of MINDO/2 with nonlinear C_3 systems has to be expected. This failure prevents us from obtaining a reasonable thermodynamic function based on MINDO/2. Remarkably enough no satisfactory agreement was found between calculated and experimental[14,46] entropy values of C_3 in spite of the fact that the calculation was performed with partition functions[19] of nonrigid rotator and anharmonic oscillator. This lack of agreement incited the ab initio study by Liskow et al.[40] They supported the idea that the deformation vibration of C_3, connected with an unusually low frequency, possesses a key position in the calculation and suggested another possibility for the discrepancy found, namely, a possible inaccuracy of the experimental value. A recent experimental work[20] indeed supported this possibility. Let us add that a MINDO/2 calculation of the entropy (performed for the wrong symmetry group) of C_3 agrees very well with the newest experimental values.[20] This agreement is of course a warning: it is just accidental and is due to the fortunate compensation of rotational, vibrational, and electronic contributions to the total entropy.

The above discussed failure with C_3 makes urgent the question concerning the applicability of the semiempirical method with higher homologues. Analysis of MINDO/1 and MINDO/2 results[29,42] suggests that with five- and higher-membered cyclics a fair description of cyclic strain is to be expected. The decision in case of four-membered rings is somewhat complicated because of uncertainty concerning the symmetry of the main representative, i.e., cyclobutane.[47] Nevertheless it seems reasonable to consider the fair agreement[29] between MINDO/2 (the calculation was performed for the partially optimized molecular geometry of C_4H_8) and observed heat of formation as a support for using the MINDO/2 procedure with C_n aggregates containing larger than three-membered rings. The most stable structures in cases $n = 6$ and 7 appear to be structures made up also of three-membered rings. However, bond lengths of these three-membered rings are 0.06–0.25 $\times 10^{-10}$ m longer than those of C_3. The description of three-membered cyclic strain should therefore not be critical for C_6 and C_7. Nevertheless nonempirical checks of the stability of these structures appear desirable.

Furthermore, there exist reasons supporting the use of MINDO/2, as follows: (a) MINDO type methods frequently reproduce heats of formation better than semiquantitative methods, (b) in absence of OH and NH bonds, MINDO/2 molecular constants lead to approximately correct entropies,[48] (c) there does not exist any other semiempirical method which would satisfy better items a and b than MINDO/2 and, finally (d) it would be hardly possible to optimize geometries of all studied aggregates on the ab initio level. Let us add that during the period of this study the MINDO/3 method[49] was not available.

Basic information on C_4, C_5, C_6, and C_7 stationary points on the respective energy hypersurfaces are summarized in Table I and Figure 1. Of eight points found on the C_4 hypersurface whose first derivatives of energy vanish, only three have been identified as local minima. The energetically most favorable isomer appears to be a rhombus of D_{2h} symmetry, a further deformed cyclic of the D_2 symmetry, and an energetically rather unfavorable third isomer represented by a regular tetrahedron. Both linear stationary points (one being a singlet, and the other one a triplet) have been identified as saddle points. Analysis of the C_5 hypersurface gave five stationary points belonging to different symmetry groups. Just two represent real minima: the energetically lower lying trigonal bipyramid (D_{3h}), and a linear structure. Four stationary points have been found with the C_6 aggregate, two of them being minima possessing C_{2v} and $D_{\infty h}$ symmetry. The lowest-lying nonlinear structure is represented by a tetragonal bipyramid with C_{2v} symmetry only. The linear minimum seems to be the only minimum of all investigated which does not possess singlet multiplicity; according to calculations this ground state can be labeled as a $^3\Sigma_g^+$ triplet. Let us mention here that our molecular geometry for open shell cases may have an approximative character. Generally, the "half-electron" wavefunction is not variationally determined. The assumption of a constant density matrix, i.e., the fact that the energy is stationary with respect to LCAO expansion coefficients, is not valid in this case. However, we have found by comparing the approximate "half-electron" gradient with the one obtained numerically by finite differences that possible error in C_6 bond lengths should be smaller then 10^{-12} m. Finally, the situation with the C_7 molecule reminds us of that which has been found with C_6. Of the two minima found, the energetically lower lying D_{5h} symmetry (pentagonal bipyramid) is followed by the $D_{\infty h}$ species.

The results of extensive MINDO/2 geometry optimizations of the C_n aggregates ($n = 4$ to 7) have two common features: (a) the C_n aggregates consist of at least two isomers, (b) the energetically most favorable isomer is, in all cases, nonlinear. Both of these findings contradict accepted ideas about the structure of the C_n systems. The intuitively made assumption of the linearity of these systems forms, without exception, a basis for all performed calculations of statistical-thermodynamic functions; therefore it is implicitly involved in all experimental data which have been obtained by means of these thermodynamic functions. It is true particularly concerning results based on the third law analysis.

TABLE II: Comparison of Calculated and Observed Thermodynamic Characteristics of the $4C(s) \rightleftharpoons C_4(g)$ Reaction

Process	ΔH°_{2400}, kJ mol^{-1}	ΔS°_{2400}, J mol^{-1} K^{-1}	log K_p[a]
$4C(s) \rightleftharpoons C_4(g; D_{2h})$[b]	904.1	210.2	−8.700
$4C(s) \rightleftharpoons C_4(g; D_2)$[b]	952.2	213.6	−9.568
$4C(s) \rightleftharpoons C_4(g; T_d)$[b]	1301.5	205.5	−17.593
$4C(s) \rightleftharpoons C_4(g)$[b]	909.9	213.6	−8.645
$4C(s) \rightleftharpoons C_4(g)$[c]	946 ± 29	198 ± 13	−10.23

[a] K_p in atm. [b] MINDO/2 calculations. [c] Experimental values were taken from ref 14 and 17.

TABLE III: Comparison of Calculated and Observed Thermodynamic Characteristics of the $5C(s) \rightleftharpoons C_5(g)$ Reaction

Process	ΔH°_{2400}, kJ mol^{-1}	ΔS°_{2400}, J mol^{-1} K^{-1}	log K_p[a]
$5C(s) \rightleftharpoons C_5(g; D_{3h})$[b]	970.7	208.6	−10.231
$5C(s) \rightleftharpoons C_5(g; D_{\infty h})$[b]	1162.3	249.3	−12.276
$5C(s) \rightleftharpoons C_5(g)$[b]	972.4	209.4	−10.227
$5C(s) \rightleftharpoons C_5(g)$[c]	962 ± 21	208 ± 8	−10.07

[a] K_p in atm. [b] MINDO/2 calculations. [c] Experimental values were taken from refs 14 and 17.

The calculated molecular geometries and frequencies of harmonic vibrational modes permit us to evaluate the partition functions within the RRHO approximation and the reduction of $\Delta H_f^\circ{}_{298}$ to absolute zero. A straightforward calculation of all thermodynamic functions at any temperature can follow. This allows us to evaluate the characteristics of the individual equilibrium processes (1) under the assumption that the experimental thermodynamic functions of graphite[17] will be used. Three isomers (D_{2h}, D_2, T_d) have to be considered with the C_4 aggregate. Accordingly, three processes take place in the gas phase above graphite:

$$4C(s) \rightleftharpoons C_4(g; D_{2h}) \quad (2)$$

$$4C(s) \rightleftharpoons C_4(g; D_2) \quad (3)$$

$$4C(s) \rightleftharpoons C_4(g; T_d) \quad (4)$$

ΔH°_T, ΔS°_T, and log K_p have been calculated for each of these processes; the experimental value[14] of T has been used throughout (cf. Table II). Experimental analogues of these thermodynamic characteristics obtained[17] by means of the second law analysis originate from ref 14. In ref 14 the individual C_n aggregates were identified mass spectrometrically. This technique does not permit one to distinguish among the individual isomers of the C_4 system. Correct comparison between calculated and observed data requires one to sum up weighted contributions[36] for the isomers and to compare the resulting global values with experimental characteristics. Table II comprises also data on the global process

$$4C(s) \rightleftharpoons C_4(g) \quad (5)$$

Obviously, the MINDO/2 enthalpy of (5) is somewhat underestimated. The result is encouraging as far as entropy is concerned which implies that the structures of the isomers are plausible. Besides ref 14 the log K_p of (5) for T = 3003 K is available.[15] The trend is the same, when passing from the experimental (−6.209) to the MINDO/2 value (−4.685), as in ref 14.

We proceeded analogously with the C_5 aggregate, the respective characteristics being summarized in Table III. There is indeed a good agreement between calculated and observed ΔH° and ΔS° terms. The significant difference in entropies of the nonlinear and linear isomers deserves attention. It is seen from Table III that if only the linear C_5 isomer existed, the agreement between theoretical and experimental ΔS° values would be poor. This finding supports the prediction of nonlinearity of the most stable C_5 isomer made on total energy grounds. It is also seen that the linear isomer plays quite a small role at 2400 K.

TABLE IV: Comparison of Calculated and Observed Equilibrium Constants of the Reactions $6C(s) \rightleftharpoons C_6(g)$ and $7C(s) \rightleftharpoons C_7(g)$ at 2500 K

Product of sublimation	log K_p[a]	
	$6C(s) \rightleftharpoons C_6(g)$	$7C(s) \rightleftharpoons C_7(g)$
Nonlinear isomer[b]	−10.132	−12.754
Linear isomer[b]	−13.695	−15.161
Both isomers[b]	−10.131	−12.753
Experimental[c]	≤−11.83	≤−11.09

[a] K_p in atm. [b] MINDO/2 calculations. [c] Taken from ref 14.

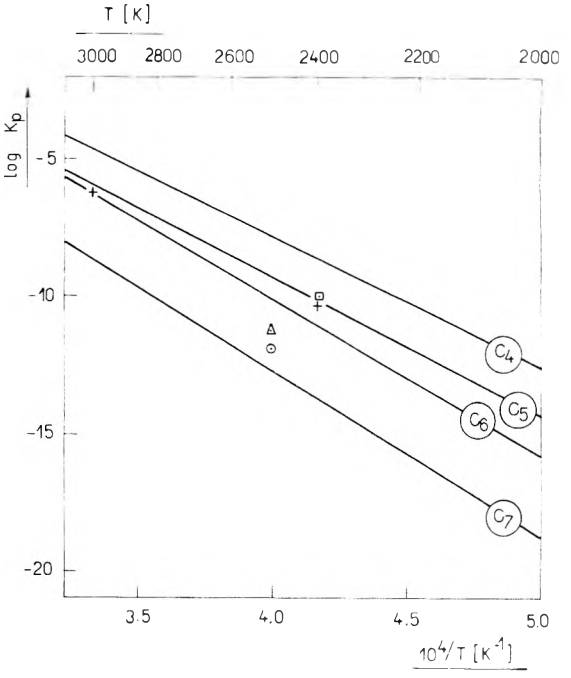

Figure 2. Temperature dependence of log K_p of the equilibria between graphite and C_4, C_5, C_6, and C_7 species calculated by means of the MINDO/2 characteristics. The indicated experimental data for C_4 (+) are taken from ref 15 and 17, for C_5 (□) from ref 17, for C_6 (○) and C_7 (△) from ref 14.

Experimental data on the thermodynamic behavior of the C_6 and C_7 aggregates are poorer. Only upper limits for the equilibrium constants of the respective processes are available in the literature.[14] Theoretical and experimental characteristics, for T = 2500 K, are compared in Table IV. It becomes clear from the log K_p values that, with these two homologues, even at high temperatures, the nonlinear isomer strongly dominates.

It can be stated (cf. Tables II–IV) that even at high temperatures the log K_p of the total process can be approximated by the value belonging to the most stable isomer. This is understandable if the pronounced differences in ΔH_f° of the individual isomers are considered. The influence of isomers with the individual C_n aggregates manifests itself most clearly in the entropy terms. A summary of information on the temperature dependences of equilibria 1 is presented in Figure 2. Table V comprises predicted standard values of heats and entropies of formation (298 K) for species $C_4(g)$ to $C_7(g)$.

In previous theoretical works,[22,23] periodicity in the stability of the C_n aggregates was found. Our results,

TABLE V: MINDO/2 Prediction of Standard Heats and Entropies of Formation of the $C_n(g)$ Species at 298.15 K[a]

Species	$\Delta H_f^\circ{}_{298}$, kJ mol^{-1}	$\Delta S_f^\circ{}_{298}$, J mol^{-1} K^{-1}
$C_4(g)$	929.7	225.2
$C_5(g)$	995.9	222.9
$C_6(g)$	1116.2	253.0
$C_7(g)$	1187.1	230.2

[a] Standard state: ideal gas at 1 atm pressure.

however, show a monotonic stability decrease with increasing n. It seems that the suggestion of stability oscillation according to the parity number n is rather due to the level of the quantum chemical method used.

The statistical thermodynamic description has been limited to the RRHO approximation. Except for diatomics, the present situation of quantum chemistry does not permit us to obtain information about the behavior of hypersurfaces in the vicinity of energy minima on a higher level of sophistication. It is desirable to know how the RRHO approximation manifests itself in the calculated equilibrium characteristics. Recently applicability of this approximation with an extensive set of reactions up to 2000 K has been reported.[50] The question is, however, whether the set of aggregates under study is comparable with the set tested.[50] Most serious deviation from the assume behavior is represented with C_3 by the anomalously high amplitude[51] of the bending vibration which is connected with strong anharmonicity.[40] According to results of Strauss and Thiele,[19] the RRHO approximation introduces into the entropy term of C_3 (2400 K) an error which in log K_p amounts to 0.9. The energy hypersurface of the C_3 molecule is quite exceptional; ab initio calculations[40] (4s 3p 1d basis set) show that the change of bond angle from 180 to 120° is connected, on the minimum energy path, with an extremely small potential energy change which amounts to about 100 cm^{-1}. We believe that the situation with higher homologues (C_4–C_7) differs dramatically from that of the C_3 molecule; according to MINDO/2 values, in their most stable forms, they are nonlinear and therefore the quite anharmonic potential described by Liskow et at.[40] should not play any important role with them. Thus we expect that our calculated MINDO/2 values of K_p are connected, due to the RRHO approximation, with errors which are smaller than one order of magnitude. The same error, roughly speaking, results from the substitution of accurate molecular constants in partition functions by MINDO/2 constants.[48] The question is whether these two sources of errors add or compensate themselves. Good agreement in the entropy term with C_4 and C_5 supports the latter possibility.

It has been already mentioned that a good reproduction of experimental entropies by means of entropies based on calculated characteristics represents just a necessary condition of the correctness of structure assignment. The most frequently used[17] thermodynamic functions of the C_5 molecule have been obtained in the following way: Starting from the linear assumption the bending frequencies have been adjusted in such a way that the partition function best fits the experimental entropy.[14] This procedure lead to $\Delta S^\circ{}_{2400} = 206.4$ J mol^{-1} K^{-1}. This value is close to the experimental one and our MINDO/2 values (see Table III). Therefore, thermodynamic functions[17] obtained by such a fitting are valuable for calculations, regardless of what the structure of C_5. However, at temperatures which differ considerably from the experimental temperature, the difference between values originating from various sources becomes serious. More specifically, e.g., at 298 K the MINDO/2 and the values based on linearity[17] amount to 222.9 and 213.4 J mol^{-1} K^{-1}, respectively (see Table V).

Summary and Conclusions

This paper deals with a MINDO/2 study of equilibria between graphite and carbon atom aggregates in the gas phase. Molecular geometry of these aggregates has been completely optimized by an automatic procedure; no a priori assumption have been made concerning their structure. Calculated molecular geometries, frequencies of harmonic vibrational modes, energies of electronically excited states, and heats of formation have been used for evaluation of thermodynamic characteristics of all components in the rigid rotator, harmonic oscillator approximation. Calculations performed concerned the C_2 to C_7 systems and special attention has been paid to the C_4 to C_7 systems. MINDO/2 failed in interpreting the geometry of the C_3 molecule: a cyclic instead of a linear structure has been obtained. This agrees with the well-known semiempirical overestimation of the stability of small cyclics.

It has been found theoretically that the C_n aggregates (n = 4 to 7) consist of at least two isomers belonging to different symmetry groups. This isomerism has been considered in the statistical thermodynamic treatment. In contradiction to earlier opinions our results suggest that the most stable forms of all homologues are nonlinear. The plausibility of this suggestion is supported by the good agreement found between calculated and observed thermodynamic characteristics of the C_4 and C_5 aggregates. This is, in particular, true about the entropy term. The finding of the nonlinearity of the C_4–C_7 systems makes the value of the all previously published thermodynamic functions based on the assumption of linearity, questionable. Simultaneously, however, nonempirical checks of the reliability of the MINDO/2 results appear desirable.

References and Notes

(1) Part IX in the series Calculations of Absolute Values of Equilibrium and Rate Constants; Part VIII: *Collect. Czech. Chem. Commun.*, **42**, 1 (1977).
(2) H. B. Palmer and M. Shelef, "Vaporization of Carbon" in "Chemistry and Physics of Carbon", Vol. 4, P. L. Walker, Ed., Marcel Dekker, New York, N.Y., 1968, p 85.
(3) O. Hahn, F. Strassmann, J. Mattauch, and H. Ewald, *Naturwissenschaften*, **30**, 541 (1942).
(4) W. A. Chupka and M. G. Inghram, *J. Chem. Phys.*, **21**, 371 (1953).
(5) R. E. Honig, *J. Chem. Phys.*, **22**, 126 (1954).
(6) P. D. Zavitsanos, *Carbon*, **6**, 731 (1968).
(7) J. Abrahamson, *Carbon*, **12**, 111 (1974).
(8) L. A. Shimp and R. J. Lagow, *J. Am. Chem. Soc.*, **95**, 1343 (1973).
(9) L. L. Danylewych and R. W. Nicholls, *Proc. R. Soc. London, Ser A*, **339**, 197 (1974).
(10) K. H. Becker, D. Haaks, and T. Tatarczyk, *Z. Naturforsch. A*, **29**, 829 (1974).
(11) V. H. Reiss, *J. Quant. Spectrosc. Radiat. Transfer*, **4**, 783 (1964).
(12) G. H. Neumann, *J. Fluorine Chem.*, 3, 209 (1973–1974).
(13) G. H. Neumann, *Z. Metal.*, **64**, 444 (1973).
(14) J. Drowart, R. P. Burns, G. De Maria, and M. G. Inghram. *J. Chem. Phys.*, **31**, 1131 (1959).
(15) P. D. Zavitsanos and G. A. Carlson, *J. Chem. Phys.*, **59**, 2966 (1973).
(16) R. H. Sanborn, *J. Chem. Phys.*, **49**, 4219 (1968).
(17) D. R. Stull and H. Prophet, *Natl. Stand. Ref. Data Ser., Natl. Bur. Stand.*, **No. 37** (1971).
(18) H. R. Leider, O. H. Krikorian, and D. A. Young, *Carbon*, **11**, 555 (1973).
(19) H. L. Strauss and E. Thiele, *J. Chem. Phys.*, **46**, 2473 (1967).
(20) F. M. Wachi and D. E. Gilmartin, *High Temp. Sci.*, **4**, 423 (1972).
(21) M. Cowperthwaite and S. H. Bauer, *J. Chem. Phys.*, **36**, 1743 (1962).
(22) K. S. Pitzer and E. Clementi, *J. Am. Chem. Soc.*, **81**, 4477 (1959).
(23) S. J. Strickler and K. S. Pitzer, "Energy Calculations for Polyatomic Carbon Molecules" in "Molecular Orbitals in Chemistry, Physics, and Biology", B. Pullman and P.-O. Löwdin, Ed., Academic Press, New York, N.Y., 1964.
(24) R. Hoffmann, *Tetrahedron*, **22**, 521 (1966).
(25) W. G. Richards, T. E. H. Walker, and R. K. Hinkley, "A Bibliography of ab initio Molecular Wave Functions", Clarendon Press, Oxford, 1971.
(26) H. Preuss and R. Janoschek, *J. Mol. Struct.*, **3**, 423 (1969).
(27) J. W. McIver and A. Komornicki, *Chem. Phys. Lett.*, **10**, 303 (1971).

(28) J. Pancíř, *Theor. Chim. Acta*, **29**, 21 (1973).
(29) N. Bodor, M. J. S. Dewar, A. Harget, and E. Haselbach, *J. Am. Chem. Soc.*, **92**, 3854 (1970).
(30) M. J. S. Dewar and N. Trinajstić, *Chem. Commun.*, 646 (1970).
(31) F. O. Ellison and F. M. Matheu, *Chem. Phys. Lett.*, **10**, 322 (1971).
(32) J. Pancíř, *Collect. Czech. Chem. Commun.*, **40**, 2726 (1975).
(33) J. W. McIver and A. Komornicki, *J. Am. Chem. Soc.*, **94**, 2625 (1972).
(34) B. E. Wilson, J. C. Decius, and P. C. Cross, "Molecular Vibrations", McGraw-Hill, New York, N.Y., 1955.
(35) R. Zahradník, Z. Slanina, and P. Čársky, *Collect. Czech. Chem. Commun.*, **39**, 63 (1974).
(36) Z. Slanina, *Collect. Czech. Chem. Commun.*, **40**, 1997 (1975).
(37) R. J. Gillespie, "Molecular Geometry", Van Nostrand-Reinhold, London, 1972.
(38) H. Eyring, *J. Chem. Phys.*, **3**, 107 (1935).
(39) G. Herzberg, "Molecular Spectra and Molecular Structure. III. Electronic Spectra and Electronic Structure of Polyatomic Molecules", Van Nostrand-Reinhold, New York, N.Y., 1966.
(40) D. H. Liskow, C. F. Bender, and H. F. Schaefer, III, *J. Chem. Phys.*, **56**, 5075 (1972).
(41) Z. Slanina, Thesis, Czechoslovak Academy of Sciences, Prague, 1974.
(42) N. C. Baird and M. J. S. Dewar, *J. Chem. Phys.*, **50**, 1262 (1969).
(43) L. L. Combs and M. Holloman, *Spectrosc. Lett.*, **5**, 319 (1972).
(44) L. L. Combs and M. Holloman, *Spectrosc. Lett.*, **6**, 257 (1973).
(45) A. K. Q. Siu and E. F. Hayes, *Chem. Phys. Lett.*, **21**, 573 (1973).
(46) R. J. Thorn and G. H. Winslow, *J. Chem. Phys.*, **26**, 186 (1957).
(47) L. S. Bartell and B. Andersen, *Chem. Commun.*, 786 (1973).
(48) Z. Slanina, P. Berák, and R. Zahradník, *Collect. Czech. Chem. Commun.*, **42**, 1 (1977).
(49) R. C. Bingham, M. J. S., Dewar, and D. H. Lo, *J. Am. Chem. Soc.*, **97**, 1285 (1975).
(50) Z. Slanina and R. Zahradník, *Collect. Czech. Chem. Commun.*, **39**, 729 (1974).
(51) C. F. Hansen, B. J. Henderson, and W. E. Pearson, *J. Chem. Phys.*, **60**, 754 (1974).

Dipole Moment of Cyclotriborazane

Donald R. Leavers

Behrend College, Pennsylvania State University, Erie, Pennsylvania 16510

and William J. Taylor*

Department of Chemistry, Ohio State University, Columbus, Ohio 43210 *(Received September 22, 1975; Revised Manuscript Received September 12, 1977)*

Publication costs assisted by the Department of Chemistry of the Ohio State University

Cyclotriborazane (CTB), $B_3N_3H_{12}$, has the *chair* conformation of cyclohexane, C_6H_{12}, but with symmetry C_{3v} rather than D_{3d}; CTB, unlike cyclohexane, may therefore possess a permanent dipole moment. From measurements of the dielectric constants and specific volumes of four solutions of CTB in *p*-dioxane we obtain 170.4 ± 6.3 mL mol^{-1} for the *partial molar polarization* of CTB at infinite dilution. With a correction of 30 ± 5 mL mol^{-1} for *distortion polarization*, the *apparent dipole moment* of CTB in solution is calculated to be 2.69 ± 0.11 D; a further correction for the *solvent effect* yields an estimate of 2.42 ± 0.16 D for the dipole moment of the *isolated* CTB molecule. This value is consistent (within their respective uncertainties) with the value of the dipole moment calculated from atomic charges estimated from x-ray intensities by Corfield and Shore. On the other hand, an unpublished ab initio SCF molecular orbital calculation by Ermler, Corliss, and Kern yields a much larger value, 5.58 D, for the dipole moment of CTB. It is concluded that the latter value is probably in error because of the use of a minimal basis set of Slater type orbitals, and the sensitivity of the result to small errors in the charges on the axial hydrogen atoms.

Introduction

Cyclotriborazane, $B_3N_3H_{12}$ (designated hereafter as CTB), is the analogue of cyclohexane, C_6H_{12}, in the boron–nitrogen system;[1,2] the two molecules are *isoelectronic*, and the x-ray diffraction study of crystalline CTB[3] shows that the molecule has the *chair* conformation of cyclohexane. The site group of the CTB molecule in the crystal is C_s but the molecule is only moderately distorted from C_{3v} symmetry; it seems safe to assume that the *isolated* molecule (e.g., in the gas phase) has strict C_{3v} symmetry, with the dipole moment along the threefold axis. The fact that relatively large dipole moments are observed for the amine–boranes[4] suggests that CTB may also have a sizable moment.

Although a great many methods for the measurement of molecular dipole moments now exist,[5] the low sublimation pressure of CTB[6] eliminates gas-phase methods, and we have therefore resorted to measurement of dielectric constants of solutions of CTB. Since CTB is slightly soluble in *p*-dioxane, the latter was selected as solvent and all measurements made at 41.1 °C; further details on the experimental methods may be found in the dissertation of Leavers.[7] The previously reported value of 3.2 D for the dipole moment of CTB[6] is significantly too large because of an error in the value of the parameter β^0 defined in the following section, and the omission of a correction for distortion polarization. In addition to rectifying these two deficiencies we have applied a correction for the *solvent effect*,[8] in order to obtain an estimate of the dipole moment of the *isolated* CTB molecule. Following the presentation of our results we discuss a previously unpublished ab initio molecular orbital calculation of the dipole moment of CTB by another group in the laboratory, as well as the information on atomic charges obtainable from the x-ray data.[3]

Rigorous Form of the Halverstadt–Kumler Equation

In the dielectric-constant-of-solutions method one calculates first the apparent molar polarizations, $\bar{P}_{2a}$, of the polar solute in a sequence of solutions of decreasing concentration, and extrapolates $\bar{P}_{2a}$ to zero solute concentration (or "infinite dilution") to obtain $\bar{P}_{2\infty}$. A *direct* extrapolation of $\bar{P}_{2a}$ is inaccurate, however,[9] and the dielectric constant, ϵ, and specific volume, v (or density) of the solution are commonly extrapolated *separately*, followed by calculation of $\bar{P}_{2\infty}$ from the Halverstadt–Kumler[10] (or Hedestrand[11]) equation. The significance of values of

TABLE I: Dielectric Constants and Specific Volumes of Solutions of Cyclotriborazane in *p*-Dioxane at 41.1 °C

N_2	ϵ	$\epsilon - \epsilon_{calcd}$	ν, mL g^{-1}	$\nu - \nu_{calcd}$, mL g^{-1}
0.003047	2.2122	−0.0003	0.98964	−0.00007
0.003798	2.2215	+0.0014	0.98965	+0.00010
0.005364	2.2340	−0.0020	0.98919	−0.00003
0.006888	2.2523	+0.0009	0.98871	−0.00019
0.006888			0.98909	+0.00019

$\bar{P}_{2\infty}$ obtained in this way has been questioned by Smith;[12,13] the problem has been reexamined by one of us on the basis of the theory of partial molar properties, and the following rigorous form of the Halverstadt–Kumler equation derived:[14]

$$\bar{P}_2^0 = \frac{3\alpha^0}{(\epsilon_1^0 + 2)^2}\tilde{V}_1^0 + \left(\frac{\epsilon_1^0 - 1}{\epsilon_1^0 + 2}\right)\bar{V}_2^0 \qquad (1)$$

Here $\bar{P}_2^0 = (\partial P/\partial n_2)_{n_1}^0$ is the *partial molar polarization* of the solute in its *standard state* of infinite dilution, which is exactly defined, and replaces the somewhat ambiguous quantity, $\bar{P}_{2\infty}$. The dielectric constant of pure solvent is denoted by ϵ_1^0, while $\alpha^0 = (d\epsilon/dN_2)^0$ is the derivative of the solution dielectric constant, ϵ, with respect to solute mole fraction, N_2, evaluated at $N_2 = 0$. The molar volume of pure solvent is represented by $\tilde{V}_1^0$, and $\bar{V}_2^0 = (\partial V/\partial n_2)_{n_1}^0$ is the partial molar volume of solute in its standard state. The latter may be computed from the relation

$$\bar{V}_2^0 = M_2\nu_1^0 + M_1\beta^0 \qquad (2)$$

where M_1 and M_2 are the molecular weights of solvent and solute, respectively, $\nu_1^0 = \tilde{V}_1^0/M_1$ is the specific volume of pure solvent, and $\beta^0 = (d\nu/dN_2)^0$ is the derivative of the specific volume of the solution, ν, with respect to N_2, evaluated at $N_2 = 0$. The present investigation will serve also as an example of the application of eq 1 and 2.

Dielectric Constant Measurements

The preparation and purification of CTB, and purification of the sample of *p*-dioxane used, as well as the experimental procedures for measurement of the dielectric constants of the solutions, have been described previously.[6,7] Table I gives, in the second column, the measured dielectric constants, ϵ, of four solutions having the mole fractions, N_2, of CTB shown in the first column; the uncertainties are estimated to be $\pm 5 \times 10^{-6}$ in the mole fractions, and ±0.0008 in ϵ. A linear relation, $\epsilon = \epsilon_1^{0'} + \alpha^0 N_2$, was fitted by the method of least squares to the values of ϵ in Table I, with equal weight assigned to each. The constants obtained were $\epsilon_1^{0'} = 2.1817 \pm 0.0021$ and $\alpha^0 = 10.12 \pm 0.42$, with *probable* errors calculated from the equations of Birge.[15] The deviations of the observed values of ϵ from the linear relation are shown in the third column of Table I; the rms deviation is ±0.0013. The least-squares value of $\epsilon_1^{0'}$, or *extrapolated* value of ϵ at $N_2 = 0$, is in excellent agreement with the value $\epsilon_1^0 = 2.182 \pm 0.003$ for pure *p*-dioxane selected for the calibration of the cell.[16] In the subsequent calculations we have used the values

$$\epsilon_1^0 = 2.182 \pm 0.003 \qquad (3a)$$

$$\alpha^0 = 10.12 \pm 0.42 \qquad (3b)$$

Volumetric Data

The specific volumes of the four solutions of CTB in *p*-dioxane used for the dielectric constant measurements were measured, using a calibrated pycnometer of volume 24.600 mL (at 20 °C), and are given in the fourth column of Table I. The final value in this column is the result of a second measurement on the solution of highest concentration using another pycnometer of volume 24.898 mL. These data were fitted by least squares to the linear relation $\nu = \nu_1^{0'} + \beta^0 N_2$, yielding the following values for the constants and probable errors:[15,17]

$$\nu_1^{0'} = (0.99035 \pm 0.00018)\ \text{mL g}^{-1} \qquad (4a)$$

$$\beta^0 = -(0.211 \pm 0.033)\ \text{mL g}^{-1} \qquad (4b)$$

The deviations of the observed values of ν from this relation are given in the final column of Table I; the rms deviation is ±0.00013 mL g^{-1}. We have taken for the specific volume of the solvent, ν_1^0, the *intercept*, $\nu_1^{0'}$, of the least-squares line, as given by eq 4a.[18]

The molar volume of the pure solvent at 41.1 °C, as obtained from eq 4a and $M_1 = 88.107$, is

$$\tilde{V}_1^0 = (87.26 \pm 0.02)\ \text{mL mol}^{-1} \qquad (5a)$$

Substitution of M_1, $M_2 = 86.546$, and eq 4 into eq 2, yields for the partial molar volume of CTB, at infinite dilution in *p*-dioxane and 41.1 °C:[20]

$$\bar{V}_2^0 = (67.1 \pm 2.9)\ \text{mL mol}^{-1} \qquad (5b)$$

Apparent Dipole Moment of Cyclotriborazane at Infinite Dilution

The partial molar polarization of CTB at infinite dilution, as obtained by substitution of eq 3 and 5 into eq 1, is[20] $\bar{P}_2^0 = (170.4 \pm 6.3)$ mL mol^{-1}. It is necessary to estimate the *distortion polarization*[21] of the CTB molecule. The electronic polarization of the isoelectronic cyclohexane molecule, as calculated from the refractive index and molar volume of the liquid at 20 °C, is 27.73 mL mol^{-1}; increasing this by the usual 5–15% to allow for atomic polarization yields 30.5 ± 1.4 mL mol^{-1} for the distortion polarization of the cyclohexane molecule. Since no refractive index data are available for CTB, we adopt an estimate of $\bar{P}_{2d} = (30 \pm 5)$ mL mol^{-1} for the distortion polarization of CTB. Substitution of these values of $\bar{P}_2^0$ and $\bar{P}_{2d}$ (and $T = 314.3$ K) into eq 17 of ref 14 yields for the *apparent* dipole moment of the CTB molecule at infinite dilution in *p*-dioxane solution:[22]

$$\mu_s^0 = (2.69 \pm 0.11)\ \text{D} \qquad (6)$$

Correction for Solvent Effect

The dipole moment, μ, of a polar solute molecule (at infinite dilution) has associated with it a field which may be expected to induce dipoles in the surrounding solvent molecules. If the mean vector sum of the induced dipoles is colinear with the dipole of the solute molecule, we need consider only its *scalar* value, μ_i, and the apparent dipole moment of the solute molecule at infinite dilution will be $\mu_s^0 = \mu + \mu_i$. The problem of calculating μ_i has been treated by Higasi;[23] for the case of a point dipole, μ, at the center of a solute molecule having the form of an *oblate* spheroid immersed in a solvent of dielectric constant ϵ_1^0, $\mu_i = A\mu$, where

$$A = \left(\frac{\epsilon_1^0 - 1}{\epsilon_1^0 + 2}\right)\left\{\left(\frac{3k^2}{k^2 - 1}\right)[1 - (k^2 - 1)^{-1/2}\arcsin(1 - k^{-2})^{1/2}] - 1\right\} \qquad (7)$$

with k the ratio of the major to the minor semiaxis for the spheroid. Finally

$$\mu = (1 + A)^{-1}\mu_s^0 \qquad (8)$$

The atomic coordinates for crystalline CTB,[3] combined with an approximate van der Waals radius of 1 Å for the

TABLE II: Gross Atomic Charges and Dipole Moment for Cyclotriborazane from a Molecular Orbital Calculation

Atom triad	Coordinates[a]		Orbital exponents			Gross atomic charge	$\Delta\mu$(D) = 4.803 $(3qz)$
	z, Å	ρ, Å	1s	2s	2p		
H_a(B)	−1.420	1.500	1.080			−0.1674	+3.43
B	−0.234	1.537	4.683	1.428	1.449	+0.1664	−0.56
H_e(N)	−0.125	2.420	1.246			+0.1894	−0.34
N	+0.234	1.462	6.672	2.019	2.061	−0.1351	−0.46
H_e(B)	+0.260	2.640	1.080			−0.2049	−0.77
H_a(N)	+1.240	1.550	1.246			+0.1517	+2.71

[a] θ = 0, 120, 240° for B, H_a(B), and H_e(B); θ = 60, 180, 300° for N, H_a(N), and H_e(N).

H atom, indicate that the isolated molecule (of symmetry C_{3v}) may be approximated as an oblate spheroid of minor semiaxis 2.2 Å (parallel to the threefold axis) and major semiaxis 3.5 Å.[7] Substitution of $k = 1.6 \pm 0.2$ and $\epsilon_1^0 = 2.182$, in eq 7 yields $A = 0.11 \pm 0.03$; combining this result with eq 6 and 8, we obtain as our estimate of the dipole moment of the *isolated* CTB molecule[22]

$$\mu = (2.42 \pm 0.16)\ \text{D} \tag{9}$$

Dipole Moment and Atomic Charges from Other Sources

An unpublished self-consistent field (SCF) molecular orbital (MO) calculation for the CTB molecule by Ermler, Corliss, and Kern has been referred to briefly in ref 3, p 1487. We are indebted to Dr. Ermler for supplying the more detailed information given in Table II. The atomic coordinates used were the best estimates of Corfield and Shore[3] for the isolated molecule having C_{3v} symmetry, with the corrections described in footnote 36 of ref 3. They are tabulated as cylindrical polar coordinates, in columns 2 and 3 of Table II. The cylinder axis, z, coincides with the threefold rotation axis, ρ is the perpendicular distance from this axis, and θ the angle of rotation about this axis (the plane midway between the planes of the B and N atoms is arbitrarily assigned the value $z = 0$). Each row of Table II refers to a triad of atoms which are equivalent under the operations of the point group C_{3v}. The triads are indicated by the symbols in the first column of Table II, where the subscripts a and e distinguish *axial* and *equatorial* H atoms, respectively, while the atom to which a H atom is bonded is indicated in parentheses. The values of the orbital exponents, ζ, in the minimal basis set of *Slater-type orbitals* (STO) are given in columns 4–6 of Table II; they are identical with a set of optimized orbital exponents obtained by Palke in a similar calculation for BH_3NH_3 (ref 24, Table II).

The expectation value of the dipole moment operator is given by

$$\langle\mu\rangle = \sum_s Z_s z_s - 2\sum_i \langle\varphi_i|z|\varphi_i\rangle \tag{10}$$

where the first sum extends over the nuclei and the second sum over the n doubly occupied MO's, φ_i; Z_s is the atomic number of the sth nucleus, z_s is its coordinate, and z is the coordinate of a typical electron. In the SCF MO procedure, in the LCAO approximation, each MO is determined as a linear combination of atomic orbitals (AO), χ_k:[25]

$$\varphi_i = \sum_k c_{ki}\chi_k \qquad (i = 1, \ldots, n) \tag{11}$$

Substitution of eq 11 into 10 yields

$$\langle\mu\rangle = \sum_s Z_s z_s - 2\sum_{kl} \rho_{kl}\langle\chi_l|z|\chi_k\rangle \tag{12}$$

where[26]

$$\rho_{kl} = \sum_i c_{ki}c_{li} \tag{13}$$

The value of $\langle\mu\rangle$ calculated for CTB from eq 12 and 13 is

$$\langle\mu\rangle = 2.194\ \text{au} = 5.58\ \text{D} \tag{14}$$

The preceding value of $\langle\mu\rangle$ is more than twice as large as the experimental value (corrected for solvent effect) given in eq 9. Some insight into possible causes of this disagreement is provided by an approximate analysis of the contribution of individual atomic charges to the dipole moment. The total number of electrons can be analyzed as follows:

$$2n = 2\sum_k \rho_{kk} + 4\sum_{k}\sum_{l>k} \rho_{kl}S_{lk} \tag{15}$$

where $S_{kl} = S_{lk} = \langle\chi_k|\chi_l\rangle$ is the overlap integral between χ_k and χ_l. On the basis of eq 15, one may adopt the view that $2\rho_{kk}$ electrons are to be assigned to the AO χ_k, and $4\rho_{kl}S_{lk}$ to an *overlap* population shared by χ_k and χ_l.[26] Alternatively, following Mulliken,[27] one may allot half of the overlap population to χ_k (and the other half to χ_l), and define the *gross* number of electrons in the kth AO as

$$q_k = 2\rho_{kk} + 2\sum_{l\neq k} \rho_{kl}S_{lk} \tag{16}$$

The *gross charge* (in atomic units) on the sth atom is then

$$q_s = Z_s - \sum_{k\subset s} q_k \tag{17}$$

where the first term on the right-hand side represents the nuclear charge, and the sum extends over those AO's centered on the sth nucleus. The gross atomic charges calculated from eq 17 for a typical atom of each triad in CTB are given in column 7 of Table II; a *negative* value of q_s (there denoted by q) corresponds to an *excess*, and a *positive* value of q_s to a *deficiency*, of electrons. Finally, the *total* dipole moment of CTB may be approximated as

$$\mu \cong \sum_s q_s z_s \tag{18}$$

where the sum extends over all atoms. The final column of Table II gives the contribution of each triad of equivalent atoms to the sum in eq 18.[28] The dipole moment calculated from eq 18 for CTB is 4.01 D.

Information on the atomic charges having a partly experimental and partly theoretical basis has been obtained by analysis of the x-ray diffraction intensities from a single crystal of CTB by Corfield and Shore.[3] A sequence of nine such adjustments is presented in Table I of ref 3, differing in the values assigned to several parameters; the *average* atomic charges, and rms deviations from these averages, are given in the third column of Table III of the present paper. The fourth column of Table III lists the contribution of each triad of atoms to the dipole moment, and its rms deviation, as calculated from the preceding charges and z coordinates. The sum of these contributions (with an uncertainty estimated from the propagation-

TABLE III: Atomic Charges and Dipole Moment for Cyclotriborazane from X-Ray Diffraction Intensities

Atom triad	z, Å	Atomic charge and rms deviation	$\Delta\mu$(D) = 4.803(3qz)
H_a(B)	−1.420	−0.29 ± 0.14	+5.9 ± 2.9
B	−0.234	+0.69 ± 0.16	−2.3 ± 0.5
H_e(N)	−0.125	+0.09 ± 0.04	−0.16 ± 0.07
N	+0.234	−0.29 ± 0.10	−1.0 ± 0.3
H_e(B)	+0.260	−0.29 ± 0.14	−1.1 ± 0.5
H_a(N)	+1.240	+0.09 ± 0.04	+1.6 ± 0.7

of-error equation) is 2.9 ± 3.1 D.

Discussion

The error estimate of ±7% for our experimental value of μ, as given in eq 9, is based on the *precision* of the data (with allowance, also, for uncertainties in the corrections for distortion polarization and solvent effect). An estimate of the probable error inclusive of *systematic* errors may be arrived at by comparison of experimental results obtained by the present method with those obtained for the same molecules in the gas phase;[29] on this basis, it seems justified to conclude that the overall error in our experimental value, μ = 2.42 D, is unlikely to exceed ±15%, and is almost certainly less than ±25%.

We discuss next possible reasons for the marked lack of agreement of the SCF MO value, $\langle\mu\rangle$ = 5.58 D, with our experimental value. Experience has shown that Hartree–Fock (HF) values of the dipole moment have a reliability of only about 1 D (see ref 30, p 241); the error in the HF values is due to neglect of electron correlation. A *minimal* basis set, such as that used in the SCF MO calculation of Ermler et al., cannot be counted upon to yield dipole moments which are close to the HF limit (ref 30, pp 78–81); in fact, errors of 2 or 3 D in calculated dipoles are not exceptional. Examination of the final column of Table II shows that, in the approximation in which the dipole moment is estimated from the gross atomic charges (see eq 18), the H atoms of the CTB molecule contribute 5.0 D (primarily because of the large separation and opposite charge of the axial H atoms bonded to B and N atoms), while the contribution of the B and N atoms, −1.0 D, is not only much smaller but of *opposite sign*. Thus, in this minimal-basis calculation the dipole moment is dominated by the charges on the H atoms, and is sensitive to errors in these charges, while the charges on the B and N atoms play a subsidiary role.

Another factor disposing the minimal-basis calculation for CTB to error is the *unbalanced* character of the basis, in the sense defined by Mulliken;[31] the result is a tendency to put too many electrons on the B atoms, and too few on the N atoms.[32] The x-ray diffraction results in Table III support this view, as they yield charges of 0.69 ± 0.16 and −0.29 ± 0.10 atomic units for the B and N atoms, respectively, compared with 0.166 and −0.135 from the SCF calculation of Table II. Correspondingly, the x-ray data yields −3.3 ± 0.6 D, rather than the SCF MO value of −1.0 D, for the contribution of the B_3N_3 ring to the dipole moment of CTB. An increase in the magnitude of this contribution, which is directed *oppositely* to the larger contribution of the H atoms, would yield a smaller overall dipole moment for the CTB molecule, bringing the SCF value into better agreement with our experimental value of 2.42 D.

Acknowledgment. The authors are grateful to Professor Sheldon G. Shore for making his laboratory facilities available, and for helpful advice during the synthesis of the CTB sample used in this investigation. We also express our appreciation to Professor C. William Kern and Dr. Walter C. Ermler for permission to publish the portions of their SCF MO calculation relevant to the dipole moment of CTB. However, the authors are solely responsible for the discussion of this calculation in the present paper.

References and Notes

(1) G. H. Dahl and R. Schaeffer, *J. Am. Chem. Soc.*, **83**, 3032 (1961).
(2) S. G. Shore and C. W. Hickam, *Inorg. Chem.*, **2**, 638 (1963).
(3) P. W. R. Corfield and S. G. Shore, *J. Am. Chem. Soc.*, **95**, 1480 (1973).
(4) J. R. Weaver and R. W. Parry, *Inorg. Chem.*, **5**, 713 (1966).
(5) A. L. McClellan, "Tables of Experimental Dipole Moments", Vol. 1, W. H. Freeman, San Francisco, Calif., 1963; Vol. 2, Rahara Enterprises, El Cerrito, Calif., 1974.
(6) D. R. Leavers, J. R. Long, S. G. Shore, and W. J. Taylor, *J. Chem. Soc. A*, 1580 (1969).
(7) D. R. Leavers, Ph.D. Dissertation, Ohio State University, 1971, Chapter 3.
(8) C. P. Smyth, "Dielectric Behavior and Structure", McGraw-Hill, New York, N.Y., 1955, pp 39–51.
(9) J. W. Smith, "Electric Dipole Moments", Butterworths, London, 1955, pp 52–55.
(10) I. F. Halverstadt and W. D. Kumler, *J. Am. Chem. Soc.*, **64**, 2988 (1942), eq 5.
(11) G. Hedestrand, *Z. Phys. Chem. B*, **2**, 428 (1929), eq 8.
(12) J. W. Smith, *Sci. Prog.*, **36**, 483 (1948).
(13) J. W. Smith, *Trans. Faraday Soc.*, **48**, 802 (1952).
(14) W. J. Taylor, *J. Phys. Chem.*, **79**, 1817 (1975).
(15) R. T. Birge, *Phys. Rev.*, **40**, 207 (1932).
(16) A. A. Maryott and E. R. Smith, *Natl. Bur. Stand. Circ.* **No. 514**, 12 (1951).
(17) The erroneous value of β^0 inadvertently used in ref 6 was based on a single preliminary measurement of specific volume.
(18) The extrapolated value is in relatively good agreement with the value 0.9900 mL g^{-1} for pure *p*-dioxane at 41 °C calculated from the data of Herz and Lorentz.[19]
(19) W. Herz and E. Lorentz, *Z. Phys. Chem. A*, **140**, 406 (1929).
(20) The probable errors of $\bar{V}_2^0$ and $\bar{P}_2^0$ have been estimated on the assumptions that the errors of ν_1^0, β^0, ϵ_1^0, and α^0 are distributed normally and are uncorrelated.
(21) R. J. W. LeFèvre, "Dipole Moments", 2nd ed, Methuen, London, 1948, pp 10–13.
(22) In estimating the error in eq 6 from those in $\bar{P}_2^0$ and $\bar{P}_{2d}$, and also the error in eq 9 from those in eq 6 and A, we have assumed the *least favorable* combination of errors.
(23) K. Higasi, *Sci. Pap. Inst. Phys. Chem. Res. (Jpn.)*, **28**, 284 (1936), eq 18.
(24) W. E. Palke, *J. Chem. Phys.*, **56**, 5308 (1972).
(25) C. C. J. Roothaan, *Rev. Mod. Phys.*, 23, 69 (1951).
(26) W. J. Taylor, *Phys. Rev.*, **87**, 214 (1952).
(27) R. S. Mulliken, *J. Chem. Phys.*, **23**, 1833 (1955).
(28) If z_s in eq 18 is in Å, as in Table II, one must multiply the right-hand side by 4.803 to obtain μ in debyes.
(29) See Table 18.1, p 48 of ref 8, and Table 12, p 129 of ref 9.
(30) H. F. Schaefer, III, "Electronic Structure of Atoms and Molecules: A Survey of Rigorous Quantum Mechanical Results", Addison-Wesley, Reading, Mass., 1972.
(31) R. S. Mulliken, *J. Chem. Phys.*, **36**, 3428 (1962).
(32) C. W. Kern, R. M. Pitzer, and O. J. Sovers, *J. Chem. Phys.*, **60**, 3883 (1974).

Longitudinal Acoustic Vibrational Mode of *n*-Paraffins and Tetraalkylammonium Ions and Estimation of Their Molecular Dimension

Hiroyasu Nomura,* Shinobu Koda, Fumio Kawaizumi, and Yutaka Miyahara

Department of Chemical Engineering, Synthetic Chemistry, Faculty of Engineering, Nagoya University, Chikusa-ku, Nagoya-shi, 464 Japan
(Received June 6, 1977)

Using a laser Raman spectrometer, the longitudinal acoustic (LA) modes are measured for *n*-paraffins in the solid and liquid states, and on five types of tetraalkylammonium bromide in the solid and dissolved states. A slight deviation from the linear relation between the frequency of LA band and the reciprocal carbon number is observed for *n*-paraffins having small carbon numbers. This deviation is due to the changes of (E/ρ), where E is Young's modulus and ρ the density. LA bands of tetraalkylammonium bromides in the dissolved state do not differ much from those in the solid state. For tetramethylammonium and tetrapropylammonium bromides, splitting of the LA modes into two bands is observed. The ionic dimensions of tetraalkylammonium cations are calculated from the frequencies of their LA modes. The values of ionic radius thus obtained are compared with those determined by various methods and found to be reasonable.

Introduction

It has been reported that the Raman spectrum of solid *n*-paraffins contains in the low frequency region 26–500 cm^{-1} a peak whose fundamental frequency is inversely proportional to the chain length.[1-3] These observations can be interpretated by an elementary theory of longitudinal vibration, in which the carbon chain is treated as a solid rod and the frequency ν is given by the equation

$$\nu = \frac{m}{2l}\left(\frac{E}{\rho}\right)^{1/2} \quad (1)$$

where l is the length of the rod; E, Young's modulus; ρ, the density; and m, the vibration order. The values of Young's modulus for a methylene chain given by eq 1 are in close agreement with those determined by the different methods.[4,5] This fact shows the validity of the vibration theory expressed by eq 1. For chains with less than about 18 carbons, however, the simple relation of eq 1 does not hold exactly and an empirical relation between peak frequency and chain length has been proposed.[2] Since the vibration under consideration is regarded as a symmetrical accordion-type longitudinal vibration of a string of beads with antinodes at the chain ends, it has been termed as the LA (longitudinal acoustic) mode.[6]

Recently, the length of the straight-chain system in crystallized polyethylene[7-9] and poly(decamethylene sebacate)[7] has been determined on the basis of the LA modes. In liquid and in solution, similar LA modes have been observed[10] and this fact indicates that a considerable number of molecules in solution exist in the same extended state as in the solid.

The purposes of this investigation are twofold; (1) Experimental results of the LA mode are given for *n*-paraffins in the solid and liquid states and also on five types of tetraalkylammonium bromides in the solid and dissolved states. The results are compared to each other. (2) The molecular shapes and ionic dimension of the tetraalkylammonium ions in aqueous solutions thus obtained are discussed.

Experimental Section

The apparatus used consisted of an argon ion laser manufactured by Coherent Radiation Co. Ltd. and a JRS-U1 laser Raman spectrometer of Japan Electron Laboratory Co. Ltd. To obtain the Raman spectra of lower *n*-paraffins in the solid state, a Harney-Miller variable temperature Raman cell was used. The details of the experimental procedure and data reductions have been previously described.[11] The *n*-paraffins and tetraalkylammonium bromides were of extra pure grade. Aqueous solutions at concentrations of 2 M were used except for tetraamylammonium bromide, for which a saturated solution (concentration less than 2 M) was used.

TABLE I: Frequency (cm^{-1}) of the LA Mode of *n*-Paraffins in the Solid and Liquid States

	Solid				Liquid
C_n[a]	m = 1		m = 3		m = 1
7	311[b]	315			311
10	231[b]	233			231
11		209	502		209
12	194[b]	197	493		196
13		184	450		183
14		172	436		172
16	150[b]	152	393		150
18	133[c]	139	358[c]	359	
20	114[c]	117	327[c]	320	

[a] Number of carbon atoms in *n*-paraffins. [b] Reference 12. [c] Reference 2.

Results and Discussion

(1) *n-Paraffins in Solid and Liquid States.* The Raman spectra and frequencies of the observed LA bands are summarized in Figure 1 and Table I, respectively. As is seen in Table I, our results are in excellent agreement with those of Mizushima and Shimanouchi.[12] For samples with from 7 to 16 carbon atoms, their LA bands were observed in the liquid state. Shaufele[13] pointed out that there are no longitudinal modes for *n*-paraffin in the liquid state at frequencies lower than 200 cm^{-1}. The highest Raman peaks in Figure 1 correspond very well to those of $(TGT'G')_\infty$ assigned by Shaufele.[13] However, as is shown in Figure 1, the highest peaks are not due to the LA mode of *n*-paraffin. The frequency of each LA band in the liquid state was equal to that in the solid state. For *n*-paraffins with more than 18 carbon atoms, LA bands were hardly detectable, as seen in Figure 1. These experimental results clearly indicate that the conformation of *n*-paraffin molecules, which is in the all-trans form in the solid state, is partially held even in the liquid state. With an increase

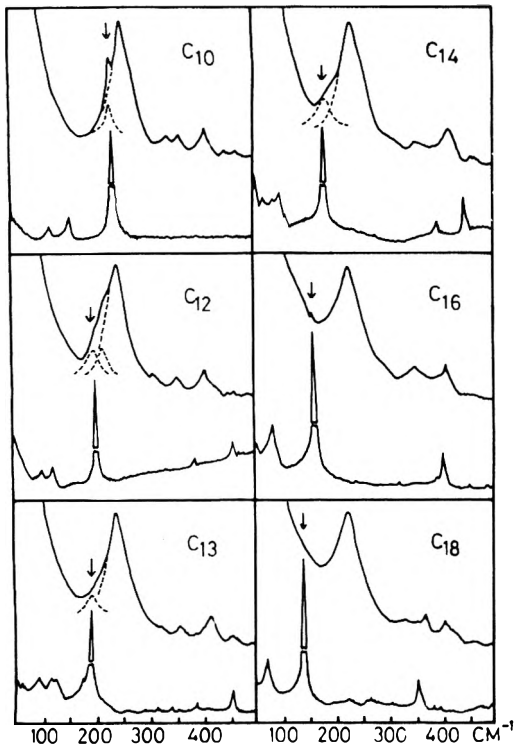

Figure 1. Low-frequency Raman spectra of *n*-paraffins in the solid (at −50 °C) and liquid state (at room temperature). The upper lines correspond to liquid state and the lower ones to solid.

TABLE II: Frequency (cm^{-1}) of the LA Mode of Tetraalkylammonium Bromides in the Solid and Dissolved State

C_n[a]	Solid	Liquid
3	454, 462	458
5	428	418
7	316, 337	310, 336
9	265	253
11	226	221

[a] Sum of carbon and nitrogen atoms in tetraalkylammonium bromides.

in carbon number, or chain length of *n*-paraffin, the number of possible conformation of molecules increases owing to internal rotation. This leads to a smaller portion of *n*-paraffin molecules taking the trans form. Similar results for polymethylene in the liquid state have been ascribed to a kinked conformation of the chains.[13]

The following equation has been presented for the LA bands of polymethylene chains[2]

$$(cm^{-1}) = A(m/n) + B(m/n)^2 + C(m/n)^3 + D(m/n)^4 + E(m/n)^5 + F(m/n)^6 \quad (2)$$

where $A = 2495 \pm 86\ cm^{-1}$, $B = -(5.867 \pm 2.855) \times 10^3\ cm^{-1}$, $C = (6.253 \pm 3.537) \times 10^4\ cm^{-1}$, $D = -(3.485 \pm 2.058) \times 10^5\ cm^{-1}$, $E = (7.329 \pm 5.676) \times 10^5\ cm^{-1}$, $F = -(4.724 \pm 5.964) \times 10^5\ cm^{-1}$ and n is the number of chain units. Frequencies calculated using eq 2 are compared with the observed values in Table I.

Connolly and Kandalic[14] have calculated the core width and the length of *n*-paraffins on the basis of their second virial coefficients. They obtained 1.26 Å for the core length of one C–C bond. This value is in excellent agreement with 1.275 Å, obtained from eq 1. From these results, it is concluded that the deviation from the linear relation between the frequency of the LA band and the reciprocal carbon number in *n*-paraffins is mainly due to the changes of (E/ρ) in eq 1.

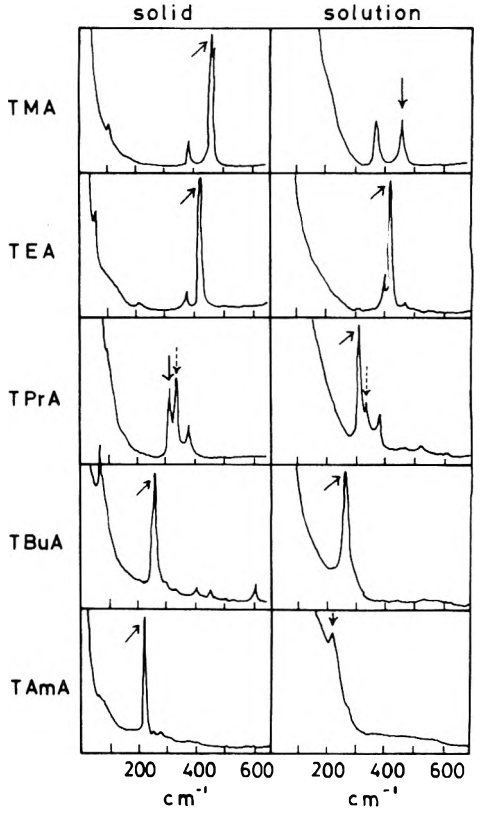

Figure 2. Low-frequency Raman spectra of tetraalkylammonium bromide in the solid (at −50 °C) and dissolved state (at room temperature). The solid arrow shows the LA mode of the all-trans form and dotted arrow shows that of the gauche form.

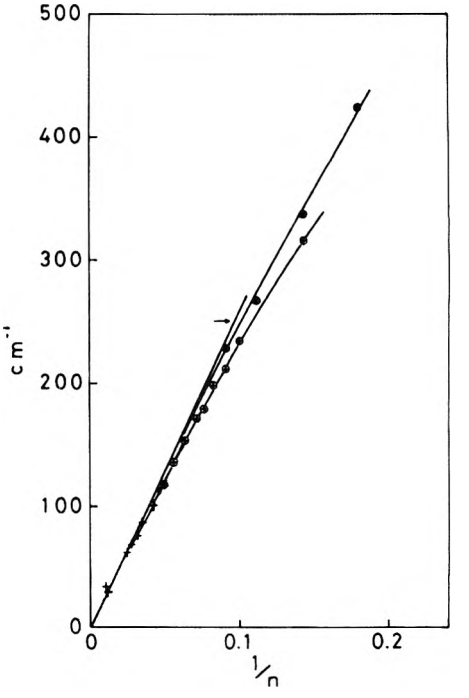

Figure 3. Relationship between the frequencies of the LA mode and the reciprocal carbon number: (●) TAA ions; (○) *n*-paraffins (this work); (+) *n*-paraffins (Shimanouchi et al.[1,2]).

(2) *Tetraalkylammonium Ions in Solid and Dissolved States.* The LA bands of tetraalkylammonium ions were identified by the following criterion: the frequency of the band decreases as the length of the carbon chain (involving nitrogen atom) increases. The Raman spectra and the frequencies of the observed LA bands for tetraalkylammonium ions in the solid and dissolved states are summarized in Figure 2 and Table II, respectively. The

TABLE III: Ionic Radius of the Tetraalkylammonium Ion

	r(R-S)[a]	r(SPT)[b]	$r(\overline{V}_+^\circ)$[c]	$r(V_w)$[d]	r(LA mode)
Me_4N^+	3.47	2.51	2.70-2.78	2.80	2.70
Et_4N^+	4.00	2.08	3.20-3.37	3.37	2.99
$(n\text{-Pr})_4N^+$	4.52	3.49	3.62-3.86	3.78	4.17
$(n\text{-Bu})_4N^+$	4.94	3.81	3.94-4.24	4.13	5.40
$(n\text{-Am})_4N^+$				4.43	6.69

[a] Reference 20. [b] Values determined from comparison with the scaled particle theory and the salting coefficients, ref 21. [c] Values cited in ref 21. Values calculated from the relationships between the partial molar volume of ions and ionic radius. [d] Effective radius of the van der Waals volume calculated by the present authors using the method of Bondi in ref 22. The following values are used in the calculation, $r_w(N) = 1.55$, $r_w(C) = 1.70$, $r_w(H) = 1.20$, and $d_{C-N} = 1.465$ Å.

relationship between the frequency of the LA band and the reciprocal carbon number is shown in Figure 3 along with the corresponding relationship for *n*-paraffins. As is seen in Table II and Figure 2, the LA band of tetraalkylammonium ions in the dissolved state does not differ much from that in the solid state. The limiting slope of the relationship between the frequency of the LA band of the tetraalkylammonium ion and the reciprocal carbon number is nearly equal to that for *n*-paraffins.

The x-ray crystallographic studies have shown that in tetraethylammonium[15] and tetrapropylammonium[16] bromides the alkyl chains are in the all-trans form, and the following values are given to their bond lengths and bond angles: C–C, C–N = 1.55 Å; ∠C–N–C = 105° and ∠C–C–C = 106°. These values for the tetraalkylammonium ions correspond very well to the values of *n*-paraffins. On the other hand, slight differences exist for the force constant K and for the deformation constant K_2: 4.13 and 0.43 mdyn/Å for the tetraethylammonium ion,[17] and 3.2 and 4.0 mdyn/Å for *n*-butane, respectively.

As the molecular weight of nitrogen is equivalent to that of a $-CH_2-$ unit, the density of the tetraalkylammonium ion should be nearly equal to that of *n*-paraffins. For this reason, the differences between the frequency of the LA band of the tetraalkyammonium ions and that of *n*-paraffins are attributed mainly to the differences in their Young's modulus. The fact that the frequencies of the LA band of the tetraalkylammonium ions do not differ much from those in the solid state indicates that the molecular dimension of the tetraalkylammonium ions in dissolved state should be comparable to that in the solid state.

For tetraalkylammonium ions, the ratio of molecules remaining in the all-trans form in solution was estimated by the following procedure: For each tetraalkylammonium ion, the values of the ratio, $r = I_a/I_{1457}$ were calculated both in the solid and dissolved states, where I_a is the intensity of the accordion (LA) band and I_{1457} is that of the band at 1457 cm^{-1} which has been assigned as the deformation band of $-CH_3$. The ratios r(solution)/r(solid) can be considered as a measure of the population ratio of molecules taking the same molecular structure as in the solid. Figure 4 shows the relation between r(solution)/r(solid) and the number of atoms included a chain (nitrogen atom being considered). In Figure 4, the values of r(solution)/r(solid) up to tetrabutylammonium ion are ca. 1, with the exception of the tetrapropylammonium ion. The values of approximately 1 indicate that each tetraalkylammonium ion holds mainly the same molecular dimension in aqueous solutions as in the solid state. The smaller intensity ratio of tetraamylammonium ion is ascribed to the rotational conformation of $-CH_2-$ chains in the ion.

In Figure 2, the splitting of the LA mode of the Raman spectra into two peaks is seen for tetramethylammonium in the solid state and tetrapropylammonium bromide in the solid and dissolved states. The occurrence of the splitting of the LA mode may be associated with the

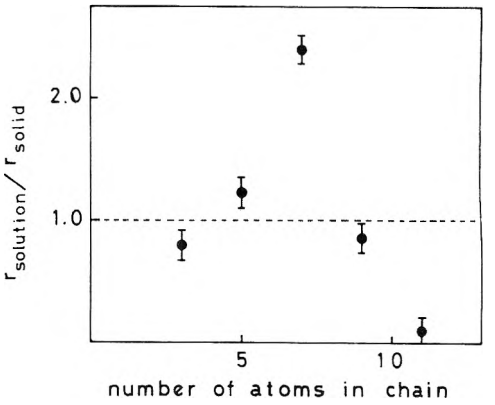

Figure 4. Relationship between r(solution)/r(solid) and the number of atoms in the tetraalkylammonium ion chains.

existence of the terminal methylene groups taking a gauche conformation. The peak at higher frequency is assigned to the LA mode of the gauche conformation. An interpretation of the occurrence of the LA band arising from the molecules taking the gauche form, especially for the tetrapropylammonium ion, is given from the point of its relationship with the phase transition reported for tetraalkylammonium iodides.[17] For tetrapropylammonium iodide in the solid state, two phase transitions have been observed. One at lower temperature, −43 °C, is considered to result from a change of crystal structure and the other at higher temperature, 35 °C, from a conformational change in the cations. On the contrary, for tetramethyl-, ethyl-, and butylammonium iodides, the second phase transition has not been observed. The fact that the experiment was carried out at −50 °C and with considerably rapid cooling, 2 °C/min, is strongly related to the appearance of the LA band of the gauche chain in tetrapropylammonium bromide in the solid state. However, as shown in Figure 2, an inversion in the intensity relation of two peaks was observed as to the two LA modes of tetrapropylammonium bromide. In addition the "true" LA band is stronger in the dissolved state. These experimental results indicate that the all-trans form of the methylene chain is more stable than the gauche form in aqueous solutions.

The ionic dimension of tetraalkylammonium cations can be estimated from the frequencies of their LA bands; the results are summarized in Table III. In Table III is included other ionic dimensions for tetraalkylammonium ions obtained by various methods.

In general, the values of $r_{R_4N^+}$ (LA mode) are larger than the corresponding values of $r_{R_4N^+}$(SPT). With an increase of the chain length in the tetraalkylammonium ions, the values of $r_{R_4N^+}$(LA mode) increase more rapidly than any other values of $r_{R_4N^+}$. However, for the first three types of tetraalkylammonium ions, $r_{R_4N^+}$(LA mode) falls between $r_{R_4N^+}$(SPT) and $r_{R_4N^+}$(empirical). Each value for the ionic radius shown in Table III has each different significance as it should be. The molecular dimension expressed by

$r_{R_4N^+}$(LA mode) is the ionic volume in the extended state, because the LA mode arises from the molecule taking the all-trans form. Therefore $r_{R_4N^+}$(LA mode) does not correspond to $r_{R_4N^+}$(SPT), which represents the hard core volume of ions and it follows the general relation that $r_{R_4N^+}$(LA mode) > $r_{R_4N^+}$(SPT).

In conclusion, it was confirmed that the molecular structure of the tetraalkylammonium ion in aqueous solution is an extended one, such as the all-trans from in CH_2 chains, especially for lower members of *n*-paraffins. The ionic radii of the tetraalkylammonium ion shown in the first to forth columns of Table III, correspond to an effective radii in aqueous solution. In addition, *n*-paraffins containing long CH_2 chains are, on the average, not in such an extended state and therefore their effective ionic radius should be much smaller than that obtained from the LA band.

References and Notes

(1) S. Mizushima and T. Shimanouchi, *J. Am. Chem. Soc.*, **71**, 1320 (1949).
(2) R. F. Schaufele and T. Shimanouchi, *J. Chem. Phys.*, **47**, 3605 (1967).
(3) R. F. Shaufele, *Macromol. Rev.*, **4**, 67 (1970).
(4) I. Sakurada, T. Ito, and K. Nakamai, *J. Polym. Sci.*, **C15**, 75 (1966).
(5) T. Shimanouchi, M. Asahina, and S. Enomoto, *J. Polym. Sci.*, **B9**, 93 (1962).
(6) W. L. Peticolas, G. W. Hibler, J. L. Lippert, A. Peterlin, and H. G. Olf, *Appl. Phys. Lett.*, **18**, 87 (1971).
(7) M. J. Folkers, A. Keller, J. Stejny, P. L. Goggin, G. V. Fraser, and P. J. Hendra, *Colloid Polym. Sci.*, **253**, 354 (1975).
(8) H. G. Olf, A. Peterlin, and W. L. Peticolas, *J. Polym. Sci.*, **12**, 359 (1974).
(9) J. L. Koenig and D. L. Tabb, *J. Macromol. Sci., Phys.*, **B9**, 141 (1971).
(10) H. Okabayashi, M. Okuyama, T. Kitagawa, and T. Miyazawa, *Bull. Chem. Soc. Jpn.*, **47**, 1075 (1974).
(11) H. Nomura and Y. Miyahara. *Bull. Chem. Soc. Jpn.*, **48**, 2779 (1975).
(12) S. Mizushima and T. Shimanouchi, *Nippon Kagaku Zasshi*, **64**, 1064 (1943).
(13) R. F. Shaufele, *J. Chem. Phys.*, **49**, 4168 (1968).
(14) J. F. Connolly and G. A. Kandalic, *Phys. Fluids*, **3**, 463 (1960).
(15) N. C. Stephenson, *Acta Crystallogr., Sect. B*, **17**, 587 (1964).
(16) A. Zalkin, *Acta Crystallogr., Sect. B*, **10**, 557 (1957).
(17) J. T. Edsall, *J. Chem. Phys.*, **5**, 225 (1937).
(18) T. Shimanouchi and S. Mizushima, *Nippon Kagaku Zasshi*, **64**, 1215 (1943).
(19) J. Levkov, W. Kohr, and R. A. Mackay, *J. Phys. Chem.*, **75**, 2066 (1971).
(20) R. A. Robinson, and R. H. Stokes, "Electrolyte Solutions", 2nd ed, Butterworths, London, 1959.
(21) W. L. Masterton, D. Bolocofsky, and T. P. Lee, *J. Phys. Chem.*, **75**, 2809 (1971).
(22) A. Bondi, *J. Phys. Chem.*, **68**, 441 (1964).

Relaxation Times for Acid Ionization and Internal Proton Transfer in Polypeptides in the Neighborhood of the Helix–Coil Transition

L. Madsen and L. J. Slutsky*

Department of Chemistry, University of Washington, Seattle, Washington 98195

(Received January 14, 1977; Revised Manuscript Received July 22, 1977)

Relaxation frequencies and normal coordinates are calculated for the system of coupled reactions formed by the acid ionizations at glutamyl residues in poly-L-glutamic acid. The results suggest that the perturbation of overall and internal ionization equilibria constitute a reasonable alternate interpretation of relaxations which have been attributed to perturbation of the helix–coil equilibrium.

I. Relaxation Times for Intramolecular Proton Transfer

The kinetics of the proton-transfer reactions involved in the relaxation of fluctuations in the overall and internal ionization equilibria in solutions of proteins and uniform polypeptides has been the object of some interest.[1-4] The role of perturbation of proton-transfer equilibria in determining, and perhaps in complicating, the interpretation of relaxation spectra in the neighborhood of a reversible pH-induced conformational transition is also an object of concern.[5-7] We wish here to discuss the normal modes of the system of acid ionization reactions (reaction 1) of side

$$-AH_i \underset{k_{bi}}{\overset{k_{fi}}{\rightleftharpoons}} -A_i^- + H^+ \qquad (1)$$

chains in the helical (i = 1) and coil (i = 2) regions of a uniform polypeptide coupled to the ionization of an indicator (i = 3), to consider the application of these results to the interpretation of spectra observed in solutions of poly-L-glutamic acid in the neighborhood of the helix–coil transition,[8-9] and to briefly comment on the possible relevance of these computations to the interpretation of the acoustic relaxation observed in solutions of uniform polypeptides and proteins.

The secular equation corresponding to eq 1 is

$$\begin{vmatrix} \omega_1^0 - \omega & K_{b1}[-A_1^-] & k_{b1}[-A_1^-] \\ k_{b2}[-A_2^-] & \omega_2^0 - \omega & k_{b2}[-A_2^-] \\ k_{b3}[-A_3^-] & k_{b3}[-A_3^-] & \omega_3^0 - \omega \end{vmatrix} = 0 \qquad (2)$$

where $\omega_i^0 = k_{bi}(K_i + [H^+] + [-A_i^-])$, $[X_j]$ represents the equilibrium concentration (moles/liter) of the jth species, and ω is the reciprocal relaxation time.

In Figures 1 and 2 the eigenvalues of eq 2 are plotted, as a function of pH, for the case of solutions of poly-glutamic acid (PLGA) and bromocresol purple indicator with the polymer concentration (6.3×10^{-4} mol of residue/L) and indicator concentration (3×10^{-5} M) taken to be those employed by Cummings and Eyring[8] in their electric-field-jump study of aqueous poly-L-glutamic acid. The pK_a (6.47) and the bimolecular rate constant (k_{b3} =

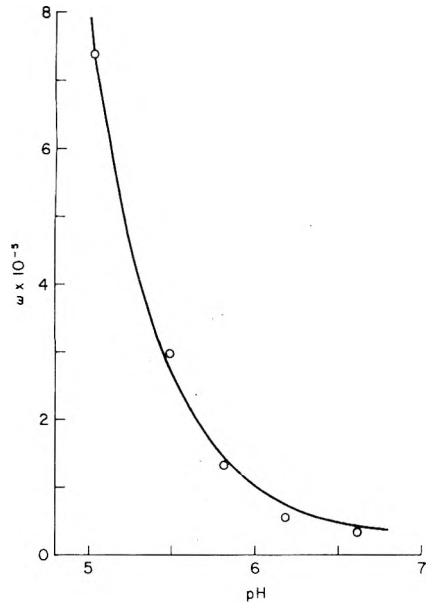

Figure 1. Calculated relaxation frequencies for proton exchange between poly-L-glutamic acid (6.3×10^{-4} residue molar) and bromocresol purple (3×10^{-5} M) as a function of pH. Circles are the relaxation frequencies determined by Cummins and Eyring.

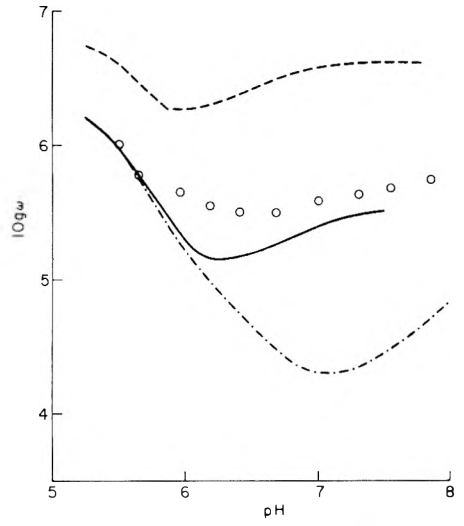

Figure 2. Calculated relaxation frequencies for overall ionization (- - -) and internal proton transfer (solid and broken, -·-·, curves). The solid curve is calculated with the aid of Hill's expression for the potential at distance r from a cylindrical polyelectrolyte[12] with geometrical properties of the helix and coil from the work of Rinaudo and Domard.[11] The lower broken curve (-·-·) is calculated neglecting the electrostatic effect of neighboring residues on the ionization kinetics of a given protonated glutamyl residue. Circles are the relaxation frequencies observed in ref 9.

7.7×10^{10} s^{-1} M^{-1}) for the indicator are those determined by Lentz, Hutchins, and Eyring.[10] Values of pK_a for helical and coil residues are derived from the titration curves of Rinaudo and Domard[11] and the bimolecular rate constant for recombination at the glutamyl residues is taken to be 5×10^{10} M^{-1} s^{-1} by analogy with simple carboxylic acids.[14]

The normal modes correspond fairly closely to overall ionization, proton exchange between helical and coil residues, and proton exchange between peptide and indicator. However in a conductiometrically sensed E-jump experiment the admixture of overall dissociation in the mode qualitatively describable as intramolecular proton transfer is a matter of some importance. Hence, if the internal transfer is represented by $A_1H + (1 - b)A_2^- = A_1^- + (1 - b)A_2H + bH^+$, the coefficient ($b$) which specifies the

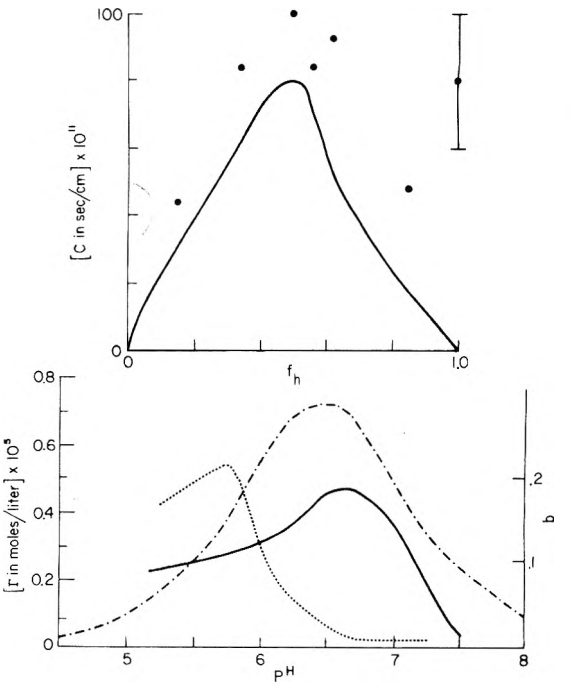

Figure 3. The chemical factor Γ for intramolecular proton transfer (solid curve in lower panel) and indicator–proton exchange (broken curve in lower panel) and the contribution of acid dissociation (b) to the normal mode qualitatively described as intramolecular exchange as a function of pH. The upper panel gives calculated and observed values of the absorption amplitude (C) as a function of the fraction of the polymer present in the helical state (f_h) under the experimental conditions of ref 15. The bar in the upper panel represents the average experimental error.

partial dissociative character is plotted, as a function of pH, in Figure 3.

In a spectrophotometric E-jump experiment peptide–indicator exchange is the mode which would be observed. The computed relaxation frequencies for this mode plotted in Figure 1 are in very good agreement with those observed by Cummings and Eyring. It does not appear necessary to include the helix–coil transition in the kinetic basis set to explain the results of ref 8.

In basic solution, and close to neutrality, the basis set must be expanded to include reactions of the form

$$-A^- + H_2O \underset{k_b'}{\overset{k_f'}{\rightleftharpoons}} -AH + OH^- \qquad (3)$$

In Figure 2 the calculated relaxation frequencies for overall ionization and internal proton transfer for poly-L-glutamic acid with eq 1 and 3 as a basis are compared with the times observed by Yasunaga, Tsuji, Sano, and Takenaka[9] in a conductiometrically sensed pulsed E-field experiment. The relaxation frequencies are calculated for the polymer concentration (10^{-4} residue molar) of ref 9 with values of pK_a, as a function of pH, derived from the titration curve given in ref 9.

The experimental relaxation, which is interpreted by Yasunaga et al. as being the time for the helix–coil transition, is found to be independent of polymer concentration as is the calculated time for internal proton transfer. The calculated relaxation frequencies exhibit a minimum slightly on the acid side of neutrality as do the experimental values of τ^{-1}. However the calculated times for the internal proton transfer are an order of magnitude greater than the times observed in ref 9 and it might legitimately be concluded that internal proton transfer is not what is observed by Yasunaga et al. Alternately it might be argued that the local concentration of hydrogen ion in the immediate neighborhood of the polymer, and

hence the rate of intramolecular proton transfer, is significantly higher than the bulk concentration. There does exist a plausibility argument in favor of the second of these propositions.

In a medium of dielectric constant D and inverse Debye length κ, the electrostatic free energy change associated with the transfer of a proton from an infinite distance to distance r from a uniformly charged cylinder of radius ρ with an average linear charge density Ze'/l is[12]

$$W = -\frac{Ze^2K_0(\kappa r)}{lD\kappa\rho K_1(\kappa\rho)} \tag{4}$$

where e is the charge of the electron, K_0 and K_1 are modified Bessel functions of the second kind of order 0 and 1. Rinaudo and Domard[11] estimate ρ = 8 Å for the poly-L-glutamic acid extended coil, 16 Å for the helix. If f and f' are respectively the average degrees of ionization of coil and helical residues (in this case estimated from the titration curve in ref 9 then for the extended coil Z/l = f/3.6 charges/Å, for the helix $Z/l = f'/1.5$ Å.

In order to estimate the rate of diffusion-controlled proton transfer one wishes to estimate W and hence $[H^+]$ at $r = \rho + r_d$ where r_d is the effective radius for reaction in the Debye–Smoluchowski[13] theory. It has been found that r_d = 2.7 Å gives a good account of the rates of the bimolecular step of the proton-transfer reactions of a number of amino acids and small peptides[14c] and this value is used here.

The choice of the rather large value of ρ suggested in ref 11 rather than the smaller diameter of the PLGA helix (13.5 Å) estimated by Tanford[15a] will minimize the electrostatic enhancement of the local hydrogen ion concentration at the polymer surface and hence the calculated rate of intramolecular proton exchange. The relaxation frequencies calculated from the parameters given in the foregoing and displayed in Figure 2 are in fair agreement with the experimental results of Yasunaga and his coworkers. The agreement could no doubt be improved by ad hoc selection of the geometrical parameters.

The difference between the average degree of ionization of residues in helical and coil segments of the molecule determines the dissociative component of both the helix–coil transition and intramolecular proton exchange. In the transition region where both helical and coil segments are large the average change in dipole moment associated with the transfer of a proton from a helical to a coil residue will be large. We would thus argue that one might reasonably expect to observe this mode in a conductiometrically sensed pulsed E-field experiment and thus that perturbation of internal proton-exchange equilibria is a reasonable alternate interpretation of the relaxation observed in ref 9 and that a strong case can be made for the proposition that proton transfer is responsible for the relaxation observed in ref 8.

Less directly the change in local charge density or in molecular dipole moment associated with an intramolecular proton transfer is electrostrictively coupled to the pressure field of an ultrasonic wave even if, as is the case in a uniform polypeptide, the transfer is between chemically equivalent groups and there is no intrinsic volume change. If the proposition that the volume change for intramolecular proton transfer is sufficiently great to account for the observed relaxation amplitudes can be made plausible, then the possibility that the ultrasonic relaxation observed in solutions of uniform polypeptides[16] in the neighborhood of the helix–coil transition is in significant part due to perturbation of internal charge-transfer equilibria is worthy of consideration as is the possibility that this mechanism is responsible for the acoustic absorption observed in protein solution near neutral pH. In the following, an argument, albeit at best semiquantitative, is presented in support of the proposition that the acoustic relaxation amplitudes associated with intramolecular proton transfer are comparable with those observed in PLGA.

II. Relaxation Amplitudes

The degree of advancement, δ, of a single normal reaction represented by the equation $\Sigma_i g_i[A_i] = 0$ may be defined in terms of the coefficient (g_i) of any species (A_i) by $\Delta[A_i] = g_i\delta$ where $\Delta[A_i]$ is the displacement of the concentration of the ith species from its equilibrium value. The initial value of δ when a reaction, initially at equilibrium, is subjected to a step variation in some external parameter such as the electric field, E, is then $\sigma_0 = (\partial \ln K/\partial E)(d\delta/d \ln K)(\Delta E) = (\partial \ln K/\partial E)\Gamma\Delta E$.

In the absence of significant dispersion the excess ultrasonic absorption α at frequency f associated with a single process with relaxation time τ is[17] $\alpha = C\tau f^2/[1 + (2\pi\tau f)^2]$.

In dilute aqueous solutions, where C_p and C_v are very nearly equal and the temperature fluctuation associated with the passage of an ultrasonic wave has a neglible effect on the equilibrium of a reaction with a moderate ΔH

$$C = 2\pi^2 c\rho\Gamma(\Delta V)^2/\bar{V}RT \tag{5}$$

where ρ is the density of the solution, c is the velocity of sound, ΔV is the volume change (per mole) for the process in question, and V is the volume per mole of the solvent.

The value of Γ for any normal reaction is readily calculated from the equilibrium composition. To estimate the amplitude of ultrasonic absorption and response to a pulsed electric field associated with the normal modes of the system of reactions represented by eq 1, values of ΔV and $\partial \ln K/\partial E$ must be approximated. Experimental amplitudes are available only for ultrasonic absorption. We will thus be principally concerned with the calculation of the volume change for transfer of a proton from a residue in a helical segment of the poly-L-glutamic acid helix to a residue in a random coil segment.

The electrostrictive volume change associated with intramolecular proton transfer at constant molecular geometry may be estimated by appropriate differentiation of an approximate expression for the electrostatic free energy change (ΔW). If a helical segment of length L and total charge Z' is modeled as a cylinder of radius ρ with exclusion radius a, the electrostatic free energy in a medium of dielectric constant D and Debye length κ^{-1} is[12]

$$W = \frac{Z'^2e^2}{DL}\left\{\frac{K_0(\kappa a)}{\kappa a K_1(\kappa a)} + \ln(a/\rho)\right\} = \frac{e^2}{D}Z'^2g'(\kappa) \tag{6a}$$

and for a random coil of total charge Z and radius of gyration R, fully penetrated by solvent[15c]

$$W = \frac{3Z^2e^2}{2DR}\left\{(\kappa R)^{-2} - 3\left[\frac{(\kappa R)^2 - 1 + (1+\kappa R)^2e^{-2\kappa R}}{2\kappa^5 r^5}\right]\right\} = \frac{3Z^2e^2g(\kappa)}{2D} \tag{6b}$$

Thus, for the transfer of a single proton from a random coil to a helical segment, $\Delta W = (e^2/D)[2Z'g'(\kappa) - 3Zg(\kappa)]$ and, since κ is proportional to $D^{-1/2}$, $\partial\kappa/\partial P = -(\kappa/2D)\cdot(\partial D/\partial P)$. Thus, differentiating at constant values of the geometrical parameters

$$\Delta V = \frac{\partial \Delta W}{\partial P} = \frac{Ne^2}{D^2}\frac{\partial D}{\partial P}\left\{2Z'g'(\kappa) - 3Zg(\kappa) + \frac{\kappa}{2}\frac{\partial[2Z'g'(\kappa) - 3Zg(\kappa)]}{\partial \kappa}\right\} \quad (6c)$$

where N is Avogadro's number and ΔV is the volume change per mole of protons transferred. Introducing the abbreviations $y' = \kappa a$ and $y = \kappa R$

$$\Delta V = \frac{Ne^2}{D^2}\frac{\partial D}{\partial F}\left\{\left[\frac{2K_0(y')}{y'K_1(y')} + \frac{K_0^2(y')}{K_1^2(y')} - 1 + 2\ln\left(\frac{a}{\rho}\right)\right]\frac{Z'}{L} + \frac{-9}{4y^3}\left[(1-3y)^{-2} + \frac{(1+y)(2y^2+3y+3)e^{-2y}}{y^2}\right]\frac{Z}{R}\right\} \quad (6d)$$

We wish to compare the calculated ultrasonic absorption with the measurements of Barksdale and Stuehr[16] in 0.03 M NaBr. In this case the radius of the counterion (Na^+) is 0.98 Å and κ^{-1} is 18 Å. Taking Tanford's estimate of the diameter of the PLGA helix, $\rho = 6.75$ Å and the exclusion radius $a = 7.73$ Å.

Nagasawa and Holtzer[18] have determined the titration curves of PLGA in 0.02 and 0.05 M NaCl. We have estimated the degrees of dissociation of residues in helical and coil segments (designated respectively f' and f) at an ionic strength of 0.03 by interpolation between values estimated from their results at higher and lower ionic strength. We take Z'/L equal to $f'/1.5$ Å.

An estimate of the charge density in the random coil is more difficult. Near a midpoint of the helix coil transition the length of a coil segment is approximately $(\sigma)^{-1/2}$ or 16 residues. The radius of gyration is then about $(16/6)^{1/2}A\beta$[15b] where β, the length of a "statistical segment", is about three times the interresidue spacing or 11.4 Å. Brant and Flory[19] have determined the "expansion parameter" A for PLGA in 0.3 M sodium phosphate to be 1.34. The results of Rice[20] suggest that A might be 10–15% greater at the lower value of the ionic strength of interest here. We have thus taken R to be 28 Å and Z/R to be $(16f/28)$ Å^{-1}. As long as R is significantly larger than the Debye length the calculated volume change is not very sensitive to the parameters which characterize the relatively less densely-charged coil.

The pressure derivate of the dielectric constant of water has been determined by Owen and Brinkley,[21] $(Ne^2/D^2)(\partial D/\partial P) = 10.1 \times 10^{-8}$ cm^3/mol. When the appropriate Debye length and the geometrical parameters are substituted eq 6d becomes $\Delta V = 10.1(1.3f' - 0.1f)$ cm^3/mol (eq 6e). At the midpoint of the transition $f' \sim f \sim 0.5$ so $\Delta V \sim 6$ cm^3/mol.

In Figure 3, the amplitude calculated from eq 5 and 6e and the pH dependence of f and f' are compared with experiment. The computed amplitudes are systematically less than the observed, but the disagreement does not exceed experimental error.

The electrostrictive volume change calculated in this work results from the coexistence of helical and coiled regions of the molecule with different equilibrium charge densities and, in the simple model advanced here, would be zero for poly-DL-glutamic acid where there is no helix–coil transition. Thus the observed absence of pH dependent excess absorption[22] in the DL polymer cannot be taken as a demonstration that either the helix–coil transition or the mechanism proposed here is responsible for the observed excess acoustic attenuation. We would therefore conclude, as have Eggers and Funck,[23] that neither the times observed in the E jump or in ultrasonic experiments can be unambiguously attributed to a conformational transition. We would further argue that, in proteins or other spatially nonuniform polyelectrolyte systems near neutral pH where the value of Γ, and hence the amplitude, of any process which is principally acid or basic dissociation is necessarily small, intramolecular charge exchange is likely to be a significant contributor to the observed relaxation spectrum.

References and Notes

(1) J. G. Kirkwood and J. B. Shumaker, *Proc. Natl. Acad. Sci. U.S.A.*, **38**, 855, 863 (1952).
(2) R. D. White and L. J. Slutsky, *Biopolymers*, **11**, 1973 (1972); *J. Colloid Interface Sci.*, **37**, 727 (1972).
(3) R. Zana and J. Lang, *J. Phys. Chem.*, **74**, 2735 (1970).
(4) P. J. Heywood, J. F. Rassing, and E. Wynn-Jones, *Adv. Mol. Relaxation Processes*, **8**, 95 (1976).
(5) R. C. Parker, L. J. Slutsky, and K. Applegate, *J. Phys. Chem.*, **72**, 3177 (1968).
(6) F. Dunn and L. W. Kessler, *J. Phys. Chem.*, **74**, 2736 (1970).
(7) R. D. White, S. Pattison, and L. J. Slutsky, *J. Phys. Chem.*, **75**, 161 (1971).
(8) A. L. Cummings and E. M. Eyring, "Chemical and Biological Applications of Relaxation Spectrometry", E. Wynn-Jones, Ed., Reidel Publishing Co., Boston, Mass., 1975.
(9) T. Yasunaga, Y. Tsuji, T. Sano, and H. Takenaka, *J. Am. Chem. Soc.*, **98**, 813 (1976).
(10) D. J. Lentz, J. E. C. Hutchins, and E. M. Eyring, *J. Phys. Chem.*, **78**, 1021 (1974).
(11) M. Rinaudo and A. Domard, *Biopolymers*, **12**, 2211 (1973).
(12) T. L. Hill, *Arch. Biochem. Biophys.*, **57**, 229 (1955).
(13) P. Debye, *Trans. Electrochem. Soc.*, **82**, 265 (1942).
(14) M. Eigen and L. De Maeyer, *Tech. Org. Chem.*, **8**, 1034 (1963).
(15) (a) C. Tanford, "Physical Chemistry of Macromolecules", Wiley, New York, N.Y., 1961, pp 468–500; (b) *ibid.*, 150–170; (c) *ibid.*, 509–512.
(16) A. D. Barksdale and J. E. Stuehr, *J. Am. Chem. Soc.*, **94**, 3334 (1972).
(17) K. F. Herzfeld and T. A. Litovitz, "Absorption and Dispersion of Ultrasonic Waves", Academic Press, New York, N.Y., 1959.
(18) M. Nagasawa and A. Holtzer, *J. Am. Chem. Soc.*, **86**, 538 (1964).
(19) D. A. Brant and P. J. Flory, *J. Am. Chem. Soc.*, **87**, 2771, 2788 (1965).
(20) S. Rice in "Biophysical Science", J. Oncley, Ed., Wiley, New York, N.Y., 1959, p 69.
(21) B. B. Owen and S. R. Brinkley, *Phys. Rev.*, **64**, 32 (1943).
(22) R. Zana, *J. Am. Chem. Soc.*, **94**, 3646 (1972).
(23) F. Eggers and Th. Funck, *Stud. Biophys.*, **57**, 101 (1976).

Equilibria and Ion Activities in Aqueous Sulfur Dioxide Solutions[1]

Albin Huss, Jr. and C. A. Eckert*

Department of Chemical Engineering, University of Illinois, Urbana, Illinois 61801 *(Received July 7, 1977)*

Publication costs assisted by the National Science Foundation

The equilibrium of the first dissociation of aqueous sulfur dioxide to bisulfite ion has been studied by two independent techniques. The results of both conductometric and spectrophotometric investigations are in excellent agreement and indicate a value of $K_1 = 0.0139 \pm 0.0002$ mol/L at 25 °C, using in the latter a molecular absortivity for hydrated SO_2 of 498 ± 6 L mol^{-1} cm^{-1} at 276 nm. Activity coefficients for the H^+, HSO_3^- ion pair have also been evaluated and are well represented by the Guggenheim expression up to modest ionic strengths (0.06 M) with a specific interaction parameter, β, of 0.3 ± 0.08. These data appear to resolve the conflicting results reported by previous investigations.

Introduction

The solution behavior of sulfur dioxide is not only of theoretical interest, but of substantial practical importance in the study of the mass transfer and chemistry in scrubber systems for stationary power plants as well as for the modeling of aerosol plumes. For any rational investigation it is essential that the equilibrium constant for the dissociation of hydrated sulfur dioxide, K_1

$$SO_2 \cdot H_2O \overset{K_1}{\rightleftharpoons} H^+ + HSO_3^- \quad (1)$$

be known precisely, and that the solution chemical activities be well characterized.

Despite numerous investigations, the range of values reported[2-8] for K_1 at 25 °C is substantial, 0.0126–0.0172 M, apparently with the upper value[3] being the accepted one at present.[4]

The use of this upper value[3] leads to an unacceptable anomaly in the ionic activities. Spectroscopic studies[9] were used to generate an expression for the mean activity coefficient of the H^+, HSO_3^- ion pair by following the 276-nm peak with an assumed molecular extinction coefficient of 608 M^{-1} cm^{-1}. Although the range of applicability of these authors' expression is limited (HSO_3^- ≤ 0.008 M), the predicted activity coefficients are substantially lower than those generally accepted for 1–1 electrolytes. For example, at an ionic strength of 0.008 M this expression predicts a mean activity coefficient of 0.85, while the activity coefficients previously reported for 1–1 electrolytes of comparable size (Lewis and Randall[10]) are all within the range of 0.905–0.915. This suggests that either the extinction coefficient or equilibrium constant, or possibly both, are inaccurate.

This study has been carried out to obtain a more definitive value of K_1 and a thermodynamically consistent expression for the activity coefficients of the hydrogen–bisulfite ion pair. Conductometric and ultraviolet spectrophotometric experiments were performed to obtain these results.

Experimental Section

The conductance equipment consisted of the conductivity cell and a Beckman Model RC-18 conductivity bridge, equipped with a Wagner ground and added capacitance to balance the circuit, with an accuracy of 0.1% or better. The conductivity cell was a Teflon cylinder with a cavity of 15 cm long by 2 cm i.d. with platinum wire loops as electrodes secured in shallow grooves 1 cm apart on opposite sides of the cylinder and separated by a glass rod at the bases. Platinum wire leads were welded to these electrodes and pushed through undersized holes in the cylinder wall to give an excellent seal. A cell constant of 0.5096 cm^{-1} was determined by calibrating with 0.01 and 0.001 N KCl–water solutions and the equivalent conductance equation suggested by Fuoss et al.[11] The cell was thermostatted at 25 ± 0.01 °C by immersion in a constant temperature oil bath. To minimize the time lag required for temperature equilibration and any subsequent sulfur dioxide losses from the conductivity cell, all solutions were prethermostatted in a constant temperature water bath.

The aqueous sulfur dioxide solutions were prepared by saturating deoxygenated water with sulfur dioxide gas (standard grade from the Linde Division of Union Carbide Corp.) and diluting to the desired concentrations. The resulting solutions were all in the pH range 1–3 and 0.1 M or less in total concentration of sulfur species. At these conditions the experimental conductance measurements should only be affected by the hydrated sulfur dioxide–bisulfite equilibria (eq 1).

To prevent oxidation of the sulfur dioxide, all solutions were prepared and loaded into the conductivity cell in an inert-atmosphere glove bag. The water used in all solutions was first deionized and then deoxygenated by sparging with nitrogen for 4–6 h. The total concentration of sulfur species in the +4 oxidation state was determined by iodometry. A known volume of sample was pipetted into an excess of standardized iodine solution of known volume. The iodine reacts with the hydrated sulfur dioxide and bisulfite ions to form sulfate ions. The excess iodine is then determined by back titration with arseneous acid. The end point was detected by a starch indicator.

Spectrophotometric measurements were made with a Beckman ACTA CII UV–visible spectrophotometer. The instrument was operated in the double beam mode with deionized water in the reference cell. In the present study all absorbance values were between 0.40 and 2.1 A, by varying the path length of the matched pairs of absorption cells. The temperature of the absorption cells was maintained at 25 ± 0.1 °C by containment in thermostatted cell holders.

As in the conductometric studies, extreme care was taken in both preparation and handling of samples to prevent oxygen contact with the solutions and possible oxidation of the sulfur dioxide. Sample preparation and the analysis of the total sulfur dioxide concentration were the same as that described above.

Results

Conductometric. The techniques used to obtain thermodynamic dissociation constants from electrolytic

TABLE I: Conductivity of Aqueous SO_2 at 25 °C

SO_2 concn, mol/L	Equiv conductance, cm^2/equiv ohm	SO_2 concn, mol/L	Equiv conductance, cm^2/equiv ohm
0.0005215	371.5	0.01787	231.3
0.001043	357.3	0.01967	225.1
0.002497	333.0	0.02775	200.4
0.004942	305.3	0.03583	188.9
0.006404	291.9	0.03897	183.7
0.008724	274.1	0.05587	159.5
0.009813	269.1	0.06834	150.6
0.01287	252.2		

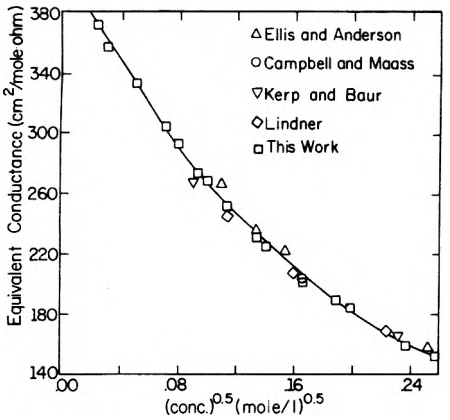

Figure 1. Equivalent conductance of aqueous sulfur dioxide solutions at 25 °C.

conductance data are well established (Fuoss and Accascina,[12] Fuoss et al.,[13] and Burg et al.[14]). The last of these methods[14] was used, with application of the Rosenbrock[15] minimization scheme to the equations to obtain the best fit of experimental conductance data, scanning parameter space for values of the association constant K_a and the critical apprach distance a. The criterion used to obtain the best values of K_a and a was a minimum in the function of equivalent conductance Λ

$$\sum_{\text{data points}} \{[\Lambda(\text{exptl}) - \Lambda(\text{calcd})]/\Lambda(\text{exptl})\} \quad (2)$$

The experimental conductance data (listed in Table I) and the best fit by the modified Fuoss equation are shown in Figure 1. The calculated and experimental equivalent conductances are in excellent agreement, with a standard deviation of ±0.6%. Figure 1 also contains equivalent conductance data from four other investigations, all in reasonable agreement with the data of this work.

The values of the dissociation constant and the critical approach distance, a, obtained from the best fit of the experimental conductance data (this work only) are 0.0139 M and 8.8 Å, respectively. The critical approach distance of 8.8 Å is slightly higher than the range of 4–5 Å which is generally accepted as reasonable for the H^+, HSO_3^- ion pair (Johnstone and Leppla[5] and Kielland[16]). Using a more physically reasonable value of 5 Å, however, results in a change of only 0.1% in the thermodynamic equilibrium constant. The limits of error on the experimental dissociation constant in this work are estimated to be 0.0139 ± 0.0002 M (±1.5%).

Spectrophotometric. A typical ultraviolet spectrum of an aqueous sulfur dioxide solution is shown in Figure 2. The absorption near 210 nm is due to the bisulfite ion and the peak at 276 nm is from hydrated sulfur dioxide. The spectrophotometric absorbance data of this study for the 276-nm peak are given in Table II, along with some values of the ratio of the 276-nm absorbance to that at 255 nm. This ratio remained constant over the entire sulfur(IV)

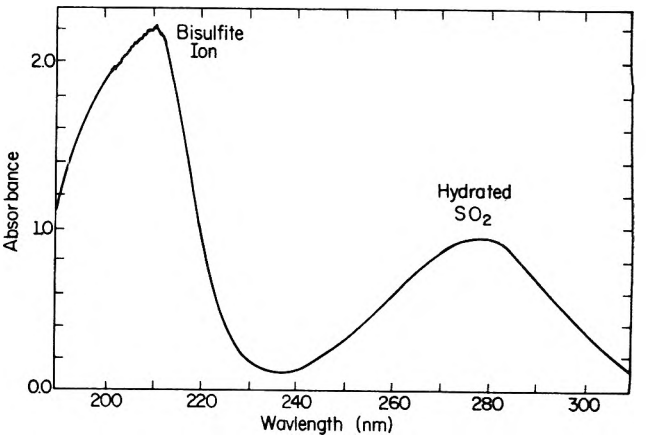

Figure 2. Typical UV spectrum of aqueous sulfur dioxide solution.

TABLE II: Spectrophotometric Absorbance Data of Aqueous SO_2 at 25 °C

Sulfur(IV) concn, mol/L	Cell path length, cm	Absorbance at 276 nm	A_{276}/A_{255}
0.001023	1.0	0.031	
0.001256	1.0	0.045	
0.001826	1.0	0.091	
0.002093	1.0	0.117	
0.004032	1.0	0.360	
0.00448	1.0	0.420	
0.01063	1.0	1.627	
0.01296	1.0	2.143	
0.02369	0.10	0.512	2.28
0.02712	0.10	0.610	2.31
0.03290	0.10	0.790	
0.04320	0.10	1.118	
0.05046	0.10	1.388	
0.05653	0.10	1.602	
0.06418	0.10	1.867	
0.07285	0.10	2.170	
0.04339	0.050	0.572	
0.04929	0.050	0.673	
0.05870	0.050	0.830	2.34
0.06668	0.050	0.983	2.32
0.08744	0.050	1.366	2.30
0.09320	0.020	0.585	2.33
0.1038	0.020	0.660	2.36
0.09633	0.020	0.612	2.31
0.1054	0.020	0.685	2.34
0.1102	0.020	0.715	2.35
0.1201	0.020	0.797	2.30
0.1438	0.020	0.986	2.32
0.1566	0.020	1.086	2.34
0.1765	0.020	1.246	
0.1799	0.020	1.270	2.31
0.2001	0.020	1.440	2.29
0.2135	0.020	1.550	2.32

concentration range studied, indicating negligible $S_2O_5^{2-}$ formation in this work ($S_2O_5^{2-}$ absorbs at 255 nm and is formed at very high sulfur(IV) concentration by the equilibrium $2HSO_3^- \rightleftharpoons H_2O + S_2O_5^{2-}$). Since the bisulfite ion is transparent in the 276-nm region and no appreciable $S_2O_5^{2-}$ is present, the concentration of hydrated sulfur dioxide can be calculated from Beer's law using the appropriate molecular absorptivity. The concentration m of bisulfite ions can then be determined by subtracting the hydrated sulfur dioxide concentration from the total concentration of sulfur in the +4 oxidation state, as follows:

$$m_{HSO_3^-} = m_{S^{4+}} - m_{SO_2 \cdot H_2O} \quad (3)$$

and used to solve for the mean ionic activity coefficients

$$\gamma_{\pm} = \left[\frac{K_1 m_{SO_2 \cdot H_2O}}{(m_{HSO_3^-})^2}\right]^{1/2} \quad (4)$$

To analyze the spectrophotometric data of this study an accurate value of the hydrated sulfur dioxide molecular absorptivity, ϵ, must be known. Since the reported literature values range from 500 L mol^{-1} cm^{-1} (Scoggins[20]) to 610 L mol^{-1} cm^{-1} (Bhetty[21]), a new method was devised to evaluate indirectly the molecular absorptivity from the absorbance measurements of this study.

Ionic activity coefficients are generally expressed by an equation originally proposed by Guggenheim:[22]

$$\ln \gamma_{\pm} = -\frac{A_\gamma |Z_+ Z_-| I^{1/2}}{1 + B_\gamma a_i I^{1/2}} + 2\beta I \qquad (5)$$

In eq 5, A_γ and B_γ are the Debye–Hückel constants, β is the specific interaction parameter, and a_i is the closest approach distance. The procedure used to determine the molecular absorptivity assumes that for concentrations less than 0.01 M the mean ionic activity coefficients of the H^+, HSO_3^- ion pair are accurately described by the first term of eq 5 (the classical Debye–Hückel expression) using a value of 5 Å for a_i. The validity of this assumption was justified by a comparison of experimental activity coefficients for other 1–1 electrolytes of comparable size[10] with those predicted by the Debye–Hückel expression, which accurately represented the activity coefficient data to ±0.5% up to 0.01 M. Substitution of the Debye–Hückel expression in eq 4 results in

$$\exp\left[\frac{-2.352(m_{HSO_3^-})^{0.5}}{1.0 + 1.643(m_{HSO_3^-})^{0.5}}\right] = \frac{K_1 m_{SO_2 \cdot H_2O}}{(m_{HSO_3^-})^2} \qquad (6)$$

Further substitution of eq 3 and Beer's law into eq 6 relates the absorbance A for a pathlength l to K_1 in terms of ϵ

$$\frac{A}{\epsilon l} = \frac{\left(m_{S^{4+}} - \frac{A}{\epsilon l}\right)}{K_1} \times \exp\left[\frac{-2.352\left(m_{S^{4+}} - \frac{A}{\epsilon l}\right)^{0.5}}{1.0 + 1.643\left(m_{S^{4+}} - \frac{A}{\epsilon l}\right)^{0.5}}\right] \qquad (7)$$

With the absorbance data for concentrations less than 0.01 M from this work and Ratkowsky and McCarthy's[9] results the unknown parameters of eq 7 can be evaluated.

Since the molecular absorptivity, ϵ, should remain constant over this limited concentration range the criterion used to obtain the best values of K_1 and ϵ was a minimum in the function

$$\sum_{\substack{\text{data} \\ \text{points}}} [\epsilon(\text{exptl}) - \epsilon(\text{av})]^2 \qquad (8)$$

where ϵ(av) is the average of all the experimental ϵ values for a given value of K_1. A scanning of parameter space for values of K_1 and ϵ to obtain the best fit of the experimental data to eq 7 results in a sharp minimum in the standard deviation in ϵ, occurring when the dissociation constant is approximately 0.0138 ±0.0004 M. This result further supports the value of 0.0139 ± 0.0002 M as determined conductometrically. The corresponding molecular absorptivity is 498 ± 6 L mol^{-1} cm^{-1}.

Using the dissociation constant and molecular absorptivity as calculated above, activity coefficients can now be calculated for the remaining data of concentration greater than 0.01 M using eq 4. The resulting mean ionic activity coefficients are shown in Figure 3 as a function of the bisulfite ion concentration. When these data are fit to the entire eq 5, the resulting value of β, the specific interaction parameter, is 0.3 ± 0.08. This value compares very favorably with those of other 1–1 electrolytes of comparable size (Guggenheim and Turgeon[23]). Also seen in Figure 3 are the mean activity coefficients calculated using Tartar and Garretson's[3] value of the equilibrium constant, 0.0172 M, and the molecular absorptivity of Ratkowsky and McCarthy,[9] 608 L mol^{-1} cm^{-1}. As shown, the resulting activity coefficients are substantially lower than the range generally accepted for 1–1 electrolytes.

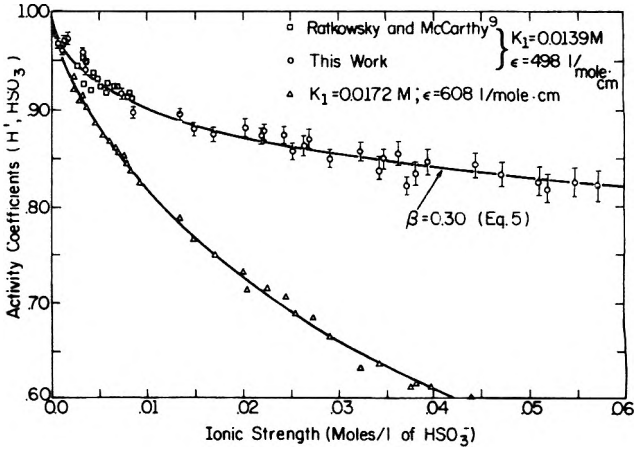

Figure 3. Mean ionic activity coefficients for the H^+, HSO_3^- ion pair at 25 °C.

The results of this work are in excellent agreement with those of Britton and Robinson[6] (K = 0.0139 M), Ellis and Anderson[7] (K = 0.0139 M), and Deveze and Rumpf[8] (K = 0.0142 M), but considerably lower than the often used value of 0.0172 M as determined by Tartar and Garretson[3] and Beilke and Lamb.[4]

We conclude from both conductivity and spectrophotometric data that the dissociation of hydrated sulfur dioxide in water at 25 °C is accurately described by a thermodynamic dissociation constant of 0.0139 ± 0.0002 mol L^{-1}, and the Guggenheim equation for the activity coefficients with a value for the interaction parameter, β, of 0.3.

References and Notes

(1) Supported in part by the National Science Foundation and the U.S. Environmental Protection Agency.
(2) N. Yui, *Tokyo Inst. Phys. Chem. Bull.*, **19**, 1229 (1940).
(3) H. V. Tartar and H. H. Garretson, *J. Am. Chem. Soc.*, **63**, 808 (1941).
(4) S. Beilke and D. Lamb, *AIChE J.* **21**, 402 (1975).
(5) H. F. Johnstone and P. W. Leppla, *J. Am. Chem. Soc.*, **56**, 2233 (1934).
(6) H. T. S. Britton and R. A. Robinson, *Trans. Faraday Soc.*, **28**, 531 (1932).
(7) A. J. Ellis and D. W. Anderson, *J. Chem. Soc. London*, 1765 (1961).
(8) D. Deveze and P. M. Rumpf, *Compt. Rend.*, **258**, 6135 (1964).
(9) D. A. Ratkowsky and J. L. McCarthy, *J. Phys. Chem.*, **66**, 516 (1962).
(10) G. N. Lewis and M. Randall, Revised by K. S. Pitzer and L. Brewer, "Thermodynamics", 2nd ed, McGraw-Hill, New York, N.Y., 1961.
(11) R. M. Fuoss, J. E. Lind, Jr., and J. J. Zwolenik, *J. Am. Chem. Soc.*, **81**, 1557 (1959).
(12) R. M. Fuoss and F. Accascina, "Electrolytic Conductance", Wiley-Interscience, New York, N.Y., 1959.
(13) R. M. Fuoss, L. Onsager, and J. F. Skinner, *J. Phys. Chem.*, **69**, 2581 (1965).
(14) R. Burg, M. G. Justice, and J. C. Justice, *C. R. Acad. Sci. Paris*, **268**, 670 (1969).
(15) H. H. Rosenbrock, *Comput. J.*, **3**, 175 (1960).
(16) J. Kielland, *J. Am. Chem. Soc.*, **59**, 1675 (1937).
(17) W. B. Campbell and O. Maass, *J. Res.*, **2**, 42 (1930).
(18) C. P. Kerp and Baar, *Arb. Kais. Gesund.*, **26**, 297 (1907).
(19) J. Lindner, *Monatsh. Chem.*, **33**, 613 (1912).
(20) M. W. Scoggins, *Anal Chem.*, **42**, 1091 (1970).
(21) M. K. Bhetty, *Anal. Chim.*, **55**, 263 (1971).
(22) E. A. Guggenheim, *Phil. Mag.*, **19**, 588 (1935).
(23) E. A. Guggenheim and J. C. Turgeon, *Trans. Faraday Soc.*, **51**, 747 (1955).

The State of Electrodeposited Hydrogen at Ruthenium Electrodes

S. Hadži-Jordanov,† H. Angerstein-Kozlowska, M. Vukovič,‡ and B. E. Conway*

Chemistry Department, University of Ottawa, Ottawa, Ontario, Canada *(Received July 12, 1977)*

Electrochemical measurement of H accommodation at noble metal electrocatalyst surfaces is important for evaluation of real areas of electrode preparations and hence of intrinsic electrocatalytic properties; it is also required for evaluation of the relative degrees of surface oxidation of noble metals under anodic conditions. Experiments are described which show that a region of underpotential deposition and ionization of adsorbed H atoms is difficult to define at Ru electrodes due to (a) H sorption into the metal and (b) overlap with surface oxidation and reduction processes owing to the fact that Ru surfaces already begin to be oxidized near to, or in, the potential region where H atom deposition and ionization processes occur. It is shown that some conclusions reached in other work on the state of electrodeposited H at Ru may have to be revised. In the presence of the Cl^- ion, which is strongly adsorbed at Ru, the behavior of Ru electrode surfaces in cyclic voltammetry becomes more like that of Pt.

I. Introduction

Considerable interest in the electrochemical behavior of Ru electrodes has arisen in recent years, especially on account of the use of Ru in various forms as the anode material for commercial electrolytic Cl_2 evolution.

It is well known that atomic hydrogen can be "underpotentially" deposited at Pt, Rh, and Ir electrodes. While is has been commonly thought that two states of chemisorbed H are involved at Pt below monolayer coverage,[1,2] recent work in very clean and dilute solutions demonstrates[3] that, in fact, four and sometimes five distinguishable states can be resolved, even on well-prepared single crystals. At Pd, H is both chemisorbed on the surface and sorbed into the metal.[4]

The behavior of H at Ru electrodes[5-18] is less well characterized because at bulk Ru no well-resolved current regions for H deposition and ionization were observed in potentiodynamic measurements[11,12] or in charging curves[13] as they are at Pt[1,3] although Stoyanovskaya et al.[13] reported studies on H adsorption at Ru in 1962 and 1963.

As in the case of Pt, and other electrocatalyst noble metals, characterization of the state of the surface of Ru requires, if possible, knowledge of the state and coverage of Ru by H near the reversible H_2 potential in order to provide an in-situ real-area measurement. The latter is of great importance for distinguishing real improvements in electrocatalytic performance of electrodes for reactions such as H_2 and Cl_2 evolution, or O_2 reduction, when various electrode surface preparations are made, from the more trivial, but practically important, effects of increased real surface area per apparent cm^2. Also, the state of oxidation of Ru surfaces (viz the O or OH:Ru ratios) at more positive potentials is of interest in regard to kinetics of Cl_2 and O_2 evolution on Ru or Ru-based anodes, and comparatively with regard to surface oxidation behavior of other noble metals. Electrochemical evaluation of the degree of oxidation of Ru surfaces requires knowledge of real areas or the charge for H atom coverage at the electrode metal. In a number of recent papers, the electrocatalytic properties of Ru ad-atoms[15] and of Ru alloys[16-18] were studied in relation to the states of surface oxidation[14] of the metals, the H adsorption[16] and the state of deposited Ru atoms.[15]

Previous work on H adsorption at Ru is conflicting[5,8] due to (a) the overlap[9] between regions of H deposition and surface oxide reduction, or between H ionization and surface oxide formation, a difficulty that does not arise at Pt except to some extent in alkaline solutions in cathodic potentiodynamic sweeps; (b) significant absorption of H into the metal,[6,10] and to (c) reoxidation of evolved H_2.

In a previous note[9] we showed that by using potentiodynamic sweeps over a restricted potential range, a region of the potentiodynamic current (i)–potential (V) profile near the H_2 reversible potential could be resolved at ruthenized Pt or ruthenized bulk Ru, and appeared to be associated with deposition and ionization of H. It was also shown that due to irreversibility of reduction of the surface oxide film formed on Ru electrodes that had been cycled more anodically than ca. 0.8~1.0 V E_H, H deposition processes, which might normally be observed in the cathodic sweep, are obscured by slow reduction of surface oxide. Even with more restricted anodic polarization, considerable overlap appears to exist between the "hydrogen region" on Ru and the region where initial stages of surface oxide formation and reduction arise. This is probably one of the reasons why at bulk Ru very little structure in the i–V profile had been resolved in some of the previous work.[11,12]

Potentiodynamic studies on Ru were reported by Zakumbaeva and Shapovalova[5] who presumed incorrectly (see below) that the currents in the hydrogen region were associated with H chemisorption, as at Pt. Bagotskii et al.[6] also reported potentiodynamic studies on Ru but concluded that absorption of H played an important role in the case of Ru electrodes, a factor that was recorded qualitatively in early literature.[10]

In the present paper, we describe results which lead to better identification and resolution of the processes occurring in the "hydrogen region" at Ru by (a) cyclic potentiodynamic measurements; (b) microcurrent-efficiency determinations for H_2 evolution in relation to H absorption; and (c) relative reflectance measurements.

II. Experimental Section

(i) *General Technique and Solution Preparation.* The electrochemical study of the surface processes occurring at Ru electrodes was made mainly by the potentiodynamic method. A Servomex LF 141 or a Tacussel type voltage

† On leave of absence from University of Skopje, Faculty of Technology and Metallurgy, Skopje, Yugoslavia.

‡ On leave of absence from Laboratory for Electrochemistry, Center for Marine Research, "Ruder Boskovic" Institute, Zagreb, Croatia, Yugoslavia.

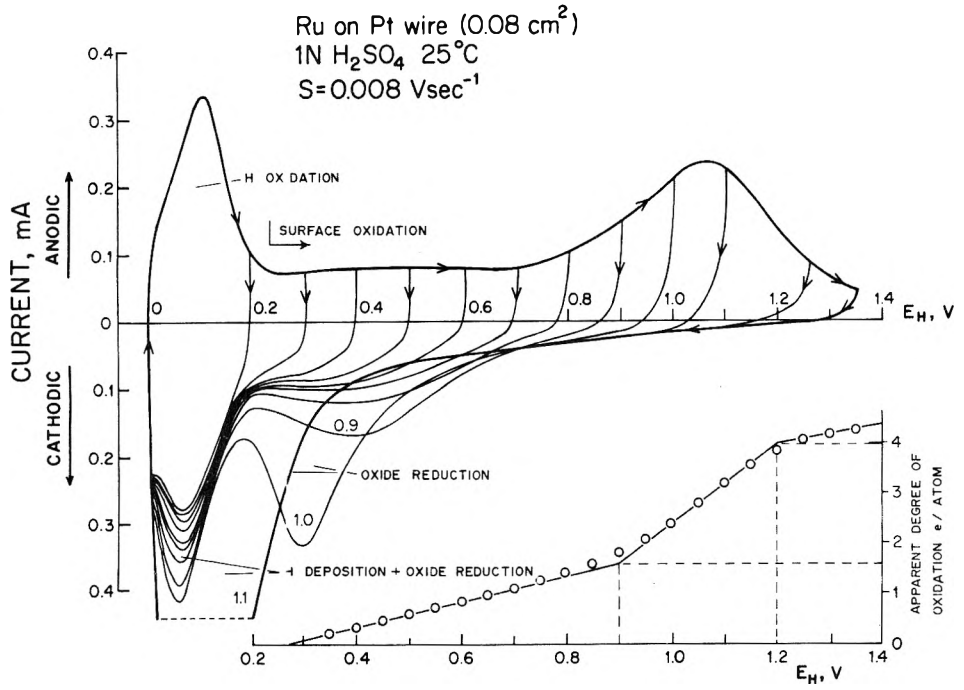

Figure 1. Potentiodynamic i–V profiles at ruthenized Pt in 0.5 M H_2SO_4 at 25 °C showing resolution of an "hydrogen region". (From ref 9.)

function generator was employed to provide various potentiodynamic voltage–time programs addressed to a Wenking potentiostat.

The general techniques employed have been described in detail previously,[19,20] as in work on Pt. All solutions were prepared in pyro-distilled water and cells were soaked in this water after having been cleaned in pure 100% H_2SO_4. The requirements for use of pyro-distilled water and characterization of impurity effects that can arise with presently available distilled waters have been fully discussed in previous papers.

Aristar grade BDH H_2SO_4 was employed for preparing all acid electrolytes used in this work.

All potentiodynamic experiments were carried out in solutions deoxygenated by passage of purified N_2 and with N_2 being passed above the previously deoxygenated solution in the cell.

(ii) *Electrode Materials.* Most electrodes were prepared by ruthenizing a Pt wire electrode, sealed in soft-glass, from an aqueous solution of $(NH_4)_2RuCl_6$ prepared in pyro-distilled water. In some experiments, in order to demonstrate that the behavior observed (see below) was not due to any other noble metal impurities in the Ru salt used for plating, Ru was dissolved anodically from a pure, zone-refined Ru rod in purified NaOH solution and this solution was used subsequently for the ruthenization. No significant difference in the behavior of the resulting ruthenized surface was apparent. Comparative experiments were also made on a polished Ru rod electrode sealed in glass. This electrode was also employed for reflectance measurements.

(iii) *Reflectance Measurements.* Relative reflectance, $\Delta R/R$, measurements were made in the parallel mode as a function of potential using a repetitive potentiodynamic linear voltage sweep.[2,28] The reflectance changes were monitored with an EMI photomultiplier and addressed repetitively to a Northern Scientific Signal averager. 20–100 sample read outs were taken periodically, giving a $(\Delta R/R_{\|}$ vs. V profile with good signal-to-noise ratio.

(iv) *Currents and Current Densities.* Owing to the problem of defining real areas of electrodes in the case of Ru by H accommodation, because of H absorption (as found in this paper and ref 6), currents rather than current densities are given on most of the graphs in this paper; similar problems arise in evaluations of charges per unit real area.

(v) *Current Efficiency in H_2 Evolution and H Absorption.* Part of the problem of understanding the behavior in the "hydrogen region" at Ru arises from the possibility of simultaneous H adsorption and absorption, as well as H_2 evolution. Microcurrent-efficiency measurements were made at a bulk Ru electrode in special cell consisting of a small vessel containing both a Pt and a Ru cathode with provision for a common counter anode. At the top of the cell is a gas exit capillary which supports a drop of dilute aqueous H_2SO_4 through which individual bubbles of the evolved H_2 pass periodically during electrolysis in the cell below. Two Pt microelectrodes in the drop are connected to an external recorder circuit which indicates the rate of appearance of the bubbles. The latter, as they appear above the capillary, cause a break in the bubble-evolution recorder circuit. Accurate and reproducible bubble evolution rates can be obtained at a given electrolysis current.

Bubble evolution rates were alternately recorded at the Pt and Ru cathodes, so that relative current efficiencies for H_2 evolution at Pt and Ru could be evaluated.

III. Results and Discussion

(i) *Form of Potentiodynamic Current–Potential Profiles.* Although, at bulk Ru, no well-resolved hydrogen region can be observed,[11,12] at ruthenized Pt or ruthenized bulk Ru electrodes an apparent "hydrogen region" can be distinguished over the potential range +0.2 to +0.05 V vs. the H_2 reversible potential (E_H) in the same solution, provided the electrode has not been too strongly oxidized (potentials not taken over ca. 0.4 V E_H); this hydrogen region can be observed in both cathodic and anodic sweeps (Figure 1).

As has been stressed, identification of a possible region of atomic H chemisorption, as at Pt, would be important in providing a basis for real electrochemical area measurement at Ru and hence proper evaluation of the significance of the oxidation charges for, and coverage by, the

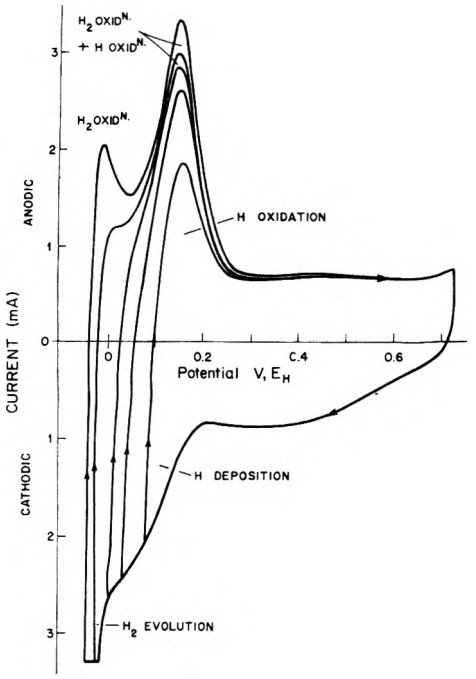

Figure 2. Potentiodynamic $i-V$ profiles at ruthenized Pt showing regions of H_2 reoxidation and ionization of ad- and absorbed H (0.5 M H_2SO_4, 25 °C).

various species in the surface oxidation of Ru that occurs at more positive potentials.[9] It would also be useful for measurement of real areas for evaluation of intrinsic electrocatalytic properties of Ru, e.g., for Cl_2 evolution.

However, the potentiodynamic currents observed in the hydrogen region at Ru electrodes do not exhibit the same behavior as those observable for H deposition and ionization at Pt, which have led to an unambiguous interpretation in terms of underpotential deposition of a monolayer of adsorbed H. Hence the question which first arises for Ru is what is the charge associated with H adsorption, as at Pt.[23,24] To answer this question experimentally turns out to be unusually difficult due to (a) coabsorption of H; (b) coadsorption of O species; and (c) coevolution of H_2; the latter problem arises because significant currents for H_2 evolution appear in the cathodic sweep at electroplated Ru at potentials somewhat more positive (in N_2-saturated solution) than they do at Pt and corresponding H_2 reoxidation currents also arise on the following anodic sweep. This behavior is probably due to the active state of the plated surface as it is not observed at a bulk Ru surface.

(ii) *Role of H_2 Reoxidation in the Sweep.* At active Ru electrodes, it is difficult to avoid significant H_2 evolution at the end of the cathodic sweep unless the potential range of the sweep is unduly restricted in the cathodic direction. These effects are larger than at Pt over the same potential range. Hence, experiments in which the hydrogen ad- or absorption region is to be investigated can be complicated by some reoxidation of evolved H_2 in the anodic sweep. If part or all of the anodic peak at 0.05–0.2 V in Figure 1 were due to oxidation of H_2 generated in the previous cathodic sweep, then stirring should diminish it. This is found to be the case but only to a relatively small extent; a small H_2 oxidation current is also seen over the whole potential range in sweeps taken to +0.6 V E_H. Holding the potential at the negative end of the sweep increases the following anodic peak but this is as expected and arises because of either (or both) H_2 evolution and reoxidation, or H absorption. However, by appropriate choice of conditions (Figure 2), a region of ad- and absorbed H

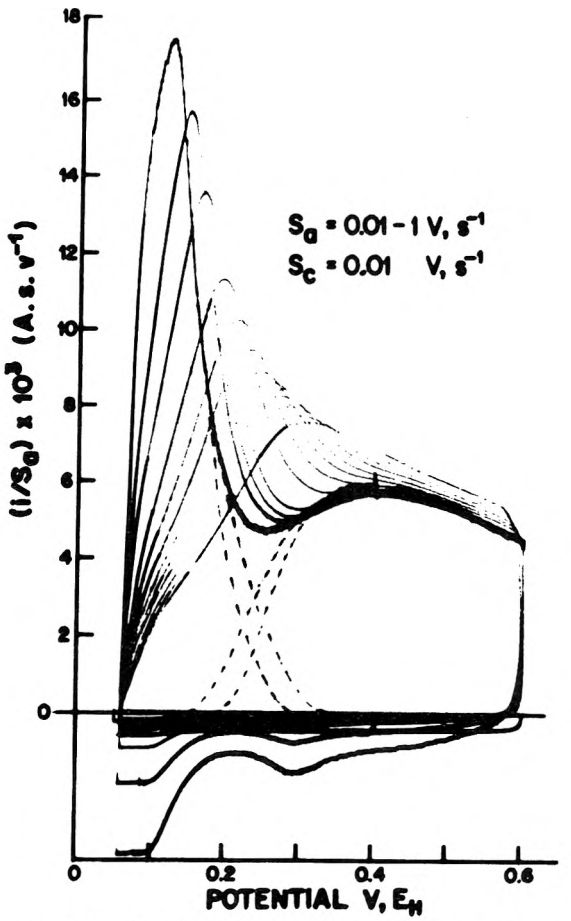

Figure 3. I_a/s values as a function of potential for anodic potentiodynamic sweeps at 0.01–1.0 V s^{-1} (for ruthenized Pt, 25 °C, 0.5 M H_2SO_4) following cathodic sweeps at 0.01 V s^{-1}.

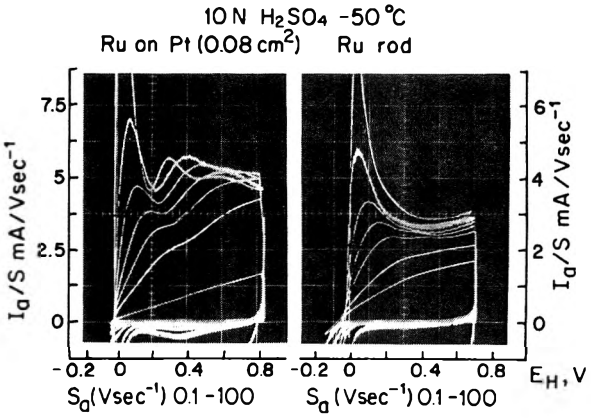

Figure 4. I_a/s values as a function of potential in fast anodic potentiodynamic sweeps at 0.1–100 V s^{-1} at a ruthenized Pt and an auto-ruthenized Ru rod electrode (–50 °C, 5 M aqueous H_2SO_4) following cathodic sweeps at 0.01 V s^{-1}.

desorption in the anodic sweep can be resolved from the region of H_2 reoxidation, although it is clear that appreciable overlap of these processes on the potential scale still occurs and is complicated (see section v) by onset of surface oxidation at potentials much lower than those where such processes commence at Pt. Attempts to improve the resolution by going to high or low temperatures were not successful (cf. ref 20).

(iii) *Absorption and Adsorption of H at Ru.* Normally underpotential deposition of chemisorbed H and its ionization would be readily identified by observation of an independence of peak currents divided by sweep rate, i_p/s, on s except in the range of sweep rates, s, over which

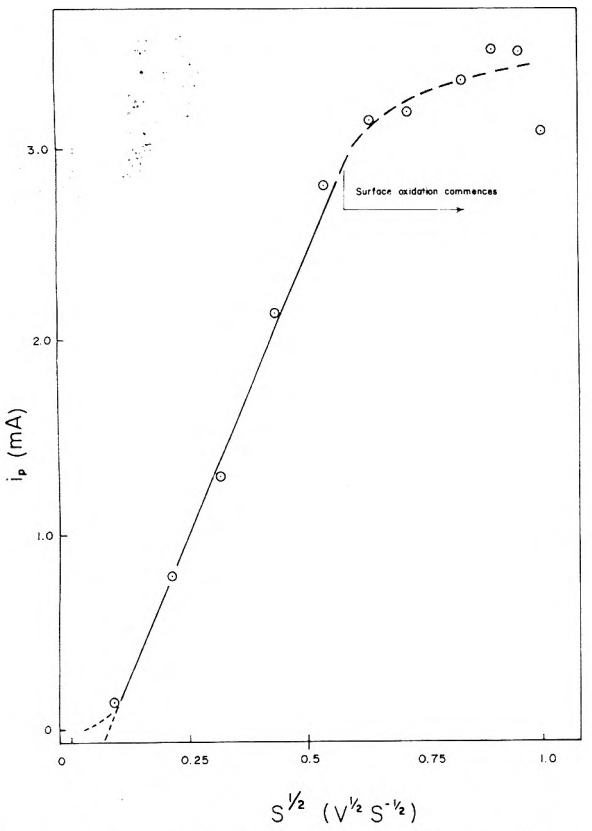

Figure 5. Plot of i_p vs. $s^{1/2}$ corresponding to the data of Figure 3.

a transition from reversible to irreversible behavior occurs.[25] At Ru, this behavior is not observed, as is shown in Figure 3. From this figure and from corresponding oscilloscope photos (Figure 4) made at faster sweep rates and low temperatures, it is clear that the quantity of charge passed in anodic sweeps over the hydrogen region at ruthenized electrodes diminishes with increasing s; in these figures, a *constant* cathodic sweep rate is employed to ensure a common state and quantity of deposited H prior to its ionization at various sweep rates in following anodic sweeps.

The peak currents for H oxidation processes can be obtained from Figure 3 by subtracting out the i/s component due to surface oxidation which arises above ca. 0.2 V E_H and multiplying by s. When the resulting corrected peak currents, i_p, corresponding to the curves of Figure 3, are plotted against $s^{1/2}$ the relation shown in Figure 5 is obtained. Up to ca. s = 0.36 V s^{-1}, i_p is linear in $s^{1/2}$ indicating the role of a diffusion process while beyond this value of s, i_p becomes less dependent on $s^{1/2}$. Since the solution is 0.5 M in H_2SO_4, the apparent diffusion limitation cannot arise from any species in solution and is hence probably associated with diffusion of H, deposited in the previous cathodic sweep, out from the metal. The linear region should extrapolate to the origin in Figure 5. The significant deviation of the experimental data from this requirement is probably due to a residual cathodic current component associated with slow surface oxide reduction. The deviation from linearity in $s^{1/2}$ at s > 0.36 V s^{-1} is probably due to appearance of oxide on the surface (see below) as, beyond this sweep rate, H oxidation currents are superimposed on currents for the initial stage of surface oxidation (see Figure 3). Also, for these sweep rates, the corrections for background surface oxidation currents become difficult to make reliably.

At the higher sweep rates, the H-ionization processes are displaced to more and more positive potentials. Then the i/s profiles for various s values approach a common line

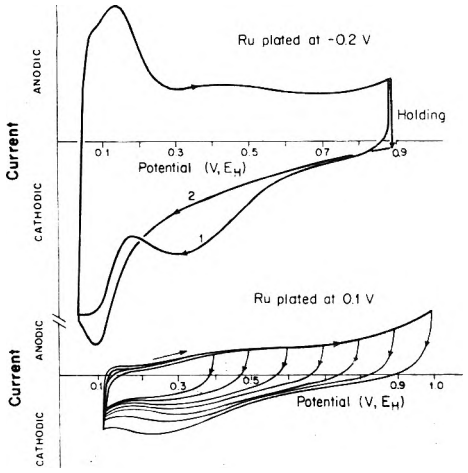

Figure 6. Comparison of potentiodynamic $i-V$ profiles at ruthenized Pt electrodes plated with Ru at either -0.2 or +0.1 V E_H (data are shown for two electrodes having different real areas).

(at potentials >0.3-0.35 V) characteristic of a true surface process (Figure 3). However, this surface process appears to be due to surface oxidation rather than to ionization of chemisorbed H.

At sufficiently high sweep rates in the *cathodic* direction, it might be supposed that mainly the surface process of H deposition, rather than H absorption, could be observed, as in the case of Pd.[4] However, irreversibility in the H deposition process and the problem of overlap with cathodic H_2 evolution makes such an experiment unproductive.

The role of H absorbed into Ru in determining the form of the $i-V$ profiles is further indicated, albeit indirectly, by the different behavior which is found (Figure 6) at electrodes that have been potentiostatically ruthenized at -0.2 V, i.e., with coevolution of H_2, or at +0.1 V in the absence of H_2 evolution. The electrode plated at +0.1 V shows much less tendency to exhibit a region of H ad- and absorption, and behaves more like a solid Ru rod electrode. Possibly, when plating is carried out with coevolution of H_2, a more disordered or expanded Ru structure is electrodeposited that is capable of admitting atomic H with increased facility. These results lead to the conclusion that a diffusion-controlled process dominates the electrochemical behavior in the hydrogen region at Ru. It cannot be associated with any concentration gradients of the aqueous proton itself under the conditions employed, so it is clear that diffusion of absorbed H within the metal must be involved. In fact, reference is made in the older literature[10] to absorption of H in Ru.

(iv) *Attempts to Resolve a Region of Underpotential Deposition/Desorption of H.* Several experiments were conducted in order to try to identify a region where only a simple process of electrochemisorption of H was involved, viz. $Ru + H^+ + e^- \rightarrow RuH_{ads}$, or the reverse process in anodic sweeps.

(a) *Sweep Experiments under Special Conditions.* Potentiodynamic experiments were made at low and elevated temperatures and at various sweep rates (Figures 3 and 4). Only in 10 N aqueous H_2SO_4 at 85 °C (Figure 7) was a small peak resolved for which i_p/s was independent of s and hence probably associated with ionization of adsorbed H. This assignment receives some confirmation from the fact that a matching peak occurs in the cathodic i/s vs. V profile at the same potential (Figure 7).

(b) *Reflectance Measurements.* At Pt, monolayer deposition of H causes characteristic changes of relative reflectance, $\Delta R/R$, distinguishable from the "double-

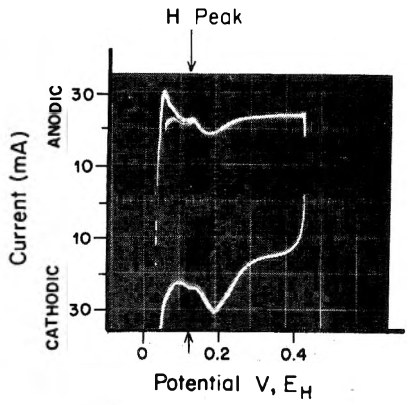

Figure 7. Fast sweep $i-V$ profiles for a Ru rod electrode at 85 °C in 10 N H_2SO_4 showing peaks for H adsorption distinguishable from those for H_2 evolution and H absorption, or the reverse processes.

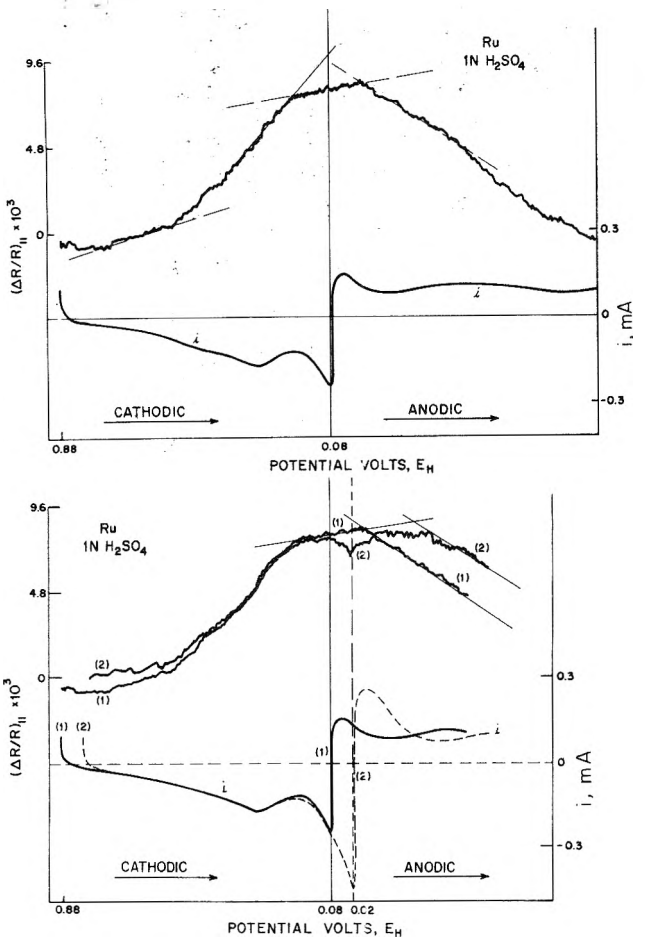

Figure 8. Relative reflectance $(\Delta R/R)_{||}$ behavior of a polished Ru rod electrode in 0.5 M H_2SO_4 as a function of potential in relation to the potentiodynamic $i-V$ profiles: (a, upper) cycled to +0.08 V, E_H; (b, lower) cycled to +0.02 V, E_H and to 0.08 V, E_H.

layer"[2,29] electroreflectance effect. In particular, near the H_2 reversible potential at high H coverage, the chemisorbed H species at Pt gives a negative $\Delta R/R$ contribution while a positive $\Delta R/R$ arises up to about half-coverage. Reflectance experiments were performed at a polished Ru rod surface in order to see if a region of similar behavior could be detected which might indicate H adsorption. The results are shown in Figure 8a,b. Figure 8a shows that below 0.2 V E_H, down to 0.08 V, a region of $(\Delta R/R)_{||}$ behavior arises which is different from that at more positive potentials and presumably corresponds to an oxide-free surface. Extending the potential to 0.02 V gives the behavior shown in Figure 8b (curve 2) which shows

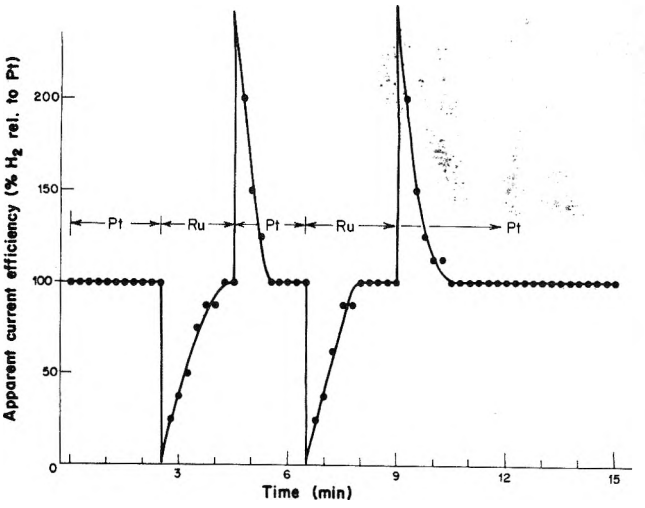

Figure 9. Relative microcurrent efficiencies for H_2 evolution (in comparison with H deposition and sorption) at Pt and Ru rod electrodes in 0.5 M H_2SO_4, 25 °C, determined in the special cell.

clearly that at potentials less positive than ca. 0.12 V E_H, a *negative* contribution in $\Delta R/R$ arises and is more or less reversible with respect to change of potential around 0.02 V E_H. This behavior is similar to that of weakly bound H at Pt and hence could be due to H adsorption. However, the possibility cannot be excluded that there is a component associated with change of the electronic properties of Ru near its surface due to H absorption. Nevertheless, it is clear that the state of the surface is optically different between 0.02 and 0.2 V E_H in the "hydrogen region" from that at more positive potentials where formation of surface oxide becomes significant (see section vi).

(v) *H Absorption and Microcurrent Efficiency of H_2 Evolution.* An attempt was made, using the apparatus described in the Experimental Section, to provide an independent and more direct proof of the role of H diffusion into and out from the metal. An aqueous solution of H_2SO_4 was electrolyzed at constant current alternately at Pt and bulk Ru cathodes in the same cell compartment with a common Pt wire anode. The rates of H_2 bubble evolution were compared at the Ru and Pt cathodes over ca. 2-min periods. Relative to values determined from the bubble evolution rate at Pt, current efficiencies for H_2 evolution at Ru were initially repeatedly lower than at Pt (Figure 9) but approached the Pt value (taken as 100%) after 2 min. This provides a clear indication of H absorption into Ru.[32] Upon returning the electrolysis to the Pt cathode, current efficiencies were apparently temporarily higher than 100% which must have been due to some continuation of H_2 evolution from the Ru electrode on open circuit due to desorption of H absorbed in the metal with recombination of form H_2. Figure 9 shows that the behavior on successive electrolyses at Pt and Ru is quite reproducible.

(vi) *Relation to Supposed H-Adsorption Behavior Observed by Bagotskii et al.*[6] Tuseeva, Skundin, and Bagotskii[6] observed a peak in cathodic sweeps at Ru at ca. 0.25 V E_H and attributed it mainly to H absorption.[33] This result requires further examination as it was not found in our initial work. A series of experiments was carried out at a Ru rod electrode in the region 0.05 to 0.4 V E_H in order to attempt to resolve the question whether the behavior in this potential range in *cathodic* sweeps is due to H deposition and diffusion processes or to reduction of an oxide species generated already at low positive potentials (0.2–0.3 V E_H) near the "hydrogen" region in the previous anodic sweep.

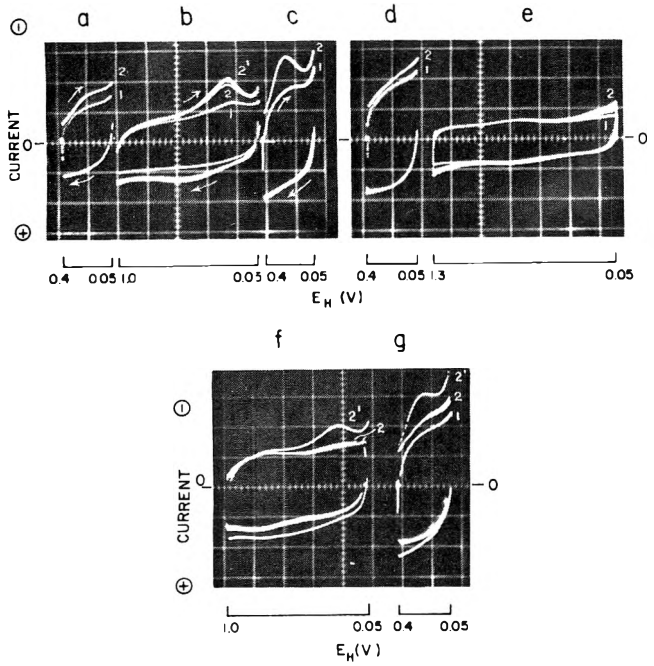

Figure 10. Potentiodynamic $i-V$ curves for a Ru rod in 0.5 M H_2SO_4 at 298 K: (a) cycled over the range 0.40–0.05 V E_H; (b) cycled between 1.0 and 0.05 V E_H; (c) cycled again over the range 0.40 to 0.05 V E_H; (d) cycled between 0.4 and 0.05 V; (e) cycled again over the range 1.3–0.05 V E_H; (f) condit oning cycle again between 1.0 and 0.05 V E_H; (g) cycled again between 0.40 and 0.05 V without and with holding at 0.40 V for 20 and 60 s. Curves 1 for repetitive sweeps; curves 2, 2' for 20 and 60 s holding at 0.40 V.

Cathodic, followed by anodic, potentiodynamic $i-V$ profiles were recorded after holding the potential at various values in the potential range 0.4–0.05 V E_H. The processes which are observable in this potential range depend on the electrochemical prehistory of the Ru electrode. Figure 10a shows the cathodic and anodic $i-V$ profiles for Ru if the electrode potential is cycled over the potential range 0.40–0.05 V. If, however, the potential is cycled first to 1.0 V (Figure 10b) and then returned to the range 0.40–0.05 V, the $i-V$ profiles of Figure 10c are generated, showing an oxide reduction peak[9] due to the prior oxidation to 1.0 V. In Figure 10b, oxide reduction peaks are, of course, observed as reported previously.[9] If the electrode had been previously cycled to +1.3 V, no reduction peak is observed (Figure 10d) on the cathodic sweep since the reduction is then too slow to be seen (the oxide is reduced in the H_2-evolution region) except at very low sweep rates. In Figure 10, curves numbered 1 are for repetitive sweep conditions while curves 2, 2' are for holding at 0.40 V for 20 and 60 s prior to application of the following cathodic sweep. Under the latter conditions, a *cathodic* peak *is* generated similar in shape to that observed by Bagotskii et al.[6]

Subsequent cycling in the range 0.4–0.05 V gives the $i-V$ profiles of Figure 10e (with and without holding for 60 s at 0.40 V) which show no cathodic peak at ca. 0.23 V. Returning to a preconditioning cycle up to 1.1 V gives the results shown in Figure 10f and subsequently those of 10g when the potential range is returned to 0.40–0.05 V. The behavior in the latter figure is similar to that in 10c. The peak at ca. 0.23 V is again generated upon holding at 0.40 V for 60 s and therefore seems to be a definite feature of the behavior of Ru.

It is useful to investigate the effect of sweep rate (s) in this potential region (0.40–0.05 V); a reversible surface process will generate profiles having constant i/s values while transition from a reversible to irreversible surface

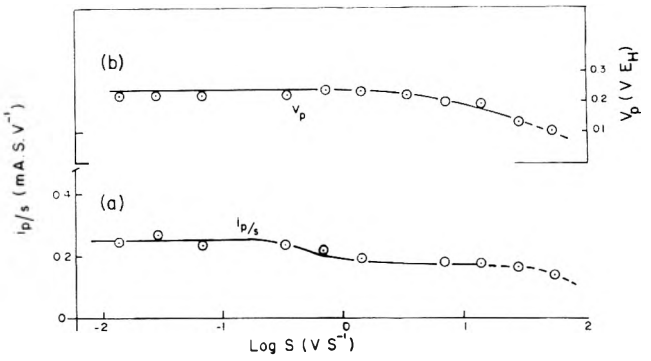

Figure 11. (a) Reduced peak currents i_p/s (pseudocapacitance) plotted vs. log s for the cathodic peak observed at a Ru rod electrode in 0.5 M H_2SO_4 at 298 K in sweeps over the potential range 0.40–0.05 V E_H. (b) Corresponding peak potentials, V_p, as a function of log s.

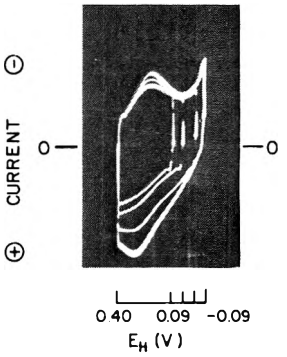

Figure 12. Effects of holding the potential for 1 s at 0.40 V on the $i-V$ profiles of the subsequent cathodic sweep, and of holding for 1 s at various less positive potentials at the end of the cathodic sweep, on the subsequent anodic $i-V$ profiles, s = 20 V s^{-1}.

process involves[25,31] a 22% diminution of peak values of i/s. If a diffusion process of H entering the Ru lattice were involved, then i would be proportional to $s^{1/2}$ (Figure 3) or i_a/s would decrease with $s^{1/2}$. Figure 11 shows the results of changing the sweep rate over a wide range (3–4 decades) expressed in terms of plots i_p/s vs. log s (cf. ref 26 and 31). Certainly i_p/s does not diminish linearly with $s^{1/2}$ as for a diffusion-controlled process; it does decrease somewhat but only by 15% over a $10^{2.5}$-fold range of s. Correspondingly, the peak potential is almost independent of log s except beyond log s = 1 where irreversibility and/or some iR drop effects arise. The s_0 value[27] is hence quite large.

The results in Figure 11 indicate that the process associated with the cathodic peak at ca. 0.23 V is (a) kinetically quite fast since[25,27,31] V_p is independent of s up to quite high s values and (b) is not simply a diffusion-controlled one, although it may contain a small component (in terms of current) that is diffusion controlled.

Since the $i-V$ profiles in Figure 10c were obtained after a number of cycles only over the region 0.4–0.05 V, and they are reproducible, they cannot arise from any continuing reduction of oxide previously formed in the preconditioning cycle to 1.0 V. Similarly the effect of holding at 0.40 V could hardly be due to such reduction. Rather, it seemed that the holding effect at 0.40 V could be due to increased formation of an almost reversibly generated state of surface oxidation. A number of experiments was therefore conducted by holding the potential at a series of values at and below 0.40 V and at the negative end of the sweep, and by varying the time of holding at 0.4 V. The results are shown in Figure 12.

It is clear from Figure 12 that the peak on the cathodic sweep at ca. 0.23 V has a peak on the corresponding following anodic sweep that *appears* to be conjugate to it,

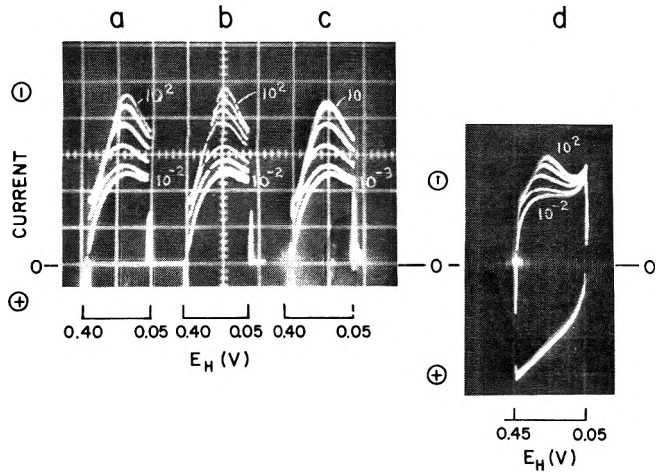

Figure 13. Effects of holding the potential at 0.4 V for various times from 10^{-3} to 100 s with 1 s hold at the end of the cathodic sweep at 0.05 V; $s = 20$ V s^{-1}: (a) 10^{-2}, 10^{-1}, 1, 10, and 10^2 s; (b) 10^{-2}, 10^{-1}, 1, 10, 1, and 10^2 s; (c) 10^{-3}, 10^{-2}, 10^{-1} 1, and 10 s; (d) as in (a) but showing common anodic profile after cathodic sweeps, following holding at 0.40 V E_H.

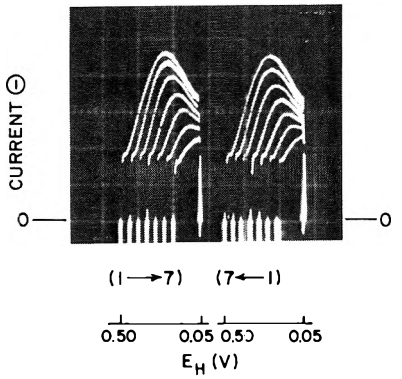

Figure 14. Effects of holding the potential for 1 s at each end of sweep from 0.50 to 0.05 V over a successive range of potentials cut (a, left) from the more positive side and (b, right) from the less positive side. s = 20 V s^{-1}.

as in a reversible electrochemical surface process,[31] e.g., H at Pt. However, if the potential range of the sweep is diminished from the negative end, the anodic peak disappears while that on the cathodic sweep remains. Hence the cathodic peak at ca. 0.23 V is in no way related to the anodic peak seen at a similar potential. Part of the anodic peak current is due to reoxidation of H_2.

The family of curves in Figure 13a–c show the effect of holding the potential at 0.4 V for various times, 10^{-2} to 100 s. The growth of the cathodic peak is approximately logarithmic in time. Although the peak potentials remain almost constant (Figure 13a,b) there can be some variation depending on electrochemical cycling history. Since the cathodic peak grows with time but is *not* matched (see Figure 13d) by corresponding behavior on the following anodic peak, this growth effect seems better accounted for by formation of a surface oxide than by deposition of H.

The dependence of the cathodic peak shape on the initial potential in the sweep for potentials <0.4 V is shown in the families of curves in Figure 14a,b. The curves in Figure 14a are generated by progressively cutting the potential range of cathodic sweeps from the more positive side (<0.5 V) while those of Figure 14b are obtained by cutting from the less positive side (>0.05 V) over the total range 0.50–0.05 V. The i–V profiles of Figure 14a,b are seen to be similar in their essential features.

The general conclusion from this part of the work is that the i–V profiles generated in these experiments (Figures 10, 12–14) do not follow the behavior expected (cf. ref 25 and 31) for a simple surface electrochemical reaction like that of H deposition/ionization at Pt. It is evident from Figures 10–14 that the behavior in the cathodic sweep in the range 0.50–0.05 V is consistent more with reduction of a surface oxide formed at and below 0.40 V than it is with deposition of H in an absorbed state as supposed in ref 6.

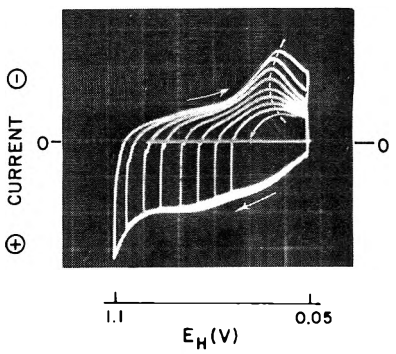

Figure 15. Family of cathodic i–V profiles after the anodic sweep at Ru has been taken successively to a series of increasingly positive values well into the oxide formation region (compare behavior with that in Figures 10, 12, 13, and 14). $s = 20$ V s^{-1}; range 0.05–1.1 V E_H.

It is useful to show the connection of the observed behavior at or below 0.40 V with the general pattern of reduction behavior of surface oxide formed at more positive potentials, as this comparison helps to identify the behavior with that of an oxide reduction process rather than with that of deposition of H under these conditions. Figure 15 illustrates this situation for a family of cathodic i–V profiles generated after making anodic sweeps to successively increasing positive potentials. The locus of cathodic peak potentials is shown and it is seen (cf. ref 20) that there are some similarities to Pt surface oxide reduction.

Reference to our recently published simulations[31] of i–V profiles for surface processes shows that the general features of the i–V profiles, shown in Figure 14 for changing quantities of the species reduced in the cathodic sweep curves, are similar to those of a surface process with an appreciable interaction "g" (cf. ref 31) factor. They are *not* characteristic of a *reversible* surface process where a series of i–V profiles taken from successively changing potentials in the range over which the surface process could occur would all fall on a common curve truncated progressively from one end.[31]

(vii) *Resolution of the Hydrogen Region from that for Surface Oxidation at Ru. Effect of Cl^- Ion.* The results in section iv showed that a region of surface oxide formation and reduction exists close, on the potential scale, to a region of H adsorption and absorption. By addition of a strongly adsorbed ion, Cl^-, it is possible[30] to effect a better separation of the H region from that of surface oxidation, as in the normal situation, e.g., at Pt. Thus, Figure 16a,b shows a series of i–V profiles for ruthenized Pt in the presence and absence of Cl^- ion; it is evident that Cl^- has a striking effect with regard to the resolution of the commencement of surface oxidation from the completion of oxidation of ad- or absorbed H. Two effects similar to those well known at Pt are involved: (a) surface oxidation is inhibited by Cl^- adsorption so that the onset of deposition of OH and O species[20] is displaced to more positive potentials; (b) the H ad-/absorption region is displaced to less positive potentials, as at Pt,[24] thus narrowing the range for H deposition and desorption processes. The overall result (Figure 16b) is a striking separation of the surface oxidation and H-oxidation regions

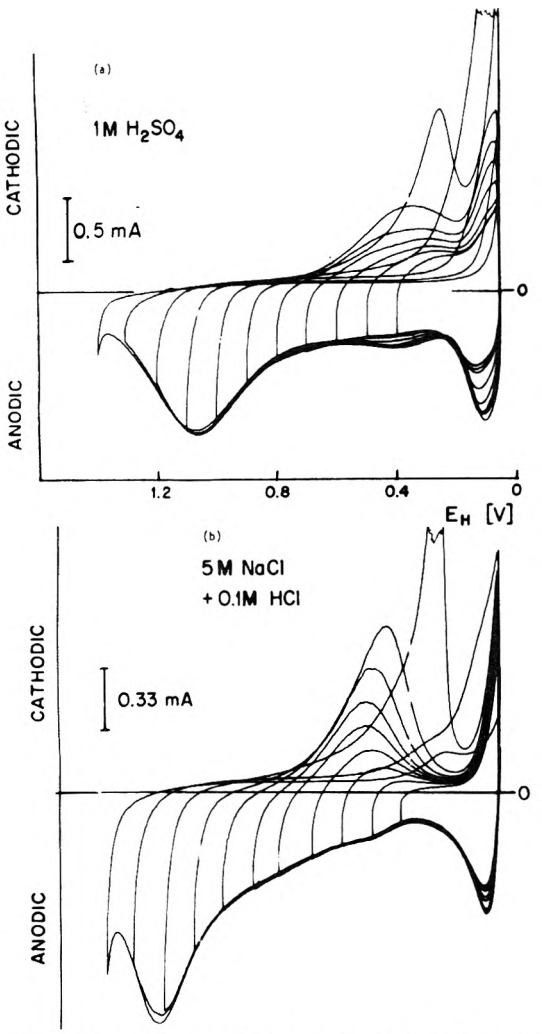

Figure 16. Series of $i-V$ profiles for a ruthenized Pt electrode in (a) 0.5 M H_2SO_4 and (b) 0.5 M H_2SO_4 + 5 M NaCl. $s = 50$ mV s^{-1}; 298 K.

which otherwise overlap. A "double-layer" region, presumably corresponding to oxide- and H-free metal (but probably with Cl^- ion adsorbed), is then revealed. The separation of the H from the oxide region achievable in Cl^- solutions (Figure 16) helps the evaluation of a reproducible relative "H charge" for Ru; however, the complications due to H absorption, treated earlier, remain, rendering quantitative evaluation of "hydrogen area" uncertain.

IV. Conclusions on H Adsorption

The results show that a region where hydrogen deposition and oxidation processes take place can be distinguished from one where surface oxide reduction and formation occurs by means of (a) reflectance measurements and (b) studies of Cl^- blocking experiments. However, within the range of potentials 0.0 to +0.2 V E_H, where H deposition processes can be distinguished, it is not possible to attribute the observed currents only to H adsorption or ionization of adsorbed H. H absorption is indicated in the experiments at various sweep rates and by direct coulombic efficiency measurements on H_2-evolution rates.

These conclusions are in conflict with those of Zakumbaeva and Shapovalova,[5] based on interpretation of two current peaks which they observed in the anodic sweep at Ru over the "hydrogen region". It seems from the present work that the more negative of these peaks is associated with H_2 reoxidation (it is increased at elevated temperatures due to more facile H_2 evolution in the previous cathodic sweep) while the second peak is the one in which there is an appreciable component due to reoxidation of sorbed H diffusing to the surface of the electrode from its interior. These workers did not apply the critical test[25,31] of examining constancy of i_p/s with s (a linearity of i_p on s) for a surface process. Had they done so, their conclusion that the observed hydrogen region currents are due to H chemisorption and ionization, which, in the light of the present work, must be considered erroneous, would not have been reached.

The reflectance changes indicate a distinguishable "hydrogen region" but this could arise from H absorption into a skin region of the Ru rod as well as from H adsorption.

These results lead to the conclusion that the charge under the hydrogen region peak at Ru electrodes cannot be used to evaluate real area and hence quantitatively the state of oxidation of the surface as a function of potential, at more positive potentials. However, in the presence of Cl^-, the charge in the H region can be used in a relative way for various surfaces of Ru provided they have been prepared similarly (cf. Figure 6).

Acknowledgment. Grateful acknowledgment is due to Hooker Chemicals and Plastics Corporation for a research grant in support of this work. We are also happy to acknowledge discusions with Drs. D. Pouli, D. Stevens, and B. V. Tilak of Hooker during the course of this work. We are indebted to Dr. F. C. Ho in this Laboratory for performing the reflectance measurements.

References and Notes

(1) F. G. Will and C. A. Knorr, *Z. Elektrochem.*, **64**, 258 (1960).
(2) A. Bewick, F. A. Hawkins, and A. M. Tuxford, *Surface Sci.*, **37**, 82 (1973); *Symp. Faraday Soc.*, **4**, 114 (1970).
(3) H. Angerstein-Kozlowska, W. B. A. Sharp, and B. E. Conway, "Symposium on Electrocatalysis", The Electrochemical Society, M. Breiter, Ed., 1974, p 94; J. Horiuti and T. Toya, *Solid State Surface Sci.*, **1**, 1 (1969).
(4) J. P. Chevillot, J. Farcy, C. Hinnen, and A. Rousseau, *J. Electroanal. Chem.*, **64**, 39 (1975).
(5) C. D. Zakumbaeva and L. B. Shapovalova, *React. Kinet. Catal. Lett.*, **2**, 117 (1975).
(6) E. K. Tuseeva, A. M. Skundin, and V. S. Bagctskii, *Electrokhimiya*, **9**, 1541 (1973).
(7) C. A. Knorr, U.S. Department of Commerce Office Technical Service P.B. report 161880 (1960); quoted *Chem. Abstr.*, **56**, 2018 (1962).
(8) V. V. Chernyl, V. S. Zorikova, Y. B. Vasil'ev, V. M. Gryaznov, N. B. Gorina and V. S. Bagotskii, *Electrokhimiya*, **8**, 1341 (1972).
(9) S. Hadzi-Jordanov, H. Angerstein-Kozlowska, and B. E. Conway, *J. Electroanal. Chem.*, **60**, 359 (1975).
(10) Quoted by B. S. Smith-Hopkins, "Chemistry of the Less Familiar Elements", Vol. 2, Stipes Publishing Co., Illinois, 1942.
(11) W. O'Grady, C. Iwakura, J. Huang, and E. Yeager, "Symposium on Electrocatalysis", The Electrochemical Society, M. Breiter, Ed., 1974, p 286.
(12) D. Galizzioli, F. Tantardini, and S. Trassati, *J. Appl. Electrochem.*, **5**, 203 (1975).
(13) T. N. Stoyanovskaya, G. P. Khomchenko, and G. D. Vovschenko, *Vest. Moscow Univ., Ser. Khim.*, **No. 5**, 30 (1962); **No. 2**, 20 (1963).
(14) L. D. Burke, J. K. Mulcahy, and S. Venkatesan, *J. Electroanal. Chem.*, **81**, 339 (1977).
(15) Watanabe and S. Motoo, *J. Electroanal. Chem.*, **60**, 267 (1975).
(16) D. N. Ross, K. Kinoshita, A. J. Scarpellino, and P. Stonehart, *J. Electroanal. Chem.*, **63**, 97 (1975); **59**, 171 (1975).
(17) H. Binder, A. Köhling, and G. Sandstede in "From Electrocatalysis to Fuel Cells", G. Sandstede, Ed., University of Washington Press, 1972, p 43.
(18) B. D. McNicol and R. T. Short, *J. Electroanal. Chem.*, **81**, 249 (1971).
(19) H. A. Kozlowska and B. E. Conway, *J. Electroanal. Chem.*, **7**, 109 (1964).
(20) H. Angerstein-Kozlowska, W. B. A. Sharp, and B. E. Conway, *J. Electroanal. Chem.*, **43**, 9 (1973).
(21) B. E. Conway, W. B. A. Sharp, H. Angerstein-Kozlowska, and E. E. Criddle, *Anal. Chem.*, **45**, 1331 (1973).
(22) S. Gottesfeld and B. E. Conway, *J. Chem. Soc., Faraday Trans. 1*, **69**, 1090 (1973).
(23) S. B. Brummer, J. I. Ford, and M. S. Turner, *J. Phys. Chem.*, **69**, 3424 (1965).
(24) M. W. Breiter, *Electrochim. Acta*, **7**, 25 (1962); see also *Ann. N.Y. Acad. Sci.*, **101**, 709 (1963).

(25) S. Srinivasan and E. Gileadi, *Electrochim. Acta*, **11**, 321 (1966).
(26) D. Gilroy and B. E. Conway, *Can. J. Chem.*, **46**, 875 (1968).
(27) H. Angerstein-Kozlowska and B. E. Conway, *J. Electroanal. Chem.*, in press; see also *Natl. Bur. Stand. Spec. Publ.*, **No. 455**, 107–124 (1976).
(28) P. Delahay, "New Instrumental Methods in Electrochemistry", Wiley, New York, N.Y., 1954.
(29) J. D. E. McIntyre and W. F. Peck, *Faraday Discuss., Chem. Soc.*, **50**, 122 (1973).
(30) M. Vukovič, H. Angerstein-Kozlowska, and B. E. Conway, *J. Electrochem. Soc.*, in press.
(31) H. Angerstein-Kozlowska, B. E. Conway, and J. Klinger, *J. Electroanal. Chem.*, **75**, 45 (1977).
(32) These authors referred to both adsorption and absorption of H but it is clear that they intended their conclusions to refer to H absorption.
(33) Time effects in kinetics can arise for other reasons but here, for current efficiencies, since only H deposition can occur, diffusion effects seem the only explanation.

Vibrational Spectra of the Tetrachlorocyclopropanes[1]

C. J. Wurrey,* R. B. Blatt, and A. B. Nease†

University of Missouri, Department of Chemistry, Kansas City, Missouri 64110 *(Received April 25, 1977)*

Publication costs assisted by the Department of Chemistry, UMKC

The infrared spectra of liquid 1,1,2,2-tetrachlorocyclopropane, *trans*-1,1,2,3-tetrachlorocyclopropane, and *cis*-1,1,2,3-tetrachlorocyclopropane have been obtained from 4000 to 400 cm^{-1}. In addition, the gas-phase infrared spectrum of 1,1,2,2-tetrachlorocyclopropane was also measured from 4000 to 200 cm^{-1}. Raman spectral data of the liquid and solid phases of these three isomers have been obtained as well. The spectral data are consistent with the C_{2v}, C_2, and C_s structures expected. Vibrational frequencies of each isomer are assigned and discussed, and are well correlated to frequencies for similar vibrations in other chlorine-substituted cyclopropanes.

Introduction

For some time cyclopropane and its derivatives have been of considerable interest to chemists. From an experimental standpoint, the novel chemistry of the cyclopropane system has intrigued researchers. From a theoretical standpoint, analyzing and interpreting the structure and bonding present in this three-membered ring system has generated much research activity. Interestingly enough, this highly strained system occurs in a large number of organic natural products; the steroid, gorgosterol, and chrysanthemic acid represent only two of the many known naturally occurring compounds containing the cyclopropane ring.

Toward the goal of determining the structure and bonding present in cyclopropane and its derivatives, vibrational spectroscopy has played a large role.[2] In order to observe and interpret spectral features and changes in these quantities, several halogen-substituted cyclopropanes have been studied among many other derivatives as well. With the exception of fluorocyclopropane, the infrared and Raman spectra of all the monohalocyclopropanes have been analyzed.[3-5] Dihalo-substituted cyclopropanes studied include 1,1-dichlorocyclopropane,[6] 1,1-dibromocyclopropane,[7] and *cis*- and *trans*-1,2-difluorocyclopropane.[8] Miller and Hartman[9] have investigated the vibrational spectra of perfluoro-, perchloro-, and perbromocyclopropane. The only tetrahalo-substituted cyclopropane studied to date is 1,1,2,2-tetrafluorocyclopropane and its -d_1 and -d_2 derivatives.[10] Neither of the other two tetrahalo-substituted patterns has been studied. In fact the only other tetrasubstituted cyclopropane studied has been 1,1,2,2-tetramethylcyclopropane.[11]

The tetrachlorocyclopropanes therefore represent a unique case. All possible isomers can be prepared, i.e., the 1,1,2,2 isomer, the trans-1,1,2,3 isomer, and the cis-1,1,2,3 isomer. Analysis of the vibrational spectra of these three isomers can therefore lead to complete and detailed knowledge of all the possible interactions and substituent effects present in this tetrasubstituted system.

Furthermore, one controversy that the vibrational spectrum of 1,1,2,2-tetrachlorocyclopropane (henceforth referred to as 1,1,2,2-TCCP) in particular might solve is the source of the cyclopropyl "group frequency" in the vicinity of 1030 cm^{-1} as discussed by Simmons et al.[12] They attribute this frequency to the cyclopropyl ring deformation vibration, but note that it is "generally missing in hexasubstituted derivatives". Rothschild[13] claims that this is "fortuitous" rather than a consequence of a "group frequency". Since 1,1,2,2-TCCP has only one methylene group, its CH_2 bending motions should be distinct and uncoupled to (and not obscured by) other methylene bending vibrations. More importantly, the different symmetries of the ring deformation mode (A_1) and the methylene rock (B_1), wag (B_2), and twist (A_2) should be of great assistance in properly assigning peaks in the region of 1030 cm^{-1}. The spectrum of 1,1,2,2-tetrafluorocyclopropane[10] solved this problem in part, but overlapping C–F stretching modes and drastic vibrational coupling between the carbons and fluorines made the determination of this problem somewhat difficult. For obvious reasons the spectrum of 1,1,2,2-tetramethylcyclopropane[11] in this region will also not be of assistance, owing to the presence of methyl rocking modes in the 1000-cm^{-1} region and strong carbon–carbon vibrational coupling. The spectrum of 1,1,2,2-TCCP should immediately clear up this controversy as no C–Cl stretches will appear higher than 800 cm^{-1} and little, if any, vibrational coupling should occur between the heavy chlorine atoms and the lighter carbon atom skeleton. In addition the spectra of the other two isomers, *trans*-1,1,2,3-TCCP and *cis*-1,1,2,3-TCCP, should also aid in clearing up this matter.

Thus, in order to properly determine and assign the cyclopropyl "group frequency" near 1030 cm^{-1} and also to analyze the spectra of a case where all possible isomeric substitution patterns can be attained, it seemed of considerable interest to obtain and analyze the vibrational

† Taken in part from the Ph.D. Thesis of A. B. Nease to be submitted to the Department of Chemistry in partial fulfillment of the requirements for a Ph.D. Degree.

spectra of the three isomeric tetrachlorocyclopropanes.

In addition to that we would also like to report an improved, one-step, high-yield, stereospecific reaction procedure to produce each isomeric tetrachlorocyclopropane. In 1946, Stevens[14] was able to isolate from among the many products of the direct reaction of chlorine and cyclopropane a sample of 1,1,2,2-TCCP. Twenty years later, Tobey and West[15] obtained a 0.9% yield of *cis*-1,1,2,3-TCCP by allowing *cis*-1,2-dichloroethylene to react with sodium trichloroacetate. More recently, Fields et al.[16] prepared all three isomers by using the appropriate dichloroethylene and (trichloromethyl)trifluorosilane as a dichlorocarbene generator. The high temperature of their reaction apparently isomerized the starting olefins and produced mixtures of *cis*- and *trans*-1,1,2,3-TCCP. Our reaction involved the use of the appropriate dichloroethylene and (bromodichloromethyl)phenylmercury (a Seyferth's reagent) as the dichlorocarbene source. Our reaction produced the tetrachlorocyclopropanes in good, stereospecific yields and is described in more detail in the next section.

Experimental Section

Each TCCP isomer was prepared stereospecifically and in good yield by allowing (bromodichloromethyl)-phenylmercury to react with the appropriate dichloroethene. The dichlorocarbene generated from the mercurial added to the double bond of the olefin preferentially and without isomerization of the olefin. 1,1,2,2-TCCP was prepared by allowing a mixture of 20 g of $C_6H_5HgCBrCl_2$ and 25 g of 1,1-dichloroethylene to reflux under nitrogen for 48 h. Similarly, *trans*-1,1,2,3-TCCP was prepared from *trans*-1,2-dichloroethylene and *cis*-1,1.2,3-TCCP was prepared with *cis*-1,2-dichlorocyclopropane as the starting olefin. Identical amounts of olefin and mercurial were used for these last two isomers but a reflux time of 24 h was all that was required to obtain products. Further workup in all cases was the same. Precipitated phenylmercuric bromide was filtered out and the starting olefin was removed by vacuum distillation. A vacuum transfer into a liquid nitrogen trap removed the TCCP from any residual mercury compounds. A final vacuum distillation resulted in the pure TCCP's. Purity of the samples amounted to 99% or better for each isomer, as measured by nuclear magnetic resonance spectroscopy and mass spectrometry. Our NMR spectra agreed with those published by Haszeldine et al.[17] These spectra were of particular importance in verifying the cis and trans isomeric structures. Overall recoverable yields of the TCCP's were as follows: 1,1,2,2-TCCP (37%), *trans*-1,1,2,3-TCCP (61%), and *cis*-1,1,2,3-TCCP (75%).

Infrared spectra were recorded with a Perkin-Elmer Model 621 spectrophotometer, which had been calibrated as in the literature. A KBr liquid cell of 0.0303 mm was used to obtain liquid-phase spectra. A typical gas cell with CsI windows was used to record the gas phase spectrum of 1,1,2,2-TCCP, which was the only isomer to have enough vapor pressure (~2 mm) to record the gas-phase spectrum. Frequencies are expected to be accurate to within ±2 cm^{-1}.

Raman spectra were recorded using a Cary Model 82 spectrometer equipped with a Spectra Physics Model 171 argon ion laser operating on the 5145-Å line. Spectra of the liquid phase were obtained with the samples sealed in a glass capillary. Spectra of the solid phase were recorded by condensing the sample on a copper block cooled to approximately −190 °C by boiling liquid nitrogen in a typical Raman cold cell. Both liquid and solid phase Raman spectra were run at minimum laser power (~200 mW) in order to prevent sample decomposition. Reported

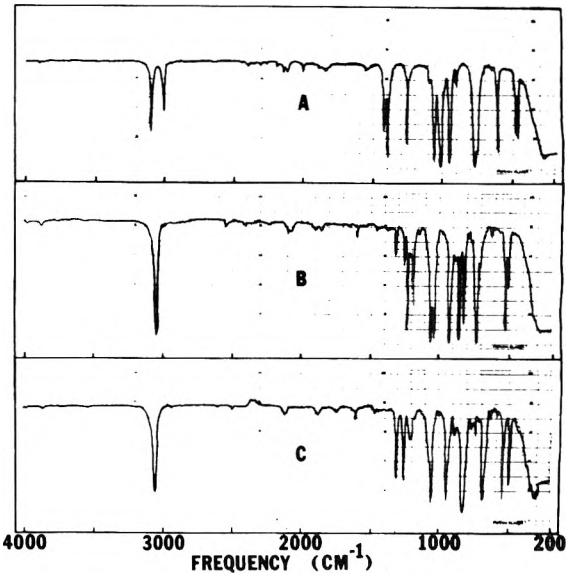

Figure 1. Infrared spectra of the liquid-phase tetrachlorocyclopropanes: (A) 1,1,2,2-TCCP; (B) *trans*-1,1,2,3-TCCP; and (C) *cis*-1,1,2,3-TCCP. All spectra were obtained using a KBr cell of 0.0303 mm thickness.

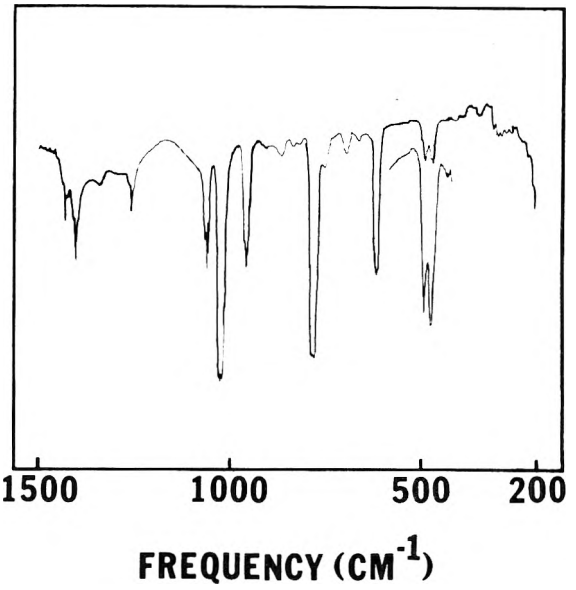

Figure 2. Gas-phase infrared spectrum of 1,1,2,2-TCCP. The spectrum was recorded at ~2 Torr vapor pressure using a 20-cm cell with CsI windows.

Raman frequencies are also expected to be accurate to ±2 cm^{-1}.

Results

The observed liquid-phase infrared spectra of all three isomers are shown in Figure 1. Figure 2 contains the mid-infrared gas-phase spectrum of 1,1,2,2-TCCP. Raman spectra of all three isomers are shown in Figure 3 (liquid phase) and Figure 4 (solid phase). Thus, spectra of all three phases have been obtained. The frequencies corresponding to the observed infrared and Raman spectra are listed in Tables I–III.

Assignment of the Spectra

The observed spectra are completely consistent with the C_{2v}, C_2, and C_s structures expected for 1,1,2,2-TCCP, *trans*-1,1,2,3-TCCP, and *cis*-1,1,2,3-TCCP, respectively.

On this basis the 21 normal vibrations of 1,1,2,2-TCCP form the following representation of the symmetry group, C_{2v}

$$7A_1 + 4A_2 + 5B_1 + 5B_2$$

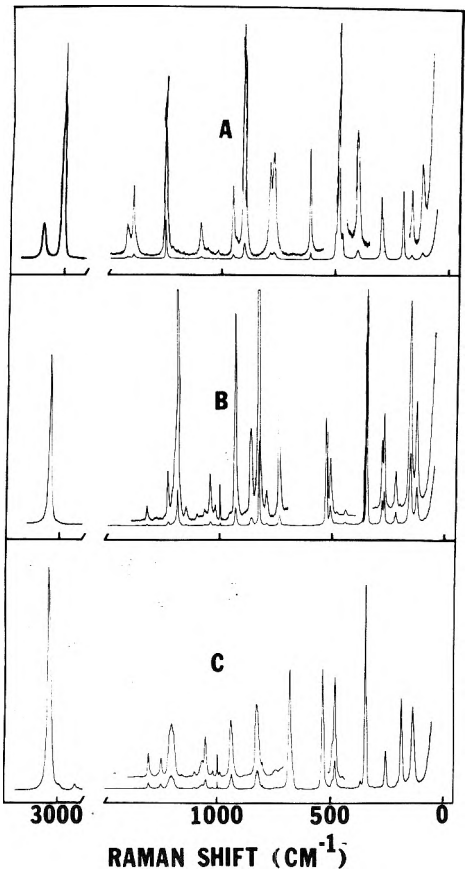

Figure 3. Raman spectra of the liquid-phase tetrachlorocyclopropanes: (A) 1,1,2,2-TCCP; (B) *trans*-1,1,2,3-TCCP; and (C) *cis*-1,1,2,3-TCCP.

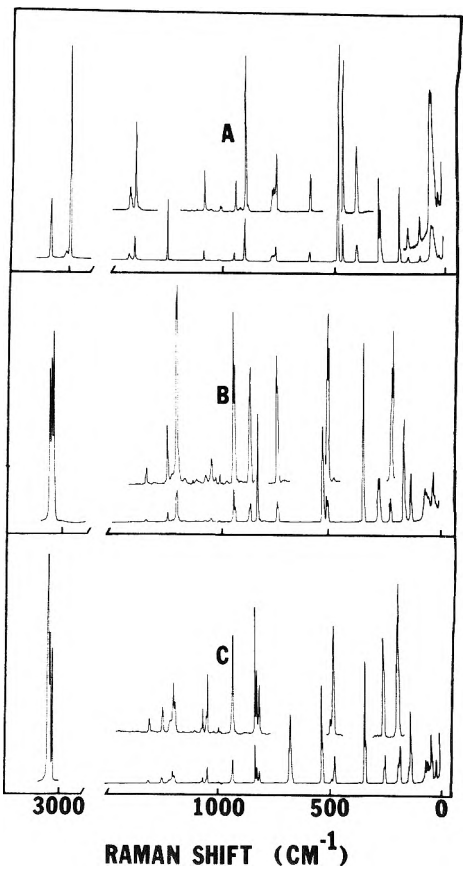

Figure 4. Raman spectra of the polycrystalline tetrachlorocyclopropanes: (A) 1,1,2,2-TCCP; (B) *trans*-1,1,2,3-TCCP; and (C) *cis*-1,1,2,3-TCCP.

The A_1 vibrations will give rise to polarized Raman peaks and C-type infrared gas-phase band contours, based on a structure using the molecular parameters of 1,1-dichlorocyclopropane.[18] A_2 vibrations are forbidden from the infrared spectrum and result in depolarized, generally weak Raman peaks. Vibrations of B_1 symmetry will have depolarized Raman peaks and B-type infrared gas-phase band contours. Finally, B_2 vibrations also give rise to depolarized Raman peaks, but will have A-type gas-phase band contours.

For the less symmetrical isomers, the following vibrational representations will occur: *trans*-1,1,2,3-TCCP (C_2 symmetry), 11A + 10B; *cis*-1,1,2,3-TCCP (C_s symmetry), 12A′ + 9A″. Vibrations of A and A′ symmetry will result in polarized Raman peaks and the B and A″ vibrations will yield depolarized Raman peaks.

In addition to Raman depolarization data and infrared gas-phase band contours, the assignment of the spectra was assisted by the use of expected group frequency correlations and also band intensities in the infrared and Raman spectra. In particular, the various vibrations in the three isomeric tetrachlorocyclopropanes resolve themselves into useful frequency groupings: CH stretches, 3000–3100 cm^{-1}; CH bendings, 1000–1400 cm^{-1}; ring vibrations, 1200–1250 and 900–950 cm^{-1}; CCl stretches, 400–800 cm^{-1}; and CCl bendings, <500 cm^{-1}.

Therefore, on these basis the following vibrational assignment was made, and it is summarized in Tables IV–VI.

1,1,2,2-TCCP. CH_2 Stretches. In the infrared spectrum of the liquid two peaks are observed in the CH stretching region at 3096 and 3010 cm^{-1}, with the higher frequency peak being the most intense. In the Raman spectrum these two peaks are also observed, with the lower frequency peak being the most intense in this case. The peak at 3006 cm^{-1} in the Raman spectrum is clearly polarized while the 3093-cm^{-1} peak is depolarized. This immediately leads to the assignment of the A_1 symmetric CH_2 stretch at 3006 cm^{-1} and the antisymmetric CH_2 stretch (of B_1 symmetry) to the peak at 3093 cm^{-1}.

CH_2 Bendings. The methylene group gives rise to four bending modes: a deformation (A_1), a twist (A_2), a rock (B_1), and a wag (B_2). In the expected CH_2 deformation region two peaks are observed (one at 1423 cm^{-1} and the other at 1396 cm^{-1}). Both of these peaks are polarized and both exhibit C-type gas-phase infrared band contours. In all spectra the 1396-cm^{-1} peak is more intense. In fact in both the infrared and Raman spectra and in all three phases the intensity ratio of these peaks is nearly constant, a good indication of Fermi resonance. We have assigned this pair of peaks as a Fermi doublet. The 1396-cm^{-1} peak is assigned as the CH_2 deformation fundamental and the 1423-cm^{-1} peak as a combination band. Two possibilities with the proper symmetry exist for this combination: 1016 (B_1) + 399 (B_1) = 1415 (A_1) and 950 (B_2) + 467 (B_2) = 1417 (A_1). As a matter of fact, this Fermi resonance enabled us to assign the B_1 and B_2 peaks properly. We prefer assigning the 1396-cm^{-1} peak as the fundamental, even though this frequency seems somewhat low for this vibration, for two reasons. First of all this peak is the more intense of the two and secondly, the only combination band of the proper symmetry which could account for this peak falls too low (902 (A_1) + 486 (A_1) = 1388 (A_1)).

Assignment of the A_2 methylene twist is also straightforward. A weak Raman peak is observed at 1092 cm^{-1} which has only a very weak counterpart in the infrared liquid spectrum and no counterpart in the gas phase infrared spectrum. This Raman peak is also depolarized. While it is also somewhat lower in frequency than the expected 1150-cm^{-1} peak, the fact that the scissoring mode is also low may help account for this.

TABLE I: Observed Frequencies of 1,1,2,2-Tetrachlorocyclopropane[a]

Raman solid	Raman liquid	IR liquid	IR gas
3085 m	3093 dp, m	3096 ms	3108 w
2998 vs	3006 p, vs	3010 m	
		2196 w	
		2150 w	
		2119 w	
		2005 w	
		1892 w	
1422 w	1423 p, w	1424 ms	1431 m, Q, C type
1397 m	1396 p, mw	1397 s	1404 m, Q, C type
1253 w	1253 p, s	1252 ms	1257 w, Q, C type
	1092 dp, w	1093 vw	
			1065 R, m
1080 w	1063, vw	1062 vs	1061 Q, m } A type
			1058 P, m
			1026 R, s
1017 vw	1016, vw	1016 vs	1021 P, s } B type
1011 vw			963 R, m
948 w	951 dp, mw	950 vs	958 Q, m } A type ?
904 m	902 p, s	900 vw	953 P, m
794 w			
788 w	787 dp, m		
777 w	770 dp, m	774 vs	780 vs, B type ?, band center
		758 ms, sh	621 R, m
611 s	610 dp, m	614 ms	615 Q, m } A type ?
608 s			610 P, m
485 vs	486 p, vvs	486 ms	486 w, Q, C type
465 m	468 dp, w	467 ms	467 w, Q, A type ?
399 m	399 dp, m		
297 m	296 p, vs		
290 m	290 dp, sh		
217 m	199 p, vs		
179 w	161 dp, mw		
127 w	114 dp, m		
66 w } lattice			
58 m } lattice			
32 m } lattice			

[a] Abbreviations used in this table are as follows: v = very; s = strong; m = medium; w = weak; p = polarized; dp = depolarized; sh = shoulder.

The assignment of the rock and the wag is also easily made. Very strong peaks in the infrared spectrum of the liquid fall at 1062 and 1016 cm^{-1}. The Raman spectrum in this region shows these two peaks also, but they are very weak, in fact, weaker than the A_2 CH_2 twist. The gas-phase infrared spectrum conclusively confirms the assignment, however. The definite A-type band contour at 1061 cm^{-1} means that this peak is of B_2 symmetry, namely, the CH_2 wag. The B-type band contour centered at 1023 cm^{-1} therefore arises from the B_1 CH_2 rock.

Thus the cyclopropyl "group frequencies" in this region arise from CH bending vibrations and *not* the ring deformation motion, which is confidently assigned in the next section. In fact, further verification of this point can be seen in the assignment of the cis and trans isomers, both of which have peaks in this region attributable to CH bendings, *not* ring vibrations.

Ring Vibrations. The cyclopropane skeleton itself will give rise to three vibrations: a ring breathing (A_1), a ring deformation (A_1), and an antisymmetric ring stretch (B_2).

The assignment of the ring breathing motion is evident from the Raman spectrum. The peak at 1253 cm^{-1} is the most intense Raman peak outside the CCl and CH peaks and is strongly polarized. In addition, its counterpart in the gas-phase infrared spectrum has a clear-cut C-type band contour. Thus this assignment is made with great confidence.

A search of the Raman spectrum reveals another strong, polarized peak at 902 cm^{-1}, which has no observable gas-phase infrared counterpart and only a weak liquid-phase infrared peak at 900 cm^{-1}. However, the Raman polarization and intensity data together are sufficient evidence to positively assign this peak to the A_1 ring deformation. The lack of infrared intensity for this vibration is also observed for 1,1-dibromocyclopropane.[7]

In this same region of the gas-phase infrared spectrum is an A-type band contour centered at 958 cm^{-1}. The Raman counterpart to this peak occurs at 951 cm^{-1} and is depolarized. The intensity of this peak in the Raman spectrum is considerably greater than the observed intensities of the CH_2 rock and wag at 1016 and 1061 cm^{-1}, as one would expect for a ring vibration. Thus this peak is assigned to the B_2 antisymmetric ring stretching vibration.

CCl_2 Stretches. Four carbon–chlorine stretches, one in each symmetry block of C_{2v} symmetry, are predicted. For the most part, they will give rise to usually strong infrared bands and Raman peaks of variable intensity, over the range 400–800 cm^{-1}.

By far and away, the most intense Raman peak, at 486 cm^{-1}, has to be assigned to the totally symmetric, in-phase CCl stretch. This peak is strongly polarized and has a C-type infrared gas-phase band contour.

Candidates for the other CCl stretches are observed as strong or very strong infrared peaks at 614 and 774 cm^{-1}. The gas-phase infrared band contours corresponding to these peaks are somewhat obscured by hot bands, but the band centered at 615 cm^{-1} does have some recognizable P–Q–R structure and the peak at 780 cm^{-1} is of the same general shape as the definite B-type contour observed at 1023 cm^{-1}. Both of these peaks are also depolarized in the Raman effect. Thus they can be easily assigned as the B_2

TABLE II: Observed Frequencies of *trans*-1,1,2,3-Tetrachlorocyclopropane

Raman solid	Raman liquid	IR liquid
3052 m		3051 s
3048 m	3044 p, s	
3040 m		
		2462 w
		2108 w
		2084 w
		1929 w
		1902 w
		1865 w
		1616 w
	1467 vw	
1330 vw	1329 dp, vw	1331 w
		1265 w
1233 vw	1235 dp, w	1236 s
1194 w	1192 p, m	1193 ms
1190 w		
	1102 p, vw	
1061 vw	1069 p, w	1068 vs
1040 vw	1042 p, w	1044 vs
1037 vw		
1020 vw	1020 p, vw	
999 vw	999 p, vw	
935 w	933 p?, mw	933 vs
930 vw		
866 sh, vw		
862 vw	863 dp, w	864 vs
828 s	830 p, s	830 s
743 w		
738 sh, vw	738 dp, mw	737 vs
		708 w
		636 w
533 m	533 p, s	533 s
516 w	513 dp, mw	514 m
510 w		
353 vs	352 p, vvs	
	284 dp, m	
278 m	274 p, m	
271 m		
228 s		
223 vs	221 dp, w	
161 s	157 p, ms	
133 m	128 dp, m	
70 w		
63 w		
53 w	lattice	
37 w		
28 w		
22 w		

[a] Abbreviations used in this table are as follows: v = very; s = strong; m = medium; w = weak; p = polarized; dp = depolarized; sh = shoulder.

TABLE III: Observed Frequencies of *cis*-1,1,2,3-Tetrachlorocyclopropane

Raman solid	Raman liquid	IR liquid
3048 vs	3047 p, s	3048 ms
3040 s		
3030 s		
	2769	
1309 vw	1306 p, w	1307 m
1251 w	1250 dp, w	1252 m
1247 w		
1218 sh, w		
1203 w	1202 p, m	1205 m, br
1193 w		
	1101 p, vw	
1078 sh, w		
1070 w	1067 dp?, w	1065 m, sh
1055 w		
1049 w	1051 p, mw	1051 s
	1019 vw	
	999 vw	
	988 w	
936 m	937 dp?, m	937 s
		879 w
836 m		
828 w	823 dp, m	821 vs
817 w		
		762 w
		737 w
678 s	681 p, s	678 s
548 m		
537 w	536 p, s	536 s
498 w		
479 m	482 dp, ms	481 ms
353 s	346 p, vvs	
347 sh, m	340 p?, sh, w	
265 sh, w		
259 m	256 p?, ms	
197 sh, w		
187 m	185 p?, s	
150 sh, w		
143 s		
135 sh, m	133 dp, s	
75 w		
66 w		
63 w		
57 w	lattice	
48 m		
43 w		
27 w		

[a] Abbreviations used in this table are as follows: v = very; s = strong; m = medium; w = weak; p = polarized; dp = depolarized; sh = shoulder; br = broad.

symmetric CCl_2 stretch, out of phase (614 cm^{-1}), and the B_1 CCl_2 antisymmetric stretch, in phase (774 cm^{-1}).

This assignment makes the final A_2 CCl_2 antisymmetric stretch, out of phase, readily assignable to the Raman peak at 787 cm^{-1}. This peak has almost the same Raman intensity as the B_1 peak at 770 cm^{-1}, but has only a very weak infrared counterpart in the solid phase and no counterpart in the liquid phase. There is also a medium to strong shoulder in the infrared spectrum at 758 cm^{-1}, which does not appear in the Raman spectrum. This peak is easily assigned to the combination band 467 (B_2) + 290 (B_2) = 757 (A_1). The fact that this peak is absent from the Raman spectrum substantiates the assignment of this peak to a combination band. (We discard another possible combination band, 467 (B_2) + 296 (A_1) = 763 (B_2), as being too high in frequency for this peak.)

Notice that antisymmetric CCl_2 stretches fall higher than the corresponding symmetric stretches and give rise to stronger infrared bands (obviously excepting the symmetry forbidden A_2 vibration). In the Raman spectrum, the A_1 vibration is incredibly intense while the other three are of much less intensity and nearly equal to each other in intensity. Finally, it can be noted that the out-of-phase vibrations are higher in frequency than the in-phase vibrations. These facts assist in the assignment of the other isomers of tetrachlorocyclopropane.

CCl_2 Bendings. Eight CCl_2 bending vibrations are predicted: in-phase and out-of-phase deformations (A_1 + B_2), wags (A_1 + B_2), rocks (A_2 + B_1), and twists (A_2 + B_1).

Gas phase band contour data are available for only one of these low frequency vibrations. The peak centered at 467 cm^{-1} in the infrared gas-phase spectrum is also obscured by hot bands, but has a band contour shaped very much like the other A-type bands at 1061 and 958 cm^{-1}. This peak is also observed as a depolarized shoulder at 468 cm^{-1} in the Raman effect. It can distinctly be observed in the infrared liquid-phase spectrum, where it is more intense than the nearby A_1 CCl_2 stretch at 486 cm^{-1}. On this basis it can be attributed to the B_2 CCl_2 wag.

Assignment of the A_1 vibrations is easily made. Very intense, strongly polarized peaks are observed in the

TABLE IV: Assignment of Fundamental Frequencies for 1,1,2,2-Tetrachlorocyclopropane

Symmetry block	Frequency, cm^{-1}	Assignment
A_1	3006	CH_2 symmetric stretch
	1396	CH_2 deformation
	1253	Ring breathing
	902	Ring deformation
	486	CCl_2 symmetric stretch, in phase
	296	CCl_2 wag, in phase
	199	CCl_2 deformation, in phase
A_2	1092	CH_2 twist
	787	CCl_2 antisymmetric stretch, out of phase
		CCl_2 twist, out of phase
	114	CCl_2 rock, out of phase
B_1	3093	CH_2 antisymmetric stretch
	1016	CH_2 rock
	770	CCl_2 antisymmetric stretch, in phase
	399	CCl_2 twist, in phase
	161	CCl_2 rock, in phase
B_2	1061	CH_2 wag
	951	Antisymmetric ring stretch
	614	CCl_2 symmetric stretch, out of phase
	467	CCl_2 wag, out of phase
	290	CCl_2 deformation, out of phase

TABLE V: Assignment of Fundamental Frequencies for *trans*-1,1,2,3-Tetrachlorocyclopropane

Symmetry block	Frequency, cm^{-1}	Assignment
A	3044	CH stretch in phase
	1192	Ring breathing
	1068	CH bend
	1044	CH bend
	933	Ring deformation
	830	CCl stretch, in phase
	533	CCl_2 symmetric stretch
	352	CCl_2 deformation
	274	CCl bend
	228	CCl bend
	157	CCl_2 twist
B	3051	CH stretch, out of phase
	1331	CH bend
	1235	CH bend
	(933[a])	Antisymmetric ring stretch
	863	CCl stretch, out of phase
	738	CCl_2 antisymmetric stretch
	513	CCl_2 wag
	284	CCl bend
	222	CCl bend
	128	CCl_2 rock

[a] Not directly observed. Tentatively assigned to be degenerate with the ring deformation of A symmetry. See text for discussion.

Raman spectrum at 296 and 199 cm^{-1}. These can be assigned to the A_1 CCl_2 wag and the A_1 CCl_2 deformation, respectively. This is consistent with the expectation that the deformation should be lower in frequency than the wag, as was observed in 1,1-dichlorocyclopropane.[6]

The assignment of the 399-cm^{-1} peak to the B_1 block was discussed previously in an earlier section. This peak then must be due to the CCl_2 twisting motion. No peak corresponding to the A_2 CCl_2 twist could be observed; either it is of too low intensity or accidentally degenerate with another vibration, even in the solid phase. The two CCl_2 rocks are also of A_2 and B_1 symmetry and are expected to

TABLE VI: Assignment of Fundamental Frequencies for *cis*-1,1,2,3-Tetrachlorocyclopropane

Symmetry block	Frequency, cm^{-1}	Assignment
A'	3047	CH stretch, in phase
	1306	CH bend
	1202	Ring breathing
	1051	CH bend
	(937[a])	Ring deformation
	879	CCl stretch, in phase
	681	CCl_2 antisymmetric stretch
	536	CCl_2 symmetric stretch
	346	CCl_2 deformation
	340	CCl bend
	256	CCl bend
	185	CCl_2 rock
A''	3047	CH stretch, out of phase
	1250	CH bend
	1067	CH bend
	937	Antisymmetric ring stretch
	823	CCl stretch, out of phase
	482	CCl_2 wag
	(256[a])	CCl bend
	(185[a])	CCl bend
	133	CCl_2 twist

[a] Not directly observed. Tentatively assigned to be accidentally degenerate with other modes. See text for discussion.

be lowest frequency vibrations. The depolarized peaks occuring at 114 and 161 cm^{-1} are assigned as the A_2 rock and B_2 CCl_2 rock, respectively. Preliminary normal coordinate analysis appears to bear out the assignment of the A_2 mode lower than the B_1 vibration.[19]

The last vibration to be assigned is the B_2 CCl_2 deformation. This peak occurs as a depolarized shoulder at 290 cm^{-1} in the liquid phase. However, solid phase data are much better resolved and this peak clearly stands out from the A_1 CCl_2 wag at 297 cm^{-1}.

That this assignment for 1,1,2,2-TCCP (as well as those for the cis and trans isomers) is reasonable is borne out in Table VII, which compares the assignment of similar vibrations in a series of chlorine-substituted cyclopropanes. In all cases, ring vibrations are assigned at ~1200 cm^{-1} and from 860 to 950 cm^{-1}. Peaks in the region 1000–1200 cm^{-1} are confidently assigned to CH_2 vibrations and CH bendings, these being the source of the cyclopropyl "group frequency" near 1030 cm^{-1}. It should be pointed out here that, while the spectra of deuterated isotopes are not available, arguments for the assignment of ring and CH bending modes on the basis of Raman intensities are sound. It has been firmly established in bromo- and chlorocyclopropane,[4,5] and 1,1-dibromo- and 1,1-dichlorocyclopropane[6,7] as well as the hexabromo- and hexachlorocyclopropane for the ring modes[9] that in the Raman effect, the intensity of the ring vibrations of halocyclopropanes is consistently greater than the intensity (usually weak) of CH bending modes. In fact, this information is useful for distinguishing between these vibrations.

A further result which can be derived from Table VII is that other vibrations in chlorine-substituted cyclopropanes agree reasonably well, lending credence to the assignments presented here for the tetrachlorocyclopropanes.

Finally, it can be mentioned that the presence of a number of doublets occurring in the solid phase spectrum (at 608 and 611 cm^{-1}, 788 and 794 cm^{-1}, and 1011 and 1017 cm^{-1}) would seem to argue in favor of there being two molecules in the unit cell. Although these splittings could

TABLE VII: Comparison of Vibrational Frequencies of Chlorine-Substituted Cyclopropanes, $C_3H_nCl_{6-n}$

Mode	C_3H_5Cl[a]	$C_3H_4Cl_2$[b]	1,1,2,2-TCCP[c]	*trans*-TCCP[c]	*cis*-TCCP[c]	C_3Cl_6[d]
CH_2 stretch	3096, 3064	3106, 3096	3093			
	3016	3022	3006			
CH(Cl) stretch	2977			3051, 3044	3047, 3047	
CH_2 deformation	1447, 1421	1444, 1409	1396			
CH bend	1293, 1262			1331, 1235	1306, 1250	
CH_2 twist	1164, 1071	1212, 1164	1092			
CH_2 wag	1048, 1026	1130, 1037	1061			
CH bend				1068, 1044	1067, 1051	
CH_2 rock	809, 766	809, 772	1016			
Ring breathing	1201	1238	1253	1192	1202	1226
Ring deformations	931, 874	952, 874	951, 902	933, 933	937, 937	906
CCl stretch	633	717, 500	787, 770, 614, 486	863, 830, 738, 533	879, 823, 681, 536	964, 850, 607, 420
CCl_2 wag		404	467, 296	513	482	182
CCl_2 twist		300	399	157	133	?
CCl_2 deformation		272	290, 199	352	346	315, 235
CCl_2 rock		443	161, 114	128	185	195, 130
CCl bend	322			284, 274	340, 256	
	287			228, 222	256, 185	

[a] Reference 5. [b] Reference 6. [c] This work. [d] Reference 9.

possibly result from chlorine isotope effects, particularly for modes involving chlorine atoms, we feel that they are indeed due to the static field effects. Only three lattice vibrations are observed, but the lattice region is somewhat broad and unresolved, suggesting the possible presence of a number of further lattice modes. The solid phase spectra of the other isomers exhibit many lattice vibrations and peak splittings, also suggestive of more than one molecule per unit cell. We conclude that there are at least two molecules per unit cell for all three isomers, however, the evidence for the 1,1,2,2 isomer is not as strong as we would like.

trans-1,1,2,3-TCCP. CH Stretches. The carbon–hydrogen stretching vibrations are easily observed at 3044 cm^{-1} in the Raman spectrum and at 3051 cm^{-1} in the infrared spectrum. That this mutual exclusion of frequencies should occur is not unexpected when one considers that the part of the molecule involved in these vibrations derived from *trans*-1,2-dichloroethylene, which does have a center of symmetry. The Raman band, which is polarized, can thus be assigned to the in-phase CH stretch and the 3051-cm^{-1} infrared absorption to the corresponding out-of-phase vibration. Notice that in the solid phase spectrum this mutual exclusion is no longer observed, owing to lower site symmetry in the polycrystalline material.

CH Bendings. Four CH bendings resulting from the in-phase and out-of-phase deformations of the CH bonds will give rise to peaks in the range 1000–1300 cm^{-1}. These four peaks are observed at 1331, 1235, 1068, and 1044 cm^{-1}. All four of these have weak Raman peaks characteristic of CH bendings (as opposed to ring vibrations) and medium to strong infrared counterparts. The higher two frequencies correspond to depolarized Raman peaks while the lower two frequencies result from polarized Raman lines. Therefore the assignment of 1331 and 1235 cm^{-1} to B vibrations and 1068 and 1044 cm^{-1} to A vibrations is easily made. The peak at 1265 cm^{-1} in the infrared spectrum of the liquid has no Raman counterpart. This fact immediately suggests its assignment as an overtone or combination band, and in fact this peak can be accounted for by three possible combinations: 738 (B) + 533 (A) = 1271 (B); 1044 (A) + 228 (A) = 1272 (A); 1044 (A) + 222 (B) = 1266 (B). We favor this latter assignment.

Notice that once again strong infrared bands are observed in the 1030-cm^{-1} vicinity and can confidently be assigned to CH and CH_2 bending vibrations and not ring vibrations. This will also be shown to be the case for CH bendings in *cis*-1,1,2,3-TCCP later, as it was shown for CH_2 bendings in 1,1,2,2-TCCP previously.

Ring Vibrations. The ring breathing vibration is readily observed as the moderately strong, polarized Raman peak at 1192 cm^{-1}. Another polarized (ρ = 0.49) peak in the Raman spectrum is observed at 933 cm^{-1}. This can be assigned to the A ring deformation vibration. No depolarized peak in the Raman spectrum can be found in the region 870–1220 cm^{-1}, which may be assigned to the antisymmetric ring stretch. However, the high depolarization value of the 933-cm^{-1} peak (most other totally symmetric vibrations in this molecule have ρ values on the order of 0.15 or less) and the fact that this peak has a very strong infrared counterpart lead us to believe that these two ring vibrations might accidentally be degenerate. In 1,1,2,2-TCCP and 1,1-dibromocyclopropane,[7] the ring deformation

vibration had no infrared counterpart while the antisymmetric ring stretch in both of these molecules had a very strong absorption. In hexachlorocyclopropane,[9] these two modes *are* degenerate (by virtue of symmetry) at 906 cm^{-1}. Therefore we tentatively assign the antisymmetric ring stretch as well as the ring deformation to the peak at 933 cm^{-1}. A similar circumstance occurs in the cis isomer as well.

CCl Stretches. A symmetric and an antisymmetric carbon–chlorine stretch will arise from the CCl_2 group, while in-phase and out-of-phase carbon–chlorine stretches result from the two CHCl groups. In general, one would expect the CCl_2 stretches to be lower in frequency than the CHCl stretches with the stretches of A symmetry the more intense in the Raman effect and the stretches of B symmetry the more intense in the infrared spectrum. The second most intense peak in the Raman spectrum, at 533 cm^{-1}, is clearly polarized and must be assigned to the symmetric CCl_2 stretch. The corresponding antisymmetric CCl_2 stretch is observed at 738 cm^{-1} and is very strong in the infrared spectrum and depolarized in the Raman effect. The CHCl stretches can now be easily assigned to the two peaks at 863 and 830 cm^{-1}. The former of these two peaks is depolarized in the Raman spectrum and more intense than the latter peak in the infrared spectrum while the 830-cm^{-1} peak is polarized and much more intense in the Raman spectrum than the 863-cm^{-1} band. Thus they can be assigned with the in-phase CCl stretch (830 cm^{-1}) lower in frequency than the out-of-phase mode (863 cm^{-1}).

CCl Bendings. From the CCl_2 group four bending vibrations will occur: a scissors (A), a twist (A), a wag (B), and a rock (B). At the same time, the CHCl groups will give rise to in-plane and out-of-plane bendings of the CCl bonds, both in-phase and out-of-phase. The most intense Raman peak, at 352 cm^{-1}, is definitely due to the CCl_2 deformation, while the other very intense low frequency Raman peak at 157 cm^{-1} must also derive from the CCl_2 group and is therefore assigned to the CCl_2 twist. The other obviously polarized peak in the Raman spectrum occurs at 274 cm^{-1} and is assigned then to a CCl bending vibration. The other CCl bend appears only in the spectrum of the solid at 228 cm^{-1}. In the liquid phase Raman spectrum the depolarized peak at 222 cm^{-1} is asymmetrically shaped on the high-frequency side, but the two bands are resolved only in the solid phase. No other low frequency peak splits up in the solid phase. Therefore the 228-cm^{-1} peak is assigned to the other CCl bend of A symmetry and the 222-cm^{-1} peak can be assigned to the similar CCl bending of B symmetry. Another depolarized Raman peak occurs at 284 cm^{-1} and it can now be assigned to the CCl bend of B symmetry analogous to the peak at 274 cm^{-1} which resulted from the corresponding A mode. Finally, only two other peaks occur in the Raman spectrum. These are the depolarized lines at 53 and 128 cm^{-1} and these are assigned as the CCl_2 wag and rock, respectively.

cis-1,1,2,3-TCCP. CH Stretches. Both CH stretching frequencies in this isomer are degenerate, occurring at 3047 cm^{-1} in the liquid phase Raman spectrum (polarized) and at 3048 cm^{-1} in the infrared spectrum. The solid phase Raman data shows three peaks in this region, but it is not possible to confidently assign these peaks because they could arise from overtones or combination bands or factor group splitting. A similar degeneracy of the CH stretches occurs for *cis*-1,2-dichloroethylene[20] and it is not surprising that it also occurs for the same fragment in *cis*-1,1,2,3-TCCP.

CH Bendings. As in the spectra for the trans isomer, the CH bendings can be easily attributed to peaks in spectral range 1000–1300 cm^{-1}. Polarized peaks which arise from A′ CH bending modes occur at 1306 and 1051 cm^{-1}. A depolarized peak at 1250 cm^{-1} is also observed and can be assigned as one of the A″ CH bendings. The other CH bending mode is observed at a shoulder of medium to strong intensity at 1065 cm^{-1} in the infrared spectrum of the liquid. In the Raman spectrum of the liquid this peak appears to be depolarized but is quite weak and good depolarization data could not be obtained due to the overlapping of the bands. The solid phase spectrum, however, is quite clear and well resolved. The A′ CH bending vibration gives rise to a doublet at 1049 and 1055 cm^{-1} and the A″ vibration occurs at 1070 cm^{-1}. Once again cyclopropyl "group frequencies" occur in this region and can be confidently assigned as resulting from CH bending modes. Notice that due to the different symmetry of this isomer (C_s) the totally symmetric CH bends occur at ~1300 and ~1050 cm^{-1} and the A″ bends at ~1250 and ~1060 cm^{-1}, while for the trans isomer (C_2 symmetry), B vibrations occur at ~1330 and ~1240 cm^{-1} and the totally symmetric modes result in the lower frequencies at ~1070 and ~1040 cm^{-1}.

Ring Vibrations. In the same region as the CH bending modes there is another polarized Raman peak at 1202 cm^{-1}, which is readily assignable to the ring breathing vibration. As in the case of the trans isomer the other two ring modes appear to be degenerate and give rise to the depolarized peak at 937 cm^{-1} in the Raman spectrum. No other peaks in this region can be assigned to the ring deformation mode, we therefore tentatively assign it and the antisymmetric ring stretch to the 937 cm^{-1} peak. This peak is strong in the liquid infrared spectrum and could well be the result of both vibrations.

CCl Stretches. Two very strong, polarized peaks occur in the Raman spectrum of the liquid sample at 536 and 681 cm^{-1}. By analogy to the assignment for the trans isomer these peaks can be readily assigned to the symmetric and antisymmetric CCl_2 stretches, respectively. Notice that, once again, these two peaks are in the same symmetry block for this isomer and in different symmetry blocks for the trans isomer. This is another result of the change in symmetry between these two isomers. Two peaks (at 879 and 823 cm^{-1}) occur in the liquid phase infrared spectrum which can by analogy with the trans isomer be assigned to the stretches of the CHCl group. The peak at 823 cm^{-1} has a depolarized Raman counterpart and is thus assigned to the A″ CCl stretch. The other peak mysteriously does not have a Raman counterpart but we tentatively assign this 879-cm^{-1} peak to the A′ CCl stretch similarly to this assignment for the trans isomer as well as *cis*- and *trans*-1,2-dichloroethylene.[20]

CCl Bendings. Once again the most intense Raman band (at 346 cm^{-1}) has to be assigned to the CCl_2 deformation. Another strong, polarized Raman peak is observed at 185 cm^{-1}, and because of its intensity and low frequency can be assigned to the rocking vibration of the CCl_2 group. Two other low frequency, polarized Raman peaks occur at 256 cm^{-1} and as a shoulder at 340 cm^{-1}. This shoulder is clearly resolved in the spectrum of the polycrystalline solid and cannot be assigned as a combination or overtone band. Therefore it must be a fundamental and we assign it to the CCl bend of A′ symmetry. The peak at 256 cm^{-1}, then, is due to the other CCl bend of A′ symmetry.

CCl_2 vibrations of A″ symmetry include the CCl_2 wag and CCl_2 twist. These vibrations can easily be assigned by comparison to the assignment of the trans isomer. In

the trans isomer the wag occurs at 513 cm^{-1} and the twist at 157 cm^{-1}. Depolarized Raman peaks occur in the spectrum of the cis isomer at 482 and 133 cm^{-1} and can therefore be attributed to the CCl_2 wag and twist, respectively. A search of the low frequency Raman spectrum for any other peaks shows that there are no other peaks in this region, polarized or depolarized. Thus we look to the solid phase data to assign the A″ CCl bendings. Both the peaks near 190 and 260 cm^{-1} have shoulders or are asymmetrical in addition to showing evidence of factor group splitting (~6 cm^{-1}). In the liquid phase, both of these peaks have quite high depolarization ratios ($\rho = 0.53$ for the 185-cm^{-1} peak and $\rho = 0.51$ for the 256-cm^{-1} peak) in comparison to the other A′ modes, for which ρ values are 0.18 or less. On this basis we tentatively assign the two CCl bends of A″ symmetry to be accidentally degenerate with the peaks at 185 and 256 cm^{-1}.

It is somewhat disturbing that this rather large number of accidental degeneracies occurs for this isomer. In all cases, absolutely no other peaks can be found in the appropriate frequency range which could be assigned. However, in all of the cases there are from two to three peaks observed in the solid phase spectrum, some of which certainly arise from factor group splitting, but the others may well be due to the removal of these degeneracies in the polycrystalline phase. Perhaps these degeneracies are a result of the different symmetry of this molecule. The fact that accidental degeneracies (five altogether) are *not* isolated incidents may be suggestive of unusual interactions in this isomer. Perhaps normal coordinate analysis might bear this out. We are also currently investigating the spectra of other tetrahalocyclopropanes and hope that further information on this topic might result.

Summary and Conclusions

All three isomeric possibilities of tetrachlorocyclopropane have been synthesized by a new reaction procedure which resulted in high yields and stereospecific products. The vibrational spectra for 1,1,2,2-TCCP, *trans*-1,1,2,3-TCCP, and *cis*-1,1,2,3-TCCP have been obtained for liquid and solid phases. In addition, the relatively high vapor pressure of the 1,1,2,2 isomer (~2 Torr) enabled its gas phase infrared spectrum to be recorded.

Using Raman depolarization data, infrared gas-phase band contours, band intensities, and group frequency correlations, virtually all of the 63 total vibrational frequencies for these three isomers have been assigned. Comparison of frequencies of similar vibrations among several chlorine-substituted cyclopropanes further corroborates these assignments.

As a result of these assignments the concept of the cyclopropyl "group frequency" near 1030 cm^{-1} as being due to a ring deformation vibrations has been refuted. Peaks in this region can confidently be attributed to CH bending vibrations instead, and clarification of the source of the cyclopropyl "group frequency" has been made. Other characteristic frequencies observed for the tetrachlorocyclopropanes, at least, include the CH_2 symmetric stretch near 3000 cm^{-1}, the CH_2 antisymmetric stretch near 3090 cm^{-1}, and the carbon–hydrogen stretch of the CHCl group near 3050 cm^{-1}. Ring vibrational frequencies are also nearly a group frequency with the ring breathing occurring from 1200 to 1250 cm^{-1} and the ring deformation and antisymmetric ring stretch falling in the region 900–950 cm^{-1}

As a final note, the fact that all three isomers have at least one element of symmetry and the fact that all possible interactions can be observed lend themselves nicely to a normal coordinate study. In fact, we are currently investigating the normal coordinates of the tetrachlorocyclopropane system using both redundant and nonredundant sets of internal coordinates and we hope to be able to report the results of that study shortly.

Acknowledgment. This research was supported in part by a Faculty Research Grant from the UMKC School of Graduate Studies. The authors also gratefully acknowledge Professor James R. Durig for kindly letting us obtain the Raman data.

References and Notes

(1) This article in part was reported at the 12th Midwest Regional Meeting of the American Chemical Society, Oct 28, 1976, Kansas City, Mo. paper no. 607.
(2) See, for example, C. J. Wurrey and A. B. Nease, "Vibrational Spectroscopy of Three-Membered Ring Compounds" in "Vibrational Spectra and Structure", J. R. Durig, Ed., in preparation and references cited therein.
(3) M. I. Kay, Ph.D. Thesis, Rensselaer Polytechnic Institute, 1962. (Available from University Microfilms, Inc., *cf. Diss. Abstr.*, **25**, 130 (1964–1965)).
(4) W. G. Rothschild, *J. Chem. Phys.*, **44**, 3875 (1966).
(5) T. Hirokawa, M. Hayashi, and H. Murata, *J. Sci. Hiroshima Univ., Ser. A*, **37**, 301 (1973).
(6) J. M. Freeman and P. J. Robinson, *Can. J. Chem.*, **49**, 2533 (1971).
(7) C. J. Wurrey and L. E. Firment, *Spectrochim. Acta, Part A*, **30**, 1115 (1974).
(8) N. C. Craig, T.-N. Hu Chao, E. Cuellar, D. E. Hendriksen, and J. W. Koepke, *J. Phys. Chem.*, **79**, 2270 (1975).
(9) F. A. Miller and K. O. Hartman, *Spectrochim. Acta, Part A*, **23**, 1609 (1967).
(10) N. C. Craig, G. J. Anderson, E. Cuellar-Ferreira, J. W. Koepke, and P. H. Martyn, *Spectrochim. Acta, Part A*, **28**, 1175 (1972).
(11) V. T. Aleksanyan, M. R. Aliev, M. Y. Lukina, O. A. Nesmeyanova, and G. A. Khotimskaya, *Izv. Akad. Nauk SSSR, Ser. Khim.*, 807 (1968).
(12) H. E. Simmons, E. P. Blanchard, and H. D. Hartzler, *J. Org. Chem.*, **31**, 295 (1966).
(13) W. G. Rothschild, *J. Chem. Phys.*, **44**, 1712 (1966).
(14) P. G. Stevens, *J. Am. Chem. Soc.*, **68**, 620 (1946).
(15) S. W. Tobey and R. West, *J. Am. Chem. Soc.*, **88**, 2478 (1966).
(16) R. Fields, R. N. Haszeldine, and D. Peter, *Chem. Commun.*, 1081 (1967).
(17) R. Fields, R. N. Haszeldine, and D. Peter, *J. Chem. Soc. C*, 165 (1969).
(18) W. H. Flygare, A. Narath, and W. D. Gwinn, *J. Chem. Phys.*, **36**, 200 (1962).
(19) C. J. Wurrey and A. B. Nease, unpublished results.
(20) K. Tanabe and S. Saeki, *Bull. Chem. Soc. Jpn.*, **47**, 2545 (1974).

Spectrophotometric Study of the Radicals Produced by the Reduction of *syn*- and *anti*-Azobenzene[1]

P. Neta* and Haim Levanon[2]

Radiation Laboratory and Chemistry Department, University of Notre Dame, Notre Dame, Indiana 46556 *(Received June 6, 1977)*

Publication costs assisted by the Division of Basic Energy Sciences, U.S. Department of Energy

The radicals produced by one-electron reduction of *syn*- and *anti*-azobenzene, A_s and A_a, in various media were studied by spectrophotometric pulse radiolysis. In aqueous solutions both forms of A are reduced by e_{aq}^- ($k = 3 \times 10^{10}$ M^{-1} s^{-1}) and by various alcohol radicals ($k_{A+(CH_3)_2COH} = 4 \times 10^8$ and $k_{A+(CH_3)_2CO^-} = 2 \times 10^9$ M^{-1} s^{-1}). Similar reactions are observed in neat *i*-PrOH. The transient spectra exhibit an intense absorption in the 350–400-nm region and a weaker one at 550–600 nm. Shifts of the maxima with pH are attributed to the acid–base equilibria $\dot{A}H_2^+ \rightleftarrows \dot{A}H \rightleftarrows \dot{A}^-$ with pK values of 2.9 and 13.7, respectively, in aqueous solutions. In THF solutions the main peak of $\dot{A}^-$ is at 430 nm. All the kinetic and spectral parameters are identical whether one starts with the syn or anti isomer. Product analysis shows radiolytic conversion only in the direction $A_s \rightarrow A_a$. In MTHF glasses the spectra of $\dot{A}_s^-$ and $\dot{A}_a^-$ are different, the latter being an order of magnitude more intense. It is concluded that in solution at room temperature $\dot{A}_s^-$ is rapidly converted into $\dot{A}_a^-$.

Introduction

It has been recently demonstrated that the anion radicals of *cis*- and *trans*-stilbene, S, differ in their physicochemical properties such as optical and ESR absorption spectra and protonation rates in alcoholic solutions.[3,4] These observations led to the quantitative study of the electron transfer

$$\dot{S}_c^- + S_t \rightleftarrows S_c + \dot{S}_t^- \quad (1)$$

and the direct isomerization[3]

$$\dot{S}_c^- \rightleftarrows \dot{S}_t^- \quad (2)$$

The kinetics and equilibrium of reaction 1 were determined by optical pulse radiolysis experiments[4] whereas reaction 2 is too slow to be monitored under those conditions.

In the present study we searched for similar phenomena in the analogous compounds *syn*- and *anti*-azobenzene (A). In general, it is expected that isomerization around an N=N bond would be more facile than that around a C=C bond.[5] The results presented here show that the reaction

$$\dot{A}_s^- \rightarrow \dot{A}_a^- \quad (3)$$

is very fast and no experimental evidence was found to indicate a reaction in the opposite direction. Consequently, the electron transfer reaction similar to (1) becomes negligible.

Experiments in protic solvents showed that $\dot{A}^-$ can protonate rapidly in two consecutive steps and the corresponding pK values were determined.

Experimental Section

The two isomers of azobenzene where prepared photochemically from a commercial sample as described in the literature[6] and were identified spectrophotometrically.[7,8] Fresh solutions were prepared immediately before each experiment and their absorption spectra were recorded to confirm that no thermal isomerization took place. The alcohols and the inorganic compounds were Baker Analyzed reagents. THF and MTHF were dried and distilled under vacuum over K–Na alloy.[9] For large quantities, THF was refluxed over $LiAlH_4$ and freshly distilled under a stream of dry nitrogen for each experiment. Water was purified by passage through two Millipore systems, first the Milli-RO and then the Milli-Q. The half-life of hydrated electrons in this water, containing 2-methyl-2-propanol at pH 11, was found to be greater than 40 μs at dose rates similar to those used in the present experiment.

The computer controlled pulse radiolysis apparatus was that described previously[10,11] except for the radiation source which in this case was an ARCO LP-7 linear accelerator. Pulses of 5-ns duration were used and the total radical concentration produced by each pulse was in the range of 2–4 μM. Pulse conductometric experiments were carried out using the apparatus described previously.[12]

Results and Discussion

Transient Spectra in Aqueous Solutions. Preliminary experiments with azobenzene were carried out in neutral aqueous solutions containing 2-propanol as a scavenger for OH and H. A transient spectrum with maxima around 350 and 550 nm was observed. The kinetics of formation of this spectrum consisted of two steps (Figure 1): an initial build up attributed to rapid reaction with the hydrated electron

$$A + e_{aq}^- \xrightarrow{k_4} \dot{A}^- \quad (4)$$

followed by the slower electron transfer from the 2-propanol radical

$$A + (CH_3)_2\dot{C}OH \xrightarrow{k_5} \dot{A}^- + (CH_3)_2CO + H^+ \quad (5)$$

In order to confirm that the same radical is produced in both reactions 4 and 5 the transient spectrum was recorded at different times. The spectrum observed after completion of reaction 5 (80–100 μs after the pulse) was found to be identical with that recorded ~1 μs after the pulse, i.e., when only reaction 4 is complete. Further confirmation was obtained from experiments in the presence of 2-methyl-2-propanol instead of *i*-PrOH, where reaction 5 is eliminated. In this case the formation of the transient consisted of the rapid reaction 4 only. The spectra recorded ~1 μs after the pulse using solutions of A_a and A_s are shown in Figure 2. It is clearly seen that the spectra obtained from both isomers are identical, suggesting that the structure of the radical is common for both starting materials. It is also seen in Figure 2 that the spectra in

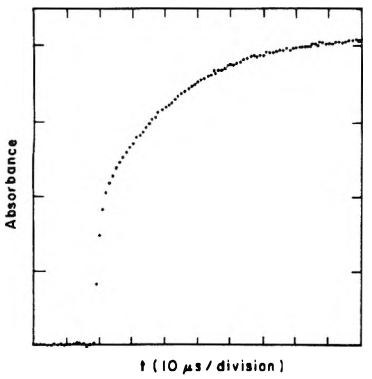

Figure 1. Formation of the azobenzene transient absorption in aqueous solution containing 2-propanol: $[A_a] = 1 \times 10^{-4}$ M, [*i*-PrOH] = 1 M, pH 7, λ 350 nm.

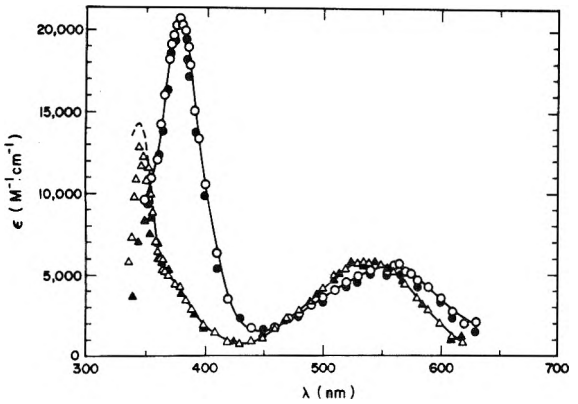

Figure 2. Absorption spectra observed ~1 μs after the pulse with *syn*- and *anti*-azobenzene in aqueous solutions containig 2-methyl-2-propanol: [A] = 1×10^{-4} M, [*t*-BuOH] = 1 M; (O) A_s, 1 M NaOH; (●) A_a, 1 M NaOH; (Δ) A_s, pH 7, (▲) A_ϵ, pH 7. Extinction coefficients were calculated using $G = 2.8$ and thiocyanate dosimetry. The difference between the ▲ and Δ data points below 360 nm results from the difference in the parent compound absorption; the dashed line is the corrected curve for both isomers.

neutral and alkaline solutions are different. This finding suggests that $\dot{A}^-$ protonates rapidly in neutral solution.

To examine the acid–base equilibria of the azobenzene radical it is advantageous to be able to cover the whole pH range. Solutions containing *t*-BuOH are only useful at pH > 4 since the conversion of e_{aq}^- into H in acid solution may result in the formation of a different radical from azobenzene (see below). Experiments were, therefore, carried out in the presence of *i*-PrOH, where azobenzene is expected to undergo one-electron reduction at all pH values. Typical spectra are shown in Figure 3. At pH 14 the spectrum is identical with that observed in the presence of *t*-BuOH (Figure 2),[13] confirming that the reaction of the $(CH_3)_2\dot{C}OH$ radical with azobenzene is an electron transfer process. The spectra taken in neutral solutions containing either *i*-PrOH (Figure 3) or *t*-BuOH (Figure 2) differ only slightly, i.e., the absorption in the 400–500-nm region is slightly higher in *t*-BuOH than in *i*-PrOH solutions. This difference is attributed to the contribution of the absorption of the H adduct to A, which is formed only in *t*-BuOH. This assignment was also confirmed by experiment with solutions containing both *t*-BuOH and N_2O so that A can react with H atoms only. The spectrum of the transient at pH 1 was recorded with *i*-PrOH solutions only. As stated above, the reaction of the H atoms with azobenzene does not necessarily lead to the same species, but may result in substantial addition to the rings.

The pH dependence of the absorption in the presence of *i*-PrOH is shown in the insert of Figure 3. From the results p*K* values of 2.9 and 13.7 were determined. These

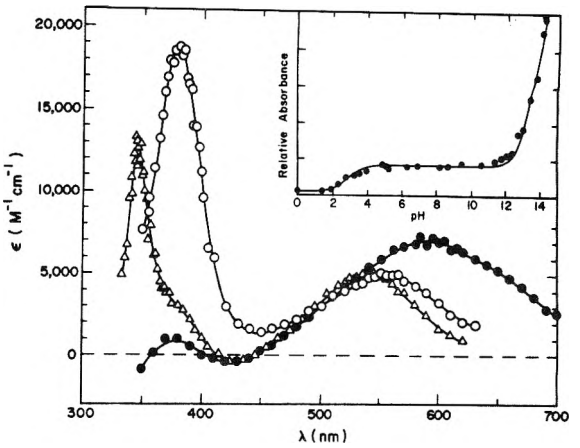

Figure 3. Absorption spectra observed with azobenzene in aqueous solutions containing 2-propanol. The spectra were recorded 80–100 μs after the pulse, after reaction 5 was complete: [A] = 1×10^{-4} M, [*i*-PrOH] = 1 M; (O) 1 M NaOH; (Δ) pH 7; (●) pH 1. Extinction coefficients were calculated using $G = 6$, equal to that used in the thiocyanate dosimetry. The insert shows the effect of pH on the transient absorption at 390 nm. The best-fit curve was calculated using $pK_1 = 2.9$ and $pK_2 = 13.7$.

values are assigned to the protonation of the azobenzene anion radical in two successive steps

$$\underset{\dot{A}H_2^+}{(C_6H_5NHNHC_6H_5)^+\cdot} \underset{pK\ 2.9}{\rightleftarrows} \underset{\dot{A}H}{C_6H_5NH\dot{N}C_6H_5} \underset{pK\ 13.7}{\rightleftarrows} \underset{\dot{A}^-}{(C_6H_5N{=}NC_6H_5)^-\cdot} \quad (6)$$

In order to verify these protonation steps, a pulse conductometric experiment was carried out. The irradiation of an unbuffered neutral aqueous solution containing 1×10^{-4} M azobenzene and 0.5 M *t*-BuOH resulted in practically no net change in conductance. (The change ~10 μs after the pulse was ≤3% of the conductance measured after irradiation of a reference solution containing CH_3Cl.) It is, therefore, concluded that in neutral solution the azobenzene anion captures one proton rapidly to produce the neutral species ȦH, while the spectrum observed at pH 14 is assigned to $\dot{A}^-$.

Transient Spectra in 2-Propanol. The spectrum observed in neat *i*-PrOH was found to be identical with that in neutral aqueous solution, and is, therefore, assigned to the protonated radical ȦH. Since it was possible to observe the spectrum of $\dot{A}^-$ in water at high pH, an attempt was made to observe it also in 2-propanol as solvent using $(CH_3)_2CHO^-$ as the base. The solutions were prepared by first dissolving Na metal in *i*-PrOH and then adding the azobenzene. The spectrum recorded has a main peak at 390 nm and a smaller one at 550 nm. This spectrum, which is quite different than that in neutral solution, is assigned to $\dot{A}^-$ (Figure 4). It should be also noted that the same spectrum is obtained when starting from either *syn*- or *anti*-azobenzene. The p*K* for the protonation of $\dot{A}^-$ in *i*-PrOH was also determined as shown in Figure 5. The inflection point in the best-fit curve corresponds to a concentration of 1.4×10^{-2} M *i*-PrO^-Na^+, from which the equilibrium constant for the process

$$\dot{A}H + i\text{-}PrO^- \rightleftarrows \dot{A}^- + i\text{-}PrOH \quad (7)$$

was calculated to be $K_7 = 930$.

The results in aqueous solutions (Figure 3) showed an equilibrium constant $K_8 = 110$ for

$$\dot{A}H + OH^- \rightleftarrows \dot{A}^- + H_2O \quad (8)$$

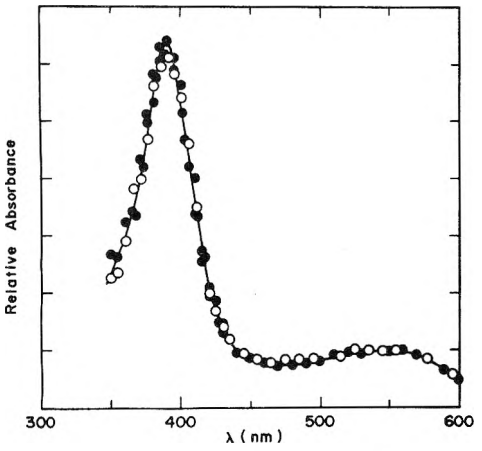

Figure 4. Absorption spectrum of $\dot{A}^-$ in 2-propanol recorded ~50 μs after the pulse; [A] = 1 × 10^{-4} M, [*i*-PrO⁻Na⁺] = 4 × 10^{-2} M; (O) A_s, (●) A_a.

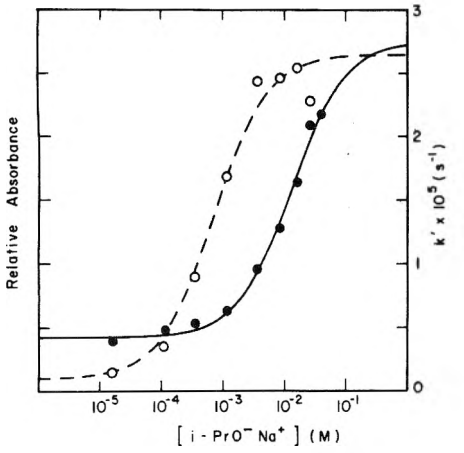

Figure 5. Determination of the p*K* values of ÀH and of $(CH_3)_2\dot{C}OH$ in neat 2-propanol. The values on the abscissa were determined by diluting an aliquot of the solutions with water and measuring the pH: (●) absorption of azobenzene transient at 390 nm (left ordinate); (O) pseudo-first-order rate constant, *k'*, for the reduction of azobenzene by the 2-propanol radical (right ordinate). In both experiments [A] was kept constant (1 × 10^{-4} M).

As a first approximation, the values in the two solvents can be compared using the equations

$$-\log K_7 = -\log \left\{ \frac{[\dot{A}^-][H^+]}{[\dot{A}H]} \frac{[ROH]}{[RO^-][H^+]} \right\} = pK_{\dot{A}H} - pK_{ROH} \quad (9)$$

$$-\log K_8 = -\log \left\{ \frac{[\dot{A}^-][H^+]}{[\dot{A}H]} \frac{[H_2O]}{[OH^-][H^+]} \right\} = pK_{\dot{A}H} - pK_{H_2O} \quad (10)$$

If one neglects the effect of solvent and uses pK_{H_2O} = 15.75 and pK_{ROH} = 17.1[14] the values of $pK_{\dot{A}H}$ calculated from eq 9 and 10 are similar. However, pK_{ROH} in the alcohol solution should be higher than that measured in water according to the relationship[15]

$$pK_{ROH}(\text{in ROH}) - pK_{ROH}(\text{in } H_2O) = \frac{121.6n}{\langle r \rangle}\left[\frac{1}{D_{ROH}} - \frac{1}{D_{H_2O}}\right] \quad (11)$$

where *D* is the dielectric constant, ⟨*r*⟩ is the average radius of the ions, and $n = 1 + z^2(RO^-) - z^2(ROH) = 2$. Assuming[16] ⟨*r*⟩ ≈ 3.5 Å eq 11 yields pK_{ROH}(in ROH) ≈ 20.

TABLE I: Rate Constants for Reduction of Azobenzene

Solute	Solvent	Reducing radical	Rate constant, M^{-1} s^{-1}
A_a	H_2O[a]	e_{aq}^-	(3.3 ± 0.3) × 10^{10}
A_s	H_2O[a]	e_{aq}^-	(3.2 ± 0.3) × 10^{10}
A_a	H_2O[a]	$\dot{C}H_2O^-$	1 × 10^9
A_s	H_2O[a]	$\dot{C}H_2O^-$	1 × 10^9
A_a	H_2O	$(CH_3)_2\dot{C}OH$	4 × 10^8
A_a	H_2O[a]	$(CH_3)_2\dot{C}O^-$	2 × 10^9
A_a	*i*-PrOH	$(CH_3)_2\dot{C}OH$	3 × 10^7
A_a	*i*-PrOH[b]	$(CH_3)_2\dot{C}O^-$	2 × 10^9
A_s	*i*-PrOH[b]	$(CH_3)_2\dot{C}O^-$	2 × 10^9

[a] 1 M NaOH. [b] Containing 0.04 M *i*-PrO⁻Na⁺.

From this value $pK_{\dot{A}H}$(in ROH) = 17.

During these experiments it was noticed that the reduction of azobenzene by the *i*-PrOH radical became faster at high basicity. This result indicates that the radical dissociates to produce the anion

$$(CH_3)_2\dot{C}OH \rightleftarrows (CH_3)_2\dot{C}O^- + H^+ \quad (12)$$

which is known to be a stronger reductant,[17] i.e., reaction 5 is replaced by the more rapid reaction

$$A + (CH_3)_2\dot{C}O^- \rightarrow \dot{A}^- + (CH_3)_2CO \quad (13)$$

The change in the observed rate of reduction can be used to estimate pK_{12} in *i*-PrOH. The results in Figure 5 (dashed line) show an inflection point at 7.7 × 10^{-4} M *i*-PrO⁻Na⁺. Applying the same considerations as discussed above for ÀH, $pK(CH_3)_2\dot{C}OH$(in ROH) is calculated to be ~16. The p*K* of $(CH_3)_2\dot{C}OH$ in water is 12.[17]

Kinetics of Reduction of Azobenzene. From the above discussion it is clear that azobenzene undergoes one-electron reduction by various species (e.g., reactions 4, 5, and 13) with a wide range of reactivities. The main reaction is the direct reduction by the electron (reaction 4) which is very fast. The rate constant for this reaction was determined for both *syn*- and *anti*-azobenzene in aqueous solutions containing 1 M base and 0.1 M methanol. The half-life for the decay of the e_{aq}^- absorption at 600 nm was found to be ~40 μs in the absence of A. Increasing the concentrations of A_s or A_a in the range of 2–12 μM gave correspondingly higher pseudo-first-order rates. A linear plot of the rates vs. concentration yielded k_4 = (3.3 ± 0.3) × 10^{10} for A_a and (3.2 ± 0.3) × 10^{10} M^{-1} s^{-1} for A_s. Observation of the formation of $\dot{A}^-$ at 380 nm gave similar results but the accuracy was limited by interference of the slow secondary electron transfer.

The electron transfer from $\dot{C}H_2O^-$ according to a reaction equivalent to (13) was monitored by following the formation of the $\dot{A}^-$ absorption at 380 nm. The rate constants were found to be 1 × 10^9 M^{-1} s^{-1} for both isomers.

Reduction by the 2-propanol radical was studied in both neutral and alkaline aqueous solutions. As mentioned above, the reduction by the dissociated form $(CH_3)_2\dot{C}O^-$ (reaction 13) was found to be faster than that by the neutral form $(CH_3)_2\dot{C}OH$ (reaction 5). Rate constants of k_5 = 4 × 10^8 and k_{13} = 2 × 10^9 M^{-1} s^{-1} were determined (Table I). The rates of these reactions were also measured in neat *i*-PrOH yielding k_5 = 3 × 10^7 and k_{13} = 2 × 10^9 M^{-1} s^{-1}. The higher value of k_5 in water is probably due to the energy gain in the hydration of the H^+ produced in this reaction.

It should be noted that the second-order decay of the azobenzene radicals was sufficiently slow not to interfere with the formation and could be observed on the millisecond time scale.

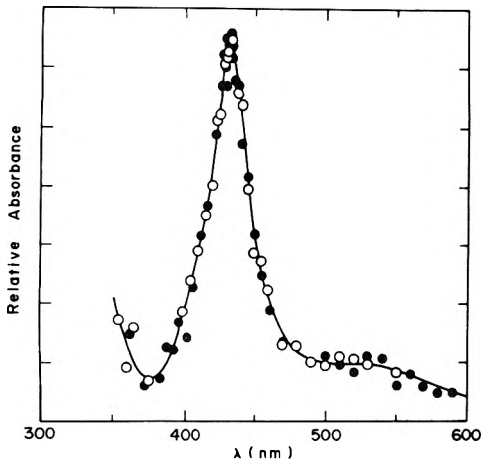

Figure 6. Absorption spectrum of $\dot{A}^-$ in THF: [A] = 1×10^{-4} M; (○) A_s, (●) A_a.

Identification of $\dot{A}^-$. The results presented so far show that the anion radical monitored in solution at room temperature is identical whether it is produced from A_s or A_a. The exact identity of this species cannot be elucidated from the experiments above. One limitation is the fact that the pK values for the protonation of $\dot{A}^-$ in water and in 2-propanol are too high to allow the experimental determination of the spectra of $\dot{A}^-$ in the plateau region (see Figure 3 and 5). The spectra assigned to $\dot{A}^-$ in Figures 2–4 represent a mixture with a small fraction of ȦH. The positions of the maxima, however, are not affected under these experimental conditions and are attributed to $\dot{A}^-$. The main peak is at 380 nm in water and at 390 nm in *i*-PrOH and in all cases it was identical for the *syn*- and *anti*-azobenzene. However, the equilibrium between $\dot{A}^-$ and ȦH may form a channel by which $\dot{A}_s^-$ and $\dot{A}_a^-$ can interconvert. For example, in aqueous solutions such a mechanism is represented by

$$\left.\begin{matrix}\dot{A}_s^- + H_2O \\ \dot{A}_a^- + H_2O\end{matrix}\right\rightleftharpoons \dot{A}H + OH^- \qquad (14)$$

This mechanism can be eliminated by using an aprotic solvent. Experiments were, therefore, carried out in tetrahydrofuran and the spectra observed for $\dot{A}^-$ produced from either *syn*- or *anti*-azobenzene were found to be identical (Figure 6). The spectrum in THF has a maximum at 430 nm and only a shoulder at 500–540 nm. Red shifts in the main peak of 10 and 50 nm are thus observed in going from water to 2-propanol to THF.

In view of the fact that the *cis*- and *trans*-stilbene anion radicals have different spectra, it seems unlikely that two isomeric azobenzene radicals exist with completely identical spectra. Furthermore, the spectra of the parent azobenzenes are also different for the two isomers.[7,8] If $\dot{A}^-$ exists in one configuration only, one can expect radiolytic isomerization of azobenzene via production of $\dot{A}^-$ which is then oxidized by the solvent positive ion back to A. Vacuum sealed solutions of either A_s or A_a in THF at room temperature were prepared and their optical spectra were monitored before and after pulse irradiation. When starting with A_s the absorption in the spectral range of 400–500 nm was found to decrease considerably. This indicates that A_s is converted into A_a. Conversion in the opposite direction when starting with A_a should result in an increase in the absorption in that region. However, no such increase could be experimentally observed. Since part of the azobenzene was destroyed to form products with new absorption in the UV, observation of the isomerization

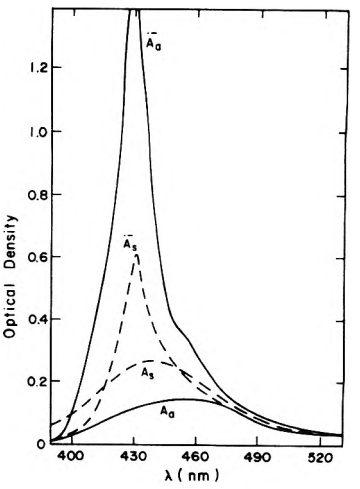

Figure 7. Absorption spectra of $\dot{A}_s^-$ and $\dot{A}_a^-$ in MTHF glass at 77 K. The spectra before irradiation were taken for comparison. A_a was irradiated for 15 min and A_s for 45 min. The dose rate was $\sim 3 \times 10^{17}$ eV g^{-1} min^{-1}. The optical path was 3 mm.

below 400 nm was less sensitive but generally confirmed the above results.

It appears that the anion radical produced from either isomer yields upon oxidation the anti isomer predominantly:

$$\left.\begin{matrix}A_s + e_{THF}^- \\ A_a + e_{THF}^-\end{matrix}\right\rightarrow \dot{A}^- \xrightarrow{ox} A_a \qquad (15)$$

The intermediate cannot, therefore, be a mixture of $\dot{A}_s^-$ and $\dot{A}_a^-$. Although some intermediate configuration or a free rotating structure cannot be ruled out, it is more likely that in solution the observed $\dot{A}^-$ is in its anti form. The assignment of the ESR proton hyperfine splittings[18] to $\dot{A}_a^-$ supports this conclusion.

If the intermediate observed is indeed $\dot{A}_a^-$, the conversion of $\dot{A}_s^-$ into $\dot{A}_a^-$ is too rapid to observe at room temperature. Experiments were, therefore, carried out at liquid nitrogen temperature in MTHF glass. Frozen solutions of A_s and A_a were irradiated and the optical spectra were compared (Figure 7). The spectrum of $\dot{A}_a^-$ in the glass is identical with that observed in THF solutions at room temperature. The spectrum obtained using A_s has its maximum also at 430 nm but the intensity per unit dose is almost an order of magnitude lower. These findings, combined with the results obtained with THF solution at room temperature, lead to the conclusion that under the latter conditions $\dot{A}_s^-$ is converted into $\dot{A}_a^-$ very rapidly ($\ll 1$ μs). The same direct isomerization is expected to take place also in alcoholic and aqueous solutions rapidly enough to predominate over mechanism 14.

Acknowledgment. We thank Professors A. M. Trozzolo and M. Szwarc for helpful discussions and Mrs. Hedva Levanon for the preparation and purification of the azobenzene isomers.

References and Notes

(1) The Research described herein was supported by the Division of Basic Energy Sciences, U.S. Department of Energy. This is Document No. NDRL-1773 from the Notre Dame Radiation Laboratory.
(2) On leave from the Department of Physical Chemistry, The Hebrew University, Jerusalem, Israel.
(3) (a) S. Sorensen, G. Levin, and M. Szwarc, *J. Am. Chem. Soc.*, **97**, 2341 (1975); (b) H. C. Wang, G. Levin, and M. Szwarc, *ibid.*, **99**, 2642 (1977).
(4) H. Levanon and P. Neta, *Chem. Phys. Lett.*, **48**, 345 (1977).
(5) P. Haberfield, P. M. Block, and M. S. Lux, *J. Am. Chem. Soc.*, **97**, 5804 (1975).
(6) G. S. Hartley, *J. Chem. Soc.*, 633 (1938).
(7) S. Malkin and E. Fischer, *J. Phys. Chem.*, **66**, 2482 (1962).
(8) J. H. Collins and H. H. Jaffe, *J. Am. Chem. Soc.*, **84**, 4708 (1962).

(9) T. T. Tuttle, Jr., and S. I. Weissman, *J. Am. Chem. Soc.*, **80**, 5342 (1958).
(10) L. K. Patterson and J. Lilie, *Int. J. Radiat. Phys. Chem.*, **6**, 129 (1974).
(11) R. H. Schuler, P. Neta, H. Zemel, and R. W. Fessenden, *J. Am. Chem. Soc.*, **98**, 3825 (1976).
(12) J. Lilie and R. W. Fessenden, *J. Phys. Chem.*, **77**, 674 (1973).
(13) The 380-nm peak is slightly higher in Figure 2 than in Figure 3 because in the former case $G = 2.8$ was used in the calculation, neglecting the conversion of H into e_{aq}^- at high pH.
(14) J. Murto, *Acta. Chem. Scand.*, **18**, 1043 (1964).
(15) R. G. Bates, "Determination of pH, Theory and Practice", Wiley, New York, N.Y., 1965, p 195.
(16) A. Spernol and K. Wirtz, *Z. Naturforsch. A*, **8**, 522 (1953).
(17) See, e.g., P. Neta, *Adv. Phys. Org. Chem*, **12**, 223 (1976).
(18) E. T. Strom, G. A. Russell, and R. Konaka, *J. Chem. Phys.*, **42**, 2033 (1965).

Rate Constant Measurements for the Reactions of HCO with NO and O_2 in the Gas Phase

Kazuhiko Shibuya, Takayuki Ebata, Kinichi Obi,* and Ikuzo Tanaka

Department of Chemistry, Tokyo Institute of Technology, Ohokayama, Meguro-ku, Tokyo 152, Japan (Received May 31, 1977)

The behavior of the HCO radical produced by the flash photolysis of gaseous acetaldehyde has been studied with and without so-called radical scavengers at room temperature. The analysis of the results gives rate constants of $(8.5 \pm 1.0) \times 10^{-12}$ and $(5.6 \pm 0.9) \times 10^{-12}$ cm^3 molecule^{-1} s^{-1} for the reactions of the HCO radical with NO and O_2, respectively.

Introduction

The HCO radical is a very important triatomic free radical which participates in many chemical reactions. Especially it is thought to be an intermediate species in the photochemistry of the polluted atmosphere[1] and in the combustion of most hydrocarbons.[2] In spite of its important role in many oxidation phenomena, kinetic data on the elementary processes have been mainly based on product analyses.

The first report of direct kinetic measurements on HCO was made by Washida, Martinez, and Bayes.[3] By their flow experiment with a photoionization mass spectrometer, they reported rate constants for the reactions of the HCO radical with atomic and molecular oxygen of $(2.1 \pm 0.4) \times 10^{-10}$ and $(5.7 \pm 1.2) \times 10^{-12}$ cm^3 molecule^{-1} s^{-1}, respectively.

Studies of flash photolysis and kinetic absorption spectroscopy present additional complementary information on HCO radical reactions. We report rate constants of the HCO radicals with NO and O_2 in this paper.

Experimental Section

The HCO radical was generated by the flash photolysis of acetaldehyde with irradiation at wavelength longer than 200 nm. The reaction vessel was a cylindrical quartz cell of 10 cm diameter and 1 m length. The cell contained a multiple reflection mirror system,[4] which increased the length of the absorption path up to a 54 m. Two flash photolysis lamps were mounted parallel to the cell and filled with 150 Torr of argon and 1.5 Torr of hydrogen. The electric circuit for the flash system was of the same design as reported by Welge et al.[5] The capacitor bank consisted of eight capacitors (8 μF each charged to 6.4 kV) gave a 1300-J, 10-μs half-width light pulse.

Decay of the HCO radical concentration was measured by the variation of the optical absorbance around 613.8 nm assigned to the (0, 9, 0)–(0, 0, 0) band of $\tilde{A}^2A''$–$\tilde{X}^2A'$ system.[6] The absorption spectrum of the HCO radical was recorded by a Nikon P-250 spectrograph. The spectroscopic flash lamp was filled with argon at pressure of 1 atm and the discharge energy was 50 J with a 8-μs half-width duration. All absorption spectra were recorded on Kodak 2475 recording films and the measurements were made over the linear part of the characteristic curve of the plates.

Acetaldehyde was purified by many thaw–freeze–pump cycles. NO and O_2 (Takachiho Chemical Ind., 99.99%) were used without further purification. Helium was used as a diluent gas after passing through activated charcoal in a cold trap at liquid nitrogen temperature. The reaction mixtures were left in a 20-L glass bulb for about 4 h before experiments to assure complete mixing.

Results and Discussion

The photolysis of acetaldehyde has been intensively studied in the gas phase.[7-12] Three different primary processes occur with varying degrees of relative importance which depend on experimental conditions.[11,12]

$$CH_3CHO + h\nu \begin{cases} \rightarrow CH_3 + HCO & (1) \\ \rightarrow CH_4 + CO & (2) \\ \rightarrow CH_3CO + H & (3) \end{cases}$$

Conclusive evidence for primary process 1 was found by flash photolysis[12] and process 2 was proved by the use of scavengers.[7] The main dissociation process occurs via process 1 in the photolysis of acetaldehyde at 313 nm and the quantum yield of process 2 increases with excitation energy. Hydrogen is a minor product from dissociative excitation in the wavelength region 235–350 nm which corresponds to its ($\pi^* \leftarrow$ n) absorption band.[10,11] Primary process 3 is therefore certainly of little importance.

Acetaldehyde (10, 20, and 30 Torr) and a mixture of acetaldehyde (20 Torr) and helium (510 Torr) were flash photolyzed and the concentration of HCO radicals was measured at various delay times. Figure 1a shows the typical decay of the HCO radical in the photolysis of the mixture of acetaldehyde and helium. The decay curve apparently displays second-order disappearance as shown in Figure 1b. If the reaction of the HCO radical with acetaldehyde was dominant as regards the disappearance of the HCO radical, the decay curve should be exponential. Therefore, the HCO radical reacts very slowly with the parent molecule, acetaldehyde, but is consumed by radical–radical reactions.

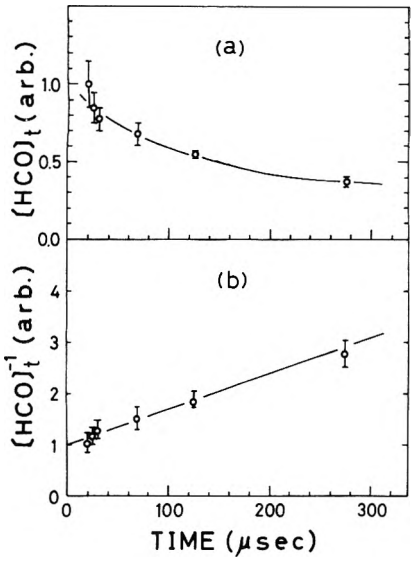

Figure 1. Time variation of (a) HCO concentration and (b) its inverse in the flash photolysis of a mixture of CH_3CHO (20 Torr) and He (510 Torr). The solid lines represent the numerical simulation using the same initial concentration of 6×10^{13} molecule cm^{-3} for HCO and CH_3.

The reaction scheme relating to the decay of the HCO radical would be

$$HCO + HCO \rightarrow \text{products} \quad (4)$$

$$CH_3 + HCO \rightarrow \text{products} \quad (5)$$

$$CH_3 + CH_3 \rightarrow \text{products} \quad (6)$$

Hence the following equations are obtained:

$$-d[HCO]/dt = 2k_4[HCO]^2 + k_5[HCO][CH_3] \quad (I)$$

$$-d[CH_3]/dt = k_5[CH_3][HCO] + 2k_6[CH_3]^2 \quad (II)$$

The simulation was made to obtain the observed decay profile, using values of 3.7×10^{-11}, 4.3×10^{-11}, and 3.6×10^{-11} cm^3 $molecule^{-1}$ s^{-1} for k_4, k_5, and k_6, respectively,[13] and assuming that the initial concentrations of HCO and CH_3 radicals were equal. The solid line in Figure 1b shows the results of the simulation. The probable values of the initial concentrations of HCO and CH_3 were determined to be $(6 \pm 2) \times 10^{13}$ molecule cm^{-3}.

When a suitable amount of NO or O_2 is added to the samples, reactions of the HCO radical with added scavengers predominate over the second-order radical reactions. Under these conditions, the decay will be governed by the reaction

$$HCO + Q \rightarrow \text{products} \quad (7)$$

where Q represents the radical scavengers, that is, NO or O_2.

Typical decay plots of HCO radical are shown in Figure 2a ([NO] = 0.036 Torr) and 2b ([O_2] = 0.071 Torr). Apparently these plots display the pseudo-first-order decay. Therefore, most of HCO radicals react with NO and O_2.

In order to evaluate the rate constants, k_7^Q, numerical simulations were performed by considering the effects of the second-order radical reactions. Since the CH_3 radical also reacts with the scavengers

$$CH_3 + Q \rightarrow \text{products} \quad (8)$$

then the decay profiles are expressed as follows:

$$-d[HCO]/dt = k_7^Q[HCO][Q] + 2k_4[HCO]^2 + k_5[HCO][CH_3] \quad (III)$$

$$-d[CH_3]/dt = k_8^Q[CH_3][Q] + k_5[HCO][CH_3] + 2k_6[CH_3]^2 \quad (IV)$$

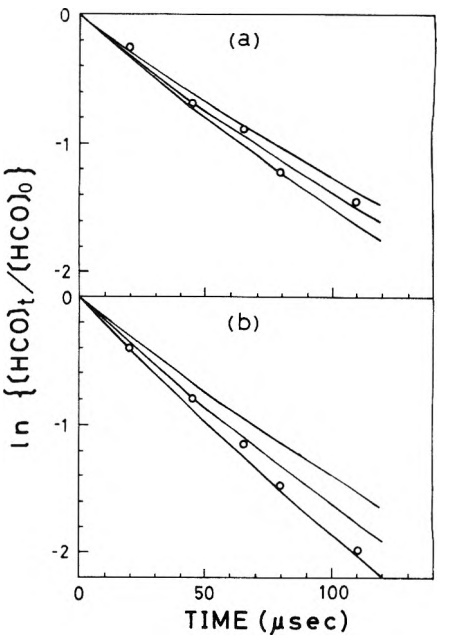

Figure 2. Time variation of ln $\{[HCO]_t/[HCO]_0\}$ for the reactions of HCO with the scavengers NO and O_2: (a) NO (0.036 Torr)/CH_3CHO (20 Torr)/He (510 Torr), $k_7^{NO} = 7, 8, 9 \times 10^{-12}$ cm^3 $molecule^{-1}$ s^{-1}, respectively, from the top; (b) O_2 (0.071 Torr)/CH_3CHO (20 Torr)/He (510 Torr), $k_7^{O_2} = 4, 5, 6 \times 10^{-12}$ cm^3 $molecule^{-1}$ s^{-1}, respectively, from the top.

Using the initial concentrations of HCO and CH_3 radicals estimated above and the rate constants k_4, k_5, k_6, and k_8^Q, the decay curves of the HCO radical were calculated at given pressures of scavengers (solid lines in Figure 2a and 2b). The values of k_8^Q used were $(4.8 \pm 0.4) \times 10^{-13}$ and $(3.2 \pm 0.3) \times 10^{-12}$ cm^3 $molecule^{-1}$ s^{-1} for NO and $(3.0 \pm 0.3) \times 10^{-13}$ and $(5.2 \pm 0.5) \times 10^{-13}$ cm^3 $molecule^{-1}$ s^{-1} for O_2 at total pressures of 20 and 530 Torr, respectively, where the standard deviations are quoted.[14] The values of k_7^Q or $k_7^Q[Q]$ were obtained from the curves fit for the experimental plots similar to Figure 2a and 2b at various pressures of NO and O_2. In the flash photolysis of the mixture of acetaldehyde and O_2, the CH_3CO radical is produced and the following chain reactions are known to occur:[15]

$$CH_3CO + O_2 \rightarrow CH_3CO_3 \quad (9)$$

$$CH_3CO_3 + CH_3CHO \rightarrow CH_3CO_3H + CH_3CO \quad (10)$$

However, after one flash was irradiated to the mixture, the concentration of O_2 was decreased only a few percent and the effect of the chain reaction was negligible within experimental error. Besides, in the experiment with NO, we could not observe the decrease of the concentration of NO due to the chain reaction. In order to avoid the pressure changes of the scavengers, we performed one flash for each mixture.

The values of $k_7^Q[Q]$ vs. the concentrations of NO and O_2 are plotted in Figures 3 and 4 , respectively. The linear relations obtained indicate that the rate constants, k_7^Q, are independent of the concentration of scavengers. The bimolecular rate constants k_7^Q, were evaluated from the slopes of these plots. The rate constants obtained are listed in Table I.

The bimolecular reaction of the HCO radical with NO is proposed[16]

$$HCO + NO \rightarrow HNO + CO \quad (11)$$

but the information on the third body effect has not yet been reported. In our experiments, the value for k_7^{NO}

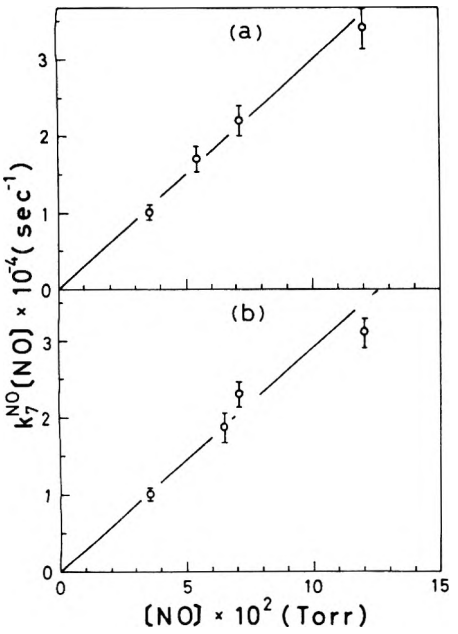

Figure 3. Plots of the HCO radical decay rate against NO concentration in the photolysis of (a) NO/CH_3CHO (20 Torr) and (b) NO/CH_3CHO (20 Torr)/He (510 Torr).

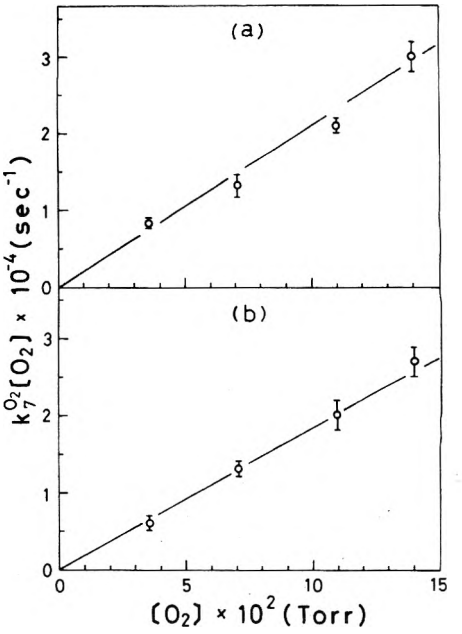

Figure 4. Plots of the HCO radical decay rate against O_2 concentration in the photolysis of (a) O_2/CH_3CHO (20 Torr) and (b) O_2/CH_3CHO (20 Torr)/He (510 Torr).

TABLE I: Rate Constants k_7^Q for the Reactions of HCO Radicals with NO and O_2

Scavenger	Total press, Torr	Rate constants,[a] cm^3 $molecule^{-1}$ s^{-1}
NO	20	$(8.6 \pm 0.9) \times 10^{-12}$
	530	$(8.4 \pm 0.9) \times 10^{-12}$
		$(14 \pm 2) \times 10^{-12}$ [b]
O_2	20	$(6.0 \pm 0.9) \times 10^{-12}$
	530	$(5.3 \pm 0.7) \times 10^{-12}$
	4	$(5.7 \pm 1.2) \times 10^{-12}$ [c]
		$(3.8 \pm 0.6) \times 10^{-12}$ [b]

[a] The errors cited are estimates of the standard deviation. [b] Reference 21. [c] Reference 3.

remained constant when 510 Torr of helium was added to a mixture of acetaldehyde and NO (total pressure 20 Torr). Accordingly the termolecular reaction might be negligible in this system.

The flash photolysis of mixtures of acetaldehyde and O_2 was first carried out by McKellar and Norrish,[17] and the HCO absorption bands were not detected because of their experiments with too large a partial pressure of O_2 (>2.5 Torr).

Reactive collisions of HCO and O_2 are thought to occur as follows:[1,3,17-20]

$$HCO + O_2 \rightarrow HO_2 + CO \quad (12)$$

$$\rightarrow OH + CO_2 \quad (13)$$

$$\xrightarrow{+M} HCO_3 \quad (14)$$

The HO_2 forming process was directly confirmed by LMR experiments,[18] and ab initio Hartree–Fock calculations[19] suggested that the association of HCO and O_2 yielded the excited state of HCO_3 which decomposed readily.

The total pressure at which Washida et al. measured the rate constants of the reaction of the HCO radical and O_2 was about 4 Torr and in our experiment the total pressures were 20 and 530 Torr. From their value and our results the rate constant for the reaction of the HCO radical and O_2 did not depend on the total pressure within experimental error limits. These results suggest that the reaction of the HCO radical and O_2 takes place through a bimolecular reaction in the pressure range studied.

References and Notes

(1) P. A. Leighton, "Photochemistry of Air Pollution", Academic Press, New York, N.Y., 1961.
(2) A. G. Gaydon, "Spectroscopy of Flames", Chapman & Hall, London, 1957.
(3) N. Washida, R. I. Martinez, and K. D. Bayes, *Z. Naturforsch. A*, **29**, 251 (1974).
(4) J. U. White, *J. Opt. Soc. Am.*, **32**, 285 (1942).
(5) K. W. Welge, J. Wanner, F. Stuhl, and A. Heindrichs, *Rev. Sci. Instrum.*, **38**, 1728 (1967).
(6) D. A. Ramsay, *J. Chem. Phys.*, **21**, 960 (1953); G. Herzberg and D. A. Ramsay, *Proc. R. Soc. London, Ser. A*, **233**, 34 (1955); J. W. C. Johns, S. H. Priddle, and D. A. Ramsay, *Discuss. Faraday Soc.*, **35**, 90 (1963).
(7) F. E. Blacet and J. D. Heldman, *J. Am. Chem. Soc.*, **64**, 889 (1942).
(8) G. Herzberg, *Proc. Chem. Soc.*, 116 (1959).
(9) R. B. Cundall and A. S. Davies, *Progr. React. Kinet.*, **4**, 149 (1967).
(10) T. Bérces, *Comp. Chem. Kinet.*, **5**, 277 (1972).
(11) C. S. Parmenter and W. A. Noyes, Jr., *J. Am. Chem. Soc.*, **85**, 416 (1963).
(12) A. S. Archer, R. B. Cundall, G. B. Evans, and T. F. Palmer, *Proc. R. Soc. London, Ser. A*, **333**, 385 (1973).
(13) V. N. Kondratiev, "Rate Constants of Gas Phase Reactions", National Bureau of Standards, Washington, D.C., 1972.
(14) N. Basco, D. G. L. James, and R. D. Suart, *Int. J. Chem. Kinet.*, **2**, 215 (1970); N. Basco, D. G. L. James, and F. C. James, *ibid.*, **4**, 129 (1972).
(15) C. A. McDowell and L. K. Sharpies, *Can. J. Chem.*, **36**, 251 (1958).
(16) J. Heicklen and N. Cohen, *Adv. Photochem.*, **5**, 157 (1968).
(17) J. F. McKellar and R. G. W. Norrish, *Proc. R. Soc. London, Ser. A*, **254**, 147 (1960).
(18) H. E. Radford, K. M. Evenson, and C. J. Howard, *J. Chem. Phys.*, **60**, 3178 (1974).
(19) N. W. Winter and W. A. Goddard, III, *Chem. Phys. Lett.*, **33**, 25 (1975).
(20) T. L. Osif and J. Heicklen, *J. Phys. Chem.*, **80**, 1526 (1976).
(21) C. B. Moore, private communication.

The Hydrated Electron as Studied by the Fractional Charge MO Model

J. Oakey Noell[1a] and Keiji Morokuma[1*]

Department of Chemistry, The University of Rochester, Rochester, New York 14627 and the Institute for Molecular Science, Myodaiji, Okazaki 444, Japan *(Received July 15, 1977)*

The fractional charge MO model we have recently proposed for the representation of solvent molecules is used to investigate the properties of hydrated electrons. Calculations are performed for two possible conformers (tetrahedral and octahedral) of the first shell of the trapping site. For either model a single shell is insufficient to provide binding of the electron. Additional shells lead to strong binding with respect to the preformed trapping cluster. Estimates of the energy required to form such hosts from bulk water indicate that the trapped electron is, in all cases, unstable with respect to a bulk neutral cluster. It appears that once an initial hydration sphere has been formed the electron is capable of orienting a second layer. A close analogy is found between two shell models employing fractional charges and calculations in which all molecules beyond the first shell are treated as a polarizable bulk semicontinuum. The spin density at all first shell proton sites is found to be negative.

I. Introduction

The properties of excess electrons trapped in solvent hosts have been the subject of vigorous interest, both experimental and theoretical, for a number of years. Concomitant with this interest, numerous extensive reviews are available in the literature.[2] One phase of this problem which has proven to be most challenging is the determination of the geometric structure of the trapping sites, particularly in the hydrated electron. Natori and Watanabe originally proposed the possibility of a tetrahedral, tetracoordinate trapping site resulting from a site vacancy in crystalline ice structures.[3] Once trapped the electron could, in principal, deepen its hole by induced orientation of the surrounding water molecules. This model was adopted recently by Kawabata as a plausible explanation of induced trapping sites by irradiation of crystalline ice at low temperatures.[4] For the amorphous alkaline ices, other preexisting traps would dominate such induced sites. Kevan et al., using an ESR spin-echo technique on alkaline glasses, have formulated a hexacoordinate, octahedral, bond oriented model for the trapping site of the electron.[5]

From a theoretical viewpoint, Newton[6] has examined several conformations as potential trapping sites, focusing his attention primarily on the tetrahedral, dipole oriented model of Natori and Watanabe. His studies treated the excess electron and the first solvent shell explicitly within an ab initio MO framework with the rest of the solvent represented by a polarizable semicontinuum. This innovative appendum to the ab initio MO technique is an extension of earlier more classical continuum techniques.[7] It allows for a direct investigation of the structural characteristics of the first hydration sphere, including the evaluation of spin densities. The inherent limitation of this technique is that the cavity must be spherical if one is to avoid a multidimensional, numerical integration. Even the one-dimensional integration is quite expensive, making the explicit inclusion of more than a very limited number of molecules unfeasible.

We have recently proposed a new technique for the theoretical investigation of problems in the solution phase.[8] A specified number of molecules, for example, the solute and a small number of solvent molecules, are chosen to be a solute core. These molecules are explicitly considered in the normal ab initio MO framework. Additional solvent molecules provide an external potential for the solute core through their inclusion as fractional charges situated at atomic centers. This model has been used to examine the hydration of Li^+, F^-, and H_3N–HF and the solution phase proton affinity of amines. The method appears to be particularly well suited to the problem of the hydrated electron in that it will yield a MO description of the excess electron and its first solvent sphere (as does Newton's method) and furthermore it allows for direct determination of the effects of successive solvation shells (which Newton's method does not). It might also be noted that, for systems of the size studied here, our method requires a little less than half of the computer time necessitated by Newton's technique.

The primary emphasis of this paper will be an examination of the binding of the electron by the two proposed trappings sites. We will also discuss our results concerning the current controversy over the sign of the spin density at the proton sites. Where possible, our results will be compared with those of Newton[6] as well as with the results of Kawabata[3] and Kevan et al.[5]

II. Computational Methods

We wish to examine the energetics of trapping an electron in a water host. In envisioning this process one may qualitatively divide it into two parts. First it is necessary to form a trap or solvent host for the electron from the bulk water. This process is, of course, destabilizing in nature. Once this host has been prepared, one must examine the subsequent stabilization of the electron.

The energetics for the second process were evaluated by calculating the solvent host with and without the excess electron, i.e., $e^-(H_2O)_l(h_2o)_m(h_2o)_n$ and $(H_2O)_l(h_2o)_m(h_2o)_n$. The first hydration shell, characterized here by capital letters, was explicitly included within the ab initio framework as part of the solute core. The second and third shell waters, denoted by lower-case letters, were represented by fractional charges, a technique which has been discussed in detail in previous publications.[8] All water molecules were fixed at their experimental geometry (r(O–H) = 0.956 Å, ∠HOH = 105.2°).[9] The split valence shell 4-31G basis with standard parameters[10] was used, supplemented, in those instances in which the excess electron was included, by two diffuse s functions (exponents of 0.05 and 0.01)[6] situated at the cavity center. The fractional charges employed were those that yield the calculated dipole moment of 2.56 D (q_O = −0.9314, q_H = 0.4657), a

TABLE I: Energetics of Hydration in kcal/mol

	Model	A(l = 4, m = 8, n = 16)			B(l = 6, m = 12, n = 24)
	R, Å 2.50	3.00	3.50	4.0	3.086
$l\mathrm{H_2O} \rightarrow (\mathrm{H_2O})_l$	10.3	7.7	5.1	3.4	10.9
$l\mathrm{H_2O} + m\mathrm{h_2o} \rightarrow (\mathrm{H_2O})_l(\mathrm{h_2o})_m$	−4.6	−15.5	−23.1		−9.4
$l\mathrm{H_2O} + m\mathrm{h_2o} + n\mathrm{h_2o} \rightarrow (\mathrm{H_2O})_l(\mathrm{h_2o})_m(\mathrm{h_2o})_n$	−27.9	−48.1	−62.8		−19.8
$e^- + (\mathrm{H_2O})_l \rightarrow e^-(\mathrm{H_2O})_l$	−5.0	−10.3	−10.2		−10.9
$e^- + (\mathrm{H_2O})_l(\mathrm{h_2o})_m \rightarrow e^-(\mathrm{H_2O})_l(\mathrm{h_2o})_m$	−56.9	−56.1	−49.3		−89.0
$e^- + (\mathrm{H_2O})_l(\mathrm{h_2o})_m(\mathrm{h_2o})_n \rightarrow e^-(\mathrm{H_2O})_l(\mathrm{h_2o})_m(\mathrm{h_2o})_n$	−115.7	−108.5	−95.5		−171.7

choice which is quite reliable for outer shell solvent molecules.[8] The open shell computations were performed within the UHF framework.[11] A modified version of the GAUSSIAN 70 programming system was used for all computations.[12]

An evaluation of the energy required to create an electron trapping site from bulk water is not amenable to a direct MO investigation. Nonetheless we found it necessary to be able to estimate the magnitude of this destabilization. Two contributions were considered, the surface tension term resultant upon the change in the effective number of surface molecules due to cavity formation, and the difference in hydrogen bond energy between a bulk water cluster and a trapping site cluster. The former contribution was calculated in the manner prescribed by Newton.[13] Our estimate of the second contribution requires further discussion. Suppose we wish to prepare a host consisting of four water molecules. What we need to know is how much energy we lost in taking a "bulk" water cluster of four molecules, separating them to isolated waters, followed by bringing them back together in the conformation of the trapping site. It is evident that to perform such calculations for each of the trapping sites we have considered, we will need a means of estimating the hydrogen bond energy of a bulk water cluster of arbitrary size. This estimate must be consistent with the basis set and other approximations used in our binding calculations. Our approach was to approximate the energy of a bulk complex of n molecules by what its energy would be assuming it to be the optimum conformer consistent with the I_h structure of ice. This energy was, in turn, estimated as the average hydrogen bond energy per molecule in I_h ice multiplied by the number of hydrogen bonds which are possible in an n molecule cluster. The average hydrogen bond energy per molecule was evaluated by consideration of the binding between a central water molecule and its four surrounding nearest neighbors in the I_h structure. Using identical geometric and basis set parameters as were used for the electron binding calculations, we obtain a stabilization of 30.1 kcal/mol for the process $\mathrm{H_2O} + (\mathrm{h_2o})_4 \rightarrow \mathrm{H_2O}(\mathrm{h_2o})_4$ yielding an average hydrogen bond energy per molecule of 7.5 kcal/mol. As an example, we would now estimate the energy required to take four bulk waters and separate them into monomers as 22.5 kcal/mol since one can, at most, form only three hydrogen bonds with four water molecules. The estimates which we have made in this way are expected to be too large in that it is known that the I_h structure of water maximizes hydrogen bond interactions.[14]

III. Energetics and Structure

The two first shell conformational models which we examined were briefly outlined in the Introduction. The first (model A) has a tetracoordinate, tetrahedral first shell (Figure 1a), in which the positive end of each water dipole is directed toward the cavity center. The water molecules were oriented, one with respect to the others, such that the total complex was of C_{2v} symmetry. We define R as

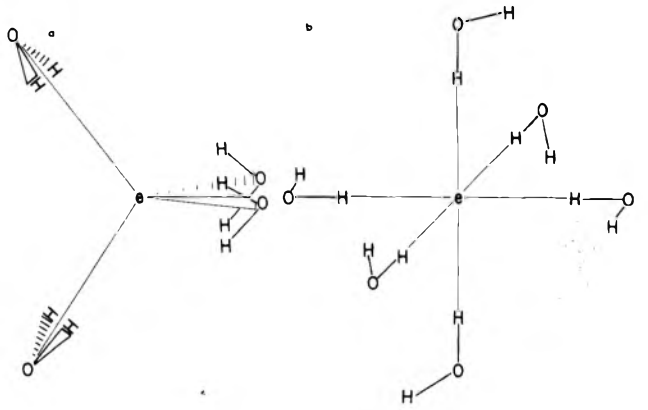

Figure 1. (a) Model A first shell conformation, tetracoordinate C_{2v} symmetry. (b) Model B first shell conformation, hexacoordinate D_2 symmetry.

the distance from the center of the cavity to an oxygen atom of a first shell water. Calculations were done for R = 2.5, 3.0, 3.5, and 4.0 Å.

The second conformational model (model B) has a hexacoordinate, bond-oriented first shell (Figure 1b), with the distance from the cavity center to the first shell oxygens (R) being fixed at 3.086 Å.[6] The external hydrogen atoms of the first shell water molecules were assumed to be such that the complex $(\mathrm{H_2O})_6$ had D_2 symmetry.

The second and third shells were constructed in an identical manner for both first shell conformations. Two water molecules were hydrogen bonded to each oxygen atom of the preceding shell. All geometric parameters for these complexations were taken to be those of the experimental dimer[15] except that the dihedral angle between the proton donor molecular plane and the bisector plane of the proton acceptor was set at its optimal value for interaction with the electron. Two and three shell anionic clusters formed in this manner are not necessarily the most stable possible structure with respect to isolated water monomers. This choice of the dihedral angle does, however, yield the maximum binding of the electron with respect to a preformed cluster. Consequently, as we add each additional shell we are most probably overestimating its importance in binding of the electron. Also, it should be immediately apparent that the model adopted here does not include the effects of conformational averaging, an effect which might be important for outer solvation shells.

The results collated in Table I are the relevant energies for construction of a solvent host from isolated water molecules (surface tension is not included here) followed by trapping of an electron by this prepared host. Focusing one's attention on the last three rows of this table, one notes the same trends for both conformational models A and B. The first shell provides only modest stabilization of the electron with respect to a preformed cluster, a stabilization which in no case is sufficient to compensate for the energy required to prepare the host (see Table II). The addition of second and third solvation shells results in strong binding of the electron with respect to the neutral

TABLE II: Energetics of Solvent Host Preparation[a]

Model	Surface tension E_{st}	N_{HB}[b]	Hydrogen bond breakage E_{HB}[c]
A(l = 4, m = 8, n = 16)		(3, 12, >28)	(22.5, 90.0, >210)
R = 2.5 A	6.3		
3.0 A	11.9		
3.5 A	18.1		
4.0 A	24.9		
B(l = 6, m = 12, n = 24) R = 1.13 A	10.3	(6, 21, >42)	(45.0, 157.5, >315)

[a] All energies are in kcal/mol. [b] N_{HB} is the maximum number of hydrogen bonds for (l, $l + m$, $l + m + n$) bulk waters. [c] E_{HB} is the energy required to remove (l, $l + m$, $l + m + n$) waters from the bulk.

host cluster. It is important to note that for either model, the third shell is of equal significance to the second shell with respect to binding the electron. A single test calculation indicated that a fourth hydration sphere constructed in the manner prescribed here would also lead to significant increased stabilization of the electron. The implication of these results is that if one constructs successive hydration shells under the constraint that they be optimally oriented for binding of an electron, then each shell will result in significant stabilization. This is, of course, a nonphysical result and indicates that it is necessary to make an estimate of the energy required to form the host clusters from bulk water.

As was outlined in the previous section, two contributions which we need to consider are the surface tension energy E_{ST} and the loss in hydrogen bond energy E_{HB} attendant upon going from bulk water to isolated monomers. These data are given in Table II. The first effect is clearly a minor one with respect to the second, though it is of qualitative significance in determining the equilibrium R for model A. As one expects, the hydrogen bond energy which is lost on removing water molecules from the bulk increases roughly on a one-to-one basis with the number of water molecules. By contrast, the binding of the electron by a prepared host increased linearly with the number of hydration shells. As successive hydration shells are added, one therefore expects to reach a point where the orientation of the shell costs more energy due to loss of hydrogen bonding, than is gained via electron stabilization.

This inference is borne out in Table III. Here the results of the first two tables are combined to give the energy required to reorient the bulk water molecules in the presence of an excess electron. Though our estimates indicate that none of the ordered, anionic clusters are stable with respect to neutral, bulk clusters plus an isolated electron, it is important to note that for either model, there is a sharp break in the stability of these complexes upon addition of a third hydration shell. It seems evident from these computations that the electron is not capable of orienting three hydration shells. On the other hand, one notes that little if any energy is required to orient a second hydration sphere, assuming that the first shell has been previously constructed. This is particularly true for the model A first shell conformation. An interesting aside in this regard is Kawabata's[4] implication that the initial trapping sites are formed by the irradiation, presumably a high energy process. It should also be noted that our choice of a saturated orientation for the second hydration sphere is too restrictive. It may be possible to find a partially oriented two shell conformation such that the anionic cluster is lower in energy than the neutral, bulk cluster.

Concordant with the above discussion, it is of interest to note that there is a close correspondence between the model A two-shell calculations reported here and the semicontinuum model of Newton.[6] His reported value of −2.51 eV (−57.81 kcal/mol) at R = 2.65 Å for binding of the electron with respect to the solvent host is in excellent agreement with our values of −56.9 and −56.1 kcal/mol at 2.5 and 3.0 Å, respectively.

It is difficult to evaluate the relative stabilities of model A and model B in that we have just seen that fully orientated calculations predict that neither conformation is bound with respect to bulk clusters. If one uses Table III as a measure, it is evident that the dipole oriented model is favored. This result is dictated primarily by the fact that hosts of the model A conformation require less energy per molecule to form than do hosts of model B stereochemistry. Once formed model B hosts actually bind the electron somewhat more tightly than do hosts of model A (−4.94 kcal/mol of molecule compared with −4.68 kcal/mol based on second shell stabilizations). Rather than emphasize differences between the two models in this regard, however, it is probably more important to note the great similarity. Both models require substantial energy to form host trapping sites. Once formed, these sites supply substantial binding for an excess electron.

These similarities are reflected also in the wavefunction for the trapped electron. The energies of both the highest occupied molecular orbital (HOMO) the trapped electron and of the lowest vacant orbital of the neutral solvent host are collected in Table IV. On perusal of this table and of Table I it is apparent that there is little correlation between the eigenvalue of the neutral host LUMO and the binding of the electron. In particular, it is notable that the eigenvalue rapidly becomes more positive (less negative) as one increases R for model A. The binding of an electron, on the other hand, decreases only slowly as the cavity size increases. There is, however, a nearly quantitative agreement between the binding of the electron and the HOMO eigenvalue of the anionic cluster. These two results, taken together, imply that the excess electron should here be interpreted as a localized charge which is stabilized by an ordered hydration structure. This implication is further supported by the fact that the coefficients of the s orbitals localized about the cavity center are the dominant contributions to the HOMO. Not surprisingly, the bound electron becomes more localized

TABLE III: Energetics of Electron Hydration[a]

Model	A(l = 4, m = 8, n = 16)				B(l = 6, m = 12, n = 24)
R, A	2.5	3.0	3.5	4.0	2.13
$e^- + H_2O_l$[b] $\rightarrow e^-(H_2O)_l$	34.1	31.8	35.5	41.9	54.8
$e^- + H_2O_{l+m} \rightarrow e^-(H_2O)_l(h_2o)_m$	34.9	30.4	35.7		68.4
$e^- + H_2O_{l+m+n} \rightarrow e^-(H_2O)_l(h_2o)_m(h_2o)_n$	>72.9	>65.3	>69.3		>133.8

[a] All energies are in kcal/mol, negative numbers would denote stabilization. [b] H_2O's on the left-hand side of equations are bulk water molecules.

TABLE IV: MO Energies (in eV)

	LUMO of host	HOMO of trapped e⁻
Model A		
R = 2.5 Å, l = 4	1.51	−0.11
l = 4, m = 8	−0.96	−2.44
l = 4, m = 8, n = 16	−3.54	−5.00
R = 3.0 Å, l = 4	2.96	−0.36
l = 4, m = 8	0.82	−2.39
l = 4, m = 8, n = 16	−1.50	−4.67
R = 3.5 Å, l = 4	4.47	−0.40
l = 4, m = 8	2.55	−2.12
l = 4, m = 8, n = 16	0.44	−4.15
R = 4.0 Å, l = 4	5.06	−0.37
Model B		
R = 3.086 Å, l = 6	1.00	−0.67
l = 6, m = 12	−2.47	−4.15
l = 6, m = 12, n = 24	−6.00	−7.69

TABLE V: Spin Densities in 10^3 (bohr units)$^{-3}$

System	No. of hydration shells 1	2	3
Model A			
R = 2.5 Å	−2.55	−3.85	−3.92
R = 3.0 Å	−1.84	−2.28	−2.32
R = 3.5 Å	−1.12	−1.32	−1.32
R = 2.65 Å[a]		−2.9	
R = 2.50 Å[b]		−3.54	
Model B			
R = 3.086 Å	−4.06	−4.48	−4.54

[a] From ref 4 (dielectric semicontinuum technique). [b] Our calculation using the dielectric semicontinuum technique.

near the center (smaller coefficient on the more diffuse primitive function) as one adds hydration shells to the cluster.

IV. Spin Density

The sign of the spin density at the nearest neighbor proton sites has been the subject of some debate. Knight shift data on metal ammonia solutions implied negative densities for the proton of ammoniated electron.[16] Newton's calculations[6,17] based on tetracoordinate solvation models confirmed this prediction, and indicated that negative densities should be expected for the hydrated electron as well. Kevan et al. however interpreted their results as being indicative of positive spin densities at nearest neighbor proton sites.[5] It is therefore of considerable interest to examine the qualitative nature of the spin densities predicted by our hydration models. The spin densities at the nearest neighbor proton sites are listed in Table V. The salient point is that for all models the spin density is negative. In fact, model B, that model formulated by Kevan et al., yields a more negative spin density than does model A.

As was found in the energetic analysis, there is a close correspondence between calculations in which the second shell is represented by fractional charges and semicontinuum (one hydration shell + continuum) computations.

General profiles of the spin density are given for model A (R = 2.5 Å) and model B in Figures 2 and 3, respectively. For either model all first shell proton sites are negative. The oxygen atom as well as the larger part of the interatomic regions are of positive spin density. It is not unreasonable to expect that first shell structures intermediate between the two cases examined here would follow these same general trends. As these are the type of conformations which are expected to be able to localize an

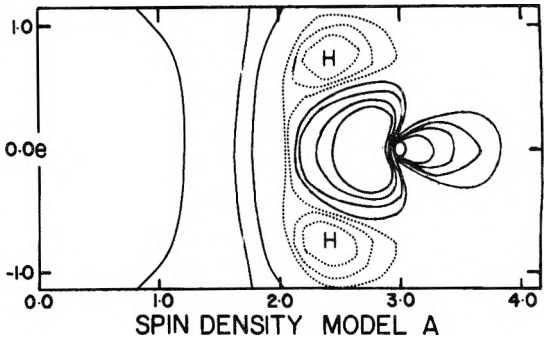

Figure 2. Spin density contour map for model A, R = 3.0 Å, two solvation shells. Ordinate and abscissa markings are in Å. Contours plotted (units of au^{-3}) are 0.005, 0.0025, 0.001, 0.0005, −0.001, −0.0005, −0.00025. Solid lines denote positive spin densities; dashed lines indicate negative spin densities. The excess electron is localized about the coordinate origin.

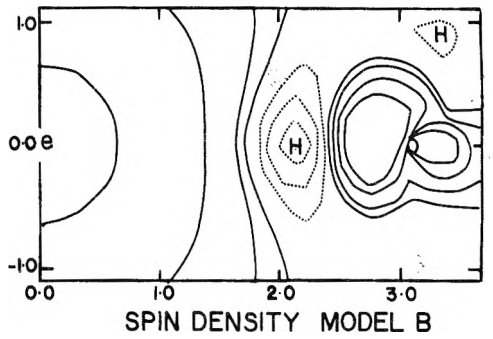

Figure 3. Spin density contour map for model B, R = 3.086 Å, two solvation shells. All conventions are the same as those of Figure 2. The contours plotted are also the same as in Figure 2.

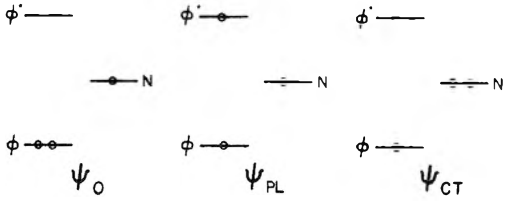

Figure 4. Schematic representation of the electronic configurations considered in our model of spin polarization.

electron the inference to be drawn from our calculations is that the first shell spin densities should be positive for any strongly bound electron. The following model for the spin polarization resulting from the excess electron is consistent with these results.

As depicted in Figure 4, we consider a three orbital scheme involving the occupied σ O–H bonding orbital (φ), the vacant σ^* O–H orbital (ϕ^*), and the half-occupied orbital denoted by N in which the excess electron resides. The total wavefunction may then be written as

$$\Psi = C_0\psi_0 + C_{CT}\psi_{CT} + C_{PL}\psi_{PL} \quad (1)$$

where ψ_0 is the ground state configuration:

$$\psi_0 = |\phi\phi N\alpha\beta\alpha \quad (2)$$

ψ_{CT} is the charge transfer configuration:

$$\psi_{CT} = |\phi N N\alpha\beta\alpha| \quad (3)$$

and ψ_{PL} is the polarization configuration. (Only the doublet which leads to nonzero spin densities need be considered).

$$\psi_{PL} = |\phi\phi^* N(2\alpha\alpha\beta - \beta\alpha\alpha - \alpha\beta\alpha)/\sqrt{6}| \quad (4)$$

The coefficient of the ground state configuration may be assumed to be approximately 1. The coefficient for the

CT configuration may be estimated from its first-order perturbation contribution.

$$C_{CT} = (E_0 - E_{CT})^{-1} \langle \psi_0 | H | \psi_{CT} \rangle \quad (5)$$

The corresponding first-order contribution to C_{PL} is expected to be small, and the most important contribution would be a second-order term due to the coupling with CT.

$$C_{PL} = (E_0 - E_{PL})^{-1} C_{CT} \langle \psi_{CT} | H | \psi_{PL} \rangle \quad (6)$$

The spin density at the hydrogen may, as usual,[18] be written as the expectation value of the spin density operator:

$$\rho_H = \langle \Psi | \hat{\rho}_H | \Psi \rangle \quad (7)$$

the principal nonzero contribution of which is

$$\rho_H \approx C_{PL} C_0 \langle \psi_{PL} | \hat{\rho}_H | \psi_0 \rangle \quad (8a)$$

$$\approx (E_0 - E_{CT})^{-1} (E_0 - E_{PL})^{-1} \langle \psi_0 | H | \psi_{CT} \rangle \times \langle \psi_{CT} | H | \psi_{PL} \rangle \langle \psi_{PL} | \rho_H | \psi_0 \rangle \quad (8b)$$

If the sign of the orbitals are taken to be as defined in the Appendix, then it may be argued (see Appendix) that $(E_0 - E_{CT}) < 0$, $(E_0 - E_{PL}) < 0$, $\langle \psi_0 | H | \psi_{CT} \rangle < 0$, $\langle \psi_{CT} | H | \psi_{PL} \rangle > 0$, and $\langle \psi_{PL} | \hat{\rho}_H | \psi_0 \rangle > 0$. As a consequence, invoking this spin polarization mechanism, one obtains a negative spin density at the proton site, and a positive spin density on the oxygen atom.

From an interpretistic viewpoint, it should be noted that the sign of the polarization mixing with the ground state, and hence the sign of the proton spin densities, is being dictated by the CT contribution. In fact, if one considers only the first-order contribution to C_{PL} in the spirit of McConnell's[18] work on π radicals in hydrocarbons, then a positive proton spin density would be predicted. Also, it should be noted that the analysis outlined above should be applicable only if the electron is highly localized, and hence spin polarization effects are not swamped by spin delocalization. As an example of a trapping site not capable of localizing the electron in space, we carried out calculation for an excess electron in the presence of a single, bond-oriented water molecule. Here we did find positive spin densities at all atomic sites.

V. Conclusion

The calculations reported here indicate that for either model A or model B, construction of the fully oriented solvent host from bulk water is energetically expensive. Once constructed one finds binding of the electron only if one has two or more hydration shells. In no case did we find this stabilization sufficient to yield an anionic cluster which would be stable with respect to an optimal bulk aggregate. If, on the other hand, one could create a partial trap, via a vacancy defect or by some other means, our results seem to indicate the feasibility of the electrons deepening its hole by orienting up to two hydration shells. Orientation beyond two shells is energetically unrealistic in all cases. In accord with this projected plausibility of orienting two shells we find good agreement between our two shell fractional charge calculations and Newton's semicontinuum calculations.

We find little difference in the capacity to bind electrons between model A and model B. If forced to a decision, one would have to say that model B binds electrons more strongly, though it is energetically less feasible to construct the fully oriented host.

We find negative spin densities at all first shell proton sites. This is in agreement with Newton's calculations but is not consistent with the inference Kevan drew from his ESR data. We have formulated a spin polarization mechanism involving charge transfer coupling with the polarization excitation which supports our conjecture that, for localized electrons, the proton spin densities will be negative. For less structured first shells, in which the electron is not so tightly bound, it is possible that spin delocalization will predominate yielding positive densities at all atomic sites. The origin of the disparity regarding the sign of the spin density between our calculations (as well as Newton's) and the experimental results of Kevan is not evident. One possible source is that our models probably more accurately represent a crystalline ice whereas Kevan did his work in alkaline glasses.

Acknowledgment. We thank Drs. M. Newton, L. Kevan, and S. Nagase for many helpful discussions. J.O.N. gratefully acknowledges the aid of Sherman Clarke and Elon Huntington Hooker Graduate Fellowships. The work is in part supported by the Center for Naval Analyses of the University of Rochester and in part by the National Science Foundation.

VI. Appendix

Here we wish to rationalize our assignment of the signs of the matrix elements necessary for evaluation of the proton spin density. Our σ molecular orbitals are defined as

$$\phi = C_1 \chi_O + C_2 \chi_H$$
$$\phi^* = C_3 \chi_H - C_4 \chi_O \quad (A.1)$$

where χ_O and χ_H are atomic functions on the oxygen and hydrogen atoms, respectively, and all coefficients, C's, are assumed to be positive. We will make use of the well-known Mulliken approximations:

$$(ab|aa) = S_{ab}/2\{(aa|aa) + (bb|aa)\}$$
$$\langle a|h|b\rangle = C S_{ab} \{\langle a|h|a\rangle + \langle b|h|b\rangle\} \quad (A.2)$$

where S_{ab} is the overlap between orbitals a and b. We have assumed C to be 1.0.[19] Consider first the matrix element $\langle \psi_0 | H | \psi_{CT} \rangle$. Keeping only terms which will be first order in $S_{\phi,N}$, one may write

$$\langle \psi_0 | H | \psi_{CT} \rangle = S_{\phi,N} \{\langle \phi | h | \phi \rangle + \langle N | h | N \rangle\} + \langle \phi | h | N \rangle + (\phi\phi | \phi N) + (\phi N | NN) \quad (A.3)$$

Employing eq A.2 one may write

$$= S_{\phi,N} \{2\langle \phi | h | \phi \rangle + {}^1/_2(\phi\phi | \phi\phi) + {}^1/_2(\phi\phi | NN) + 2\langle N | h | N \rangle + {}^1/_2(NN | \phi\phi) + {}^1/_2(\phi\phi | NN)\} \quad (A.4)$$

It is useful now to make the following definitions:

$$E_{\phi,\phi} = 2\langle \phi | h | \phi \rangle + (\phi\phi | \phi\phi) \quad (A.5)$$

$$E_{N,N} = 2\langle N | h | N \rangle + (NN | NN) \quad (A.6)$$

Essentially these are the energies of two electron systems, the electrons residing respectively in ϕ and N. In both cases, all nuclei are to be included in the one electron operator. One expects that these energies will be negative. With these definitions one has

$$\langle \psi_0 | H | \psi_{CT} \rangle = S_{\phi,N} \{E_{\phi,\phi} - {}^1/_2(\phi\phi | \phi\phi) + {}^1/_2(\phi\phi | NN) + E_{N,N} - {}^1/_2(NN | NN) + {}^1/_2(\phi\phi | NN)\} \quad (A.7)$$

With the orbital sign choice of eq A.1, the overlap $S_{\phi,N}$ will

be positive. If intramolecular Coulomb repulsions are assumed to be greater than intermolecular terms, i.e.

$$(\phi\phi|\phi\phi) > (\phi\phi|NN) \quad (A.8)$$

$$(NN|NN) > (\phi\phi|NN) \quad (A.9)$$

then one must conclude that $\langle\Psi_0|H|\Psi_{CT}\rangle < 0$.

The treatment of the matrix element $\langle\psi_{CT}|H|\psi_{PL}\rangle$ is formally analagous to the case just treated. The final expression one has, in analogy to eq A7 is

$$\langle\psi_{CT}|H|\psi_{PL}\rangle = (-3/\sqrt{6})S_{\phi^*,N}\{E_{NN} - {}^1/_2(NN|NN) + {}^1/_2(NN|\phi^*\phi^*) + E_{\phi,\phi^*} - {}^1/_2(\phi\phi|\phi^*\phi^*) + {}^1/_2(\phi\phi|NN)\} \quad (A.10)$$

Using the same arguments employed earlier, one is here led to the conclusion that $\langle\psi_{CT}|H|\phi_{PL}\rangle > 0$.

The final matrix element to be examined is $\langle\Psi_0|\hat{\rho}_H|\Psi_{PL}\rangle$ this may be written as

$$\langle\psi_0|\hat{\rho}_H|\psi_{PL}\rangle = \langle\phi\phi N\alpha\alpha\beta|\sum_k \Delta_H(k)S_{kz}/M_s|\phi\phi^*N \times (2\alpha\alpha\beta - \beta\alpha\alpha - \alpha\beta\alpha)/\sqrt{6}|\rangle \quad (A.11)$$

$$= (2/\sqrt{6})\langle\phi|\Delta_H|\phi^*\rangle \quad (A.12)$$

Employing the orbital signs of eq A.1, this will clearly be a positive number.

References and Notes

(1) (a) Department of Chemistry, University of Rochester, Rochester, N.Y. 14627; (b) Institute for Molecular Science, Okazaki, Japan 444.
(2) (a) J. Jortner and N. R. Kestner, "Electrons in Fluids, the Nature of Metal Ammonia Solutions", Springer Verlag, New York, N.Y., 1973; (b) W. L. Jolly, "Metal Ammonia Solutions", Dowden, Hutchinson and Ross, Stroudsberg, Pa., 1972; (c) R. F. Gould, *Adv. Chem. Ser.*, **No. 50** (1965); (d) G. Lepoutre and M. J. Sienko, "Metal Ammonia Solutions", W. A. Benjamin, New York, N.Y., 1963.
(3) M. Natori and T. Watanabe, *J. Phys. Soc. Jpn.*, **21**, 1573 (1966).
(4) K. Kawabata, *J. Chem. Phys.*, **65**, 2235 (1976).
(5) (a) B. L. Bales, M. K. Bowman, L. Kevan, and R. W. Schwartz *J. Chem. Phys.*, **63**, 3008 (1975); (b) P. A. Narayana, M. K. Bowman, L. Kevan, V. F. Yudanov, and Yu. D. Tsvetkov, *ibid.*, **63**, 3365 (1975); (c) S. Schlick, P. A. Narayana, and L. Kevan, *ibid.*, **64**, 3153 (1976); (d) L. Kevan, *J. Phys. Chem.*, **79**, 2846 (1975).
(6) (a) M. D. Newton, *J. Chem. Phys.*, **58**, 5833 (1973); (b) M. D. Newton, *J. Phys. Chem.*, **79**, 2795 (1975).
(7) (a) J. Jortner, *J. Chem. Phys.*, **30**, 839 (1959); (b) *Mol. Phys.*, **5**, 257 (1962); (c) K. Fueki, D. Feng, and L. Kevan, *Chem. Phys. Lett.*, **4**, 313 (1969); (d) K. Fueki, D. Feng, L. Kevan, and R. E. Christofferson, *J. Phys. Chem.*, **75**, 2297 (1971).
(8) (a) J. O. Noell and K. Morokuma, *Chem. Phys. Lett.*, **36**, 465 (1975); (b) J. O. Noell and K. Morokuma, *J. Phys. Chem.*, **80**, 2675 (1976).
(9) G. Herzberg, "Electronic Spectra of Polyatomic Molecules", Van Nostrand, Princeton, N.J., 1966.
(10) R. Ditchfield, M. D. Newton, W. J. Hehre, and J. A. Pople, *J. Chem. Phys.*, **54**, 724 (1971).
(11) J. A. Pople and R. K. Nesbet, *J. Chem. Phys.*, **21**, 571 (1953).
(12) W. J. Hehre, W. A. Lathan, R. Ditchfield, M. D. Newton, and J. A. Pople, GAUSSIAN 70, Program No. 236, Quantum Chemistry Program Exchange, Indiana University, Bloomington, Ind., 1973.
(13) The surface tension term was calculated as $E_{ST} = 4\pi\gamma(r_c^2 - r_c'^2)$, where r_c is the distance from the cavity center to the outer surface of the first hydration shell. r_c' is the analogous distance assuming the water molecules to be close packed spheres. The water molecules were assumed to be spheres of radius 1.5 Å. This yields r_c' = 3.337 Å and r_c' = 3.621 Å for a tetrahedral and an octahedral model, respectively. γ was assumed to be 72 erg/cm^2 (0.104 kcal/mol Å^2).
(14) R. A. Horne, "Water and Aqueous Solutions, Structure Thermodynamics and Transport Processes", Wiley-Interscience, New York, N.Y., 1972.
(15) T. R. Dyke and J. S. Muenter, *J. Chem. Phys.*, **60**, 2929 (1974).
(16) (a) T. R. Hughes, Jr., *J. Chem. Phys.*, **38**, 202 (1963); (b) B. B. Wayland and W. L. Rice, *ibid.*, **45**, 3150 (1966).
(17) M. D. Newton, personal communication.
(18) H. M. McConnell, *J. Chem. Phys.*, **24**, 764 (1956).
(19) M. J. S. Dewar, "The Molecular Orbital Theory of Organic Chemistry", McGraw-Hill, New York, N.Y., 1969, p 82.

COMMUNICATIONS TO THE EDITOR

Nanosecond Temperature-Jump Technique with an Iodine Laser

Sir: The temperature-jump method is probably the most widely used of all relaxation techniques in the study of very fast reactions in solution. In commercially available instruments a high-voltage capacitor is discharged through an electrolyte solution. It is therefore not possible to achieve heating times shorter than $RC/2$ of the measuring cell.[1] Direct optical heating of the solvent, however, is not limited by the electrical resistance of a discharge circuit and the sample especially.[2] Here the heating time is governed by the emission time of the pulsed light source and the lifetime of the excited state. In the case of water the relaxation time of the vibrational rotational excited states in the near-IR is about 10^{-12} s.[3] If an oscillator–amplifier laser chain is used as an energy source heating times shorter than 10^{-12} s can in principle be achieved, but the optical damage thresholds of the sample and the cuvet normally prohibit heating times shorter than 10^{-11} to 10^{-10} s.

From the absorption spectrum of water[4] it is apparent that a suitable wavelength for direct absorption of enough laser energy to cause a temperature-jump greater than 1 K in a volume of 0.1 cm^3 exists above 1.15 μm. An assessment as to which degree of absorption would be the most suitable for producing spatially homogeneous temperature jumps at 50% or more laser energy consumption can be made by examining this dependence theoretically. Inhomogeneities inside the measuring cell causing temperature gradients that are above 10% should be avoided, because they generate locally different relaxation amplitudes as well as unwanted shock waves which may disturb the detection channel. From Figure 1 we see that under these conditions such a temperature jump can only be achieved if the product of the absorption coefficient and the thickness of the heated layer lies between 0.15 and 0.2. Thereby the assumption is made that by means of a single reflection the laser beam passes through the sample twice. For an absorption layer thicker than 0.1 cm, which is necessary for the detection beam perpendicular to the heating beam the laser wavelength should be in the range from 1.15 to 1.36 μm. For mixtures of H_2O and D_2O this interval is shifted to longer wavelengths.[5]

Taking the above into consideration we have chosen an iodine laser which operates at 1.315 μm where the absorption coefficient of water is 0.76 cm^{-1}. As can easily be seen from Figure 1 the inhomogeneity of heating is around

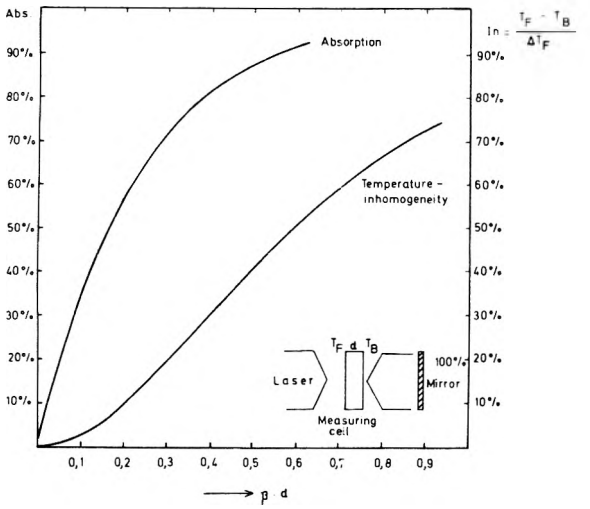

Figure 1. Dependence of the absorption of initial laser energy and temperature inhomogeneity in the measuring cell on the product of absorption coefficient (β) and thickness of the heated layer (d) with the laser beam passing twice through the cell.

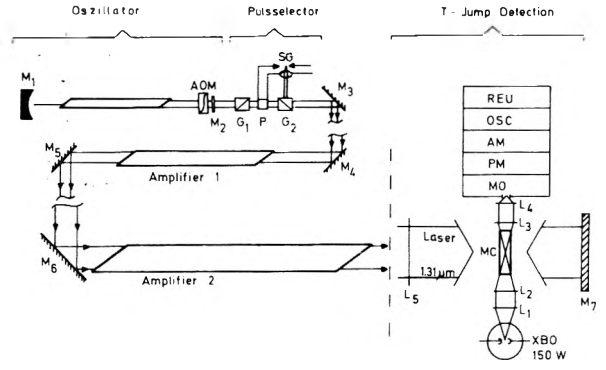

Figure 2. Experimental arrangement of the iodine laser T-jump: M, mirrors; AOM, acousto-optical mode locker; G, Glanprism; P, Pockels cell; SG, spark gap, MC, measuring cell; L, lenses; MO, monochromator; PM, photomultiplier; AM, amplifier; OSC, oscilloscope; and REU, registration unit.

6% at an absorption of 49% laser energy if a single reflection is allowed and the water layer is 0.2 cm thick.

The experimental arrangement is shown schematically in Figure 2. The laser can be operated in two different ways. As an oscillator–amplifier chain with two amplification stages using acousto-optical mode locking for obtaining a train of short pulses and a Pockels cell for single pulse selection. This system produces 1–3 J in 3 ns. If the amplifiers are operated separately as oscillators in the multimode version they produce 1–30 J in about 3 μs. Higher energies could be achieved if the system is scaled up.[6] Figure 3 shows time-resolved measurements of the laser pulses from the oscillator–amplifier chain in the TEM_{00} mode and from an oscillator in the multimode operation obtained with a valvo XA 1003 vacuum photodiode on a Tektronix 7904 oscilloscope and on a Biomation 8100, respectively.

This versatile iodine laser being part of a temperature-jump system has been tested by measuring the protonation of tropaeolin O and phenolphthalein in aqueous solution.[7] As an example Figure 4 shows the relaxation signal obtained from phenolphthalein with a single heating pulse. Three advantages of this kind of laser T-jump technique can be stated from our results. There is enough energy available for T-jumps of some Kelvin with characteristic time constants of 2 μs or 2 ns in a volume of 0.1 mL containing solvents such as H_2O, D_2O, and alcohols. No additives are required to assist in heat

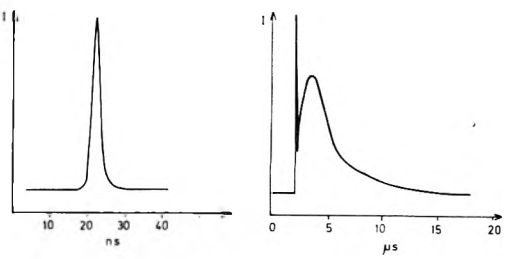

Figure 3. Time-resolved iodine laser pulses.

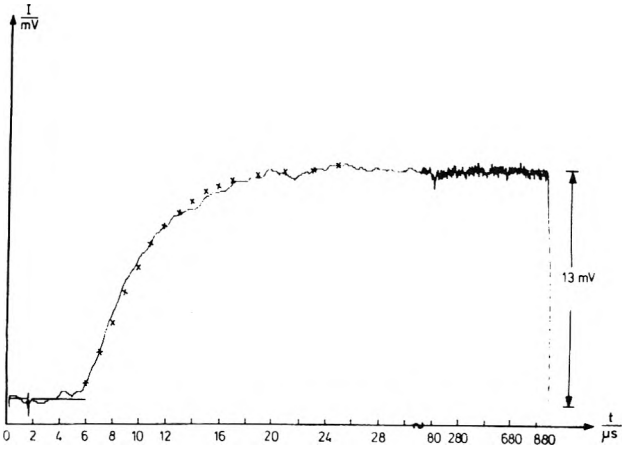

Figure 4. Relaxation signal of a glycine buffered aqueous solution of phenolphthalein at pH 9.6, temperature 298 K registered with a Biomation 8100. (X) computed points for the relaxation trace.

transfer. Shock waves and different relaxation amplitudes inside the measuring cell can be avoided so that the observation of relaxation times from nanoseconds to seconds at different temperatures is possible.

Acknowledgment. The authors thank Dr. S. Witkowski and Professor Dr. H. Gerischer for the encouraging support of this work and the Deutsche Forschungsgemeinschaft for a research grant.

References and Notes

(1) E. F. Caldin, *Chem. Br.*, **11**, 4 (1975); G. G. Hammes in "Techniques of Chemistry", Vol. VI, Part II, A. Weissberger, Ed., Interscience, New York, N.Y., 1974.
(2) E. M. Eyring and B. C. Bennion, *Annu. Rev. Phys. Chem.*, **19**, 129 (1968).
(3) D. M. Goodall and R. C. Greenhow, *Chem. Phys. Lett.*, **9**, 583 (1971).
(4) J. V. Beitz, G. W. Flynn, D. H. Turner, and N. Sutin, *J. Am. Chem. Soc.*, **92**, 4130 (1970).
(5) D. H. Turner, G. W. Flynn, N. Sutin, and J. V. Beitz, *J. Am. Chem. Soc.*, **94**, 1154 (1972); G. W. Flynn and N. Sutin in "Chemical and Biochemical Applications of Lasers", Vol. I, C. B. Moore, Ed., Academic Press, New York, N.Y., 1974, Chapter 10.
(6) K. Hohla, G. Brederlow, W. Fuss, K. L. Kompa, J. Raeder, R. Volk, S. Witkowski, and K.-J. Witte, *J. Appl. Phys.*, **46**, 808 (1975).
(7) M. C. Rose and J. Stuehr, *J. Am. Chem. Soc.*, **90**, 7205 (1968).

Fritz-Haber-Institut der Max-Planck-Gesellschaft D-1000 Berlin 33, West Germany — **J. F. Holzwarth***, **A. Schmidt**, **H. Wolff**
Max-Planck-Institut, für Plasmaphysik, D-8046 Garching Projektgruppe für Laserforschung D-1000 Berlin 33, West Germany — **R. Volk**

Received July 11, 1977

Laser Induced Decomposition of Fluoroethanes

Publication costs assisted by Kansas State University

Sir: The use of intense infrared radiation to promote selective chemical processes[1-3] has led us to examine the high-power, pulsed CO_2 laser induced unimolecular de-

composition of fluoroethanes. We previously have studied the unimolecular decomposition of these molecules by chemical activation techniques.[4] These molecules are well suited to CO_2 laser photolysis since the characteristic C–F stretching frequency overlaps the 00°1–10°0 and 00°1–02°0 CO_2 transitions. The excitation process must be multiphoton since the threshold energies[5] for HF elimination from fluoroethanes are ~60 kcal mol^{-1} vs. the 3 kcal mol^{-1} CO_2 photon energy. This multiphoton requirement raises the problem of absorption and retention of this energy during the 150-ns laser pulse while the molecules are simultaneously undergoing approximately 10^7/Torr collisions per second with other molecules. The multiphoton absorption mechanism, which is not well understood,[6] will be accepted as fact[7] and the major concern of the present investigation is the demonstration that multiphoton laser photolysis can initiate the HF elimination reaction without a significant contribution from *intermolecular* transfer of the initially absorbed energy, which ultimately leads to bulk heating of the reaction mixture. The latter possibility has several different regimes of energy relaxation; in this work identification of the different regimes is not attempted and reactions resulting from *intermolecular* transfer of energy will be termed a "thermal" component. A means of monitoring a "thermal" component is the addition of a second molecule to the reaction mixture which itself does not absorb the laser energy sufficiently to react but which does possess a unimolecular reaction pathway with a threshold energy comparable to that for HF elimination. The decomposition of the monitor molecule, relative to that for the fluoroethanes, provides a measure of the extent of the "thermal" reaction. The excitation of a molecule possessing two distinctly different decomposition pathways allows an examination of the question of the *intramolecular* selectivity of the reactions initiated by laser excitation. In the ideal situation, the energy absorption gives a localized energy distribution close to one reaction path of the two competing processes. In the present work we have studied C_2H_5F, CH_3CF_3, and CH_2FCH_2Br. In principle, the first two molecules offer competing channels of HF elimination vs. C–C bond rupture. However, the threshold energy for C–C bond rupture is ~25 kcal mol^{-1} higher than for HF elimination and a strong discrimination would result just because of the minimum energy requirement. The CH_2FCH_2Br molecule is much better because the threshold energies for the HF and HBr elimination pathways differ[5] by only ~6 kcal mol^{-1}.

We wish to report experiments for which intermolecular energy relaxation was minimized and the HF elimination reactions of C_2H_5F and CH_3CF_3 are truly laser induced:

$$CH_3CF_3 + mh\nu \rightarrow CH_2CF_2 + HF$$
$$k_{uni} = 10^{14} \exp(-68700/RT)$$
$$CH_3CH_2F + mh\nu \rightarrow CH_2CH_2 + HF$$
$$k_{uni} = 10^{13.4} \exp(-59900/RT)$$

After finding proper conditions for these reactions, CH_2FCH_2Br was examined to ascertain whether or not the absorbed energy was statistically distributed prior to decomposition:

$$CH_2FCH_2Br + mh\nu \rightarrow HF + CH_2CHBr$$
$$\rightarrow HBr + CH_2CHF$$

The experiments were done by placing small cells, fitted with NaCl windows, at various positions in the path of the TEA Lumonics-103 laser beam, which was mildly focused with a 40-cm focal length lens. After a small number of irradiations (~10) the contents of the cell were analyzed by gas chromtography with a H_2-flame detector. Care was taken to ensure that starting materials were pure. Further experimental conditions are cited in figure captions and elsewhere.[8a]

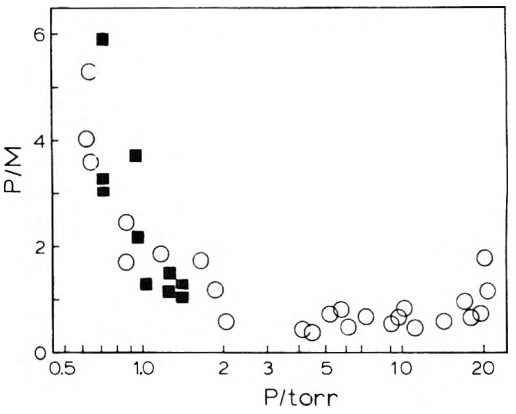

Figure 1. Pressure dependence of the "thermal" and laser induced reactions. The ordinate, P/M, is the ratio of the yield of the pumped molecule to the yield of monitor molecule. All of these experiments were done by placing the cell 25 cm behind the focusing lens; the energy density was 2.5 J/cm^2 for photolysis with the R(16) line of the 00°1–10°0 transition: (○) CH_3CF_3 with 25% cyclopropane; (■) CH_3CF_3 with 50% CH_3CH_2F.

The extent and pressure dependence of the "thermal" contribution was monitored by adding either CH_3CH_2F or cyclopropane to the cell for CH_3CF_3 (irradiated with the R(16) line of the 00°1–10°0 band) and by adding CH_3CF_3 to C_2H_5F (irradiated with the P(18) line of the 00°1–02°0 band). If intermolecular energy transfer is extensive, formation of C_2H_4 or C_3H_6 will be observed from irradiation of CH_3CF_3 in the presence of fluoroethane or cyclopropane. Similarly, CH_3CF_3 will give $C_2H_2F_2$ if the "thermal" contribution is significant for irradiation of C_2H_5F. All monitor molecules were shown not to react when irradiated alone under the conditions used for Figure 1. Cyclopropane gave no reaction[8b] upon irradiation with either of the lines mentioned above, but CH_3CF_3 was the preferred monitor for C_2H_5F because of ease of analysis. The pressure dependence of the competition between the laser and "thermal" components is illustrated for CH_3CF_3 in Figure 1. For pressures $\gtrsim$1 Torr, *intermolecular* energy transfer is sufficiently rapid that "thermal" decomposition of the monitoring molecule is significant. However, the rapidly diminishing yields of either propene or ethene for pressures $\lesssim$1 Torr shows that CH_3CF_3 elimination can be directly induced by absorption of laser energy. At higher pressures the specific laser decomposition of CH_3CF_3 may be augmented by "thermal" processes. Since the monitoring reactions have lower threshold energies than CH_3CF_3, the "thermally" induced reactions of C_2H_5F and cyclopropane will occur to a somewhat greater extent than for CH_3CF_3. The results for photolysis of CH_3CH_2F with 12% added CH_3CF_3 as a thermal monitor are qualitatively similar to those shown in Figure 1.

The dependence of percent conversion per flash (expressed in terms of volume of sample actually irradiated) on the incident laser energy was investigated for C_2H_5F and CH_3CF_3 at a total pressure of 0.6 Torr; the relative concentrations of the monitoring molecules are given in the figure caption. The incident energy was varied by attenuating the laser beam with layers of poly(vinyl chloride) film without changing the focusing optics. The extent of reaction varied linearly with the log of the energy density;[9] the slopes of the lines in Figure 2 are 6 ± 1 and 9 ± 1 for CH_3CF_3 and C_2H_5F, respectively. At the lower energy densities, contribution from the "thermal" com-

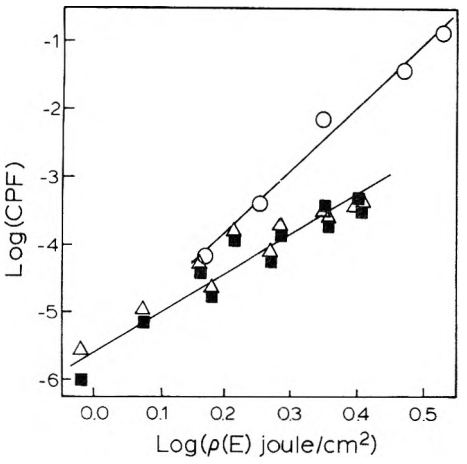

Figure 2. Dependence of the conversion per flash (in the irradiated volume) upon the *incident* laser energy density: (O) pumping CH_3CH_2F with the P(18) line of the 00°1–02°0 transition with 12% CH_3CF_3; (■) pumping CH_3CF_3 with the R(16) line of the 00°–10″0 transition with 50% CH_3CH_2F; (Δ) pumping CH_3CF_3 with 25% cyclopropane. The slope of the lines drawn through the data points are 9 ± 1 for C_2H_5F and 6 ± 1 for CH_3CF_3. The total pressure for these experiments was 0.6 Torr.

ponent was negligible; however, at the maximum energy a minor "thermal" contribution was identified by the monitoring molecules. Thus, the slopes are upper limits to the true values for the laser induced reaction. Even at the highest energy, HF elimination[10] was still the only reaction observed for C_2H_5F or CH_3CF_3. Based upon the sensitivity of our detection system, the practical threshold for observation of reaction was 2 J/cm^2. Variation of the wavelength of irradiation by selection of different CO_2 lines only showed effects consistent with the change in energy density illustrated in Figure 2.

The question of *intramolecular* relaxation of the absorbed laser energy was studied by irradiating bromofluoroethane with the P(36) line of the 00°1–02°0 band. If *intramolecular* energy randomization were minimal, excitation by absorption of laser energy would be expected to excite the molecule to favor HF elimination. In contrast the RRKM statistical[4] yields would greatly favor HBr because of the lower threshold energy. Experiments at 0.6 Torr using 3.1 J/cm^2 showed a pronounced favoring for HBr elimination over HF elimination; the measured ratio was bout 10:1. This ratio is consistent with an RRKM calculation[11] if the mean excitation energy in the CH_2F-CH_2Br molecule was 75 kcal mol^{-1}. If randomization has occurred, the RRKM calculated k_E values also can be used to estimate the mean energy in CH_3CH_2F and CH_3CF_3. At 1 Torr the collision rate is $\sim 10^7$ s^{-1} which can be taken as the lower limit to the rate constant.[4c] For this limit the molecules must have ~70 and ~85 kcal mol^{-1} for C_2H_5F and CH_3CF_3, respectively.[4a] Providing that these reactions occur via a RRKM mechanism, these molecules evidently acquire energy from the laser field in significant excess of the threshold energy.

Acknowledgment. We thank Dr. Wayne C. Danen (Kansas State University) for useful suggestions and discussions. This work was supported by the National Science Foundation (MPS 75-02793).

References and Notes

(1) R. V. Ambartzumian and V. S. Letokov, *Acc. Chem. Res.*, **10**, 61 (1977).
(2) D. F. Dever and E. Grunwald, *J. Am. Chem. Soc.*, **98**, 5055 (1976).
(3) (a) I. Glatt and A. Yogev, *J. Am. Chem. Soc.*, **98**, 7087 (1976); (b) A. Yogev and R. M. J. Benmair, *Chem. Phys. Lett.*, **46**, 290 (1977).
(4) (a) H. W. Chang, N. L. Cralg, and D. W. Setser, *J. Phys. Chem.*, **76**, 954 1972); (b) K. C. Klm, D. W. Setser, and B. E. Holmes, *ibid.*, **77**, 725 (1973); (c) P. J. Marcoux, E. E. Seifert, and D. W. Setser, *Int. J. Chem. Kinet.*, **7**, 473 (1975); *J. Phys. Chem.*, in press (1977).
(5) (a) E. Tschuikow-Roux and W. J. Quiring, *J. Phys. Chem.*, **75**, 295 (1971); (b) P. Cadman, M. Day, A. W. Kirk, and A. F. Trotman-Dickenson, *Chem. Commun.*, 203 (1970); (c) S. W. Benson and H. E. O'Neal, "Kinetic Data on Gas Phase Unimolecular Reactions", National Bureau of Standards, Washington, D.C., 1970, p 89.
(6) (a) D. S. Frankel, *J. Chem. Phys.*, **65**, 1696 (1976); (b) S. Makamel and J. Jortner, *ibid.*, **65**, 5204 (1976); (c) M. F. Goodman, J. Stone, and D. A. Dows, *ibid.*, **65**, 5052, 5062 (1976).
(7) M. J. Coggiola, P. A. Schulz, Y. T. Lee, and Y. R. Shen, *Phys. Rev. Lett.*, **38**, 17 (1977).
(8) (a) W. C. Danen, W. D. Munslow, and D. W. Setser, *J. Am. Chem. Soc.*, **99**, 6961 (1977). (b) Our finding of no laser induced decomposition for cyclopropane differs from reports in the literature, E. Grunwald, *Chem. Eng. News*, **54** (48), 18 (1976); M. L. LeSiecki and W. A. Guillory, *J. Chem. Phys.*, **66**, 4317 (1977), presumably because of our less severe focusing conditions.
(9) M. C. Gower and K. W. Billman, *Appl. Phys. Lett.*, **30**, 514 (1977); *Opt. Commun.*, **20**, 123 (1977).
(10) W. Braum and W. Tsang, *Chem. Phys. Lett.*, **44**, 354 (1976). These authors observed mainly elimination reactions from alkyl chlorides and bromides, but for the iodides radicals were formed from C–I bond rupture.
(11) T. H. Richardson, unpublished results; the threshold energies used in the calculation were 60 and 54 kcal/mol for HF and HBr elimination, respectively.

Department of Chemistry
Kansas State University
Manhattan, Kansas 66506

T. H. Richardson
D. W. Setser*

Received July 11, 1977

Kinetics of the Cl + C_2H_2 Reaction. Stratospheric Implication

Publication costs assisted by Centre National de la Recherche Scientifique, France

Sir: Termination of Cl atom chains in the stratosphere would essentially occur via

$$Cl + CH_4 \rightarrow CH_3 + HCl \quad (1)$$

which would result, at least temporarily, in the interruption of ozone depletion in the earth's stratosphere.[1]

Another hydrocarbon, acetylene, has been recently suggested by Lee and Rowland[2] as a species which would also remove Cl atoms. To estimate the effect of C_2H_2, these authors have studied the kinetics of the Cl + C_2H_2 reaction by a competitive method.

We have also performed in 1972 a kinetic study of this reaction which led to an absolute rate constant determination.[3] This study was made in relation to the inhibition of hydrocarbon flames by chlorinated compounds[4] in order to explain the chemical mechanism of the inhibition.

The Cl + C_2H_2 reaction was studied by the flow discharge–mass spectrometer method. Typical experimental conditions for the rate constant measurements were as follows: pressure, 0.50–2.00 Torr (diluent, helium); temperature, 295–500 K; (C_2H_2), 0.1–5 × 10^{14} mol cm^{-3}; (Cl), 1–3 × 10^{15} atoms cm^{-3}. The rate constant for the elementary reaction

$$Cl + C_2H_2 \rightarrow \text{products} \quad (2)$$

was found to be temperature independent in the 295–500 K range: $k_2 = (2.0 \pm 0.5) \times 10^{-13}$ cm^3 molecule^{-1} s^{-1}.

The products of the overall reaction were also identified. The main products HCl, $C_2H_2Cl_2$, and C_2HCl were simultaneously detected in the flow reactor; when the excess of Cl atoms was increased, other chlorinated compounds were also observed as $C_2H_2Cl_4$ and C_2Cl_4. Stoichiometry

was measured (Cl consumed/C_2H_2 consumed) and reached high values (6 or 8) when chlorine atoms concentrations were increased. Fast secondary reactions must exist in agreement with the experimental observation of the products and the value of stoichiometry.

The initial step proposed was unambiguously the addition reaction

$$Cl + C_2H_2 \rightarrow C_2H_2Cl^* \quad (3)$$

because the zero activation energy observed makes negligible the abstraction path

$$Cl + C_2H_2 \rightarrow HCl + C_2H \quad (4)$$

which is 9 kcal/mol endothermic. Following the initial addition step (3), fast secondary reactions occurring in our system were considered and a mechanism of the overall reaction was suggested, where the excited or stabilized C_2H_2Cl radical could undergo reactions with chlorine atoms leading to the formation of C_2HCl (by an abstraction reaction) or $C_2H_2Cl_2$ (by an addition reaction).

A comparison of our kinetic results with the measurements of Lee and Rowland allows to indicate the actual stratospheric significance of the reaction of chlorine atoms with acetylene. Our value for the rate constant of reaction 2 is lower than the determination of Lee and Rowland. The value of k_2 estimated by these authors is $k_2 = 10^{-10}$ cm^3 molecule^{-1} s^{-1}, that corresponds to effective addition in 2–5 collisions. Our value, $k_2 = 2 \times 10^{-13}$ cm^3 molecule^{-1} s^{-1}, gives an efficiency of the addition reaction of 10^{-3}.

Following reaction 3 Lee and Rowland considered that $C_2H_2Cl^*$ could undergo either stabilization (5) or decomposition (6):

$$C_2H_2Cl^* + M \rightarrow C_2H_2Cl + M \quad (5)$$

$$C_2H_2Cl^* \rightarrow C_2H_2 + Cl \quad (6)$$

In our system, since a pressure dependence study of k_2 could not be carried out, it is not possible to exclude the occurrence of the decomposition reaction of $C_2H_2Cl^*$ (6) which may not be negligible, compared to stabilization reaction 5 at pressures near 1 Torr. Furthermore reaction 6 could also not be negligible compared to the reactions of $C_2H_2Cl^*$ with excess of Cl atoms. A comparison with the similar addition reaction H + C_2H_2 (7) does not give any clear indication about the pressure dependence of the rate constant: from the results of Volpi and Zocchi[5] it seems that the stabilization reaction of $C_2H_3^*$ became predominant at 1–2 Torr (with H_2 and Ar as third bodies), while the works of Michael and Weston,[6] and Michael and Niki[7] have shown a pressure dependence on k_7 in the pressure ranges 2–17.3 and 0.52–1.67 Torr, respectively.

Thus, if the decomposition reaction of $C_2H_2Cl^*$ is not negligible near 1 Torr with He as a diluent the rate constant of step 3 would be higher than 2×10^{-13} cm^3 molecule^{-1} s^{-1} and the difference with the data of Lee and Rowland[2] would be consequently reduced. In addition the agreement between the two determinations would be good if we consider the efficiency of stabilization of $C_2H_2Cl^*$ by He to be 1/500 at 1–2 Torr.

Considering the stratospheric impact of the Cl + C_2H_2 reaction, we can compare it with the Cl + CH_4 reaction for which the rate constant has been also determined in our experimental system.[8] At 30 km altitude using the stratospheric mixing ratios of 10^{-10} and 10^{-6} for C_2H_2 and CH_4, respectively, and considering our values of the rate constants calculated at $T = 226$ K, the rate ratio $k_2(C_2H_2)/k_1(CH_4)$ is 5×10^{-4}.

However, if we admit there is a pressure dependence of k_2 at low pressures, then k_2 would equal about 2×10^{-12} cm^3 molecule^{-1} s^{-1} at 9 Torr which is the pressure corresponding to an altitute of 30 km. That gives for $k_2(C_2H_2)/k_1(CH_4)$ a value of 5×10^{-3}, which also agrees with the upper limit of 10^{-2} given by Lee and Rowland.[2] This upper limit was calculated considering that about 1% of the $C_2H_2Cl^*$ radicals would be stabilized at 30 km.

Finally, whatever the fraction of stabilized C_2H_2Cl could be, the rate constant found for k_2 makes insignificant the Cl + C_2H_2 reaction in stratospheric processes compared to the Cl + CH_4 reaction.

References and Notes

(1) F. S. Rowland and M. J. Molina, *Rev. Geophys. Space Phys.*, **13**, 1 (1975).
(2) F. S. C. Lee and F. S. Rowland, *J. Phys. Chem.*, **81**, 7, 684 (1977).
(3) G. Poulet, J. Barassin, G. Le Bras, and J. Combourieu, *Bull. Soc. Chim. Fr.*, **1**, 1 (1973).
(4) G. Le Bras, I. Hajal, J. Combourieu, and P. Laffitte, *J. Chim. Phys.*, **64**, 1153 (1967).
(5) G. G. Volpi and F. Zocchi, *J. Chem. Phys.*, **44**, 4010 (1966).
(6) J. V. Michael and R. E. Weston, Jr., *J. Chem. Phys.*, **45**, 3632 (1966).
(7) J. V. Michael and H. Niki, *J. Chem. Phys.*, **46**, 4969 (1967).
(8) G. Poulet, G. Le Bras, and J. Combourieu, *J. Chim. Phys.*, **71**, 101 (1974).

CNRS
Centre de Recherches sur la Chimie
de la Combustion et des Hautes Tempêratures
45045 Orleans Cedex, France

G. Poulet
G. Le Bras*
J. Combourieu

Received July 22, 1977

The Role of the Termination Reaction H + CH_3 → CH_4 in the Pyrolysis of Propane in the Temperature Range 1100–1300 K

Sir: Propane pyrolysis is a famous industrial process. Besides ethylene, the most important fine chemical feedstock in the chemical industry, hydrogen, methane, ethane, and propylene have also been found to be major products. This process has been investigated with many techniques and at various temperatures.[1-7] Recently Lifshitz et al. studied this pyrolysis with a shock tube in the temperature range 1100–1300 K using mixtures of propane and argon as reactants.[3] This mixture was heated to a desired temperature by a reflected shock wave, maintained and allowed to react at that temperature for a period of 700 μs, and rapidly cooled by expansion waves. A series of such experiments was carried by them for different reactant compositions and reaction temperatures. Lifshitz and Frenklach then proposed the following reaction scheme as a mechanism of the generation of these products:[2]

$$C_3H_8 \rightarrow CH_3 + C_2H_5 \quad (1)$$

$$CH_3 + C_3H_8 \rightarrow CH_4 + i\text{-}C_3H_7 \quad (2a)$$

$$CH_3 + C_3H_8 \rightarrow CH_4 + n\text{-}C_3H_7 \quad (2b)$$

$$H + C_3H_8 \rightarrow H_2 + i\text{-}C_3H_7 \quad (3a)$$

$$H + C_3H_8 \rightarrow H_2 + n\text{-}C_3H_7 \quad (3b)$$

$$i\text{-}C_3H_7 \rightarrow C_2H_4 + CH_3 \quad (4a)$$

$$n\text{-}C_3H_7 \rightarrow C_2H_4 + CH_3 \quad (4b)$$

$$i\text{-}C_3H_7 \rightarrow C_3H_6 + H \quad (5a)$$

$$n\text{-}C_3H_7 \rightarrow C_3H_6 + H \quad (5b)$$

$$C_2H_5 \rightarrow C_2H_4 + H \quad (6)$$

$$CH_3 + CH_3 \rightarrow C_2H_6 \quad (7)$$

TABLE I: Comparison of Computer Simulation Results with Data from Shock Tube Experiments

Run	Data source	Product generation rate, mol cm s^{-1}					% conversion	Temp, K	Initial C_3H_8, mol cm^{-3}
		H_2	CH_4	C_2H_4	C_2H_6	C_3H_6			
	Experiment[a]	2.46E − 6	1.15E − 6	2.21E − 6	3.57E − 7	2.89E − 6	0.88		
A_1	Computer A[b]	1.32E − 6	7.61E − 7	1.48E − 6	2.74E − 7	9.87E − 7	0.81	1132	2.064E − 7
	Computer B[c]	1.42E − 6	8.80E − 7	1.69E − 6	3.14E − 7	1.02E − 6	0.90		
	Experiment	2.84E − 6	1.69E − 6	3.58E − 6	8.06E − 7	2.08E − 6	1.68		
A_2	Computer A	3.28E − 6	1.70E − 6	3.69E − 6	8.49E − 7	2.30E − 6	1.78	1160	2.315E − 7
	Computer B	3.12E − 6	1.88E − 6	3.76E − 6	8.00E − 7	2.19E − 6	1.77		
	Experiment	5.75E − 5	2.76E − 5	7.83E − 5	1.79E − 5	2.33E − 5	30.10		
A_3	Computer A	7.75E − 5	1.41E − 5	8.71E − 5	3.57E − 5	4.29E − 5	40.06	1298	2.262E − 7
	Computer B	3.99E − 5	2.28E − 5	5.57E − 5	1.59E − 5	2.35E − 5	24.39		
	Experiment	4.78E − 6	4.75E − 6	6.36E − 6	7.80E − 7	5.82E − 6	0.87		
B_1	Computer A	4.65E − 6	4.19E − 6	5.35E − 6	4.70E − 7	4.07E − 6	0.67	1100	9.797E − 7
	Computer B	5.56E − 6	4.88E − 6	6.49E − 6	6.77E − 7	4.76E − 6	0.80		
	Experiment	6.47E − 5	4.88E − 5	6.94E − 5	1.61E − 5	4.46E − 5	8.44		
B_2	Computer A	6.11E − 5	3.63E − 5	6.89E − 5	1.57E − 5	4.48E − 5	8.12	1206	9.770E − 7
	Computer B	5.11E − 5	3.59E − 5	6.12E − 5	1.21E − 5	3.85E − 5	7.12		
	Experiment	2.55E − 4	1.88E − 4	3.03E − 4	4.68E − 5	1.36E − 4	28.87		
B_3	Computer A	3.77E − 4	1.28E − 4	4.18E − 4	1.43E − 4	2.32E − 4	42.65	1292	1.065E − 6
	Computer B	2.37E − 4	1.43E − 4	2.99E − 4	7.68E − 5	1.58E − 4	30.10		
	Experiment	7.05E − 7	5.97E − 7	8.28E − 7	1.29E − 7				
C_1	Computer A	9.33E − 7	6.29E − 7	1.06E − 6	1.48E − 7	7.20E − 7	0.47	1110	2.572E − 7
	Computer B	1.14E − 6	7.59E − 7	1.33E − 6	2.10E − 7	8.57E − 7	0.58		
	Experiment	5.70E − 6	2.98E − 6	6.30E − 6	1.48E − 6	3.80E − 6	3.16		
C_2	Computer A	5.27E − 6	2.39E − 6	5.90E − 6	1.56E − 6	3.53E − 6	2.93	1180	2.219E − 7
	Computer B	4.73E − 6	2.62E − 6	5.68E − 6	1.36E − 6	3.20E − 6	2.77		
	Experiment	1.69E − 5	9.83E − 6	1.90E − 5	4.17E − 6	9.05E − 6	8.24		
C_3	Computer A	2.81E − 5	7.77E − 6	3.10E − 5	1.11E − 5	1.65E − 5	14.76	1248	2.360E − 7
	Computer B	1.83E − 5	9.25E − 6	2.32E − 5	6.61E − 6	1.13E − 5	10.74		

[a] Data illustrated in ref 3. [b] Results of computer simulation with rate constant assigned in ref 2. [c] $k_1 = 10^{14.23} \exp(-71.7 \times 10^3/RT)$, $k_2 = 10^{12.9} \exp(-12.2 \times 10^3/RT)$, $k_8 = 2.0 \times 10^{14}$ (1000 Torr), 1.6×10^{14} (300 Torr).

According to this mechanism, Lifshitz and Frenklach also duplicated one of the reported shock tube experiments[3] (the one at 1206 K) by a computer-simulated experiment using appropriate rate constants.[2] They demonstrated that the shock tube experiment and the computer-simulated experiment lead to same end product distributions within experimental error.

From the above mechanism they eliminated many possible elementary reactions which, according to their calculation, do not have any influence on the composition of the reaction product. Of interest to us, one of the eliminated reactions is the following radical combination process:

$$H + CH_3 \rightarrow CH_4 \qquad (8)$$

This process has been recently studied in our laboratory.[8,9] Its rate constant, k_8, is pressure dependent. At a pressure of 1000 Torr, k_8 was determined as 2.0×10^{14} cm^3 mol^{-1} s^{-1} which is larger than the estimation of Lifshitz and Frenklach for this rate constant by a factor of 80. A rough calculation using this newly determined constant and the reported steady state radical concentrations of their typical experiment showed that process 8 should not be a negligible radical termination process in comparison with process 7. This finding induced us to prepare our own computer-simulation experiment to investigate the effect on the product distributions of the addition of process 8 to the mechanism of the propane pyrolysis.

A CDC Model 6000 computer was used for this calculation. All nine experiments that were carried out and described by Lifshitz et al.[3] have been run through a computer program written for the above mechanism (reactions 1–7) using the rate constants suggested by Lifshitz and Frenklach.[2] These computer-calculated results are shown in Table I as Computer A. In this table, the calculated average rate of products generation over 700 μs are presented. Also listed in Table I are the reported generation rates from the shock tube experiment[3] (described in the table as Experiment). It is apparent that the agreement between these two sources (experiment and computer A) is excellent as long as the temperature is less than 1206 K. At high temperatures (runs A_3, B_3, and C_3), however, there are two serious discrepancies: first, the yield ratio of methane to ethane is greater than one in the experiment while it was calculated to be less than one from computer A; and second, reaction conversions calculated in computer A are higher than those measured from the experiment by 30% or more.

The computer calculation was then repeated with the addition of process 8 to the program. The effect of the cooling phase on the product distribution was assumed negligible in this calculation because Lifshitz et al. established that only a few percent of products is added in this phase.[2] k_8 was given a value of 1.6×10^{14} and 2.0×10^{14} cm^3 mol^{-1} s^{-1} at system pressures of 300 and 1000 Torr, respectively, according to our previous determination.[8,9] This addition caused an immediate increase in the rate of methane generation and a decrease in the rate of generation of hydrogen and ethane. The first discrepancy mentioned above disappeared comfortably. According to the computer calculations, process 8 contributes only 2% to the total methane generation at a temperature of 1100 K. This share increases to 10% at 1200 K and 40% at 1300 K. Process 8 is therefore an indispensable radical termination step in the propane pyrolysis at the temperature of 1200 K or higher.

In order to lessen the second discrepancy, various values have also been tried for the rate constants of reaction 1.

Calculated rates in the Computer B rows in Table I were obtained when k_1 was assigned a value of $10^{14.24}\exp(-71.7 \times 10^3/RT)$. To our satisfaction, this optimum value not only leads to good conversion agreement for the computer B results with experiment but, itself, also corresponds reasonably well to the $10^{14.41}\exp(-67 \times 10^3/RT)$ and $10^{14.78}\exp(-75 \times 10^3/RT)$ values proposed for k_1 by Laidler et al.[5] and Herriott et al.,[6] respectively.

Acknowledgment. We gratefully acknowledge the support of this research by the National Science Council of the Republic of China.

References and Notes

(1) A. M. Benson, *AIChE J.*, **13**, 903 (1967).
(2) A. Lifshitz and M. Frenklach, *J. Phys. Chem.*, **79**, 686 (1975).
(3) A. Lifshitz, K. Scheller, and A. Burcat, *Proc. 7th Int. Shock Tube Symp.*, **690** (1973).
(4) D. A. Leathard and J. H. Purnell, *Proc. R. Soc. London, Ser. A*, **305**, 517 (1968).
(5) K. J. Laidler, N. H. Sagert, and B. W. Wojciechowski, *Proc. R. Soc. London, Ser. A*, **270**, 242 (1962).
(6) M. M. Papic and K. J. Laidler, *Can. J. Chem.*, **49**, 535 (1971).
(7) G. E. Herriott, R. E. Eckert, and L. F. Albright, *AIChE J.*, **18**, 84 (1972).
(8) J. T. Cheng, Y. S. Lee, and C. T. Yeh, *J. Phys. Chem.*, **81**, 687 (1977).
(9) J. T. Cheng, MS Dissertation, National Tsing Hua University, 1976; J. T. Cheng and C. T. Yeh, *J. Phys. Chem.*, **81**, 1982 (1977).

Institute of Chemistry
National Tsing Hua University
Hsinchu, Taiwan, Republic of China

Wen-hong Kao
Chuin-tih Yeh*

Received April 28, 1977

Parametrizations of the Rotation Group

Publication costs assisted by The Graduate School, University of Kentucky

Sir: The irreducible representations of the three-dimensional pure rotation group are usually given in terms of Euler's parametrization, that is, successive rotations ψ, θ, ϕ about the z, y, and z axes, respectively.[1] For the representation of dimension $2j + 1$

$$D^{(j)}_{m'm}(\phi,\theta,\psi) = (-1)^{m'-m}e^{-im'\phi}e^{-im\psi} \times \sum_\sigma (-1)^\sigma \frac{[(j+m)!(j-m)!(j+m')!(j-m')!]^{1/2}}{(j+m-\sigma)!(j-m'-\sigma)!\sigma!(m'-m+\sigma)!} \times (\cos {}^1/_2\theta)^{2j+m-m'-2\sigma}(\sin {}^1/_2\theta)^{2\sigma+m'-m} \quad (1)$$

Other parametrizations are preferable in particular problems. For example, when working with finite subgroups of the rotation group a parametrization in terms of the axis and angle of rotation is especially convenient. The irreducible representations for this parametrization have been examined in considerable detail[2] without recognizing that they may be obtained by an elementary calculation. Indeed, the irreducible representations for any desired parametrization may be obtained by the following argument.

Let R denote a 3×3 orthogonal matrix with $\det R = +1$, interpreted as a change of reference system: $(xyz) \rightarrow (x'y'z')$. The elements in the third row and third column implicitly define the three independent parameters ξ, η, ζ characterizing the rotation, as these five quantities are related by two conditions: $R_{31}^2 + R_{32}^2 = R_{13}^2 + R_{23}^2 = 1 - R_{33}^2$. Now R_{33} is the cosine of $\angle z0z' = \theta$, and, from the matrix for a rotation in terms of Euler's angles,[3] $R_{31} + iR_{32} = e^{i\phi}\sin\theta$, $R_{13} + iR_{23} = -e^{-i\psi}\sin\theta$. Straightforward eliminations in conjunction with (1) yield the general formula

$$D^{(j)}_{m'm}(\xi,\eta,\zeta) = (-1)^{m'm} \times \frac{[{}^1/_2(R_{31} - iR_{32})]^{m'}[-{}^1/_2(R_{13} + iR_{23})]^m}{[{}^1/_2(1 - R_{33})]^m} \times \left\{\frac{(j+m')!(j-m')!}{(j+m)!(j-m)!}\right\}^{1/2} \times P^{(m'-m,m'+m)}_{j-m}(R_{33}) \quad (2)$$

where $P^{(\alpha,\beta)}_n(t)$ is Jacobi's polynomial[4] of degree n in t. This formula is valid for positive and negative values of m', m as the conditions $\alpha, \beta > -1$ are necessary only to ensure convergence at end points of the interval of orthogonality; integration over the group manifold is not vitiated since $D^{(j)}_{-m',-m} = (-1)^{m'-m}D^{(j)*}_{m'm}$.

If λ, μ, ν are direction cosines of the axis of rotation and Φ the angle of rotation, the matrix representing R in terms of these parameters[5] leads to

$$D^{(j)}_{m'm}(\lambda,\mu,\nu,\Phi) = (-1)^{m'-m}\frac{(\mu+i\lambda)^{m'}(\mu-i\lambda)^m}{(1-\nu^2)^m} \times (\sin {}^1/_2\Phi)^{m'-m}(\cos {}^1/_2\Phi - i\nu\sin {}^1/_2\Phi)^{m'+m} \times \left\{\frac{(j+m')!(j-m')!}{(j+m)!(j-m)!}\right\}^{1/2} P^{(m'-m,m'+m)}_{j-m'}(R_{33}) \quad (3)$$

where $\lambda^2 + \mu^2 + \nu^2 = 1$ and $R_{33} = 1 - 2(1 - \nu^2)\sin^2 {}^1/_2\Phi$. A neater form results on introducing ϑ, φ as polar angles of the rotation axis

$$D^{(j)}_{m'm}(\vartheta,\varphi,\Phi) = (-1)^{m'}(e^{-i\varphi}\sin\vartheta\sin {}^1/_2\Phi)^{m'-m} \times (i\cos {}^1/_2\Phi + \cos\vartheta\sin {}^1/_2\Phi)^{m'+m} \times \left\{\frac{(j+m')!(j-m')!}{(j+m)!(j-m)!}\right\}^{1/2} P^{(m'-m,m'+m)}_{j-m'}(R_{33}) \quad (4)$$

with $R_{33} = 1 - 2\sin^2\vartheta\sin^2 {}^1/_2\Phi$.

The irreducible representations for other parametrizations may be obtained from (2) and the appropriate matrix R with equal facility.

References and Notes

(1) E. P. Wigner, "Group Theory", Academic Press, New York, N.Y., 1959, p 167. Wigner's formula gives the matrix elements of $\exp(i\alpha J_z)\exp(i\beta J_y)\exp(i\gamma J_z)$; Equation 1 of the text follows on setting $\alpha = -\phi$, $\beta = -\theta$, $\gamma = -\psi$.
(2) H. E. Moses, *Nuovo Cimento*, **XL** A, 1120 (1965); *Ann. Phys.*, **37**, 224 (1966); **42**, 343 (1967).
(3) See, for example, P. L. Corio, "Structure of High-Resolution NMR Spectra", Academic Press, New York, N.Y., 1966, p 479.
(4) G. Szego, "Orthogonal Polynomials", American Mathematics Society, New York, N.Y., 1939, Chapter IV.
(5) Reference 3, p 477.

Department of Chemistry
University of Kentucky
Lexington, Kentucky 40506

P. L. Corio

Received July 20, 1977

Chain Expansion of Neutral Polymer Coils upon Cation Binding

Sir: Alkali and alkaline earth cation binding to the peptide group is a phenomenon of interest in problems of physical biochemistry such as salt-induced conformational transitions in proteins and carrier-mediated transport. Several proteins and polypeptides have been shown to bind these cations and undergo conformational alterations.[1-6] Model

TABLE I: Preferential Binding Parameters of Poly(vinylpyrrolidone) to LiCl

Salt concn,[a] M	$(\partial n/\partial c_2)^{\circ}_{T,\mu_1,\mu_3}$ [b]	$(\partial n/\partial c_2)^{\circ}_{T,P,c_3}$ [c]	$(\partial c_3/\partial c_2)^{\circ}_{T,\mu_1,\mu_3}$ [d]	$(\partial c_3/\partial c_2)^{corr}_{T,\mu_1,\mu_3}$ [e]	$(\partial m_3/\partial m_2)_{T,\mu_1,\mu_3}$ [f]
2	0.120	0.166	−0.197	−0.135	−237
4	0.130	0.131	−0.004	0.120	113
6	0.121	0.124	0.017	0.204	192

[a] Salt molarity. [b] Refractive increment of PVP solution after equilibrium dialysis with LiCl. [c] Refractive increment values of PVP against LiCl solution before dialysis. [d] Binding parameter expressed on a molar scale. [e] Binding parameters on a corrected molar scale. [f] Binding parameter on a molal scale basis.

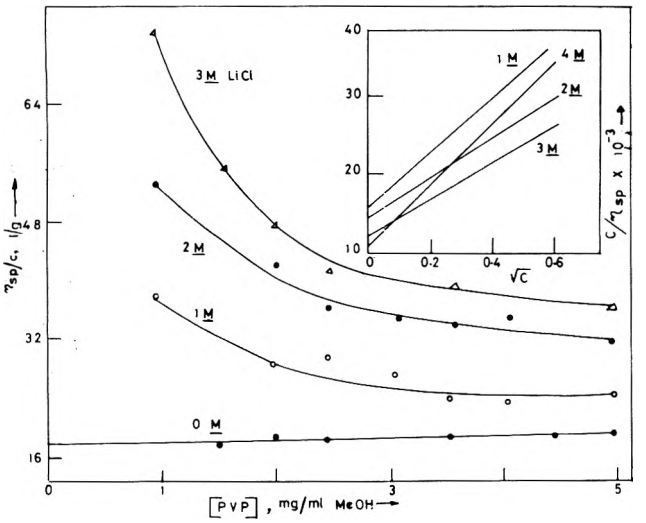

Figure 1. Huggins plot of PVP in methanolic LiCl. Insert shows Fuoss–Strauss plots of the same data for PVP.

compound studies have helped establish that the cation binds to the neutral peptide moiety and effects changes in the structural properties of the chromophore.[7] Indeed the binding can be dramatic under appropriate conditions; for example, the neutral homopolypeptide poly(ω-hydroxyethyl-L-glutamine) (PHEG) displays polyelectrolyte behavior in methanolic LiCl.[3] We report here a case of such drastic chain conformational changes induced in another neutral polymer upon ion binding.

The polymer chosen for the study was poly(vinylpyrrolidone) (PVP), purchased from Sigma Chemical Co. with a reported molecular weight of 40000. This is a neutral polymer suggested to exist in the random coil conformation[9] and indeed the case of PVP may be regarded as a severe test of the effects of ion binding to a macromolecule since PVP has a paraffin-like backbone and lactam moieties in the side chain as the only ligand for complexation. We report here results on equilibrium dialysis and viscosity studies on LiCl binding to PVP in solution.

Equilibrium Dialysis Measurements. A solution of the polymer (component 2) in a mixed solvent of known composition (H_2O component 1, LiCl component 3) was dialyzed in a closed system against the same solvent until osmotic equilibrium was reached and the preferential binding of LiCl to the polymer, $(\partial c_3/\partial c_2)_{T,\mu_1,\mu_3}$, was determined by measuring the appropriate refractive increments $(\partial n/\partial c)$ as suggested by the Timasheff expression[10]

$$\left[\frac{\partial c_3}{\partial c_2}\right]^{\circ}_{T,\mu,\mu_3} = \frac{(\partial n/\partial c_2)^{\circ}_{T,\mu_1,\mu_3} - (\partial n/\partial c_2)^{\circ}_{T,P,c_3}}{(\partial n/\partial c_3)^{\circ}_{T,P,c_2}}$$

The binding parameter can be corrected for polymer volume effects and is expressed usually on a molar basis, $[\partial c_3/\partial c_2]^{corr}_{T,\mu_1,\mu_3}$, or on a molal basis, $(\partial m_3/\partial m_2)_{T,\mu_1,\mu_3}$, scale. In Table I are shown the preferential binding parameters of LiCl to PVP in aqueous solutions at various salt concentrations. Preferential hydration occurs to PVP in 2 M LiCl, while at higher molarities, preferential binding of the salt occurs to the polymer. The highest LiCl molarity used was 6 M, since at higher salt molarities the polymer tends to "salt out" of solution. The "saturation" value in the case of PVP thus appears to be around 200 Li^+ ions per molecule of PVP (approximate degree of polymerization 360), which suggests the ion:amide ligand ratio to be greater than the value of 1:4 suggested from model compound experiments,[7] underscoring the importance of the role of solvent water in the ligand equilibrium process. The values of these binding parameters compare favorably with the extent of binding of LiCl to aqueous of the globular protein bovine serum albumin.[3,5] It thus appears that the suspicion from model compound studies that Li^+ can bind to neutral sites in polypeptides and proteins is borne out.

Viscosity Studies. The Huggins expression $\eta_{sp/c} = [\eta] + K[\eta]^2c$ relates the reduced specific viscosity $\eta_{sp/c}$ of a polymer solution to its concentration c, and for neutral polymers is a straight line with a positive slope. For polyelectrolytes that show electrolytic chain expansion, the curve increases steeply with a negative slope at low concentration.[12] In Figure 1 we compare the viscosity behavior of PVP in methanol in the presence and absence of added Li^+ ions. The induction of polyelectrolyte behavior in the presence of LiCl is obvious and supports the suggestion of Lotan[8] that Li^+ binding to a neutral polypeptide (PHEG) induces pseudopolyelectrolyte behavior in the otherwise neutral polymer. Such chain expansion was not observed for the polymer in aqueous salt solutions indicating the importance of the solvent medium.

We have also estimated the chain dimensions of PVP upon Li^+ binding from viscosity studies. Since PVP has been established[9] to possess the randomly coiled chain conformation in methanol, one can estimate the radius of gyration of the polymer from the expression[11] $[\eta] = 10\pi N/3M(R_g\,\zeta)^3$, where N is the Avogadro number, M is the molecular weight, R_g the radius of gyration, and ζ a parameter that relates the radius of gyration R_g to the hydrodynamic radius R_e of the flexible polymer chain ($R_e = \zeta R_g$) and is suggested to have a value of 0.775 for flexible random coil chains. Estimation of PVP in CH_3OH/LiCl is possible by the use of the method of Fuoss and Strauss[12] where one plots c/η_{sp} against $c^{1/2}$ and obtains $1/[\eta]$ as the intercept. Such Fuoss–Strauss plots are shown in the insert of Figure 1 for PVP in methanolic LiCl. From the intrinsic viscosities obtained from such curves, we calculated the radius of gyration of PVP in methanolic LiCl to be 280, 433, 450, 480, and 494 Å in 0, 1, 2, and 4 M LiCl, respectively, showing that chain expansion of the polymer occurs upon Li^+ binding. (Studies at higher salt molarities were not possible due to solubility problems.)

Acknowledgment. We acknowledge financial help from CSIR, India.[13]

References and Notes

(1) M. L. Tiffany and S. Krimm, *Biopolymers*, **8**, 347 (1969).
(2) T. Schleich and P. Von Hippel, *Biopolymers*, **7**, 861 (1969).
(3) M. E. Noelken, *Biochemistry*, **9**, 4122 (1970).

(4) D. W. Urry, *Proc. Natl. Acad. Sci. U.S.A.*, **68**, 810 (1971).
(5) S. F. Sun, N. O. Del Rosario, and L. A. Goldstein., *Int. J. Peptide Proteins Res.*, **5**, 337 (1973).
(6) B. C. Starcher and D. W. Urry, *Bioinorg. Chem.*, **3**, 107 (1974).
(7) (a) D. Balasubramanian and R. Shaikh, *Biopolymers*, **12**, 1639 (1973); (b) D. Balasubramanian and B. C. Misra, *ibid.*, **14**, 1019 (1975); (c) B. C. Misra, Ph.D. Thesis, I.I.T. Kanpur, India, 1976.
(8) (a) N. Lotan, *J. Phys. Chem.*, **77**, 242 (1973); (b) N. Lotan in "Peptides, Polypeptides and Proteins", E. R. Blout et al., Ed., Wiley-Interscience, New York, N.Y., 1974, p 157.
(9) (a) G. B. Levy and H. P. Frank, *J. Polym. Sci.*, **17**, 247 (1955); (b) P. Molyneux and H. P. Frank, *J. Am. Chem. Soc.*, **83**, 3169, 3175 (1961).
(10) M. E. Noelken and S. N. Timasheff, *J. Biol. Chem.*, **242**, 5080 (1967).
(11) See, for example, C. Tanford in "Physical Chemistry of Macromolecules", Wiley, New York, N.Y.
(12) R. M. Fuoss and U. P. Strauss, *J. Polym. Sci.*, **3**, 246, 602 (1948).
(13) Part of this work was presented at the VIII Jerusalem symposium in Biochemistry, 1976.

School of Chemistry **D. Balasubramanian***
University of Hyderabad **B. C. Misra**
Hyderabad 500001, India

Received June 22, 1977

Effects of Ring Substituents on the Torsional Frequency of the $-NH_2$ Group in Anilines

Publication costs assisted by Kansas State University

Sir: Recently our interest has been directed to the study of how substituent groups effect the π-electronic system of benzene compounds.[1] The results for over 75 substituted phenols suggest the OH rotor can be used as a very sensitive probe for measuring the effect of substituents on the π-electron density in aromatic compounds. Here we wish to report that substituents effect the NH_2 torsional frequency in aniline in a very similar manner.

The substituted anilines were obtained in the highest purity available from commercial sources. Infrared spectra were used to confirm each compound's purity. The low frequency infrared spectra were obtained on a Digilab FTS-14 Fourier transform spectrometer. A 6-μm beam splitter allowed us to observe the 450–75-cm^{-1} region, which proved to be the region where the torsional frequencies occur in anilines. A globar source, 4-cm^{-1} resolution, and triangular apodization function were generally used for the collection of all spectra. We employed the previously reported cyclohexane solution technique for obtaining the spectra. The dilute aniline in cyclohexane solutions (0.01–0.05 M) were placed in polyethylene and polypropylene cells, generally 5 mm in thickness.[1-3] The cell windows are easily replaced and used only once per sample. The aniline torsional frequency observed in cyclohexane solution agrees well with that observed in the gas phase.[4] The results of this study are given in Table I.

TABLE I: Torsional Frequencies (ω_τ) in Substituted Anilines and a Comparison of Torsional Frequency Shifts ($\Delta\omega_\tau$) in Anilines and Phenols as a Function of Substituent

Substituent on aniline	ω_τ, cm^{-1}	$\Delta\omega_\tau$, cm^{-1}	
		Aniline[a]	Phenol[b]
4-Nitro	322	+37	+40
4-Cyano	327	+42	+33
4-Iodo	288	+3	+3
4-Chloro		Not obsd	−8
4-Methyl	266	−19	−15
4-Fluoro	249	−36	−30
4-Methoxy	236	−49	−42
3-Methyl	289	+4	+2
2-Methyl	285	0	Unassigned see ref 2,3

[a] The change in torsional frequency, $\Delta\nu_{torsn}$, for aniline is calculated from $\omega_{torsn}^{subst\ aniline} - 285\ cm^{-1}$. [b] The $\Delta\omega_{torsn}$ for phenol is $\omega_{torsn}^{subst\ phenol} - 310\ cm^{-1}$, see ref 1. Note the aniline torsional frequency, ω_τ, = 285 cm^{-1}. The phenol torsional frequency, ω_τ, = 310 cm^{-1}.

Previously we have reported a large amount of data that suggested the OH rotor might be a very sensitive probe for measuring substituent effects on the π-electron density in aromatic rings. We think there is no question that substituents effect the π-electron density in essentially the same manner for either $-OH$ or $-NH_2$ rotors. Further, we feel that this data support the use of $\Delta\omega_\tau$ values for measuring substituent effects on the π-electron density as suggested in our earlier paper.[1]

References and Notes

(1) W. G. Fateley, G. L. Carlson, and F. F. Bentley, *J. Phys. Chem.*, **79**, 199 (1975).
(2) A. S. Manocha, G. L. Carlson, and W. G. Fateley, *J. Phys. Chem.*, **77**, 2094 (1973).
(3) G. L. Carlson and W. G. Fateley, *J. Phys. Chem.*, **77**, 1157 (1975).
(4) P. J. Krueger and R. Kydd, unpublished work presented at the International Fourier Transpose Conference held at the University of South Carolina, Columbia, S.C., June 1977.

Westington Research Laboratories **G. L. Carlson**
Beulah Road
Pittsburgh, Pennsylvania 15235
Chemistry Department **W. G. Fateley***
Kansas State University
Manhattan, Kansas 66506

Received September 9, 1977

Holographic, concave aberration corrected.

MONOCHROMATOR

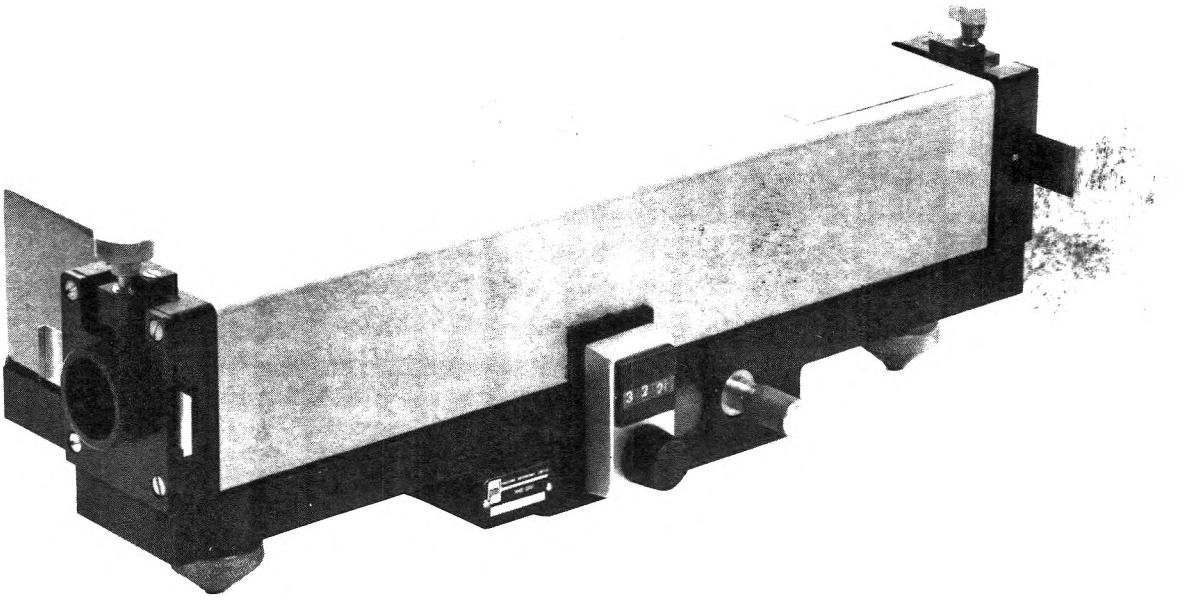

- Focal length: 204 mm
- Aperture: f/4
- Mounting: Seya Namioka + 2 flat Mirrors
- Stray light: $< 5 \times 10^{-3}$ at 220 nm
- Linear dispersion: 3.5 nm/mm
- Adjustable feet

Two bilateral, variable slits from 0-2 mm.

PRICED AT LESS THAN $1000.00

for more information

PRA

Photochemical Research Associates Inc.
University of Western Ontario
Department of Chemistry
London, Ont., Canada N6A 3K7
(519) 679-6181 Telex 064-7597

Modern Physics in Chemistry

VOLUME 1

Edited by E. FLUCK and V. I. GOLDANSKII

CONTENTS: *V. I. Nefedov*, Chemical Effects in X-Ray Spectroscopy, Part I *O. I. Sumbaev*, Chemical Effects in X-Ray Spectroscopy, Part II. *N. N. Bubnov and S. P. Solodonikov*, Electron Paramagnetic Resonance. *E. I. Fedin*, Nuclear Quadrupole Resonance. *A. L. Buchachenko*, Chemically Induced Dynamic Nuclear Polarization. *W. Meisel*, Mössbauer Double Resonance. *V. I. Goldanskii and V. P. Shantarovich*, Positronium in Chemistry. *V. G. Firsov and L. I. Ponomarev*, Mesic Chemistry.

1977, 420 pp., $36.10/£18.50 ISBN: 0-12-261201-9

Ion-Containing Polymers

PHYSICAL PROPERTIES AND STRUCTURE

By A. EISENBERG and M. KING

Volume 2 of *Polymer Physics*
Treatise Editor R. S. Stein

This volume describes the physical properties of polymers containing ionic groups ranging in concentration from the bulk to dilute solutions. Special emphasis is placed on the presence of aggregates of ions and the effects that these aggregates exert on the properties of the materials. Among the subjects discussed are: classification of ion-containing polymers by structural features and by nature of the ionic group; supermolecular structure of ion-containing polymers; glass transitions; viscoelastic properties of homopolymers; viscoelastic properties of copolymers, including ionomers; dielectric properties; polyelectrolyte complexes; conformation-dependent properties including viscosity and elasticity.

1977, 300 pp., $27.50/£19.55 ISBN: 0-12-235050-2

Methods of Molecular Quantum Mechanics

By R. McWEENY and B. T. SUTCLIFFE

Volume 2 of *Theoretical Chemistry: A Series of Monographs*/Series Editors: D. P. Craig and R. McWeeny

This book presents a unified and systematic account of the quantum mechanical methods available for the calculation and interpretation of the electronic properties of atoms and molecules. The emphasis is upon time-independent properties, in fixed-nucleus approximation, and within this field the coverage is essentially complete and self-contained. In addition to the traditional molecular orbital and valence bond methods, much space has been devoted to recent developments.

Reprinted with SI Units and Revisions
1976, 308 pp., $16.65/£8.50 ISBN: 0-12-486550-X

Send payment with order and save postage plus 50¢ handling charge.

Prices are subject to change without notice.

Chemical and Biochemical Applications of Lasers

VOLUME 3

Edited by C. BRADLEY MOORE

CONTENTS: *V. S. Letokhov and C. B. Moore*, Laser Isotope Separation. Introduction and Classification of Methods. Spectral Shifts and Selective Excitation. Selective Multistep Photoionization. Selective Two-Step Molecular Photodissociation. Photopredissociation. Molecular Dissociation in an Intense IR Field. Electronic Photochemistry. Vibrational Photochemistry. Selective Deflection of Atoms and Molecules. Non-Interchangeable Methods of Laser Isotope Separation. Economics and Engineering of Laser Isotope Separation. Conclusion. Other Applications. References. *R. V. Ambartzumian and V. S. Letokhov*, Multiple Photon Infrared Laser Photochemistry Introduction. Multiple Photon Absorption of IR Radiation: Experiment. Multiple Photon Dissociation of Polyatomic Molecules. Theoretical Interpretation of Multiple Photon Absorption and Dissociation of Polyatomic Molecules in an Intense IR Field. Molecular Isomerization by an Intense IR Field. Isotope Separation by Selective Molecular Dissociation by IR Radiation. IR Photolysis of Polyatomic Molecules. Applications to Chemical Synthesis and Materials Technology. Applications in Spectroscopy. Conclusion. References.

1977, 336 pp., $16.50/£11.70 ISBN: 0-12-505403-3

Isotopic Studies of Heterogeneous Catalysis

By ATSUMU OZAKI

CONTENTS: Analytical Methods for Isotopes. Isotopic Exchange Reactions. Studies of Catalyst Surfaces and the Absorbed State Isotopes. Reaction Path Studies. Rates of Elementary Steps. Isotope Effects. Author Index—Subject Index—Catalyst Index.

Co-published by Kodansha Ltd., and Academic Press. Academic Press Sales Territory: World except Japan.

1977, 239 pp., $25.00/£17.75 ISBN: 0-12531950-9

Foams

Edited by R. J. AKERS

This volume contains the proceedings of a Symposium held at Brunel University in September 1975, organised by the Society of Chemical Industry's Colloid and Surface Chemistry Group to review developments in the theory and application of foams. It contains 19 papers by leading authorities from many countries and, as such, is an authoritative statement of the present state of knowledge. There are reports of studies on the fundamental aspects of foams, including the interaction of microbubbles with colloidal particles and the conformation of proteins at the air-water interface. Among the applied topics considered are the clinical use of anti-foaming agents, uses of foams in papermaking and fire-fighting, and foams in brewing and food technology.

1977, 302 pp., $23.50/£12.00 ISBN: 0-12-047350-X

ACADEMIC PRESS, INC.
A Subsidiary of Harcourt Brace Jovanovich, Publishers
111 FIFTH AVENUE, NEW YORK, N.Y. 10003
24-28 OVAL ROAD, LONDON NW1 7DX

31.JA.25